Studies of CP violation in the $B_s \to J/\psi\phi$ channel, and prospects for future measurements at the ATLAS detector

Elliot James Sampson, MPhys

School of Physics, Faculty of Science and Technology

Lancaster University

A thesis submitted for the degree of

Doctor of Philosophy

January, 2026

Studies of CP violation in the $B_s \to J/\psi\phi$ channel, and prospects for future measurements at the ATLAS detector

Elliot James Sampson, MPhys.

School of Physics, Faculty of Science and Technology

A thesis submitted for the degree of *Doctor of Philosophy*. January, 2026.

Abstract

This thesis presents an analysis of the $B_s^0 \to J/\psi\phi$ decay, using the Full Run-2 proton-proton collision dataset at 13 TeV collected by the ATLAS detector at the LHC, corresponding to 139 fb^{-1} of integrated luminosity. The following quantities of physics interest are measured: the average decay width of the heavy and light B_s^0 meson states, Γ, the width difference, $\Delta\Gamma_s$, between the B_s^0 meson eigenstates, and the mass difference between light and heavy states Δm_s.

$$\Delta\Gamma_s = 0.0620 \pm 0.0034 \text{ (stat.)} \pm 0.0016 \text{ (syst.)}\text{ps}^{-1}$$
$$\Gamma = 0.6695 \pm 0.0011 \text{ (stat.)} \pm 0.0011 \text{ (syst.)}\text{ps}^{-1}$$
$$\phi_s = -0.069 \pm 0.030 \text{ (stat.)} \pm 0.020 \text{ (syst.)}\text{rad}$$
$$\Delta m_s = 17.889 \pm 0.060 \text{ (stat.)} \pm 0.061 \text{ (syst.)}\text{ps}^{-1}$$

At the time of writing, these results are not finalised and the exact values may change before official publication, and are ATLAS internal results.

Work presented in this thesis looks to develop methods with the goal of improving these results and builds on an ongoing analysis by the "BsJPsiPhi" team. There are three investigations presented in this thesis; one into the choice of the mass sidebands, a second into the use of sPlot statistical weighting as a background rejection model, and the third, a study of mass-time correlations in B_s^0 meson background. A separate study into the material budget at ATLAS, including

consideration of the material map variation systematics is also presented.

Acknowledgements

I would like to thank my supervisors throughout this process, Prof. Roger Jones, Drs. Smizanska, Barton, and Wharton without whom this thesis would not have been possible. I am also thankful to those within the "BsJPsiPhi" analysis team, especially those who came before me, allowing me to build on the foundations of their work.

I would like to acknowledge those within B06a, "the home of the hinged and ranged". Sharing an office with you was, trying at times, but ultimately a great pleasure and I did enjoy my time with you all. I truly believe you have each shaped me in some way and taught me something that I will carry throughout life. A special thanks to Ruby and Henry for those F1 chats that lasted a little longer than they should have and to Hannah for listening to my many complaints on the bus. I feel remiss to not give thanks to Chris, Adam, Niam, Beltran, Beth, Rebecca, Rachel, Martina, and Sasha, you are all wonderful people who will go far in whatever pursuit you choose. I am certainly going to miss those tea breaks going into a little too much detail about the cube rule of food and answering "Does it tea?". Of course, I cannot forget the "Higgs Boissons" pub quiz team, thank you to Katherine for the initial invite and thanks to Ishanee for the many arguments over who had the right answer.

My time on LTA was not easy, but without the support of my flatmate Mary and my friends Jackson and Thandi it would have been a considerable amount lonelier and I would be a lot less travelled. Thanks to both Neza and Alina for putting up with me in the office, your help and technical knowledge was always appreciated.

To my friends made outside of the office in Lancaster, thank you, especially my flatmates Billy, Euan, and Jack during my 3rd and 4th years living with you was a genuine pleasure and there are too many memories to recount. To Maisy, thank you for always providing a little perspective on my bad days while we chatted at the gym. To Callum and Kieran, thank you for being some of the greatest people I have met. Good luck to you all for the future!

To my high school friends, Ben, Finn, George, and Callum, your support

throughout this endeavour has been immense, but ultimately you have helped to keep me grounded. I cannot thank you enough, I always looked forward to coming home in the holidays for a catch up, I could not be more proud of you all.

To my family, simply thank you, I love you, for all you have done. Nana, Grandad, Aunty Son and Soph, thank you for being so proud of me, even though you are not quite sure of what I am doing. Mum and Dad you always picked up the phone when I called, those FaceTimes meant more to me than you probably realise. To Oliver, there is not a chance I would be where I am today without you, you made me realise completing a PhD was an option, and ultimately my competitive spirit got me through.

Finally to my darling Katherine, thank you. Your support over the last two years of this PhD is the reason I even finished it at all, I could not ask for any more from you, thank you.

Declaration

I declare that this thesis is a presentation of original research performed by the author. It has not been previously submitted, either in whole or in part, for the award of a higher degree at this, or any other university. The work presented in this thesis was made possible through the dedicated work of a large number of ATLAS collaborators, namely those associated with the $B_s^0 \to J/\psi\phi$ analysis team and the "TVPD" (formerly the Tracking Recommendations Forum) team for their assistance with the material map study. A list of the author's original contributions are summarised below:

- Evaluating the mass sideband choice for the $B_s^0 \to J/\psi\phi$ analysis.
- Using sPlot and sWeight for background rejection for the $B_s^0 \to J/\psi\phi$ analysis.
- Study of mass-time correlations in B_s^0 meson background for the $B_s^0 \to J/\psi\phi$ analysis.
- Production of the systematic uncertainties for the material map variations for ATLAS software release 22.

This thesis does not exceed the maximum permitted word length of 80,000 words including appendices and footnotes, but excluding the bibliography. A rough estimate of the word count is: 43701

Elliot James Sampson

Contents

List of Tables

List of Figures

Chapter 1

CERN, The European Laboratory for Particle Physics

1.1 CERN

Based just outside Geneva, Switzerland, situated on the Swiss-French border, is the *Conseil Européen pour la Recherche Nucléaire* or CERN, as it is commonly known, a stronghold in international particle physics research with a rich history of contributing to advancements in the sector over the last 70 years, established in 1954, [1]. CERN is home to many experiments, but most notably in the last decade to the Large Hadron Collider (LHC), a 27 km circumference circular particle accelerator, [2] and collider hosting four major experiments: ALICE, ATLAS, CMS, and LHCb [3, 4, 5, 6].

1.2 LHC

The Large Hadron Collider was first presented at a conference in 1984 as a successor to the Large Electron-Positron Collider (LEP), which was yet to be built, taking advantage of the tunnel also yet to be excavated. LEP began in 1989 with collisions at 45 GeV, and the last year of running was 2000 with collision energy of 209

GeV. LHC had its first meaningful collisions of 2.39 TeV in 2009, a year after problem solving an issue in the 2008 launch. Run 1 was a data-taking period between November 2009 and December 2012, after which the LHC went into Long Shutdown 1 (LS1), the first of many planned extended beam off times to focus on maintaining, fixing and upgrading both the LHC and the major experiments. During the shutdowns, there are targets to improve the centre of mass energy and the luminosity, as well as the hardware improvement, resulting in different run conditions and data-taking techniques. LS1 lasted between January 2013 and March 2015, immediately followed by Run 2, lasting between 2015 and 2018, going from $7 - 8$ TeV in Run 1 to 13 TeV for Run 2. Long Shutdown 2 (LS2), ended in 2022, after an extended hiatus. In July 2022, data taking began for Run 3, which is scheduled to complete at the end of 2025 after hitting 13.6 TeV centre of mass energy. Figure 1.1 shows the projected long-term schedule of the LHC until 2041.

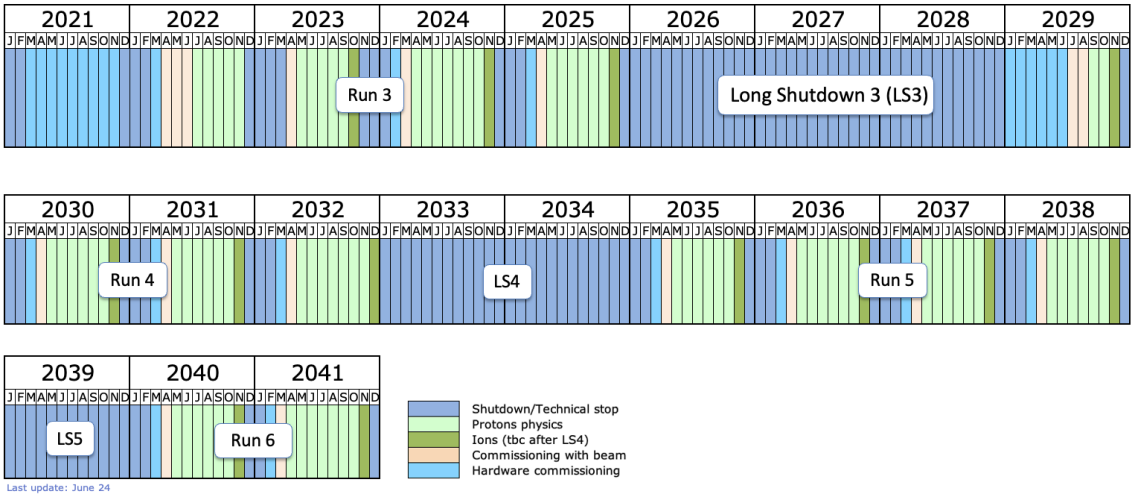

Figure 1.1: Projected LHC long-term schedule, until 2041, [7].

1.3 LHC Injector Chain

Figure 1.2 shows CERN's accelerator complex, including the LHC injector chain, covering the journey to accelerate protons to 6.8 TeV. To create proton-proton

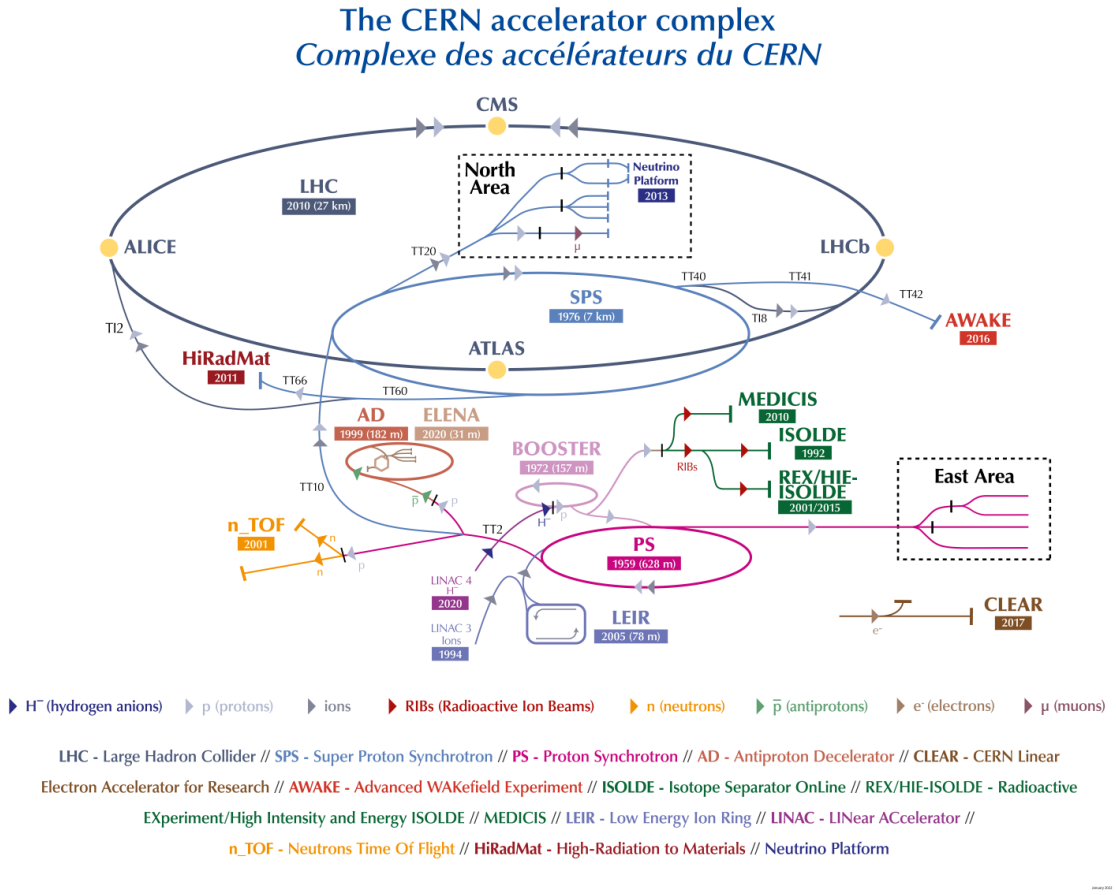

Figure 1.2: CERN Accelerator complex [8].

collisions: hydrogen atoms are stripped of their electrons through applying an electric field, the former hydrogen atoms, which are now protons, continue to the linear accelerator LINAC4. Forming them in bunches at 50 MeV, ready to be sent to the Proton Synchrotron Booster (PSB). The PSB, in turn, accelerates the bunches to an energy of 1.4 GeV where they enter the Proton Synchrotron (PS). Once accelerated to an energy of 26 GeV in the PS, the bunches are transferred to the Super Proton Synchrotron (SPS) which will prepare the bunches to be injected to the LHC rings at 450 GeV, once in the LHC ring, the proton bunches are accelerated to a final energy of 3.5 TeV, 4 TeV (Run 1), 6.5 TeV (Run 2) and 6.8 TeV (Run 3) and potentially even higher with Run 4.

The LHC can also be used for lead-lead collisions, which are primarily used

for studies in quark-gluon plasma. Lead-lead collisions are only mentioned out of completeness and are not necessary for the physics analysis within this thesis.

Figure 1.3 displays the eight octants of the LHC collider, each separated by 500 m long straight sections, which are known as "Points". ATLAS is at Point 1, with the "1" indicating which octant it is in.

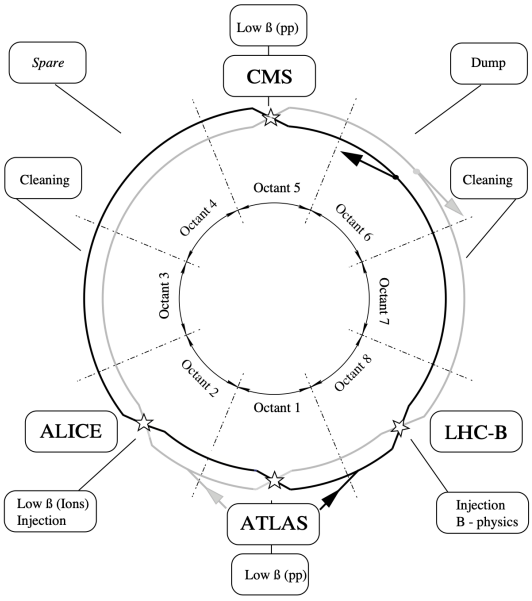

Figure 1.3: Schematic layout of LHC, showing the eight segments taken from [9]

1.4 ALICE

Based at Point 2, *A Large Ion Collider Experiment* (ALICE) is a 10,000 tonne detector that is 26 m long, 16 m high, and 16 m wide, [3]. Focusing on heavy-ion collisions at the LHC, ALICE's primary physics goal is to study the quark-gluon plasma (QGP), aiming to shed light on how matter is organised, through observing a distinct phase of strongly interacting matter created at extreme energy densities. ALICE has also measured a broad ensemble of QCD observables to characterize the QGP's properties [10].

1.5 ATLAS

The *A Toroidal LHC Apparatus* (ATLAS) detector is an LHC experiment based at Point 1 with it being 46 m long, 25 m high and 25 m wide, weighing 7000 tonnes, [4]. ATLAS is a multi-discipline detector with physics goals across Standard Model, including precision measurements, Higgs physics and measurements of the top quark. ATLAS also has beyond Standard Model (BSM) physics goals, including Supersymmetry (SUSY), CP Violation (CPV) and probing the existence of microscopic black holes. A detailed description of the ATLAS Detector is given in Chapter 2.

1.6 CMS

The *Compact Muon Solenoid* (CMS) is the second multi-purpose detector on the LHC ring, based at Point 4 in France. The complete detector is 21 metres long, 15 metres wide and 15 metres high, [5]. ATLAS and CMS are both general-purpose detectors and as such share similar physics goals, including precision Higgs measurements to understand electroweak symmetry breaking and BSM searches for SUSY, extra dimensions, and modified gravity at the TeV scale [11]. CMS aims to achieve these goals through a different detector geometry relying on a different magnet system design, meaning that CMS can be used in conjunction with ATLAS to cross reference and confirm results with one another, most notably for the discovery of the Higgs boson [12].

1.7 LHCb

The Large Hadron Collider beauty (LHCb) experiment specialises in investigating the slight differences between matter and antimatter by studying a type of particle called the "bottom quark", or "b quark". It is 21 m long, 10 m high and 13 m wide, weighing 5,600 tonnes [6, 13]. LHCb's physics goals are focussed around the

"b quark" and heavy flavour physics, as well as CPV and measuring properties of radiating B decays, amongst other key areas of interest.

Chapter 2

The ATLAS Detector

ATLAS is the largest multi-purpose detector at the LHC, with the ability to probe a wide range of physics, including physics beyond the Standard Model. The detector has a cylindrical geometry with the detector subsystems wrapped concentrically in layers around the interaction point. This chapter aims to take a deeper look into the ATLAS detector, beginning with some terminology before talking about the detector itself.

2.1 The ATLAS Coordinate System

ATLAS uses a right-handed coordinate system with its origin at the nominal interaction point (IP) in the centre of the detector and the z-axis along the beam pipe. The x-axis points from the IP to the centre of the LHC ring, and the y-axis points upwards. When describing the ATLAS detector volume, a spherical system is used, using the same origin, with the polar angle θ, defined as the angle from the beam axis (positive z) and the azimuthal angle ϕ, defined around the beam line, with the z-axis being used to determine the position along the beam line from the centre of the ATLAS detector.

2.1.1 Rapidity and Pseudorapidity

Rapidity is related to the angle between the xy plane and the direction of emission of a collision product. The equation for rapidity is:

$$y = \frac{1}{2} \ln \left(\frac{E + p_Z c}{E - p_z c} \right) \tag{2.1}$$

However, for highly relativistic environments, such as within particle physics detectors, it is often more useful to use pseudorapidity, η, which is defined as

$$\eta = -\ln \tan \frac{\theta}{2} \tag{2.2}$$

and η ranging from $+\infty$ to $-\infty$, for when the particle track is parallel to the beam line, and when $\eta = 0$ the particle track is perpendicular to the beam line. Figure 2.1 shows the cross section of the ID, and highlights the η range. It can be shown that for highly relativistic environments $y \simeq \eta$ as seen in [14].

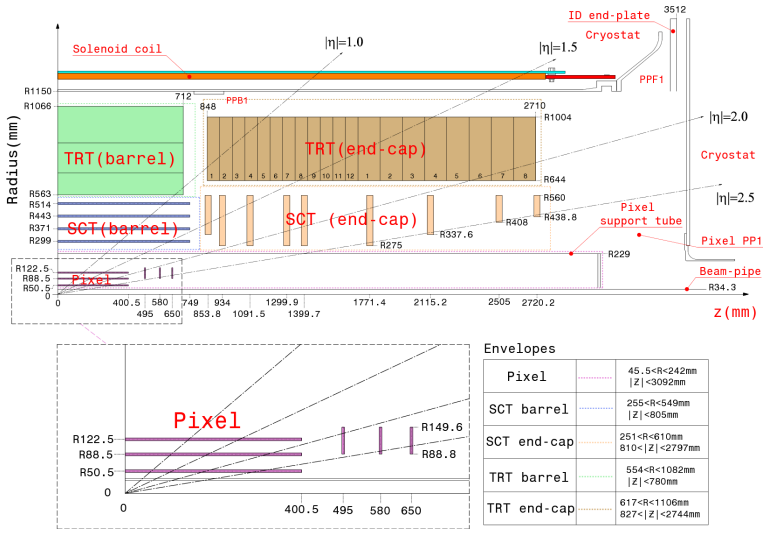

Figure 2.1: The cross-section of the inner detector layout through the beam axis. The ATLAS detector design is symmetrical in pseudorapidity. The detector region $|\eta| > 3$ is particularly challenging for track reconstruction and particle identification since particle densities and energies are at their highest. In hadron collider physics, particle production is normally constant as a function of pseudorapidity [15].

2.2 Luminosity

The luminosity of a particle collider is a measure of the rate of particle interactions produced, independent of the process. Luminosity is defined as

$$\mathcal{L} = \frac{dN}{dt} \cdot \frac{1}{\sigma_N} \tag{2.3}$$

where N is the count of events for some cross section σ_N.

The integrated luminosity is also useful to define, as this is time-independent.

$$L = \int \mathcal{L}(t)dt \tag{2.4}$$

Each run at the LHC aims to increase the overall luminosity which effectively means more data taking happening and, as such, better statistics and an increased chance for new physics discoveries to be made. Although in practice, there are trigger limitations.

The delivered integrated luminosity will be higher than the recorded luminosity due to detector inefficiencies and other loss factors, meaning recording all of the integrated luminosity is an impossible task. Figure 2.2 displays (a) the total delivered luminosity throughout data taking periods and (b) the recorded total integrated luminosity for the previous 24 months at the time of writing. Figure 2.2 (a) shows the feasibility of the goal to increase the luminosity year on year, and bodes well for the High Luminosity LHC (HiLumi LHC, or HL-LHC) as mentioned later on in 2.12. Figure 2.2(b) shows the challenges that come with recording the data; as optimistic as it is to aim for higher and higher luminosities, there is no point if the data cannot be recorded. The ramp up in luminosity has to be in accordance with data taking capacity across all four experiments outlined in Section 1.1, not just ATLAS. Current projections for the integrated luminosity are 200 fb^{-1} for 2025 and 395 fb^{-1} for 2026 during Run 3 [16].

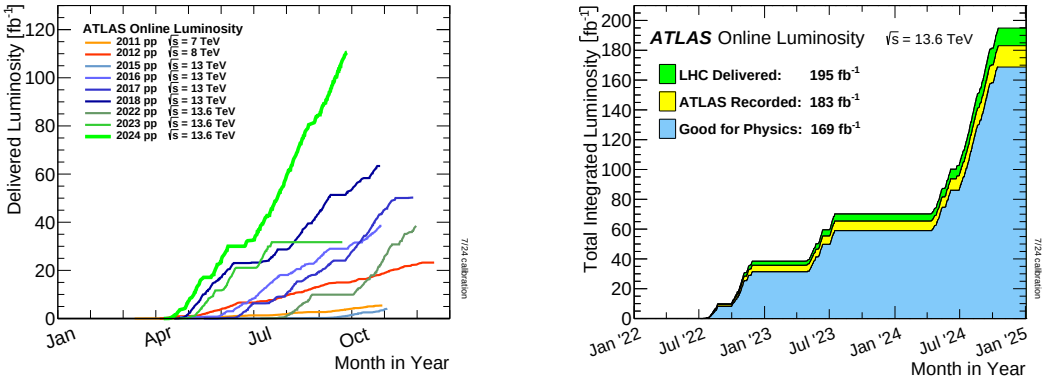

(a) Luminosity year by year

(b) Recorded Luminosity

Figure 2.2: (a) Cumulative luminosity versus day delivered to ATLAS during stable beams and for high-energy pp collisions, plot from ATLAS Luminosity public plots, [17]. (b) Cumulative luminosity versus time delivered to (green), recorded by ATLAS (yellow) and good for physics (blue) during stable beams for pp collisions at 13.6 TeV centre-of-mass energy in LHC Run 3 (2022-2024), plot from ATLAS Luminosity public plots, [18].

2.3 Pile-up

During a bunch crossing, it is possible that more than one pp collision occurs; this is defined as pile-up. In this scenario, the interaction with the highest transverse momentum as constructed from its associated vertices is designated as the hard-scatter vertex, and is the most likely candidate for interesting physics. Pile-up events are an unfortunate side effect of the pursuit of higher luminosity. The higher the luminosity, the higher the probability of a rare process happening, the more total events, increasing the overall dataset.

There are two pile-up types:

- **In time pile-up:** when additional pp collisions happen at the same time as a hard-scatter vertex and are included in the same bunch crossing.

- **Out of time pile-up:** when additional collisions happen out of time with the

interaction of interest and happen in bunch crossings just before or after the interaction of interest.

Figure 2.3 shows the mean number of interactions per crossing across the years of data taking for Run 2 as a function of recorded luminosity. This plot demonstrates that there are numerous interactions per crossing, and pile-up is an issue that must be considered. The total number of events in a bunch crossing follows a Poisson distribution, where $P(N_t)$ is the probability mass function, with the mean of ν_t events, which is the expectation value of the probability of N_t events in the same interval is given by

$$P(N_t) = \frac{{\nu_t}^{N_t}}{N_t!} e^{-\nu_t} \tag{2.5}$$

with the mean ν_t, given by the product of the delivered luminosity $\mathcal{L}$, with the inelastic cross section σ_t, and the mean bunch crossing period $\langle \Delta t_{bunch} \rangle$,

$$\nu_t = \langle N_t \rangle = \sigma_t \mathcal{L} \langle \Delta t_{bunch} \rangle \tag{2.6}$$

where the mean bunch crossing period is given by

$$\langle \Delta t_{bunch} \rangle = \frac{1}{f_{LHC} k} \tag{2.7}$$

where the LHC has a frequency of revolution of $f_{LHC} = 11.245$ kHz. For the total cross section, we assume $\sigma_t = 110$ mb. The luminosity, $\mathcal{L}$, and the number of bunches, k, depend on the running conditions.

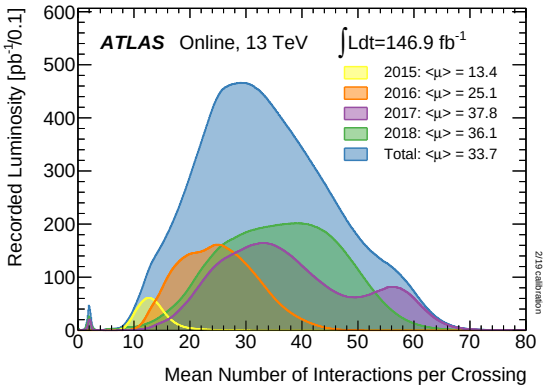

Figure 2.3: The luminosity-weighted distribution of the mean number of interactions per crossing for the 2015 – 2018 pp collision data at 13 TeV centre-of-mass energy, plot from ATLAS Luminosity public plots, [18].

2.4 Amplitude Function

Another key component of data taking at ATLAS is the beam size at the interaction point; with a smaller beam size, there is increased luminosity from higher collision rates. The beam envelope is described mathematically through the amplitude function $\beta(s)$, which is introduced to describe how the beam size varies around the accelerator and used to optimise the collision probability. As the LHC is circular, magnets are used to bend and contain the particle beam and later focus the beam for interactions. The bending and focussing can be described through Hill's equations, from which the amplitude function solutions are derived [19, 20].

$$\begin{aligned} \frac{d^2x}{ds^2} + K_x x = 0, \quad K_x &= \frac{q}{p}\frac{\partial B_y}{\partial x} + \frac{1}{\rho^2} \\ \frac{d^2y}{ds^2} + K_y y = 0, \quad K_y &= -\frac{q}{p}\frac{\partial B_y}{\partial x} \\ \frac{dz}{ds} + \frac{x}{\rho} &= 0, \end{aligned} \tag{2.8}$$

where $B_y(s)$ is the magnetic field along the path s along the y direction (only), with momentum p and charge q of the charged particles. $\rho = p/(qB_y)$ is the radius of curvature. The special linear case solution of Equation 2.8 is

$$x(s) = \sqrt{\epsilon}\sqrt{B(s)}\cos\psi(s) + \phi \tag{2.9}$$

The amplitude modulation function $\beta(s)$ varies with distance s to the minimum given by

$$\beta(s) = \beta^* \left(1 + \left(\frac{s}{\beta^*}\right)^2\right) \tag{2.10}$$

β^* is a value of the beta function at the Interaction Point, IP, where beam optics are designed to produce the narrowest focus possible. Within the LHC, this value ranges between $0.2 \rightarrow 1$m [21, 22].

2.5 Emittance ϵ

The emittance, ϵ, is defined as the amplitude, or spread of the transverse beam size, in the momentum-position phase space. Unlike the physical dimensions, the emittance is invariant with respect to the location in an accelerator. In phase space, see Figure 2.4, the beam dimension is given as the projection of the phase space ellipse onto the x-axis. The emittance, ϵ, is kept as small as possible to increase the probability of interactions, see luminosity. For the LHC, ϵ is typically within the range $\epsilon \approx 2 - 5$ μm [23].

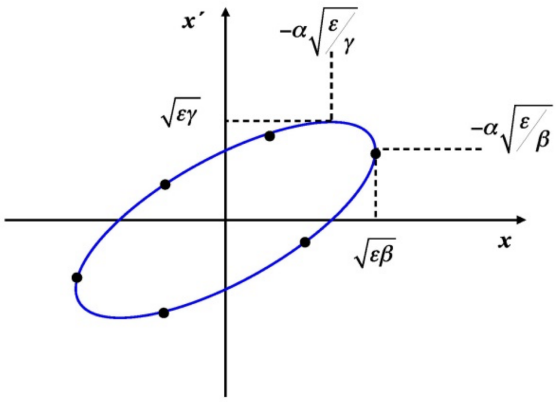

Figure 2.4: The phase space ellipse describing the transverse displacement of the beam in the x direction and its derivative $x\prime$ as a solution to Equation 2.9. Figure from [24]

2.6 Crossing angle

The crossing angle, θ_c, is the angle between interacting bunches. To maximise the luminosity, β^* must be reduced; this is done by rotating the bunches before entering the IP. The collisions with rotated bunches are called a "crab crossing", a schematic of which can be seen below in Figure 2.5

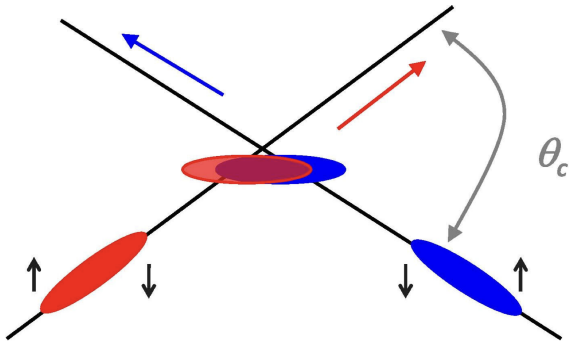

Figure 2.5: Schematic view of crab crossing of beams. [25]

2.7 ATLAS Tracking Detectors

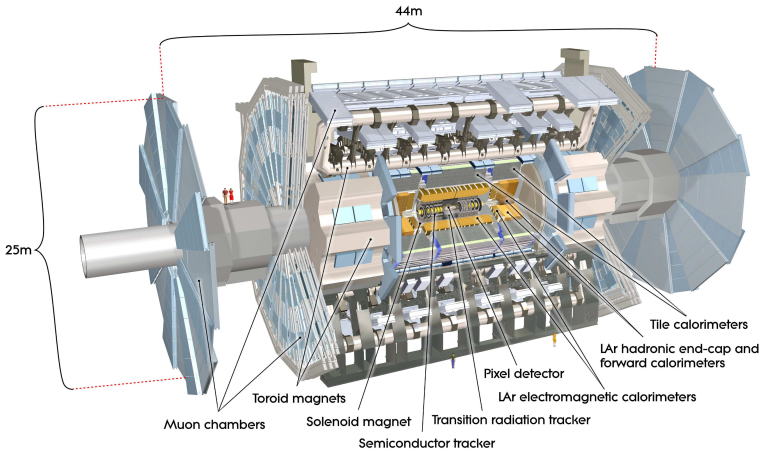

Figure 2.6: Cut-away view of the ATLAS detector. The dimensions of the detector are 25 m in height and 44 m in length, taken from [4]

Figure 2.6 is a schematic that shows the ATLAS detector, calorimeters, magnets

and inner detector. The ATLAS detector is usually described by moving away from the beam pipe in a radial direction. Following this logic, there are three main sections, the Inner Detector (ID), the calorimetry, and the Muon Spectrometer (MS) which will be discussed in this thesis, beginning with the ID.

2.7.1 ATLAS Inner Detector

ATLAS' innermost layer is the ID, made of three sensor systems all subject to a magnetic field parallel to the beam axis. The ID measures directions, momenta and charges of charged particles resulting from proton-proton collisions. Neutrinos, which do not interact with the detector, can be inferred through "missing" transverse energy. The ID has three main sections, the first being the pixel layer

2.7.1.1 Pixel Detector

Situated 33 mm from the LHC beamline, the Pixel Detector (PD) is the first point of detection within ATLAS. The pixel layer is comprised of four layers of silicon pixels. As charged particles emanate from the collision point, they deposit small amounts of energy in the PD. The position of the energy deposits are measured with a spatial precision of ≈ 10 μm and determine the origin and momentum of the particle. The PD is home to more than 92 million pixels and nearly 2000 detector elements. The PD is described in more detail in [26].

2.7.1.2 Semiconductor Tracker

Surrounding the PD is the Semiconductor Tracker (SCT), used for particle detection and track reconstruction of charged particles produced in collisions. The SCT consists of 4,000 modules of 6 million "microstrips" of silicon sensors, allowing for a precision of 25 μm for particle tracks, [27]. This layout is optimised so that each particle must cross at least four layers of silicon.

2.7.1.3 Transition Radiation Tracker

The Transition Radiation Tracker (TRT), is the final layer of the ID, made up of 300,000 thin-walled drift tubes. Each tube is just 4mm in diameter with 30 μm gold-plated tungsten wire at the centre, filled with a gaseous mixture. As the charged particle crosses the wire, it ionises the gas, creating a measurable electric signal. The TRT can provide particle information for particles that interact here. The TRT is the final array of sensors considered to be within the Inner Detector [27].

2.7.1.4 Inner Detector resolution

Resolution of the subdetector is an important factor when it comes to analysing the $B_s^0 \to J/\psi\phi$ decay, this is because the uncertainty in the lifetime measurement of the B_s^0 meson stems from the precision with which a track can be located and reconstructed. The source of the uncertainty on the track is ultimately carried through to the final uncertainty on the meson lifetime, Γ parameter. Table 2.1 shows the main characteristics for the ATLAS ID subdirectory, [28], including the Insertable B Layer (IBL) as a sub section of the detector.

Subdetector	Element size	Intrinsic resolution [μm]	Barrel layer radii [mm]	Disk layer —z— [mm]
IBL	50 μm × 250 μm	10 × 60	33.25	–
Pixel	50 μm × 400 μm	10 × 115	50.5, 88.5, 122.5	495, 580, 650
SCT	80 μm	17	299, 371, 443, 514	from 839 to 2735
TRT	4 mm	130	from 554 to 1082	from 848 to 2710

Table 2.1: Summary of the main characteristics of the ATLAS ID subdetectors, [28]

2.7.2 Tracking Parameter resolution

Another of the interesting parameters to focus on is the transverse impact parameter, d_0. The resolution of d_0 has a knock-on effect on with the overall track uncertainty. Track resolution of any given parameter, X, can be expressed as a function of transverse momentum, p_T, as seen in Equation 2.11.

$$\sigma_X(p_T) = \sigma_x(\infty)(1 \oplus \frac{p_X}{p_T}) \tag{2.11}$$

where $\sigma_X(\infty)$ is the asymptotic resolution expected at infinite momentum, p_X is a constant representing a given value of p_T for the parameter, and $\oplus$ is denoting addition in quadrature. This expression is an approximation, designed for high and low p_T environments. Table 2.2 displays the ideal $\sigma_X(\infty)$ and p_X for tracks in two η regions, corresponding to the barrel, where detector material is at a minimum, and end caps where the material is at a maximum, [29].

Track parameter	$0.25 < \|\eta\| < 0.50$		$1.50 < \|\eta\| < 1.75$	
	$\sigma_X(\infty)$	p_X (GeV)	$\sigma_X(\infty)$	p_X (GeV)
Inverse transverse momentum (q/p_T)	0.34 TeV^{-1}	44	0.41 TeV^{-1}	80
Azimuthal angle (ϕ)	70 μrad	39	92 μrad	49
Polar angle ($\cot\theta$)	0.7×10^{-3}	5.0	1.2×10^{-3}	10
Transverse impact parameter (d_0)	10 μm	14	12 μm	20
Longitudinal impact parameter ($z_0 \times \sin\theta$)	91 μm	2.3	71 μm	3.7

Table 2.2: Expected track-parameter resolutions, (RMS), at infinite transverse momentum, $\sigma_X(\infty)$ and transverse momentum, p_X, at which the multiple scattering contribution equals that from the detector resolution, see Equation 2.11. The momentum and angular resolutions are shown for muons, while the impact-parameter resolutions are shown for pions, [29].

Figures 2.7 and 2.8 show the transverse and longitudinal impact parameter resolutions for isolated pions, without a beam constraint and assuming the misalignment, miscalibration, and pile up are negligible. Figure 2.9 shows the comparison of the impact parameter resolutions for pions and muons; the muon distributions are close to Gaussian, and the pion distributions are slightly broader.

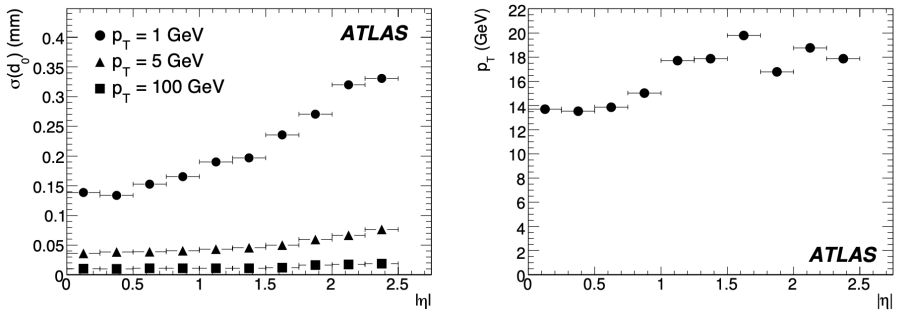

Figure 2.7: Transverse impact parameter, d_0 resolution (left) as a function of $|\eta|$ for pions with $p_T = 1, 5,$ and 100 GeV. Transverse momentum of pions, (p_X in Equation 2.11), as a function of $|\eta|$ (right), [29].

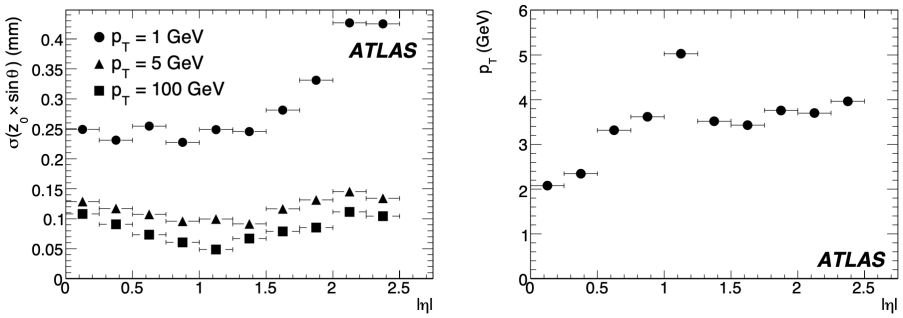

Figure 2.8: Modified longitudinal impact parameter, $z_0 \times \sin\theta$ resolution (left) as a function of $|\eta|$ for pions with $p_T = 1, 5,$ and 100 GeV. Transverse momentum, (p_X in Equation 2.11), as a function of $|\eta|$ (right), [29].

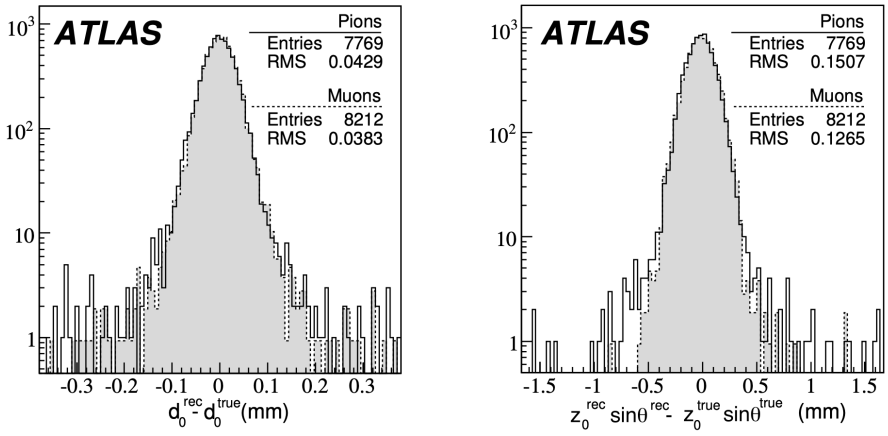

Figure 2.9: Resolution of the transverse impact parameter, d_0, (left) and the modified longitudinal impact parameter, $z_0 \sin\theta$ (right) for 5 GeV muons and pions with $|\eta| \leq 0.5$, which corresponds to the first two bins of Figures 2.7 and 2.8. [29].

2.8 ATLAS Calorimetry

Outside of the TRT and the Inner Detector, the next layer is the Electronic Calorimeter, then the Hadronic Calorimeter. ATLAS calorimetry is a system of sampling detectors sizeable enough to stop the traversing particle and measure its energy via the detection of secondary particles created by absorbing the energy of the particle. The traversing particle(s) leave a trail of secondary particles along their path in the detector volume while losing a fraction of their energy.

2.8.1 Electromagnetic Calorimetry

Designed to measure the energy of electrons and photons, the Electromagnetic Calorimeter (ECal) is the first of two calorimeters, the second being the Hadronic Calorimeter (HCal). Both of these calorimeters are sampling calorimeters, which work by alternating layers of "passive" materials which cause particle showers and "active" mediums which sample the energy deposits. Sampling calorimeters are chosen as they are more cost-effective than homogenous calorimeters, especially for large volumes. One downside of a sampling calorimeter is the inferior energy resolution. For more detail on the ECal, see [30].

2.8.2 Hadronic Calorimetry

The HCal is home to hadronic calorimetry in ATLAS. As hadrons interact with the steel absorber, showers are produced, consisting primarily of pions. These showers interact with the plastic tiles, producing scintillation light which can be read out via fibres and into photomultipliers [31].

2.8.3 Forward Calorimetry

The ATLAS Forward Calorimeter (FCal) is in the far forward region of the detector ($3.1 < \eta < 4.9$) close to the beamline, responsible for both the electromagnetic and hadronic calorimetry. Constructed from three modules within each of the end

caps, the first module is made from copper, a material choice that is optimised for electromagnetic calorimetry, both the second and final layers are tungsten, a material choice optimised for hadronic calorimetry, whilst LAr provides the active medium for both, [32].

2.8.4 Calorimetry resolution

Energy measurement with an electromagnetic calorimeter is based on the principle that the energy recorded by the detector is proportional to the energy of the incident particles. Within a calorimeter, the energy is represented by the summation of the total length of ionising tracks in the shower, which is proportional to the total number of track segments in the shower. As this track formation is a stochastic process, it introduces statistical fluctuations into the measurement. Actual energy resolution of calorimeters depends not only on the stochastic term, but also on a noise term originating from electrical readout, and an additional constant term. This is displayed in Equation 2.12, [33],

$$\frac{\sigma}{E} = \frac{a}{\sqrt{E}} \oplus \frac{b}{E} \oplus c \tag{2.12}$$

where the $\oplus$ symbol denotes summation in quadrature. The stochastic term is given by a, which relates to the shower fluctuations, b is the noise term, and c is a constant. Whilst this is introduced for electromagnetic calorimetry in 2.12, the same holds true for the other calorimetry more widely, including the hadronic and forward calorimeters within ATLAS. Table 2.3 displays representative energy resolutions for the calorimetry subsystems in ATLAS, [33].

2.9 Muon Spectrometer

The ATLAS muon detector system is paramount in this analysis as it provides ATLAS with a trigger for selecting events containing high-energy muons, such as in the decay of $B_s^0 \to J\psi\phi$. The Muon Spectrometer (MS) was designed for

Calorimeter	Resolution (%)
ECal	$\sigma(E)\frac{10}{\sqrt{E}} \oplus 0.7$
HCal	$\sigma(E)\frac{50}{\sqrt{E}} \oplus 3$
FCal	$\sigma(E)\frac{100}{\sqrt{E}} \oplus 10$

Table 2.3: Indicative resolutions of the ATLAS calorimeters, [33]

high-quality stand-alone muon measurement, with large acceptance for both muon triggering and measurement. Tracking is achieved using high-precision drift and multiwire proportional chambers. Event triggering is achieved by using dedicated fast detectors that allow bunch crossing identification, coarse position measurements and determination of the transverse momentum for trigger decisions. The precision tracking achieved by the MS uses the smaller precision detectors, including the Monitored Drift Tubes (MDT), Cathode Strip Chambers (CSC), Resistive Plate Chambers (RPC), and Thin Gap Chambers (TGC). Further information on the MS and MS triggers can be found in [4] specifically Chapter 6, and the technical design report [34].

2.9.1 Monitored Drift Tubes

The MDTs sample the muon trajectory in three high-precision measuring stations placed inside the toroidal magnets for an eta range of $|\eta| < 2.0$. MDTs are arranged in three cylindrical layers around the beam axis, and each of the three stations measures the muon with a precision in the order of 50 μm. It also provides angular information on the track segments, which is used to improve the pattern recognition for the reconstruction of the full muon track.

2.9.2 Cathode Strip Chambers

The next component of the Muon Spectrometer are the Cathode Strip Chambers (CSCs), designed to cope with the increased particle fluxes and particle track density

in the forward direction of $2 < |\eta| < 2.7$. The CSCs have a similar spatial resolution to the MDTs, having a spatial resolution in the range of 50 μm.

2.9.3 Resistive Plate Chambers

Resistive Plate Chambers (RPCs) cover the barrel region, $1.105 < |\eta| < 2.0$, and contain two detector layers, each of which has two parallel resistive plates that are separated by 2 mm, filled with ionising gas, an electronegative gas and a quencher gas. The signal is read out by two orthogonal readout strips, which allows for measurements of the particle in both ϕ and η.

2.9.4 Thin Gap Chambers

The Thin Gap Chambers (TGCs) cover a range of $1.05 < |\eta| < 2.4$, and they have been chosen for the End-cap of the ATLAS MS because of their very good rate capability. This is a result of the geometric setup, being made of multi-wire proportional chambers with a wire-to-cathode distance of 1.4 mm, allowing for timing resolution in the order of nanoseconds. These cells are filled with a gaseous mixture of Carbon Dioxide (CO_2) at 55% and n-pentane (n-C_5H_{12})(45%), with the anode being kept at a nominal potential of 2.9 kV. An additional benefit of the TGCs is the ageing characteristics; the efficiency of the chambers under irradiation is about 98% - very close to the one measured without irradiation.

2.10 ATLAS History

ATLAS has one of the richest histories within the modern LHC, being one of the two experiments involved with the discovery of the Higgs Boson in 2012, [35], [12]. ATLAS is home to much more than just the Higgs discovery, including world-leading measurements, and precision measurements of the Higgs boson properties, enhanced understanding of the top quark interactions, measurements of Standard Model properties and searches for physics beyond the Standard Model.

2.11 ATLAS Future

The future of ATLAS, and more wholly, the LHC, is focussed on the intended ramp up in luminosity and approach to the HL-LHC. With the expected luminosity increase from 1 $\times 10^{-34}$ $cm^{-2}s^{-1}$ currently, to towards 1×10^{-35} $cm^{-2}s^{-1}$. The HL-LHC has physics goals of improving Standard Model measurements, continuing work on beyond Standard Model searches, flavour physics, Higgs properties and QCD at high density and temperature. Before the HL-LHC, Run 3 will occur, which is discussed in Section 2.12.

2.12 ATLAS Run 3

At the time of writing, Long Shutdown 2 has finished and Run 3 is due to end the end of 2025. Run 3 is the final stage due to complete before transitioning into the HL-LHC, beginning with Long Shutdown 3.

There are a number of goals for Run 3. More high quality data is the priority, with the improvements made from the Long Shutdown 2. The physics goals include advancing the understanding of the Higgs boson, this stems from the increased production of the Higgs, allowing more data for its study. Another of the physics goals is to continue to search for BSM physics and test the current understanding, the Standard Model is not perfect, and needs refining which is motivation for the improved theoretical understandings and validation of predictions.

Chapter 3

ATLAS Triggers and Data Acquisition

3.1 ATLAS Triggers

The LHC produces staggering amounts of physics events, far exceeding the hardware limitations, with data volumes nearing 60 TB, from roughly 1.5 billion pp collisions per second [36]. To manage this, there are high level event selection systems known as "triggers". Triggers rapidly assess incoming events in real time, deciding which events are useful for physics analyses. Using triggers, the volume of data is reduced significantly, trimming out the uninteresting events and passing the interesting events onto more triggers.

ATLAS had a two-level trigger system, the first is the Level 1 trigger (L1), a hardware based system utilising bespoke electronics to trigger on simplified data from the calorimeters and muon detectors. The L1 triggers reduces the detector output from 40 MHz down to about 100 kHz, with an approximate latency of a few millions of a second. Once an event has passed the L1 trigger, it is passed onto the High-Level Trigger (HLT), for further processing. For a complete understanding of Triggers and Data Acquisition (TDAQ), please see both [37, 38].

Level 1 Triggers are used to identify the Regions-of-Interest (ROIs) in η and ϕ

within the detector to be investigated by the second stage of the trigger. The HLT is a software based system using multiple trigger algorithms which reject and accept events with full detector information in parallel. The rate of each HLT chain is 1.2 kHz, and roughly 1.2 GB of data is stored every second [39], the HLT is described in more detail in Section 3.1.2.

While the L1 trigger and HLT are most important for the analysis described in this thesis, it is important to mention the Run 1 DAQ geometry, given the overlap of this analysis with previous Run 1 analyses. In Run 1, there was no HLT; instead, there were the Level 1 Trigger, Level 2 Trigger and the Event Filter.

3.1.1 Level 1 Trigger

The L1 Trigger has many subdivisions, the L1 Calorimeter trigger (L1Calo), processes inputs from the calorimeter, to identify electron, photon and τ lepton candidates using the Cluster Processor (CP), and using the Jet/Energy sum Processor (JEP), for global sums of the total and missing transverse energy as well as jet identification.

The L1 Muon trigger (L1Muon), takes input from the Muon Spectrometer (MS), specifically the Resistive Plate Chambers (RPCs), and the Thin Gap Conductors (TGCs), to determine the deviation and hit pattern from that of a muon with infinite momentum. The L1Muon uses coincident requirements between inner and outer TGC stations and tile calorimeters.

At this point in the L1 trigger, some of the information is split, with the L1Calo trigger objects, electrons, jets and taus being sent to the L1 Topological Trigger (L1Topo), and the calorimeter multiplicities being sent to the Central Trigger Processor (CTP). While the L1 Muon sends L1Muon trigger objects to the L1Topo, the muon multiplicities are sent to the CTP. The L1Topo consists of two Field Programmable Gate Array (FPGA), based processor modules, identical in hardware, but programmed differently for the objects received from the L1Calo or L1Muon trigger systems.

All the multiplicity information from the L1Calo and L1Muon is gathered and sent to the CTP, which makes the trigger decision. The CTP also takes signals from detector subsystems and is responsible for dead-time, in which the trigger delays the time between consecutive L1 accepts, "at the end of Run 2, the simple dead time setting was four bunch crossings, which corresponds to an inefficiency of about 1% for a L1 rate of 90 kHz" [38].

3.1.2 High Level Trigger

After passing the L1 trigger, events undergo additional processing by the High Level Trigger using more detailed information than L1, and some new information that was unavailable to L1. The HLT operates either within ROIs identified in L1, or the full detector. For both cases, data is fetched on demand from the readout system. The HLT is a software-based system, employing thousands of trigger algorithms to accept or reject events with the full information from the detector; these decisions happen in parallel. Following the three stages of the L1 outlined above, the HLT takes over and uses detailed reconstruction algorithms to further filter events.

For Run 2, the new Inner Detector (ID), trigger exploits the merged HLT and includes information from the Insertable B-Layer (IBL), which was new for Run 2. This drastically improves tracking performance and impact parameter resolution. ID tracking also utilised Fast TracKer (FTK) [40], a specialist hardware system designed to improve HLT performance when that became available. The ID tracking algorithms are categorised into fast tracking, using pattern recognition, and precision tracking, which uses more offline tracking algorithms. Both fast and precision tracking are configured to run within an RoI from L1.

Another branch of the HLT is calorimeter reconstruction, involving a series of algorithms to convert calorimeter signals into cells and clusters. These cells and clusters are vital for determining shower shape and isolating properties of candidate particles such as muons. They are used to calculate missing transverse energy (MET) as well as candidate reconstruction for electrons, photons, taus and jet candidates.

MET is a useful quantity as this missing energy gives a better indication of the whole interaction picture, quantifying the particles that have not interacted with the detector. HLT reconstruction algorithms have access to full detector granularity, allowing improved accuracy and precision compared to that of L1. The data is split into ROIs, in which well-defined objects such as electrons, photons, muons and taus are reconstructed, and full calorimeter reconstruction is used for less well-defined sums like jets and global event quantities. Raw data is unpacked and converted into a collection of cells ready for the clustering algorithms to reconstruct energy deposits.

Muon reconstruction within the HLT is divided into fast and precision reconstruction stages. In the fast reconstruction stage, the HLT takes an L1 muon candidate as a start for the algorithm, then, using precision data from the Monitored Drift Tube (MDT) chambers in the RoI, better reconstruction of the candidates is achieved. A track fit is performed to create a Muon Spectrometer only (MS-only) muon candidate, which is back extrapolated to the interaction point, IP, and combined with information from the ID for a combined muon candidate.

The precision reconstruction stage follows a similar approach, starting with a candidate from the fast reconstruction ROIs. However, if there is no matching track for the MS-only candidate, the muon candidate is extrapolated from the ID to the MS in an inside-out fashion, which is computationally slower. Shown in Figure 3.1 is the full trigger architecture in Run 2, which is useful for visualising the subsections of the triggers and how different sections of the trigger system are linked.

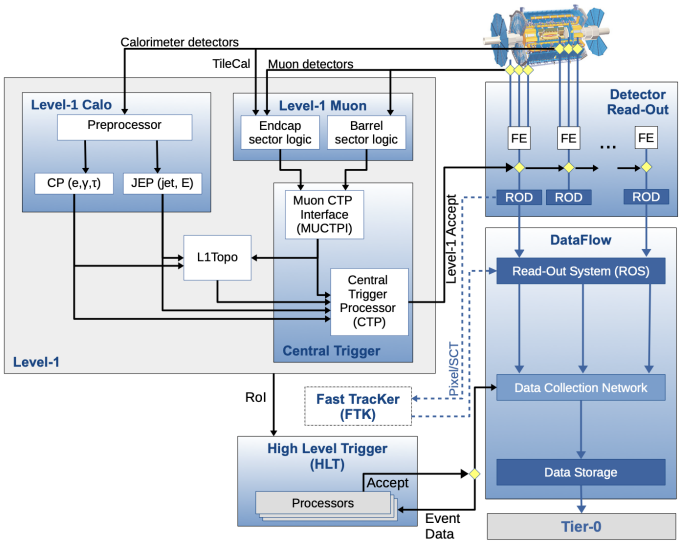

Figure 3.1: The ATLAS TDAQ system in Run 2, showing the components relevant for triggering as well as the detector read-out and data flow [41].

3.1.3 B Physics and Triggers

The analysis on which this thesis focuses is based on the $B_s^0 \rightarrow J/\psi\phi$ decay; the dominant triggers are based on the decay of $J/\psi \rightarrow \mu^+\mu^-$ with transverse momentum, p_T, thresholds in pairs of two 4 GeV muons, a 4 GeV and 6 GeV muon pair, and pair of 6 GeV muons. The analysis spans multiple data-taking periods, from 2015 to 2018 inclusive, with different instantaneous luminosity. Taking the data quality requirements from [42], specifically the performance of the ID, calorimeter systems and MS, and the uncertainty in the integrated luminosity of 139 fb^{-1} is 1.7% [43]; the primary luminosity measurements were obtained by the LUCID-2 detector [44]. LUCID-2 serves as ATLAS' dedicated luminosity monitor, providing the experiment's recorded luminosity.

ATLAS is a multi-purpose physics experiment designed to probe across many subsections of particle physics. One of these is B-Physics, the physics of the bottom quark. Whilst ATLAS is not a "B-factory" where "99% of bunch crossings end up with non-b events." [45], ATLAS was designed with a B-Physics programme in mind, and "A choice of one muon trigger gives a very simple, fast and efficient way

for b-events selection by ATLAS detector." [45] aids the pursuit of B-Physics. There are four parts of the physical hardware of the ATLAS detector that lend themselves towards B-Physics. They have been discussed before in Chapter 2, but to recap and highlight their relevance to B-Physics, the first is the MS.

The ATLAS B-physics triggers primarily select B-events containing two muons, though some triggers also target single muon or muon-electron signatures. Accurate muon identification is crucial for the ATLAS B-physics programme. In cases where muons decay before reaching the MS, the outer calorimeter layers can be used for muon identification, particularly for muons with $p_T > 3$ GeV.

The electromagnetic calorimeter (ECal) is also used in muon identification and tracking. Since muons are electrically charged particles, they can be tracked as they traverse the ECal. Additionally, the ECal can also identify the neutral π mesons by analysing their decay products, with specific reconstruction gaps assigned to pion signatures. The ECal is also essential for detecting the electronic final states in certain B-physics decays, working in conjunction with the ID.

The ID is used for track measurements with the three subsections of the Pixel Detector (PD), Semiconductor Tracker (SCT), and Transition Radiation Tracker (TRT), with the PD being 33 mm from the beam line. It allows for high precision vertexing needed for B-Physics in conjunction with the ATLAS 4T magnetic fields [46].

Having introduced the ALTAS trigger systems, now there is a choice on which B-physics decay to examine. For this thesis, the focus is on the $B_s^0 \to J/\psi\phi$ decay. The $B_s^0 \to J/\psi\phi$ decay is one of the more interesting decay channels, which can be used to probe new physics, specifically the behaviour of matter and antimatter and the asymmetry in the universe. This is done through the analysis of B meson mixing, described in Section 5.5.3, in which the superposition of light and heavy states has different lifetimes, and we can measure the differing decay widths to investigate these lifetimes. Another useful parameter from this decay is ϕ_s, the phase difference between the B meson mixing and the $\bar{B}$ meson decay. ϕ_s is precisely predicted by

the SM and any deviation could imply new physics.

3.2 ATLAS offline software

Once data has been collected by the ATLAS Data Acquisition, DAQ, systems, it is stored for analysis. The offline analysis is performed using "Athena" [47], which is a suite of custom software packages written by the ATLAS collaboration, and ROOT [48]. Athena is a framework consisting of more than 2000 packages, with a further 100 packages with dependencies on external packages like Geant4 [49], a simulation platform used to model particles passage through matter, and Monte Carlo generators, [50, 51]. Athena is under continuous development, and with major releases available yearly to be compatible with the respective year's data taking.

ROOT is also heavily used at CERN and within ATLAS for physics analyses, written by CERN scientists in 1995 and still being developed and refined with recent releases. ROOT is designed for large data files and exploits parallel data processing to minimise computing time. ROOT also contains the packages "RooFit" and "RooStat", which are specialised ROOT tools designed for both fitting and modelling and statistical analysis, respectively.

3.3 ATLAS Data Processing and Formats

3.3.1 Event Data Model

Data within ATLAS is stored in several formats, dependent on the stage of reconstruction and the analysis requirements. Most analyses use Monte Carlo (MC) simulated data, which is requested from the ATLAS MC simulation group. This simulated data becomes the foundation from which the analysis team builds their framework. An analysis typically begins with the processing of MC data, in which the format of the "data" being worked on changes depending on the progress or maturity of the analysis. For MC, the data is turned from simulated

events into analysed data, the event generator output, "EVNT", the simulated detector interaction results in "HITS", and the simulated detector output, a raw data object "RDO". RDOs are then processed into analysis object data, "AOD", before becoming a more specialised analysis-ready AOD, a derived AOD, "DAOD". DAODs are AODs that have been preprocessed for the analysis, including steps such as event filtering, data reduction and object selection to create analysis ready datasets more manageable than a full AOD for analysis. For real data from the detector, there are fewer stages of data processing, as the data is already at the RDO stage when detected by ATLAS. Similarly, an analysis will convert the RDO into an AOD, before further refining the AOD into a DAOD, before ending with analysis data files. Figure 3.2, introduces the workflow and how the data form changes throughout each stage.

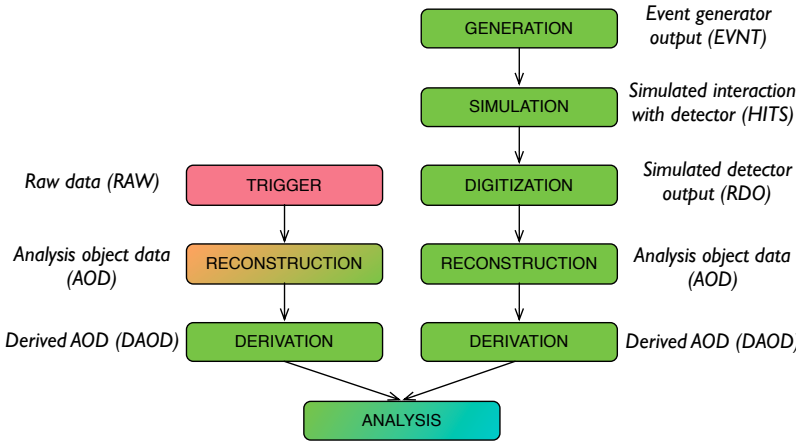

Figure 3.2: Flow diagram of the data formats in ATLAS, from [52].

Figure 3.2 shows how the data is transformed through processing, in experimental data if an event is accepted by L1, the detector sensor hit information is passed from the Front End, FE, detector electronics to the ReadOut Drivers (RODs). RODs perform initial data processing and formatting, and the data is passed to the ReadOut System (ROS), where the data is buffered so the HLT can investigate the data. After all HLT algorithms have been run, the data is stored locally and can be sent and stored around the world via the worldwide LHC computing grid. Here,

the data is stored in RAW format, containing only information about the event from the L1 and HLT. Athena accepts RAW data and processes it into the xAOD format, available in several forms, which the "x" denotes. xAODs are ROOT-readable and are much leaner, holding only the physics object information for the specific analysis. The combined performance group applied all recommended prescriptions so that in the next stage, the xAOD can be slimmed and skimmed at further request of the analysis team. The final production state is an NTuple, which is stored as a ROOT file, used specifically in the analysis. The data processing has been discussed here where a physical or simulated event has been formatted into an electronic signal and then into raw data. This process continues with the formation of tracks, seen in Section 3.5.1.

3.3.2 Monte Carlo Simulation

MC Simulation allows for probability-based modelling of events and physical processes, allowing a way to compare current understanding to experimental data. MC has a wide application, such as detector simulation or physics simulation for specific decay products and kinematic properties. It can be fine-tuned and be as specific or as general as required by the user. In ATLAS, two main MC generators are used, Pythia [50, 53] and Herwig [51, 54], although another generator, Sherpa [55, 56] is sometimes used. In some cases a combination of generators is used, with each generator having its own specialities, extensions and benefits.

As shown in Figure 3.2 for MC production, particles are generated with mutual relations and the output is stored in EVNT files. Geant4 is used to simulate the passage of particles through the detector, taking EVNT files as input and provides information on deposited energy, position and time. The output of the algorithms is stored in the format of HITS.

The HITS data are digitised by simulating the electronic response to the deposited energy; pile-up can be accounted for in this step. The digitisation output uses the same data structure as the real data, so the simulation output is

reconstructed by the same tools as used for data reconstruction, and stored in xAOD files. The derivations and NTuples can be produced using the same procedure as data production.

3.4 Worldwide LHC Computing Grid

The Worldwide LHC Computing Grid (WLCG) [57], was created to deal with the volume of data storage and analysis necessary for that of the LHC. The WLCG combines about 1.4 million computer cores and 1.5 exabytes of storage from over 170 sites in 42 countries, and it runs over 2 million tasks per day. At the end of the LHC's LS2, global transfer rates exceeded 260 GBs^{-1}. The WLCG is split into four layers, or tiers, with each tier providing a specific set of services. Figure 3.3 shows the first three tiers of the WLCG.

- **Tier 0**: the CERN Data Centre, which is located in Geneva, Switzerland. All data from the LHC passes through the central CERN hub, despite CERN only processing 20% of the data due to time requirements.

- **Tier 1**: These are fourteen large computer centres with sufficient storage capacity and with round-the-clock support for the Grid. Tier 1 sites are responsible for a multitude of tasks, including the safe-keeping of raw and reconstructed data, large-scale reprocessing and dealing with the corresponding output, distribution of data to Tier 2s and safe-keeping of a share of simulated data produced at these Tier 2s.

- **Tier 2**: There are roughly 160 Tier 2 sites, covering the majority of the globe. Tier 2 sites are typically universities and other scientific institutes, which can store sufficient data and provide adequate computing power for specific analysis tasks. They also deal with analysis level workloads, with necessary computing tasks being distributed across these sites. Tier 2 sites also handle a proportional share of simulated event production and reconstruction.

- **Tier 3**: Tier 3 sites are less restricted in definition, with no formal engagement between WLCG and Tier 3 resources; often, individuals will access these facilities through local computing resources, which can consist of local clusters in a university department or an individual PC.

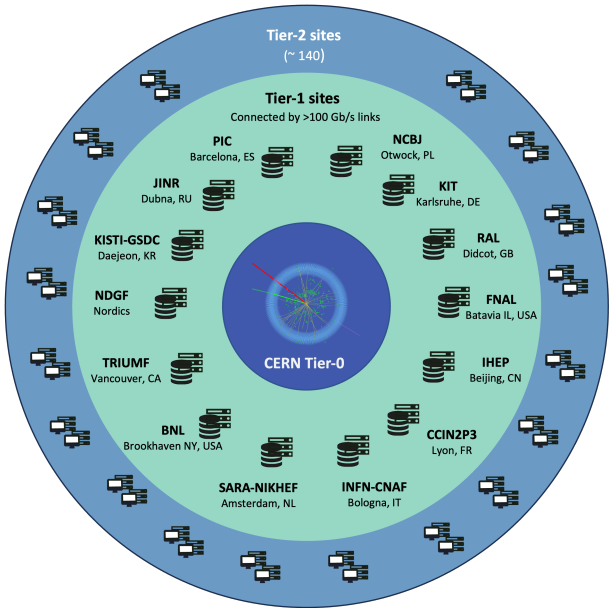

Figure 3.3: A WLCG schematic showing the first three tiers [58].

3.5 Physics Object Reconstruction

Tracking within ATLAS can be thought of as the world's worst game of dot to dot, going from physical events to electrical signals and digital hits to a reconstructed object is quite some undertaking. Athena uses pattern recognition of the hits to reconstruct objects to identify physical particles that can be assigned to each hit. If these reconstructed objects are close to the origin, they can be combined into a set of tracks; the point at which a selection of tracks meet is deemed a vertex. Figure 3.4 is a diagram displaying a simplified version of ATLAS event Tracking, with key terminology defined visually.

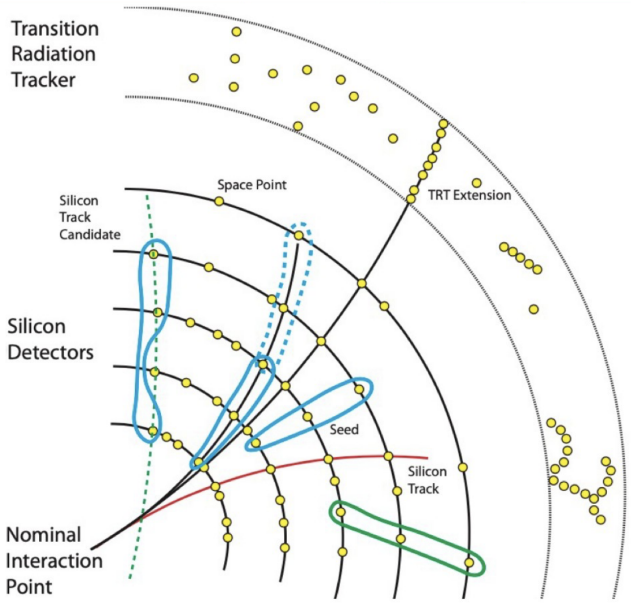

Figure 3.4: ATLAS Tracking Diagram, [59]. The yellow points represent the hits in the ID sensors. The initial seeds for the tracking algorithms are shown as blue and green boundaries. The red curve shows the successfully reconstructed tracks.

3.5.1 Tracking

Tracking within ATLAS is done in two ways, often in combination. First, there is the "Primary Tracking" which sweeps out from the beam line radially through the ID, going from a higher density of hits to a lower density of hits. It is also possible to use the ATLAS "Back-Tracking" in which you begin further out in the TRT and work towards the beam line. Figure 3.5 shows a more in-depth flow chart of both Primary Tracking and Back-Tracking. ID hits are reconstructed into tracks using a sequence of algorithms, resulting in track collections ready for analysis.

ATLAS tracks have 5 main parameters that categorise them, and an additional 6th reference point using the perigee representation, shown in Figure 3.6. To define the tracking parameters, a reference point is used, which is defined as the average position of the pp interactions or the beam spot position. With this reference point definition, the following tracking parameters are defined:

- d_0: the transverse impact parameter, defined as the point of closest approach in the

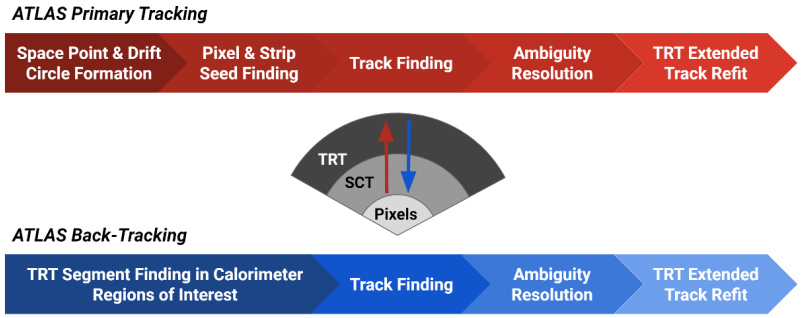

Figure 3.5: Tracking flow chart explaining both Primary Tracking, which is inside-out tracking, and Back-Tracking, which is outside-in [60].

transverse plane to the reference point.

- z_0: the longitudinal impact parameter, defined as the point of closest approach in the longitudinal plane to the reference point.
- ϕ: the azimuthal angle of the track momentum at the reference point.
- θ: the polar angle of the track momentum at the reference point.
- $\frac{q}{p}$: the charge of the reconstructed track divided by the magnitude of its momentum.

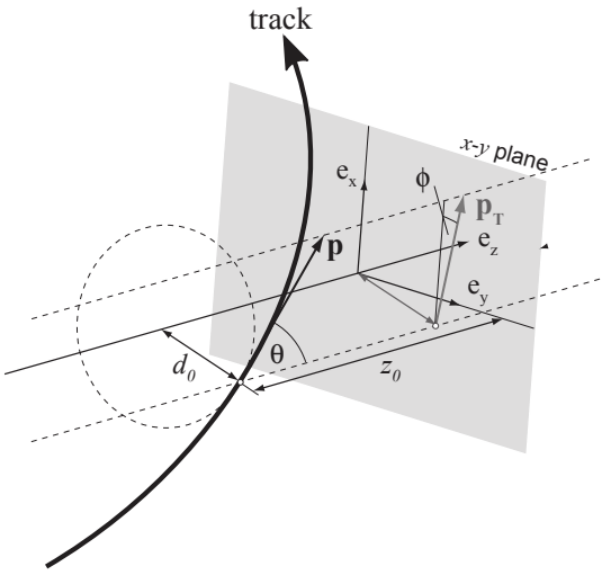

Figure 3.6: Schematic from [60] displaying the 5 ATLAS tracking parameters with respect to a reference point in the perigee representation.

Inside-out tracking

A space point in ATLAS is defined as "a measurement in the pixel detector or the combination of axial and stereo layers of the SCT detectors"[61], as shown in Figure 3.4. For Primary Vertex (PV) reconstruction to be successful, first "track seeds" are chosen, consisting of a triplet of space points in either the pixel or SCT sub-detector. Selection criteria are applied to the track seed triplets in all tracking analyses. When these criteria are met, a 4th seed point is introduced, positioned either as the innermost or outermost seed, to extend the track and provide a clearer picture of the prospective tracking arc with updated curvature.

The search is then extended through "search roads", which are extended regions of the potential track to narrow the scope of the search, increasing computational efficiency and minimising the time loss. Seeds are extended using a Kalman filter [62], searching for adjacent clusters both outwards and inwards in r, while smoothing the trajectory. The seeds that fail are checked for compatibility with the calorimeter; if failed seeds are still within an ROI, bremsstrahlung recovery is used to find seeds

in an accommodating region, allowing for an additional kink.

The result of this is a set of potential track candidates that are further refined. The Kalman filter in tracking is fast computationally, but relatively imprecise, so the tracks are passed onto an ambiguity solver.

Fake tracks are defined as an incorrect combination of unrelated clusters. Using a dedicated ambiguity solver, track candidates are scored on a range of criteria, rejecting low-quality candidates with many associated hits. Shared hits are indicative of fakes or low-quality tracks. A limited number of shared hits is permitted to retain performance in dense environments like jet cores. A neural network updates cluster information and estimates the number of contributing particles, splitting clusters with multiple contributions among track candidates. The resultant refined track candidates are then re-fit using a global chi-squared method to gain a high precision track parameter estimate, accounting for errors on the measurement and unexpected uncertainties.

Tracks can be extended into the TRT using a road search and a Kalman filter starting from the track candidate estimate. TRT hits are then added, and the entire track is refit with a global χ^2 fit, which improves momentum resolution and particle identification. The original, silicon only, track is kept and used as a comparison for the TRT extension track and through a similar process to the ambiguity solver, the score of the tracks are compared, rejecting the worse χ^2 score.

Back-Tracking

Instead of inward-out tracking, as that shown in the top half of Figure 3.5, it is possible to do outside-in tracking, a secondary back-tracking pass using unassigned hits within regions identified by ECal deposits, starting with segments of hits in the TRT.

For a short segment, silicon track seeds consisting of just two space points are constructed in the pixel and SCT detectors, specifically, only hits close to the TRT. These seeds are then extended into track candidates using the same procedures as

for the primary pass, road search, Kalman filter, ambiguity processor and global chi-squared. The track candidates are then extended back into the TRT using the collected hit segments. TRT segments that are not used by the outside-in pass are fit as TRT standalone tracks. These are typically low quality tracks with high fake rates. Performance for these back tracked tracks also decreases with increasing pile-up, but they have some utility for certain applications.

3.5.2 Muon Reconstruction

Muon reconstruction can be done separately in the ID and MS. Information from other tracking detector systems is then combined to form a fully reconstructed muon. Within the ID, charged particle tracks are reconstructed using dedicated algorithms, which serve as inputs for muon identification procedures. In the MS, the process starts by forming track segments within individual muon chambers, using these as seeds for algorithms to reconstruct the muon's path. Reconstruction typically begins in the middle MS layer, where more hits per segment are provided; the search is then extended to the inner and outer layers to achieve the full muon track from the MS.

3.5.2.1 Combined Muon Reconstruction

For combined muons, the reconstruction process uses different algorithms based on the information from ID, MS and ECal. Four types of muons are defined depending on the subdetector tracks as follows:

- **Combined, CB, muons:** The track is fitted independently in the ID and MS, then a global refit takes place using the hits from both systems to form a combined track. Outside-in tracking is used, taking the hits from MS as first seeds and extrapolating from MS into the ID. Some hits not corresponding to the final reconstructed track can be removed to improve the χ^2 fit quality.
- **Segment-tagged, ST, muons:** Using inside-out track reconstruction with

a limited number of hits in the MS. The tracks are formed in the ID and extrapolated into the MS, where only one hit can be used.

- **Calorimeter-tagged, CT, muons:** If the track from the ID cannot be connected to MS hits, but the ECAL does detect compatible energy deposits, the muon can still be reconstructed. The CT muons have the lowest purity and are only used in the regions where the full MS detail cannot be provided.

- **Stand-alone muons, SAMs:** At least two layers of MS chambers are required to reconstruct SAMs. Information is not provided from the ID; just the MS hits that are compatible with the Interaction Point are tested. SAMs are usually reconstructed in the regions not covered by the ID.

3.5.2.2 Muon Identification

Muon identification is performed by applying a set of requirements on the number of hits in the PD, SCT, and MS chambers and the maximum number of holes in the ID. There are five muon identification qualities used to fulfil the needs of the analyses at ATLAS, they are as follows:

- **Medium muons:** Medium identification criteria provide the default selection for muons in ATLAS. Selected to minimise the reconstruction and calibration associated systematic uncertainties. Medium muon identification considers CB muons, which must have at least two hits on at least two layers of the MDT. Medium muon identification also considers SAMs, which have at least three hits in each of the three layers of MDT or CSC.

- **Tight muons:** Used for optimising muon purity. Tight muon identification requires fulfilling the medium CB muons with additional cuts on the normalised χ^2 of the combined track fit on the compatibility between the momenta measured in the ID and MS.

- **Loose muons:** Used for maximising the reconstruction efficiency, while having a worse purity, but still providing a good quality muon track. All muons can be used, but CT and ST muons must be in the region of $|\eta| \approx 0$, where the CB muon reconstruction is less efficient due to the MS coverage gap.

- **High-p_T muons:** Used for maximising the resolution for muons with a transverse momentum above 100 GeV, only CB muons passing the medium criteria are considered, with a further constraint of at least three hits in three MS segments.

- **Low-p_T muons:** These muons pass the loose identification requirements and have a muon transverse momentum 2.5 GeV $< p_{T_\mu} <$ 4 GeV.

3.5.3 Vertexing

Vertexing algorithms require a collection of the charged tracks from the ID. For these tracks to be considered, they must pass the following requirements:

- Transverse momentum greater than 400 MeV.

- Pseudorapidity of the track is in the region $|\eta| < 2.5$.

- At least one hit occurs in the first two PD layers.

- Maximum allowed number of holes in the SCT is 1.

- At least 9 silicon hits.

For the vertex finding to commence, the minimum requirement is that a collection of tracks contains at least one track. After the tracks pass the selection criteria, the first vertex seed is selected. At ATLAS, the Gaussian track density seed finder is usually used; the finder uses a longitudinal Gaussian function to calculate seed finding weights, and the transverse Gaussian function is used as independent quality control. The fit of the vertex position is performed with input information about

the seed and track; the tracks that are incompatible with the vertex fix results are removed from the current vertex and can be used in the next iteration. The process is repeated until there are no tracks available for vertexing left.

ATLAS Vertex reconstruction uses two notable algorithms, the Iterative Vertex Finder, IVF, and the Adaptive Multi-Vertex Fitter, AMVF. Despite being similar, there are some key differences that make them unique. Both use the Gaussian track density seed finder as input, but then the vertex is fitted by the single vertex fitter for IVF, or the simultaneous vertex fitter for AVMF, if any previously fit vertices share tracks with the vertex candidate being currently fit. For IVF, the consequence of the vertex fitter strategy is that each track is only used for one vertex; however, in AMVF, each track can be used more than once, which gives AMVF the advantage for high pile-up events compared to IVF, as seen in Figure 3.7.

Once all vertices have been fitted, the PV is selected. The PV must contain three associated tracks, and is chosen to be the vertex with the highest sum of the squared transverse momenta, passing the selection criteria of $\sum_{\mathrm{MAX}} p_T^2$.

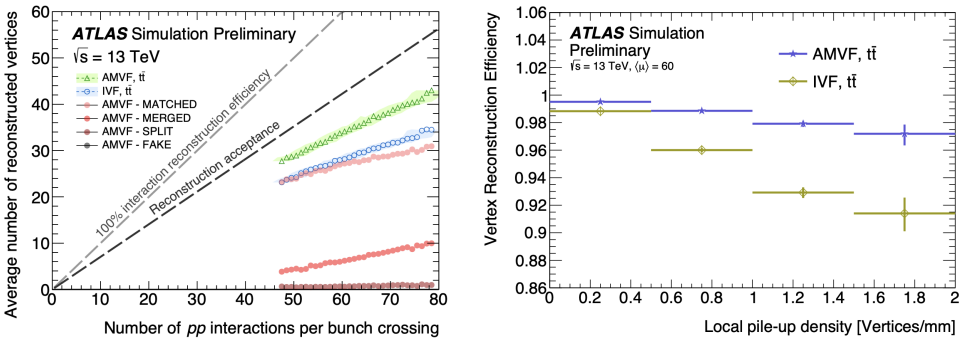

(a) (b)

Figure 3.7: (a) average number of vertices reconstructed as a function of the number of pp interactions per bunch crossing $\langle\mu\rangle$ in simulated $t\bar{t}$ events. The upper dashed line corresponds to perfect reconstruction efficiency, while the lower dashed line is a more conservative estimate of the maximum possible given the reconstructed tracks available to the vertex finder. Error bars on the data points are statistical uncertainties. Filled circles show the classification of AMVF vertices as CLEAN, MERGED, SPLIT, and FAKE.

(b) Comparison of IVF and AMVF vertex reconstruction efficiency as a function of local pile-up density. The reconstruction efficiency is the fraction of events where the true HS vertex is successfully reconstructed.

Chapter 4

History of the Standard Model

4.1 The Standard Model of Particle Physics

Humans are inherently curious, asking questions to further their understanding of the universe, exemplified in young children asking "why?". The human curiosity extends to the makeup of the universe, and our current understanding rests on the Standard Model, a theory describing the fundamental building blocks of matter and the forces that govern their interactions.

The Standard Model of Particle Physics, however, is incomplete, with the inability to describe neutrino mass, the matter-antimatter asymmetry, or provide a quantum description of gravity being just a few major deficiencies of the Standard Model. Furthermore, it only accounts for a small fraction of the universe's mass, or gravitational mass, 5%, with the other 95% split between dark matter, 27% and dark energy, 68% respectively, [63].

The Standard Model, like all scientific theories, has evolved over time. Its roots can be traced back to ancient Greece and the philosopher Democritus, proposing an atomic theory of the universe, with the word "atom" evolving from the ancient Greek combination of "a", meaning not, and "temnein", meaning to cut, to arrive at "atomos" meaning indivisible or uncuttable.

Today, scientists believe that the universe is made up of quarks and leptons, held

together by four fundamental forces. These are shown in Figure 4.1, which depicts the Standard Model.

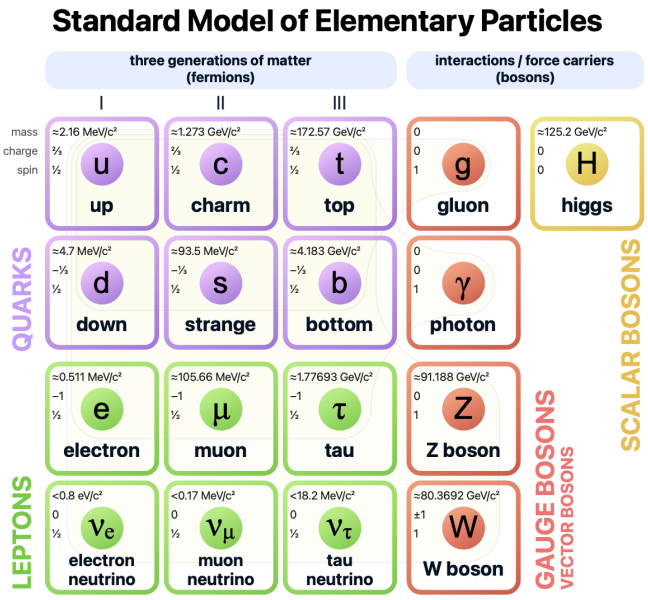

Figure 4.1: The Standard Model of elementary particles: the 12 fundamental fermions and 5 fundamental bosons [64].

The Standard Model is the current best theory for describing all the fundamental particles within the universe. The fundamental particles can be split into two groups, 12 fermions, which are the matter particles and 5 bosons, including the four gauge bosons and the scalar Higgs boson. Fermions are particles such as quarks and leptons which constitute atoms encountered in everyday life. Fermions are further split into three subgroups based on mass and labelled "generations" in the model. There exists a pair of quarks in each quark generation, an up-type quark carrying positive 2/3 electric charge and a down-type quark carrying negative 1/3 electric charge. The leptons in each generation also exist in pairs, containing a charged lepton and its associated lepton neutrino, such as the electron, e, and electron neutrino, ν_e. The electron is the lightest measured mass lepton, with the neutrino masses still to be discerned, but experimentally supported to have mass, [65].

There are five bosons, this is split based on spin into four vector bosons, where

the spin $s = 1$, and one scalar boson, where $s = 0$. The gluon, g, carries and mediates the strong interaction, the interaction which holds quarks together. The photon, γ, mediates the electromagnetic interaction, the interaction which binds the electrons to the nuclei in atoms that make up everyday life. The last of the vector bosons are the $W^{\pm}$, and Z bosons, which mediate the weak interaction responsible for beta decay, amongst other interactions. Moving to the scalar bosons, there is one in the SM, the Higgs boson, H, and it mediates the Higgs mechanism, a process in which particles acquire mass. For completeness, the final fundamental force is gravity, but there is no known mediator for this force; instead, the hypothesised graviton is the mediator. Gravity is an attractive force between massive particles.

Now that the SM of particle physics has been established, albeit briefly, the history of how the Standard Model was developed is discussed in the rest of this chapter, before moving to the mathematical foundation on which the SM is built in Chapter 5.

4.2 History of Electrons, Protons and Neutrons

The indivisible nature of the atom remained accepted until the late 19th century, when J. J. Thomson made the discovery of the electron using his cathode ray experiment, [66]. Applying a high voltage between a cathode and an anode, a beam of particles (electrons) was shot down the evacuated glass tube. Thomson then applied a magnetic field to this beam to measure the charge-to-mass ratio. The beam deflected much more than expected, leading to the conclusion that the beam was negatively charged and had a much higher charge-to-mass ratio than seen before. As these particles were negative, despite the overall atom being neutral, Thomson proposed the now infamous "plum pudding" model, in which a positively charged sphere of matter had electrons scattered throughout.

The plum pudding model, while a significant step, could not explain all atomic behaviour. In 1911, Rutherford, with Geiger and Marsden, challenged this model

with his famous gold-foil experiment, [67]. He bombarded a thin sheet of gold foil with alpha particles fired from a radioactive source. These alpha particles, with their significant mass and positive charge, should have easily passed straight through the mostly empty space within the atom according to the plum pudding model.

However, what was observed was the deflection of alpha particles. These alpha particles sometimes were deflected back at the source, prompting the birth of the planetary atomic model. The planetary atomic model involves a dense positive nucleus, made of protons, with the cloud of electrons encasing the nucleus.

It was not until 1932 when Chadwick discovered the neutron, [68], that the atomic picture was complete. According to the Bohr model, like hydrogen, all atoms have an equal number of protons and electrons, but the helium atom was too massive, twice as heavy as it should be. Chadwick bombarded beryllium atoms with alpha particles and observed an unexpected radiation emitted. This radiation did not possess a charge, yet it could knock protons out of paraffin wax. To investigate further, Chadwick measured how the radiation affected different gases. By analysing the energy and momentum transferred in these collisions, Chadwick concluded that the radiation consisted of particles with a mass similar to a proton but no electrical charge. These uncharged particles were neutrons.

4.3 History of the Photon

Given the strange nature of the photon, the now accepted wave-particle duality, its discovery is not necessarily linear, or in one single experiment. Back in the 19th century, before the electron discovery, J. C. Maxwell predicted that light is a form of electromagnetic waves, [69], this was later confirmed by the detection of radio waves by H. Hertz, [70]. This incomplete wave theory could not explain all aspects of the behaviour of light.

M. Planck was studying the "black body" spectrum, and encountered a problem: physics predicted that the energy radiated by a black body would approach infinity

at high frequencies, which was known as the "ultraviolet catastrophe". To resolve this, Planck proposed the quantisation of electromagnetic radiation: light energy travelled in discrete packets, described by Equation 4.1.

$$E = hv \tag{4.1}$$

where h is Plancks constant, equal to 6.63×10^{-34} Hz. Meaning that energy cannot be radiated at any arbitrary frequency; instead, the radiated energy has to be a multiple of Planck's constant.

A. Einstein advanced this theory, showing that if Planck's law for black body radiation is accepted, energy quanta must also carry momentum. These quanta now exhibit both wave-like and particle-like behaviours, challenging the binary separation of waves and particles, suggesting a more complex understanding is needed for the delineation of particles and waves.

This was proven with Einstein's Nobel-winning description of the photoelectric effect, [71], an experiment in which incident light was shone on a metal surface, with electrons only ejected if the light's frequency was sufficient, not its intensity. Einstein concluded that light exhibits both wave and particle properties, depending on the experimental setup.

4.4 History of Muons, Mesons and Strange Particles

Even with a seemingly complete understanding of the atom, the world of particle physics still had questions; the understanding of the inter-nuclear forces keeping the protons and neutrons together was not fully understood. If only gravity and the electromagnetic forces were involved, then these particles would repel one another, and the nucleus would decay. H. Yukawa solved this topic in 1934, when consolidating the theory into Yukawa's interaction, a model to accurately describe how the forces between particles fall exponentially with distance. This theory

provided a framework for the understanding of short range forces in particle physics. In this model, the force between particles is dependent on the mass of the particles, and the distance of separation. This relationship was crucial for explaining the strong nuclear force, which binds protons and neutrons together. Yukawa used this theory to predict a particle to have a mass of 200 to 300 of that of the electron [72].

This Yukawa particle was thought to be found in 1936, through the work of C.D. Anderson and S. Neddermeyer when they studied cosmic rays and found the existence of muons, [73]. These muons caused great contention; the mass was roughly 200 times that of the electron, somewhat off from Yukawa's prediction, and the muon interacted via the nuclear weak force, and had a lifetime inconsistent with Yukawa's prediction.

The true Yukawa particle, the pion, was not discovered until 1947 by Lattes, Muirhead, Occhialini, and Powell [74], providing strong evidence for Yukawa's theory and consolidating the understanding of the strong nuclear force. Following the discovery of the pion, in late 1947, Rochester and Butler photographed cloud chamber decays of a neutral particle decaying into two oppositely charged pions, or a proton and a pion and another decay of charged particles into a pion and a neutral particle [75]. These observations marked the discovery of the kaon, the first strange meson, revealing a new class of particles beyond those predicted by the simple Yukawa theory. These discoveries paved the way for later advancements, including the development of the quark model by Gell-Mann.

4.5 History of Quarks

The discovery of strange particles, particles with unusual decay properties, led physicists like Gell-Mann, Nakano, and Nishijima to propose a new concept called strangeness, a conserved property that helped explain these particles' behaviour. The rapid discovery of new mesons, composed of quark-antiquark pairs, and baryons, composed of three quarks, in the 1950s significantly advanced physicists'

understanding of the internal structure of these strongly interacting particles [76, 77].

Gell-Mann proposed a classification scheme known as the Eightfold Way, [78]. This framework, based on a mathematical symmetry principle (SU(3)), organised mesons and baryons into octet groups based on their properties such as spin and charge, an example of this is seen in Figure 4.2. The Eightfold Way even predicted the existence of other hadronic structures, such as the baryon decuplet, for heavier baryons. While this organisation was successful due to the symmetry from mathematics SU(3) describing this classification effectively, it remained unclear why hadrons behaved in this way.

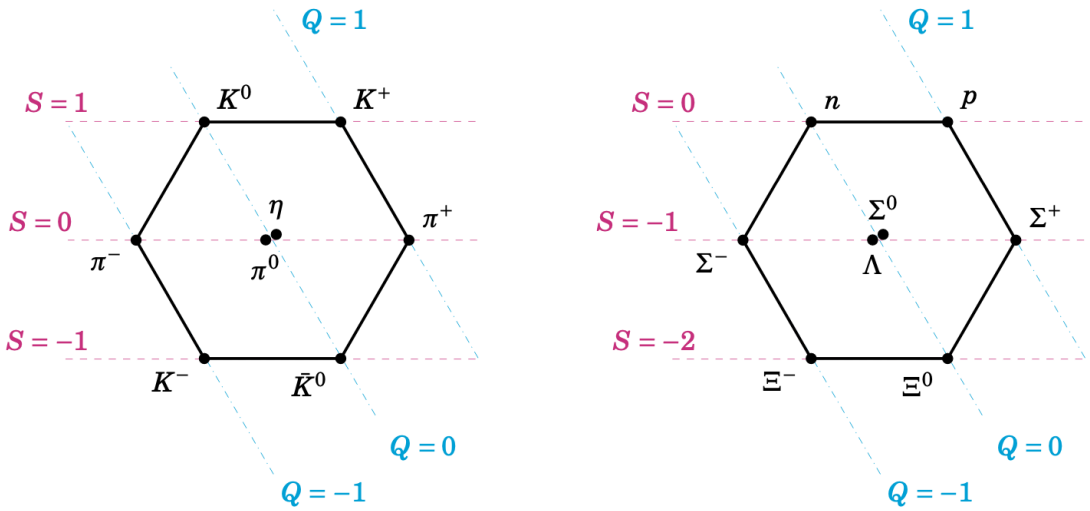

Figure 4.2: The meson and baryon octet organisation proposed by M. Gell- Mann, Figure 1.1 from [79].

In 1964, Gell-Mann continued his work, proposing that all observed hadrons have an internal structure; these elementary particles were labelled "quarks". They existed in three flavours at that time, the up, u, strange, s, both having $+2/3$ electrical charge and down, d, having $-1/3$ electrical charge. The quark model proposed that baryons are made of three quarks, while mesons consist of a quark-antiquark pair.

This underlying structure was successfully experimentally probed with the

Stanford Linear Accelerator (SLAC) in 1968, in which deep inelastic scattering was observed, demonstrating that the previously thought-to-be indivisible proton was indeed made up of point-like particles, quarks, [80].

4.6 Developing the Quark Model

The successful discovery of proton inner structure and the quark model still had unresolved problems, the Δ^{++} particle posed a significant problem. The Δ^{++} consisted of three identical up quarks in the same quantum state, violating the Pauli Exclusion Principle. Greenberg postulated another quantum number [81] to solve this, a theory which introduced quark colour charge, this was developed further by Fritzsch, Gell-Mann, and Leutwyler in 1973 [82].

The GIM mechanism, proposed by Glashow, Iliopoulos, and Maiani, addressed the suppression of certain flavour-changing processes and predicted the existence of a fourth quark. The 1974 discovery of the J/ψ meson [83, 84], composed of a charm quark and its antiparticle, confirmed this prediction in what became known as the November Revolution [85]. With two quark generations now established, the quark model successfully predicted additional particles that were subsequently discovered.

The discovery of the tau lepton in 1976 disrupted this two-generation symmetry and hinted at a third quark generation. The bottom quark was discovered in 1977 [86], followed by the top quark in 1995 [87], completing the current picture of six quark flavours in the Standard Model.

4.7 Vector Bosons

Vector bosons, specifically the vector bosons that carry the weak interaction, were a key missing piece in the Standard Model. In 1933, E. Fermi described beta decay as a contact interaction, without a mediator exchange particle, [88]. It was successful for the low energies but broke down at higher energies. The high-energy breakdown was

due to the mediating W boson no longer decaying effectively instantaneously, and thus having a meaningful lifetime that affected the kinematics of the interaction. We now know that the beta decay interaction is governed by the weak force, which has a characteristically small range. The GIM mechanism even provided mass prediction for these mediator particles, [89], which helped the design of particle accelerator experiments with these theoretical predictions. In 1968, S. Glashow, S. Weinberg, and A. Salam. created a unified theory directly predicting the W^+, W^- and Z^0 boson masses.

The Super Proton Synchrotron is a proton-antiproton collider constructed in the 1970s, specifically for the discovery of the weak interaction mediators. In 1983, the first success came with the discovery of the W^+ and W^- bosons by the UA1 and UA2 experiments at the SPS, [90], [91]. The Z^0 boson followed in July of the same year [92].

The significance of these masses posed a challenge. Nearly 20 years earlier, there had been a proposed solution to the non-zero mass; this solution was symmetry breaking, proposed in a form by P. Higgs, [93], R.Brout and F.Englert [94], with the Higgs mechanism. The Higgs mechanism allows the vector boson(s) to gain invariant mass without explicitly breaking gauge invariance as a byproduct of spontaneous symmetry breaking. It used the Goldstone boson, created by the Higgs field with four components. Three of them are absorbed by the W^+, Z^0, and W^- bosons, forming their longitudinal components, and the last one is the Higgs boson itself.

The existence of the Higgs boson, though crucial for the electroweak theory, remained undiscovered for decades. Finally, in 2012, a new boson consistent with the Higgs particle was measured at the LHC, a machine specifically built for this purpose. On July 4th 2012, the discovery of a new boson, the Higgs boson, was jointly announced by the LHC experiments, ATLAS and CMS, with a mass between 125 and 127 GeV, [35]. The Higgs boson was consistent with theoretical predictions, agreeing with expected behaviours, interactions and decays. With this discovery, the picture of fundamental particles and forces described by the Standard Model became

complete.

4.8 History of Antiparticles

Dirac's 1927 relativistic description of electrons predicted that particles could have either positive or negative energy [95] which was a novel suggestion at the time. Anderson experimentally confirmed this prediction in 1932 [96] using a cloud chamber in a magnetic field, detecting particles with the same charge-to-mass ratio as electrons but with opposite charge, the positron. This discovery established antiparticles which have become a fundamental constituent of Quantum Electrodynamics (QED).

In 1955, Segré and Chamberlain discovered the antiproton and antineutron [97] by bombarding a copper target with high-energy protons from the Berkeley synchrotron. The current understanding in particle physics is that every particle has a corresponding antiparticle, though some particles, such as photons and gluons, are their own antiparticle.

4.9 History of Neutrinos

The neutrino was first postulated by Pauli in 1930 to explain the observed energy spectrum of electrons in beta decay. Pauli proposed that a neutral, low-mass particle was also emitted, carrying away the missing energy and solving the apparent violation of energy conservation.

In 1956, Cowan and Reines provided the first experimental evidence for neutrinos [98] by observing antineutrino interactions with protons near a nuclear reactor. Whilst not a direct detection, it was confirmation of the neutrinos' participation in beta decay.

Evidence for a second type of neutrino emerged from observations of pion decay. When pions decayed into muons, the muon was always emitted in a

different direction, suggesting an additional unseen particle. To preserve energy and momentum conservation, theorists proposed two distinct neutrino types: the electron neutrino and the muon neutrino. The existence of the muon neutrino was experimentally confirmed in 1962 by Lederman, Schwartz, and Steinberger, [99].

Leptons, like quarks, exist in three generations. The tau neutrino, the final predicted neutrino, was discovered in 2000 by the DONUT collaboration [100], completing the three-generation lepton structure. The DONUT experiment produced tau neutrinos from meson decay, and identified tau neutrino interactions by detecting sudden track appearances and distinctive "kinks" from tau lepton decay.

Now that the history of the Standard Model has been introduced and all constituent particles accounted for, the next chapter, Chapter 5, discusses the mathematical framework and underlying theories of the SM.

Chapter 5

Theoretical Background

5.1 The Standard Model

The Standard Model (SM), is not just a dictionary of particles; it evolved from a series of theoretical principles underpinning the known universe into a Quantum Field Theory (QFT). The SM is a theory which reveals why particles cluster into constituent groups, how forces arise from symmetries, and why some processes are allowed while others are forbidden. In this Chapter, the aim is to explore more of the theory and theories underpinning the maths of the SM and that are needed for the later analysis in this thesis. This thesis focuses on observing a known CP-violating decay of the B_s^0 meson, see Section 5.4.2. The rest of this chapter focuses on the formal structure of the SM.

Within the SM, there is annihilation of matter upon interaction with antimatter. While there are known Charge Parity Violation (CPV) mechanisms, current understanding does not sufficiently explain the matter-antimatter asymmetry observed in the universe. Several theories can account for the asymmetry, including, but not limited to, Supersymmetry (SUSY) [101, 102] Leptogenesis, [103, 104], Baryogenesis [105, 106] and various modes of parity violation, notably CP-violation for this thesis.

The SM is constructed through the use of a gauge symmetry described by the

group:

$$\mathcal{G}_{SM} = SU(3)_C \otimes SU(2)_L \otimes U(1)_Y \tag{5.1}$$

and the spontaneous breaking of this symmetry is described by:

$$\mathcal{G}_{SM} \longrightarrow SU(3)_C \otimes U(1)_Q \tag{5.2}$$

where L is the (left) handedness, or formally chirality, Y is hypercharge, Q is electric charge, and C is the colour charge. This imposed gauge symmetry generates twelve gauge bosons, which include the three massive W^+, W^- and Z^0 bosons, and the massless photon, these four mediate the electroweak interactions. The remaining eight massless gluons carry the strong force and are described by Quantum ChromoDynamics (QCD). There is a need for spontaneous symmetry breaking, introduced in Equation 5.2, as through this mechanism, all the SM particles are afforded their non-zero mass, meaning that photons and gluons are not involved in the Higgs mechanism. The side effect of this is to create an additional scalar field, the Higgs field, the operators of which generate a scalar boson referred to as the Higgs boson.

Fermionic fields are necessary representations of the SM gauge group $\mathcal{G}_{SM}$. There are five such representations of the SM, one for the left-handed components of the quark fields, two for the right-handed quarks, and one for each of the left and right-handed lepton fields. These depend on handedness, and are either triples or singlets of $SU(3)$, and either doublets or singlets of $SU(2)$.

	$SU(3)$	$SU(2)$
Quarks	$q_{L,i} = \begin{pmatrix} q_{L,r} \\ q_{L,b} \\ q_{L,g} \end{pmatrix}$	$q_{L,i} = \begin{pmatrix} u_{L,i} \\ d_{L,i} \end{pmatrix}$
	$u_{R,i} = \begin{pmatrix} q_{R,r} \\ q_{R,b} \\ q_{R,g} \end{pmatrix}$	$u_{R,i} = \begin{pmatrix} u_{R,i} \end{pmatrix}$
	$d_{R,i} = \begin{pmatrix} d_{R,r} \\ d_{R,b} \\ d_{R,g} \end{pmatrix}$	$d_{R,i} = \begin{pmatrix} d_{R,i} \end{pmatrix}$
Leptons	$L_{L,i} = \begin{pmatrix} L_{L,i} \end{pmatrix}$	$L_{L,i} = \begin{pmatrix} \nu_{L,i} \\ l_{L,i} \end{pmatrix}$
	$l_{R,i} = \begin{pmatrix} l_{R,i} \end{pmatrix}$	$l_{R,i} = \begin{pmatrix} l_{R,i} \end{pmatrix}$

Table 5.1: Representations of the gauge group $\mathcal{G}_S M$ for the fermion fields, including quarks and leptons. The table covers the properties for $SU(3)$ and $SU(2)$. Note $q = u, d$ and $L = l, \nu$, with L, R representing left and right handedness respectively. The i index runs from 1 to 3, indicating the generation number, expanding on this, $\{u_{1,2,3}\} = \{u, c, t\}, \{d_{1,2,3}\} = \{d, s, b\}, \{l_{1,2,3}\} = \{e, \mu, \tau\},$ and $\{\nu_{1,2,3}\} = \{\nu_e, \nu_\mu, \nu_\tau\}$

From Table 5.1 it can be deduced that:

- Quark fields transform as colour triplets under $SU(3)$, the colour triplets for strong interactions quarks are afforded colour, an additional quantum number, one of "red", "blue" or "green". Note these are additional quantum numbers, not physical representations of colours, for argument's sake, they could be called "eggs", "bacon" and "sausage" and be deemed "breakfast" quantum numbers.

- The left-handed component of the fermionic field is split into doublets under $SU(2)$ transformations, whereas the right-handed components are

singlets. This reflects the experimental findings that there are no right-handed neutrinos.

- The SM provides three generations, but there is no intrinsic reason as to why there are only three, just that three is the minimum.

5.1.1 Interactions and Forces

Within the SM, as seen in Figure 4.1, in Section 4.1, there are four gauge bosons, and the Higgs boson; these bosons are force carriers for the fundamental interactions governing physics.

5.1.1.1 Electromagnetic Interactions

Electromagnetic, EM, interactions bind electrons with nuclei in atoms and molecules and are responsible for intermolecular forces. The gauge boson for the electromagnetic force is the photon, a massless particle that interacts with all electrically charged particles. Interactions of this type are governed by the theory of Quantum ElectroDynamics (QED) a gauge-invariant theory with symmetry $U(1)$. Here, the $U(1)$ symmetry reflects the conservation of electric charge. The coupling strength of the EM force is given by the constant, α, commonly known as the fine structure constant, in terms of the electric charge, e, and Planck's constant, $\hbar$:

$$\alpha = \frac{e^2}{4\pi\hbar c} \tag{5.3}$$

The EM potential between elementary charges at a distance, r, is

$$V_{em} = -\frac{\alpha}{r} \tag{5.4}$$

Equation 5.4 demonstrates that the range of the EM force is mathematically infinite but decreases rapidly with distance and is negligible at a macroscopic scale.

5.1.1.2 Weak Interactions

Both quarks and leptons are subject to weak interactions. This interaction is several orders of magnitude smaller than the EM interaction [107], making it very rare compared to both the EM and strong interactions (see Section 5.1.1.3). Neutrinos interact exclusively via the weak force, which is mediated by the charged $W^{\pm}$ bosons and the neutral Z^0 boson. The $W^{\pm}$ bosons are responsible for changes in quark flavour through charged current interactions, while neutral current, flavour preserving interactions are mediated through the Z^0 boson. Electroweak theory offers a unification of the weak and electromagnetic forces.

5.1.1.3 Strong Interaction

The way in which quarks and gluons interact is described by the strong force within QCD. This force is responsible for binding quarks and gluons together, forming mesons and baryons, gluons only act on colour charge. Quarks carry one of three possible colours, and antiquarks carry one of three anti-colours. A hadronic object is formed when the overall colour charge of a particle is colourless, with baryons being made of three quarks, q_r, q_g, q_b, and mesons being in quark antiquark pairs so that $q_i\bar{q_i}$. Here we state an important difference between QED and QCD, given that gluons carry colour, hence the "chromo" in QCD, and the photons are chargeless and colourless in QED. Gluons carry one colour and one anti-colour, as they act on both quarks and anti-quarks, and can self-interact. There are eight interacting gluons, one less than the 3^2 from three colours and three anti-colours, because of the colourless singlet state. Quark confinement is a crucial principle within the strong interaction; it is deemed physically impossible to isolate single quarks, as the energy needed to split two quarks increases with distance, and the total energy to isolate a quark is higher than the energy needed to form a $q\bar{q}$ pair.

5.1.1.4 Gravitational Interaction

Gravity is only significant in the macroscopic world, with spatial scales, large compared to the scales of particle physics. It has been observed that massive objects curve the spacetime around themselves; the curvature is physically manifested through the attractive force exerted on nearby objects. Using the Newtonian approach, it is possible to estimate and contrast the relative strength of gravity compared to the electromagnetic forces. Using the Newtonian gravitation relation for two point particles, with mass M at a distance r:

$$F = \frac{GM^2}{r^2} \tag{5.5}$$

where, G, is Newtons constant, and $G = 6.673 \times 10^{-11}$ $\mathrm{m^3kg^{-1}s^{-2}}$. This allows for an estimated relative gravitational strength of the order of 10^{-40} for two point particles with mass M and distance r compared to the EM fine structure constant of $\approx \frac{1}{137}$. The gravitational interaction is negligibly small at the high-energy scale and is not part of the SM. Additionally, there is no experimental observation of negative gravitational charge, and the gravitational forces are assumed attractive only, hypothetically mediated through the graviton in alternative quantum theories of gravity. There has also been experimental observation of gravitational waves with experiments such as LIGO detecting ripples in spacetime, [108].

5.2 Symmetry within the Standard Model

A physical system exhibits symmetry when its fundamental behaviour remains unchanged after a specific transformation. These symmetries are essential for the understanding of natural physical processes. By imposing continuous global symmetries on the Lagrangian, the mathematical description of a system's behaviour, fundamental physical laws arise. Noether's theorem [109] discovered a connection between symmetries and conservation laws, that being that for a system's Lagrangian remaining invariant under a transformation, a corresponding conserved

quantity must exist. For instance, by demanding an invariant Lagrangian under spatial transformation, this yields the conservation of linear momentum. This can be applied to many other transformations, giving rise to many more conserved quantities.

It is possible to split symmetries into two categories, in which continuous symmetries are defined as groups of transformations that can be performed smoothly and can be described by Lie groups. Discrete symmetries involve distinct transformations that are described by finite groups.

5.2.1 Continuous Symmetries

Noether's Theorem states, that if there is a continuous symmetry of a system associated to a conservative force, there must be a corresponding conservation law. Therefore, this section focusses on continuous symmetries, before discrete symmetries are discussed in Section 5.2.2. Some of the continuous symmetries from classical physics are:

- Time translation, if a physical system has the same features over a given time period, then the system's energy is conserved.
- Spatial translation, the system does not change by changing the observer's location, thus the system's momentum is conserved.
- Spatial rotation, the system does not change if an observer changes their angular position, then the conserved quantity is angular momentum in this case.

5.2.2 Discrete Symmetries

There are many discrete symmetries for the SM, but the three most common, and of particular relevance to this thesis, are parity transformation, P, charge conjugation, C, and time reversal, T, and while introduced here, they have their own section later.

- Parity, P: The symmetry under spatial inversion of coordinates, addressing whether physics is unchanged in a mirror reflection, or there is a preference to a certain "handedness", or chirality.

- Charge Conjugation, C: The symmetry under exchange of particles with their anti-particles, examining the behavioural similarities between matter and anti-matter.

- Time Reversal, T: The symmetry reversal of time's direction, scrutinising the one-directional time nature of the universe.

5.2.2.1 Parity Conjugation, P

The first of these transformations that will be discussed is parity itself, sometimes referred to as "spatial parity". Spatial parity deals with the fact that we, as physicists and mathematicians, have arbitrarily denoted a coordinate system in which we observe physical events, so a fair question is "what if we flipped the spatial coordinates, does this affect our physics?". The Parity operation converts a right-handed Cartesian coordinate system (x, y, z) into a left-handed one $(-x, -y, -z)$ through the action of the Parity operator $\hat{P}$:

$$\hat{P}\psi(\boldsymbol{r}) = \psi(-\boldsymbol{r}) \tag{5.6}$$

where $\boldsymbol{r}$ is a position vector, when (x, y, z) were previously used. A system that has the same behaviour before and after the operator, $\hat{P}$, has acted on the system is said to have parity.

5.2.2.2 Charge Conjugation, C

Charge conjugation is another transformation used for understanding particle physics. For charge conjugation to hold true, an experiment in which the charges fof all particles within a process were swapped with their anti-particle (i.e. negative particles become positive particles, such that electrons become positrons and vice

versa, for all particles in the process) the behaviour would be the same. Through the action of the operator, $\hat{C}$, particles are transformed into their anti-particles:

$$\hat{C}\psi(\boldsymbol{r}) = \bar{\psi}(\boldsymbol{r}) \tag{5.7}$$

5.2.2.3 Time Conjugation, T

The third discrete symmetry is a time reversal, sometimes Time Conjugation, if we enlist the (x, y, z) Cartesian spatial dimensions and add a fourth dimension of time (x, y, z, t), which flows forward as we experience, we have the setting for time reversal. As the name suggests, you flip the passage of time, physical processes and their laws should apply in the same way, so that the time reversal operator, $\hat{T}$, is defined as:

$$\hat{T}\psi(r, t) = \psi(r, -t) \tag{5.8}$$

5.3 CKM Mixing Matrix

In the previous section, 5.2 symmetries for the SM were introduced; however, there was no mention of the physical evidence supporting whether these symmetries are upheld. These symmetries are all broken in some form with current experimental observations. Here, the Cabibbo-Kobayashi-Maskawa, CKM, matrix is introduced to provide background on quark mixing, which is pivotal for understanding the CP violation of the combined symmetries of charge and parity.

The CKM matrix is a product of the matrices responsible for the transformation of the mass eigenstates of a quark into an interaction eigenstate:

$$\begin{aligned} d'_L &= V^{\dagger}_{dL} d_L \\ \bar{u}'_L &= V_{uL} \bar{u}_L \end{aligned} \tag{5.9}$$

where V_{uL} and V_{dL} are transformation matrices, $d' = (d', s', b')$ and $u' = (u', c', t')$ are interaction states and $d = (d, s, b)$ and $u = (u, c, t)$ are the mass eigenstates

of quarks. From Equation 5.9, it is possible to introduce the CKM matrix, as $V_{CKM} = V_{uL}^{\dagger} V_{dL}$:

$$\begin{pmatrix} d_I \\ s_I \\ b_I \end{pmatrix} = \begin{pmatrix} V_{ud} & V_{us} & V_{ub} \\ V_{cd} & V_{cs} & V_{cb} \\ V_{td} & V_{ts} & V_{tb} \end{pmatrix} \cdot \begin{pmatrix} d_M \\ s_M \\ b_M \end{pmatrix} \tag{5.10}$$

where I and M refer to the interaction and mass bases, respectively. The probability of a transition from a q_1 to q_2 is proportional to $|V_{q1}V_{q2}|^2$.

The CKM matrix relates flavour eigenstates to the mass eigenstates, as shown in Equation 5.10. In the mass basis, up-type quarks are paired with mixed down-type quarks across generations. These flavour eigenstates are transformed into mass eigenstates using a unitary mixing matrix. The CKM matrix describes the mixing between quark generations for flavour-changing weak decays; the CKM matrix is believed to be unitary, provided there are no additional generations of quarks found.

5.3.1 The Standard Parameterisation

The "standard" parameterisation of the CKM matrix introduces three Euler angles, θ_{12}, θ_{23}, θ_{13} and one CP-violating angle, δ, and is the preferred convention of the Particle Data Group [110]. This parameterisation is useful for understanding the CP phase, Equations 5.11 and 5.12 introduce the standard parametrisation:

$$\begin{bmatrix} 1 & 0 & 0 \\ 0 & c_{23} & s_{23} \\ 0 & -s_{23} & c_{23} \end{bmatrix} \begin{bmatrix} c_{13} & 0 & s_{13}e^{-i\delta} \\ 0 & 1 & 0 \\ -s_{13}e^{i\delta} & 0 & c_{13} \end{bmatrix} \begin{bmatrix} c_{12} & s_{12} & 0 \\ -s_{12} & c_{12} & 0 \\ 0 & 0 & 1 \end{bmatrix} \tag{5.11}$$

$$= \begin{bmatrix} c_{12}c_{13} & s_{12}c_{13} & s_{13}e^{-i\delta} \\ -s_{12}c_{23} - c_{12}s_{23}s_{13}e^{i\delta} & c_{12}c_{23} - s_{12}s_{23}s_{13}e^{i\delta} & s_{23}c_{13} \\ s_{12}s_{23} - c_{12}c_{23}s_{13}e^{i\delta} & -c_{12}s_{23} - s_{12}c_{23}s_{13}e^{i\delta} & c_{23}c_{13} \end{bmatrix}. \tag{5.12}$$

The matrices in 5.11 are multiplied together to result in 5.12. For both, $s_{ij} = \sin\theta_{ij}$, and, $c_{ij} = \cos\theta_{ij}$, and, δ, is the CP phase responsible for all flavour changing

processes in the established SM.

5.3.2 The Wolfenstein Parameterisation

The Wolfenstein parameterisation of the CKM matrix introduces four real parameters λ, A, ρ, and η, that would all be zero if there was no weak coupling. These four Wolfenstein parameters are related to the standard parameterisation through the following equations:

$$s_{12} = \lambda \tag{5.13}$$

$$s_{23} = A\lambda^2 \tag{5.14}$$

$$s_{13} = A\lambda^3(\rho + i\eta) \tag{5.15}$$

The Wolfenstein parameterisation approximates the matrix by expanding each element as a power series in $\lambda \equiv |V_{us}| \approx 0.22$, and based on the experimental observations that $s_{13} \ll s_{32} \ll s12 \ll 1$, the CKM matrix in Wolfenstein parameterisation takes the form:

$$V_{\text{CKM}} = \begin{pmatrix} 1 - \lambda^2/2 & \lambda & A\lambda^3(\rho - i\eta) \\ -\lambda & 1 - \lambda^2/2 & A\lambda^2 \\ A\lambda^3(1 - \rho - i\eta) & -A\lambda^2 & 1 \end{pmatrix} + \mathcal{O}(\lambda^4). \tag{5.16}$$

The Wolfenstein parameterisation exploits the experimental observation of quark hierarchy to simplify the CKM matrix. The experimental values of the Wolfenstein Parameters from data are [111]:

$$\begin{aligned} \lambda &= 0.22650 \pm 0.00048, \\ A &= 0.790^{+0.017}_{-0.012}, \\ \bar{\rho} &= \rho\left(1 - \frac{1}{2}\lambda\right) = 0.141^{+0.016}_{-0.017}, \\ \bar{\eta} &= \eta\left(1 - \frac{1}{2}\lambda\right) = 0.357 \pm 0.011. \end{aligned} \tag{5.17}$$

here, $\bar{\rho}$, and, $\bar{\eta}$, are used to minimise higher order corrections.

5.3.3 Unitarity Triangles

Taking the CKM matrix, and expressing its unitarity formally as:

$$\boldsymbol{V}^{\dagger}_{CKM} \cdot \boldsymbol{V}^{CKM} = \mathbf{1} = \boldsymbol{V}_{CKM} \cdot \boldsymbol{V}^{\dagger}_{CKM} \tag{5.18}$$

This expression leads to a set of 12 equations which provide powerful constraints on the values of the individual elements. The first two equations in 5.19 are representing three equations each, with the remaining six completing the 12 equations.

$$\begin{aligned}
|V_{ui}|^2 + |V_{ci}|^2 + |V_{ti}|^2 &= 1, \quad i = d, s, b \\
|V_{id}|^2 + |V_{is}|^2 + |V_{ib}|^2 &= 1, \quad i = u, c, t \\
V_{ud}V^*_{us} + V_{cd}V^*_{cs} + V_{td}V^*_{ts} &= 0 \\
V_{ud}V^*_{ub} + V_{cd}V^*_{cb} + V_{td}V^*_{tb} &= 0 \\
V_{us}V^*_{ub} + V_{cs}V^*_{cb} + V_{ts}V^*_{tb} &= 0 \\
V_{ud}V^*_{cd} + V_{us}V^*_{cs} + V_{ub}V^*_{cb} &= 0 \\
V_{ud}V^*_{td} + V_{us}V^*_{ts} + V_{ub}V^*_{tb} &= 0 \\
V_{cd}V^*_{td} + V_{cs}V^*_{ts} + V_{cb}V^*_{tb} &= 0
\end{aligned} \tag{5.19}$$

The final six equations, in Equation 5.19, can be represented geometrically as six triangles in the complex plane. Each of these unitarity triangles has the same area related to the size of the CP phase. Four of these triangles have one side suppressed relative to the other by $\mathcal{O}(\lambda^2)$, or $\mathcal{O}(\lambda^4)$. The remaining two triangles all have their sides of $\mathcal{O}(\lambda^3)$. The two orthogonal relations left are:

$$\begin{aligned}
V_{ud}V^*_{ub} + V_{cd}V^*_{cb} + V_{td}V^*_{tb} &= 0 \\
V_{ud}V^*_{td} + V_{us}V^*_{ts} + V_{ub}V^*_{tb} &= 0
\end{aligned} \tag{5.20}$$

From Equation 5.20, it is possible to draw the unitarity triangles, specifically

drawing from the first relationship, commonly known as the B_d^0 meson triangle, seen in Figure 5.1.

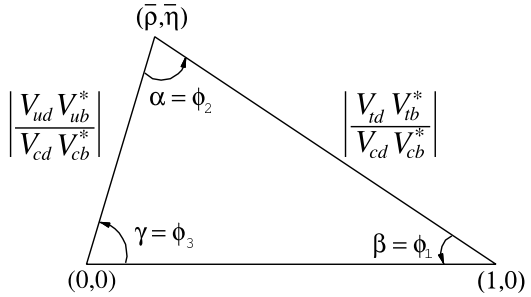

Figure 5.1: Figure showing the B_d^0 meson unitarity triangle, from [112]

This is called the B_d^0 meson unitarity triangle as the angles α, β, and γ are well measured in B_d^0 meson decays. The work described in this thesis focuses on the B_s^0 meson and the corresponding unitarity triangle is:

$$V_{us}V_{ub}^* + V_{cs}V_{cb}^* + V_{ts}V_{tb}^* = 0 \tag{5.21}$$

from which the angle

$$\beta_s = \arg\left(-\frac{V_{ts}V_{tb}^*}{V_{cs}V_{cb}^*}\right) \tag{5.22}$$

can be obtained. This is sensitive to CP violation via the element V_{ts}(at $\mathcal{O}(\lambda^4)$).

5.3.4 PMNS Matrix

The Pontecorvo-Maki-Nakagawa-Sakata (PMNS) matrix is used to describe neutrino oscillation and is equivalent to the CKM, with the neutrino flavours, $\nu_{e,\mu,\tau}$ corresponding to weak eigenstates. A combination of mass eigenstates will give a weak eigenstate; these mass eigenstates exist as free massive particles, differing from the weak eigenstates, which only exist during a weak interaction. The unitary matrix, U_{PMNS} can be written as:

$$U_{\text{PMNS}} = \begin{bmatrix} 1 & 0 & 0 \\ 0 & c_{23} & s_{23} \\ 0 & -s_{23} & c_{23} \end{bmatrix} \begin{bmatrix} c_{13} & 0 & s_{13}e^{-i\delta} \\ 0 & 1 & 0 \\ -s_{13}e^{i\delta} & 0 & c_{13} \end{bmatrix} \begin{bmatrix} c_{21} & s_{12} & 0 \\ -s_{12} & c_{12} & 0 \\ 0 & 0 & 1 \end{bmatrix} \tag{5.23}$$

which is similar to the CKM matrix given in Equation 5.12. As before, $s_{ij} = \sin\theta_{ij}$, and, $c_{ij} = \cos\theta_{ij}$, and, δ_{CP}, is the CP phase. The PMNS matrix describes different parameters from those in the CKM matrix. For the CKM matrix, when determined by measurement, the matrix has diagonal values close to one, and off diagonals nearer zero, this indicates small mixing. For the PMNS matrix, when determined by measurement, the values are near one, and similar to the unit matrix, this is indicative of a disordered mixing pattern with large mixing, [113, 114].

5.4 Symmetry breaking within the SM

As introduced in Section 5.2, there exists three main discrete symmetries in the SM, being Parity conjugation, Charge conjugation and Time conjugation. In Section 5.3, it was mentioned that these symmetries are not upheld, but are violated as observed in experiments. This section discusses the symmetry breaking seen in the SM.

5.4.1 Parity violation

Spatial parity was once thought to be universal until challenged by the scepticism of Lee and Yang in 1956, [115], stating that "parity conservation is so far only an extrapolated hypothesis unsupported by experimental evidence," when talking about the weak nuclear force. With this in mind, Wu set out to investigate this through experiment [116]. In Wu's experiment, the angular distribution of emitted electrons from aligned, supercooled cobalt 60 was measured. If parity were conserved, the angular distribution of emitted electrons should be equal. Yet the electrons were preferentially emitted opposite the spin of cobalt 60, thus breaking parity, as spin remains unchanged under spatial parity. This result, although

shocking at the time, soon had a proposed solution. While parity could indeed be violated, it was hypothesised that the combination of charge conjugation and parity, creating CP, could be conserved. Under this hypothesis, the emitted electrons observed by Wu would be accounted for, given the swap from particle to antiparticle.

5.4.2 Charge Parity, CP, violation

Whilst there was no evidence for charge conjugation breaking on its own, the recent combination of charge parity had almost goaded some physicists into checking. Cronin and Fitch, discovered violations of CP symmetry within neutral kaon decays, [117].

The K_2^0 meson, sometimes known as the long lived neutral kaon K_L, is primarily a CP eigenstate with $CP = -1$, given that the K^0 is a flavour superposition of K^0 ($s\bar{d}$) and $\bar{K^0}$ ($\bar{s}d$). The $K^0{}_2$ meson can decay into two pions; these pions have a combined CP value of $CP = +1$, because the two pions are invariant under a CP transform. This is direct evidence of CP breaking, as K_L with $CP = -1$, decays into 2π with $CP = +1$, violating CP conservation.

Thus, the combination of parity and charge conjugation is violated; if CP were an exact symmetry, the laws of nature would be the same for matter and anti-matter, which is not seen in the neutral kaon mixing. However, given the general matter abundance compared to antimatter, and from the results of Cronin and Fitch, there is an interaction mechanism to aid the explanation of the matter-antimatter asymmetry. While the strong and electromagnetic interactions are observed to be C and P invariant, the weak force is not, and maximally violates C and P symmetry, demonstrated in experimental observation of right-handed neutrinos not interacting with the weak force.

5.4.2.1 Direct CP violation

Direct CP violation, sometimes called CP violation in decay, is the only possible source of CP asymmetry in charged meson decays. The decay amplitude, Γ, of

the particle, M, into the final state, f, is different from the decay amplitude of its anti-particle into its final anti-state, expressed in Equation 5.24:

$$\Gamma(M \to f) \neq \Gamma(\bar{M} \to \bar{f}). \tag{5.24}$$

Direct CP violation in decays is often quantified with the difference of decay width of the two charge-conjugated states given by Equation 5.25

$$A_{CP} = \frac{\Gamma(M \to f) - \Gamma(\bar{M} \to \bar{f})}{\Gamma(M \to f) + \Gamma(\bar{M} \to \bar{f})} \tag{5.25}$$

where A_{CP} represents the CP asymmetry measured.

5.4.2.2 Mixing induced CP violation

Mixing-induced CP violation, sometimes called indirect CP violation, is found when the probability of oscillation from meson to anti-meson is different from the probability of anti-meson to meson, seen in Equation 5.26.

$$\text{Prob}(P^0 \to \bar{P}^0) \neq \text{Prob}(\bar{P}^0 \to P^0) \tag{5.26}$$

where P^0 and $\bar{P}^0$ represent a neutral particle and its antiparticle. This difference in oscillation probabilities indicates that the mass eigenstates are not CP eigenstates, as they do not possess a definite CP eigenvalue, meaning they are a superposition of states, and CP violation can occur.

5.4.2.3 CP violation induced by the interference of mixing and decay amplitudes

The picture of CP violation is further complicated when both the state and anti-state can decay into the same final state, f, seen in Figure 5.2. This type of induced CP violation is seen in the $B_s^0 \to J/\psi\phi$ decay.

It is possible that, when the direct decay amplitudes interfere with the mixing amplitudes, CP violation arises. In this case, as shown in Equation 5.27, the requirement for CP violation is less strict than in the other two cases.

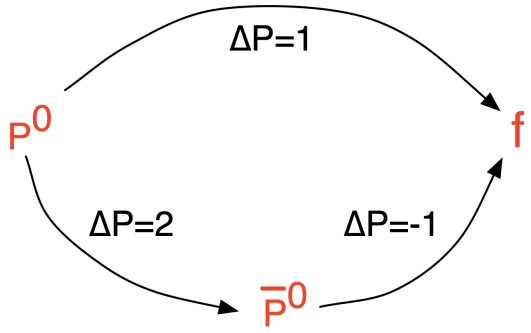

Figure 5.2: Figure displaying a decay in which both P^0 and $\bar{P}^0$ can decay into the same final state, f, [118]

$$\frac{q}{p} \cdot \frac{\bar{A}_f}{A_f} \neq 1 \Rightarrow CP \text{ violation} \tag{5.27}$$

These conditions can again be displayed, seen in Figure 5.3, and used to introduce a new quantity, useful for the study of CP violation containing meson anti-meson mixing, defined in Equation 5.28.

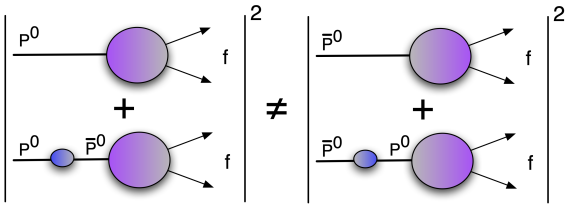

Figure 5.3: Figure displaying the conditions for CP violation induced by mixing and decay amplitudes, [118]

$$\lambda_f = \frac{q}{p} \cdot \frac{\bar{A}_f}{A_f} = |\lambda_f| e^{i\theta_f} \tag{5.28}$$

where $\bar{A}_f$ and A_f are decay amplitudes, q/p is the relative phase from meson anti-meson mixing, λ_f contains all the information on the CP asymmetry of the system, and θ_f is the weak mixing phase. If the decay amplitudes are the same, CP violation appears if

$$\left|\frac{q}{p}\right| \neq 1 \tag{5.29}$$

this type of CP violation is also called indirect CP violation.

5.4.3 Time symmetry breaking

Despite time reversal being difficult to physically test, it can be, and is, broken in entropy-based events. Entropy can be understood as order within the natural microscopic world and how order evolves into chaos. Entropy-based systems are governed by the second law of thermodynamics, stating "it is impossible for any system to undergo a process in which it absorbs heat from a reservoir at a single temperature and converts the heat completely into mechanical work, with the system ending in the same state in which it began." [119].

A physical example of a process that breaks time symmetry is the oscillation of neutral mesons, for example, the neutral B_s meson mixing, mixing discussed in Section 5.5. For now, know that the neutral B_s meson oscillates between the meson and antimeson, but the oscillation from meson to antimeson takes a different time from antimeson to meson. So that the time of transition from meson to anti-meson is $B_s \to \bar{B}_s \neq \bar{B}_s \to B_s$. This asymmetry in transition times violates the time reversal symmetry. In a time symmetric process, if the time could and was reversed, the rates $B_s \to \bar{B}_s$ and $\bar{B}_s \to B_s$ would be the same. This asymmetry is measured at the LHC in experiments such as LHCb and ATLAS, [120, 121]. The first direct observation of the T symmetry breaking was made at the CERN LEAR ring, [122].

5.4.4 CPT Theorem

Charge Parity Time, CPT, theorem states that the operation of time reversal, parity and charge conjugation is an exact symmetry for any interaction. This is a founding principle of quantum field theory, and violation of this symmetry would invalidate many established models and theories in physics. This can be explained experimentally so that particles and antiparticles must have the same mass, lifetime, and magnetic moment.

5.5 Neutral meson mixing

Neutral meson mixing theory is an essential precursor for understanding the $B_s \to J/\psi\phi$ meson mixing which is presented later in this thesis. In neutral meson mixing, the particle and antiparticle self-oscillate through flavour states, which is due to the weak interaction. The most well-known type of neutral meson mixing is the $K^0 - \bar{K}^0$ mixing, explained in Section 5.5.2.

Particle oscillation occurs when the particle and its antiparticle are distinguished by an internal quantum number that is not conserved in the weak interaction, an example of which is strangeness. Imagine an example in which there is a particle, P^0, and a respective anti-particle, $\bar{P}^0$. In this example, the quantum number violated by the weak interaction is introduced as F, so that $\Delta F = 0$, for the electromagnetic and strong interactions. For the weak interaction $\Delta F \neq 0$, and in the case of B_s mesons, $F = S$, where S is the strangeness quantum number.

Continuing this example, with a particle at time $t = 0$, occupying the state $|P^0\rangle$ or $\left|\bar{P}^0\right\rangle$ that evolves into a mixed state with an increase in time, t. This can be written as a superposition of states within the wavefunction, Ψ, so that:

$$|\Psi(t)\rangle = a(t)\left|P^0\right\rangle + b(t)\left|\bar{P}^0\right\rangle \tag{5.30}$$

where the time evolution operators, a, and, b, are governed by the Schrödinger equation:

$$i\hbar\frac{\partial}{\partial t}\Psi = \mathcal{H}\Psi \tag{5.31}$$

and

$$\Psi(t) = \begin{pmatrix} a(t) \\ b(t) \end{pmatrix} \tag{5.32}$$

and the Hamiltonian is of the form

$$\mathcal{H} = \begin{pmatrix} H_{11} & H_{12} \\ H_{21} & H_{22} \end{pmatrix} \tag{5.33}$$

where $\mathcal{H}$ is a Hermitian matrix, sometimes referred to as the "generalised mass matrix", and can be rewritten as the sum of two Hermitian matrices. The indices denote which state is interacting and acting on the other state, so that $11, 22$ are self-interacting states while $12, 21$ are states acting on one another. The two Hermitian matrices are introduced in Equations 5.34 and 5.35.

$$\boldsymbol{M} = \begin{pmatrix} M_{11} & M_{12} \\ M_{12}^* & M_{22} \end{pmatrix} \tag{5.34}$$

$$\boldsymbol{\Gamma} = \begin{pmatrix} \Gamma_{11} & \Gamma_{12} \\ \Gamma_{12}^* & \Gamma_{22} \end{pmatrix}. \tag{5.35}$$

Here, the Hamiltonian can be simplified by imposing the conditions of CPT invariance, so that M_{12} and Γ_{12} are real.

$$\begin{aligned} M_{11} =& M_{22} = M \\ \Gamma_{11} =& \Gamma_{22} = \Gamma \\ M_{12} =& M_{21} \\ \Gamma_{21} =& \Gamma_{12} \end{aligned} \tag{5.36}$$

leaving

$$\mathcal{H} = \boldsymbol{M} - \frac{i}{2}\boldsymbol{\Gamma} = \begin{pmatrix} M - \frac{i}{2}\Gamma & M_{12} - \frac{i}{2}\Gamma_{12} \\ M_{12} - \frac{i}{2}\Gamma_{12} & M - \frac{i}{2}\Gamma \end{pmatrix}. \tag{5.37}$$

This can now be diagonalised to gain the two mass eigenstates of the system, leaving the following mass eigenstates for our particle:

$$\begin{aligned} |P_1\rangle &= p\left|P^0\right\rangle + q\left|\bar{P}^0\right\rangle \\ |P_2\rangle &= p\left|P^0\right\rangle - q\left|\bar{P}^0\right\rangle \end{aligned} \tag{5.38}$$

having the following eigenvalues

$$\begin{aligned} M_1 - \frac{i}{2}\Gamma_1 =& M - \frac{i}{2}\Gamma + \frac{q}{p}\left(M_{12} - \tfrac{i}{2}\Gamma_{12}\right) \\ M_2 - \frac{i}{2}\Gamma_2 =& M - \frac{i}{2}\Gamma - \frac{q}{p}\left(M_{12} - \tfrac{i}{2}\Gamma_{12}\right) \end{aligned} \tag{5.39}$$

where

$$\frac{q}{p} = \pm\sqrt{\frac{M_{12}^* - \frac{i}{2}\Gamma_{12}^*}{M_{12} - \frac{i}{2}\Gamma_{12}}} = \sqrt{\frac{H_{21}}{H_{12}}} \tag{5.40}$$

the sign ambiguity denotes the arbitrary nature of the labels, $1, 2$ assigned, selecting opposite labels is equivalent to flipping the sign.

5.5.1 Time Evolution

The solution to Equation 5.31 yields the following for the time evolution of mass eigenstates:

$$\left|P_{\pm}^0(t)\right\rangle = \left|P_{\pm}^0\right\rangle e^{-i\left(M_{\pm} - \frac{i\Gamma_{\pm}}{2}\right)t} \tag{5.41}$$

where the $M_{\pm}$ and $\Gamma_{\pm}$ are masses and widths of the mass eigenstates, and introducing the convention from [123], $M_- - M_+ = M_2 - M_1$ and $\Gamma_+ - \Gamma_- = \Gamma_1 - \Gamma_2$. It is apparent that the observed particles are mixed states; they are linear combinations of the two flavour states $|P^0\rangle$ and $\left|\bar{P}^0\right\rangle$, with the difference between widths and masses being dependent on the system in question.

$$\begin{aligned} \Delta M =& M_- - M_+ \\ \Delta\Gamma =& \Gamma_+ - \Gamma_- \end{aligned} \tag{5.42}$$

Through subtraction of the equations in Equation 5.39, and taking the real and imaginary parts, we can write

$$\begin{aligned} \Delta M = M_- - M_+ = M_2 - M_1 =& -2\mathfrak{R}M_{12} \\ \Delta\Gamma = \Gamma_+ - \Gamma_- = \Gamma_1 - \Gamma_2 =& 2\mathfrak{R}\Gamma_{12}\cos\left(\arg\left(\frac{\Gamma_{12}}{M_{12}}\right)\right) \end{aligned} \tag{5.43}$$

The time evolution of the flavour eigenstates $|P^0\rangle$ and $\left|\bar{P}^0\right\rangle$ is given by

$$\begin{aligned} \left|P^0(t)\right\rangle &= g_+(t)\left|P^0\right\rangle + \frac{q}{p}g_-(t)\left|\bar{P}^0\right\rangle \\ \left|\bar{P}^0(t)\right\rangle &= g_+(t)\left|\bar{P}^0\right\rangle + \frac{q}{p}g_-(t)\left|P^0\right\rangle \end{aligned} \tag{5.44}$$

where

$$g_{\pm} = \frac{1}{2}\left(e^{-i\left(M_{+}-\frac{i\Gamma_{+}}{2}\right)t} \pm e^{-i\left(M_{-}-\frac{i\Gamma_{-}}{2}\right)t}\right). \tag{5.45}$$

With the time evolution of these states, it is needed to evaluate the projections of P^0 and $\bar{P}^0$ onto evolving states.

$$\begin{aligned}
\left\langle P^0 \middle| P^0(t)\right\rangle &= \frac{1}{2p}\left\langle P^0\right|\left(|P_2(t)\rangle + |P_1(t)\rangle\right) \\
&= \frac{1}{2p}\left\langle P^0 \middle| P_2(t)\right\rangle + \frac{1}{2p}\left\langle P^0 \middle| P_1(t)\right\rangle \\
&= \frac{1}{2p}\left\langle P^0\right| e^{-i\left(M_{-}-i\frac{\Gamma_{+}}{2}\right)t}\left|P_2\right\rangle + \frac{1}{2p}\left\langle P^0\right| e^{-i\left(M_{+}-i\frac{\Gamma_{-}}{2}\right)t}\left|P_1\right\rangle \\
&= \frac{1}{2p}e^{-i\left(M_{-}-i\frac{\Gamma_{+}}{2}\right)t}\left(p\left\langle P^0 \middle| P^0\right\rangle + q\left\langle P^0 \middle| \bar{P}^0\right\rangle\right) \\
&\quad + \frac{1}{2p}e^{-i\left(M_{+}-i\frac{\Gamma_{-}}{2}\right)t}\left(p\left\langle P^0 \middle| P^0\right\rangle + q\left\langle P^0 \middle| \bar{P}^0\right\rangle\right) \\
&= \frac{1}{2}\left(e^{-i\left(M_{-}-i\frac{\Gamma_{+}}{2}\right)t} + e^{-i\left(M_{+}-i\frac{\Gamma_{-}}{2}\right)t}\right)
\end{aligned} \tag{5.46}$$

Similarly,

$$\left\langle \bar{P}^0 \middle| P^0(t)\right\rangle = \left(e^{-i\left(M_{-}-i\frac{\Gamma_{+}}{2}\right)t} - e^{-i\left(M_{+}-i\frac{\Gamma_{-}}{2}\right)t}\right) \tag{5.47}$$

Using the results from Equations 5.46 and 5.47, it is possible to write down the probability, χ, of a meson in the state P^0 at $t = 0$ decaying into the state $\bar{P}^0$.

$$\begin{aligned}
\chi =& \frac{\text{Probability of state } P^0 \text{ evolving into the } \bar{P}^0 \text{ state}}{\text{Total probability of state } P^0 \text{ evolving into all possible states}} \\
=& \frac{\int_0^\infty \left|\left\langle \bar{P}^0 \middle| P^0 t\right\rangle\right|^2 dt}{\int_0^\infty \left|\left\langle \bar{P}^0 \middle| P^0 t\right\rangle\right|^2 dt + \int_0^\infty \left|\langle P^0 | P^0 t\rangle\right|^2 dt}
\end{aligned} \tag{5.48}$$

Introducing $\Gamma = \frac{\Gamma_1+\Gamma_2}{2}$, then squaring the results of 5.46 and 5.47 so that the integration in 5.48 can take place. The result of the integration is given in Equation 5.49.

$$\chi = \frac{\left(\frac{\Delta M}{\Gamma}\right)^2 + \left(\frac{\Delta\Gamma}{\Gamma}\right)^2}{\left(\frac{\Delta M}{\Gamma}\right)^2 + \left(\frac{\Delta\Gamma}{\Gamma}\right)^2 + \left|\frac{p}{q}\right|^2\left(2 + \left(\frac{\Delta M}{\Gamma}\right)^2 - \left(\frac{\Delta\Gamma}{\Gamma}\right)^2\right)} \tag{5.49}$$

Introducing $x = \frac{\Delta M}{\Gamma}$, as the oscillation parameter and $y = \frac{\Delta \Gamma}{\Gamma}$, it is possible to rewrite 5.49 with respect to x and y.

$$\chi = \frac{x^2 + y^2}{x^2 + y^2 + \left|\frac{q}{p}\right|^2 (2 + x^2 + y^2)} \tag{5.50}$$

The probability of state evolution is dependent on the difference in the masses of the mass eigenstates.

5.5.2 Kaon neutral mixing

In neutral meson mixing, the masses of the particle and antiparticle differ, leading to "light" and "heavy" mass eigenstates. The flavour states M and $\bar{M}$ are not mass eigenstates, and for kaons, the lifetimes of the mass eigenstates differ approximately by a factor of 500, [124]. $K^0 - \bar{K^0}$ are produced in the strong interaction, made up of $d\bar{s}$ and $s\bar{d}$, respectively, and can oscillate between states, $K^0 \leftrightarrow \bar{K^0}$, through the weak interaction. Consider K_1 and K_2 the CP eigenstates which are superpositions of the states $K^0 - \bar{K^0}$, seen in Equation 5.51

$$\begin{aligned} |K_1\rangle &= \frac{1}{\sqrt{2}} \left(\left|K^0\right\rangle + \left|\bar{K^0}\right\rangle \right) \\ |K_2\rangle &= \frac{1}{\sqrt{2}} \left(\left|K^0\right\rangle - \left|\bar{K^0}\right\rangle \right). \end{aligned} \tag{5.51}$$

Kaons can decay into two pion ($CP = +1$) or three pion ($CP = -1$) states. We can fix these decays to the CP states introduced before, so that their products are dependent on their CP state, seen in Equation 5.52

$$\begin{aligned} |K_1\rangle &\rightarrow 2\pi \\ |K_2\rangle &\rightarrow 3\pi. \end{aligned} \tag{5.52}$$

There is very little phase space for the 3π decay, as the lifetime of the K_2 is much longer than that of the K_1. Now we define $K_{Short} = K_S$ and $K_{Long} = K_L$ as two true mass eigenstates having a definitive lifetime, seen in Equation 5.53.

$$\begin{aligned} \tau(K_S) &= 0.9 \times 10^{-10} \text{ seconds} \\ \tau(K_L) &= 0.5 \times 10^{-7} \text{ seconds} \end{aligned} \tag{5.53}$$

To highlight the distinction between $K_{1 \text{ or } 2}$ and $K_{S \text{ or } L}$, $K_{1 \text{ or } 2}$ are CP eigenstates, while $K_{S \text{ or } L}$ are true mass eigenstates, including CP violation. Using this distinction, it is possible to write state as, ψ the wavefunction, being a linear combination of $K^0 - \bar{K^0}$:

$$\psi = \alpha \left|K^0\right\rangle + \beta \left|\bar{K^0}\right\rangle = \begin{pmatrix} \alpha \\ \beta \end{pmatrix}. \tag{5.54}$$

Following a similar formalism as Equations 5.31–5.35, we arrive at a slightly different set of equations than Equation 5.36, where the example from [125] was followed.

From the Schrödinger Equation 5.31:

$$i\hbar \frac{\partial}{\partial t} \Psi = \boldsymbol{H} \Psi \tag{5.55}$$

where $\boldsymbol{H}$ is the Hermitian matrix, sometimes referred to as the "generalised mass matrix", which can be expressed in matrix form as in Equation 5.56:

$$\boldsymbol{H} = \begin{pmatrix} M - \frac{i}{2}\Gamma & M_{12} - \frac{i}{2}\Gamma_{12} \\ M_{12}^* - \frac{i}{2}\Gamma_{12}^* & M - \frac{i}{2}\Gamma \end{pmatrix}. \tag{5.56}$$

Due to CPT invariance, and if CP symmetry is conserved, then M_{12} and Γ_{12} are real, so it becomes possible find the eigenstates by diagonalising the matrix; the results of the diagonalisation are seen in Equations 5.57–5.60.

$$M = \frac{m_1 + m_2}{2} \tag{5.57}$$

$$\Delta_M \equiv M_{12} = \frac{m_1 - m_2}{2} \tag{5.58}$$

$$\Gamma \equiv \Gamma_{12} = \frac{\Gamma_1 + \Gamma_2}{2} \tag{5.59}$$

$$\Delta\Gamma = \frac{\Gamma_1 - \Gamma_2}{2} \tag{5.60}$$

Critically, Equations 5.57–5.60 yield the mass difference and decay width parameters Δ_m and $\Delta\Gamma$, two pivotal parameters for the analysis. These parameters describe the neutral kaon system, which is why the formalism from [125] was used, differing from Section 5.5.1, where the use of [123] was used. A fuller treatment of CP violation can be found in Chapter 6 of [123]; however, a less complex approach is used to aid understanding. Insight can be gained from examining the case involving CP conservation. With this restriction, the time evolution of the CP eigenstates K_1 and K_2 follows directly from the Schrödinger equation, yielding the time-dependent wavefunctions:

$$\begin{aligned} |K_1(t)\rangle &= e^{-im_1 t - \Gamma_1 \frac{t}{2}} |K_1\rangle \\ |K_2(t)\rangle &= e^{-im_2 t - \Gamma_2 \frac{t}{2}} |K_2\rangle . \end{aligned} \tag{5.61}$$

Changing the convention to $M_- - M_+ = M_2 - M_1$ and $\Gamma_+ - \Gamma_- = \Gamma_1 - \Gamma_2$, and keeping the exponents consistent, it is possible to rewrite Equation 5.61 in the following way:

$$\begin{aligned} |K_1(t)\rangle &= e^{-i\left(M_+ - \frac{i\Gamma_+}{2}\right)t} |K_1\rangle \\ |K_2(t)\rangle &= e^{-i\left(M_- - \frac{i\Gamma_-}{2}\right)t} |K_2\rangle \end{aligned} \tag{5.62}$$

these can be written in terms of strong eigenstates:

$$\begin{aligned} \left|K^0\right\rangle_{\text{at } t=0} &\Rightarrow \frac{1}{\sqrt{2}} \left[e^{-i\left(M_+ - i\frac{\Gamma_+}{2}\right)t} |K_1\rangle + e^{-i\left(M_- - i\frac{\Gamma_-}{2}\right)t} |K_2\rangle \right] \\ \left|\bar{K^0}\right\rangle_{\text{at } t=0} &\Rightarrow \frac{1}{\sqrt{2}} \left[e^{-i\left(M_+ - i\frac{\Gamma_+}{2}\right)t} |K_1\rangle - e^{-i\left(M_- - i\frac{\Gamma_-}{2}\right)t} |K_2\rangle \right] . \end{aligned} \tag{5.63}$$

If a state, Ψ, is purely K_0 and produced at time $t = 0$ at a later time it will be a combination of $|K^0\rangle$ and $\left|\bar{K^0}\right\rangle$:

$$\begin{aligned} \left\langle K^0 \middle| \psi(t) \right\rangle &= \frac{1}{\sqrt{2}} (\langle K_1| + \langle K_2|) |\psi(t)\rangle = \frac{1}{2} \left[e^{-i\left(M_+ - \frac{i\Gamma_+}{2}\right)t} + e^{-i\left(M_- - \frac{i\Gamma_-}{2}\right)t} |K_2\rangle \right] \\ \left\langle \bar{K^0} \middle| \psi(t) \right\rangle &= \frac{1}{\sqrt{2}} (\langle K_1| - \langle K_2|) |\psi(t)\rangle = \frac{1}{2} \left[e^{-i\left(M_+ - \frac{i\Gamma_+}{2}\right)t} - e^{-i\left(M_- - \frac{i\Gamma_-}{2}\right)t} |K_2\rangle \right] . \end{aligned} \tag{5.64}$$

it is possible to calculate the probability by taking the absolute square of these states:

$$\begin{aligned}\left|\left\langle K^0\middle|\psi(t)\right\rangle\right|^2 &= \frac{1}{4}\left[e^{-\Gamma_+ t} + e^{-\Gamma_- t} + 2e^{-(\Gamma_+ + \Gamma_-)t/2}\cos(\Delta m t)\right] \\ \left|\left\langle \bar{K}^0\middle|\psi(t)\right\rangle\right|^2 &= \frac{1}{4}\left[e^{-\Gamma_+ t} + e^{-\Gamma_- t} - 2e^{-(\Gamma_+ + \Gamma_-)t/2}\cos(\Delta m t)\right]\end{aligned} \tag{5.65}$$

These expressions reveal that the K^0 and $\bar{K^0}$ states oscillate with a frequency determined by the mass difference, Δm, while simultaneously decaying with rates governed by, Γ_1, and, Γ_2, making these key parameters for any analysis dealing with CP violation and neutral meson mixing.

The mathematics presented, especially the time-dependent Schrödinger equation approach with the generalised mass matrix, provides a framework that has been extended to study mixing phenomena in other neutral meson systems, including $B_0 \leftrightarrow \bar{B}_0$, which is the focus of the $B_s^0 \to J/\psi\phi$ decay featured in the analysis. The neutral kaon mixing differs from the B_0 meson system, as the lifetime differences are much smaller, but the mass differences of the B_s^0 are substantially larger.

5.5.3 Neutral B Meson Mixing

There is commonality between the maths of neutral B mixing and neutral kaon mixing, but in practice neutral B mixing largely differs, this is due to the difference in particle signatures, amplitudes, phases and lifetimes. The kaons have respective mean lifetimes of $\tau(K_s^0) = (0.8954 \pm 0.0004) \times 10^{-10}$ s and $\tau(K_L^0) = (5.116 \pm 0.021) \times 10^{-8}$ s, whilst the B_s^0 meson has a mean lifetime of $\tau(B_s^0) = (1.520 \pm 0.005) \times 10^{-12}$ s, [124]. These lifetime differences are important for mixing processes as they affect the oscillation frequencies and decay probabilities. Similar to the kaons, CP violation can occur when both the B^0 and the $\bar{B}^0$ decay to the same final state, f. Compared to kaons, the approach with the B mesons is a bit more nuanced as the mass of the B meson is significantly higher, so lifetimes are shorter and the mass difference between the B_s^0 and the $\bar{B}_s^0$ states is smaller.

Figure 5.4, shows the mixing interactions for $B_s \leftrightarrow \bar{B}_s$ mixing as a box diagram.

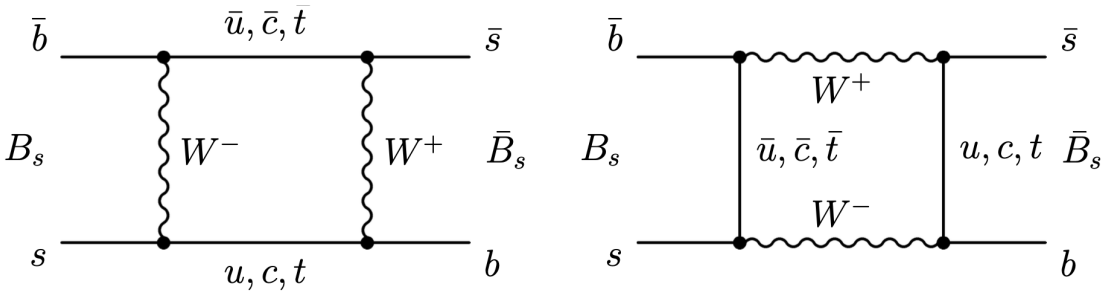

Figure 5.4: A box diagram displaying the contributions to $B_s \leftrightarrow \bar{B}_s$ mixing.

This shows that if both the B_s and the $\bar{B}_s$ can decay to the same final state, f, the direct decay amplitudes can interfere with mixing amplitudes, enabling CP violation. Under the assumption that $\Delta\Gamma \ll \Delta M$ and $\Delta\Gamma \ll \Gamma$, we can write

$$\frac{q}{p} \propto \sqrt{\frac{M_{12}^*}{M_{12}}}. \tag{5.66}$$

Assuming that the mixing process is dominated by the top quark intermediary, we can write the following,

$$M_{12}^q \propto \left(V_{tq}^* V_{tb}^*\right)^2 e^{-i(\pi - \phi_{CP})} \tag{5.67}$$

where V are elements from the CKM matrix and ϕ_{CP} is defined as

$$\mathcal{CP} \left|B_q^0\right\rangle = e^{i\phi_{CP}} \left|\bar{B}_q^0\right\rangle \tag{5.68}$$

Equation 5.68 can be written to obtain

$$M_{12}^q \propto \left|V_{tq}^* V_{tb}^*\right|^2 e^{-i\phi_q} e^{i(\pi - \phi_{CP})} \tag{5.69}$$

where

$$\phi_q = 2 \arg\left(V_{tq}^* V_{tb}^*\right). \tag{5.70}$$

Consequently we have

$$\frac{q}{p} \propto e^{-i\theta_{M_{12}}^q} \tag{5.71}$$

where

$$\theta_{M_{12}}^q = \pi - \phi_q - \phi_{CP} \tag{5.72}$$

and $\theta^q_{M_{12}}$ is referred to as the weak mixing phase. $\theta^q_{M_{12}}$ contains only CKM matrix elements and hence is "theoretically clean", whereas the ratio of the amplitude suffers from hadronic uncertainties. The mixing phase is highly constrained by the Standard Model, with negligible theoretical uncertainty, hence "theoretically clean". For the magnitude and ratio of the decay amplitudes, there are hadronic contributions in the matrix elements that contaminate the precise theoretical calculation.

It is possible to extract and separate out the "long" and "short" distance contributions by approximating the hadronic matrix elements using the low-energy effective Hamiltonians. The ratio of the amplitudes can be written as a

$$\frac{A\left(\bar{B}^0_q \to f_{CP}\right)}{A\left(B^0_q \to f_{CP}\right)} \propto \pm e^{i\phi_{CP}} \frac{\Sigma_{j=u,c} V^*_{jq} V_{jb} \left\langle f_{CP}\right| \hat{O} \left|\bar{B}^0_q\right\rangle}{\Sigma_{j=u,c} V^*_{jq} V_{jb} \left\langle f_{CP}\right| \hat{O} \left|B^0_q\right\rangle} \tag{5.73}$$

with $\hat{O}$ being the local four-quark operator, the "short-distance" contribution. Now, writing the CP asymmetry parameter, the ϕ_{CP} disappears, leaving

$$A^q_{CP} = \mp e^{-i\phi_P} \frac{\Sigma_{j=u,c} V^*_{jq} V_{jb} \left\langle f_{CP}\right| \hat{O} \left|\bar{B}^0_q\right\rangle}{\Sigma_{j=u,c} V^*_{jq} V_{jb} \left\langle f_{CP}\right| \hat{O} \left|B^0_q\right\rangle} \tag{5.74}$$

despite being poorly known, in the specific case where the decay is dominated by a single amplitude, the matrix elements cancel, leading to an expression that is considerably simpler.

$$A^q_{CP} = \eta_{f_{CP}} e^{-i\left(\phi_q - \phi^D_{f_{CP}}\right)} \tag{5.75}$$

where $\eta_{f_{CP}} = \pm 1$ is the eigenvalue of the final state f_{CP}. The two phases ϕ_q and $\phi^D_{f_{CP}}$ are responsible for CP-violation in mixing and direct decay of the B-meson to its final state, respectively.

5.6 The Search for New Physics

In general, the B physics sector is highly fruitful in the search for new physics knowledge, specifically for the B_s meson. B-hadrons are typically long-lived, allowing for the proper decay times to be measured in experiments such as ATLAS

and LHCb. The high mass of the beauty quark meaning a high range of decay channels, which enables a rich programme of physics study. CP violation is often more interesting as an indicator of new physics than a phenomenon in its own right. Decays in with one dominant decay amplitude are known as "Golden Modes" due to their great experimental interest. One of these decay modes is the $B_s \to J/\psi\phi$, which is studied in Chapter 6

Chapter 6

$B_s^0 \to J/\psi\phi$ Analysis

When searching for sources of CP violation for evidence of physics beyond the Standard Model, it is possible to examine the decays of B_s^0 mesons into the $J/\psi\phi$ final state. For a $B_s^0 \to J/\psi\phi$ decay, there is interference between direct decay and a decay that includes $B_s^0 - \bar{B}_s^0$ mixing, which can produce CP violation. The decay of the $B_s^0 \to J/\psi\phi$ is analysed using the Full Run-2 proton-proton collision dataset at 13 TeV collected by the ATLAS detector at the LHC, corresponding to 139 fb^{-1} of integrated luminosity. The CP phase ϕ_s is given by the phase difference between the mixing amplitude and the amplitude for the $b \to c\bar{c}s$ decay. In the Standard Model ϕ_s is related to the CKM elements, and predicted with high precision, $\phi_s \approx 2\arg[-(V_{ts}V_{tb}^*)/(V_{cs}V_{cb}^*)]$. The CKMFitter group determines CKM matrix parameters through global frequentist analysis of meson decay measurements. They predicted a value of $\phi_s = -0.0596^{+0.00072}_{-0.00082}$ rad, [126], by combining beauty with kaon physics observables, assuming no new physics contributions to the B_s^0 mixing and decays. Using the Standard Model as the assumption, the UTfit collaboration predicted a value of $\phi_s = 0.03700 \pm 0.00104$ rad, [127], the UTfit group performs Unitarity Triangle fits to determine CKM parameters and search for New Physics. The phase ϕ_s can also be expressed through the parameter λ through the relation $\phi_s = -\arg(|\lambda|)$, where $|\lambda|$ describes the direct CP violation in $B_s^0 \to J/\psi\phi$. Within $B_s^0 - \bar{B}_s^0$ mixing, there is the oscillation between these two particles, which involves

the oscillation of the light and heavy mass eigenstates, respectively B_L and B_H, and have associated decay widths of Γ_L and Γ_H. The difference between these widths, $\Delta\Gamma_s = \Gamma_L - \Gamma_H$, can be used to test theoretical predictions,[128], as can a related quantity, the mass difference Δm_s between the heavy and light mass eigenstates.

Measurements of the main $B_s^0 \to J/\psi\phi$ decay parameters, $\Delta\Gamma_s$, Γ_s, ϕ_s and Δm_s are presented in this chapter. There have been previous measurements of these parameters, notably by ATLAS, CDF, CMS, D0 and LHCb, [129, 130, 131, 132, 133, 134, 135, 136]. If the Standard Model is the full description of physics, these quantities from other processes should agree with those measured in this analysis. If there are non-Standard Model contributions to these physical processes, then the measured values in this analysis may differ from those recorded from these experiments. These measurements are at higher centre of mass energy and will have an increased number of events, and so better statistics, as well as procedural improvements aiming to limit systematic uncertainties. Measurements of the CP phase ϕ_s in the $B_s^0 \to \psi(2S)\phi$, $B_s^0 \to D_s^+ D_s^-$ and $B_s^0 \to J/\psi\pi^+\pi^-$ channels have also been reported by LHCb, [137, 138, 139, 140]. The mass difference Δm_s has been measured by LHCb, CMS and CDF [131, 133, 141, 142, 143, 144]

This measurement uses the complete Run 2 dataset of 139 fb^{-1} of proton-proton collisions data, recorded by ATLAS at the LHC during the period from 2015 to 2018 at a centre of mass energy of $\sqrt{s} = 13$ TeV. Compared with the previous results from ATLAS, [121], a more precise value is presented in this thesis, and this is one of the first measurements made by the ATLAS collaboration of the physics parameters Δm_s and λ where previously they were free parameters of the fit.

6.1 ATLAS Monte Carlo

The Monte Carlo, MC, generator used for this analysis was Pythia 8.210, which was tuned to ATLAS data. It generated over 100M $B_s^0 \to J/\psi\psi$ events for the study of detector response, background and systematic effects. Background events were

also generated, for the exclusive $B_d^0 \to J/\psi K^{0*}$ and $\Lambda_b \to J/\psi p K^-$ decays and the inclusive $b\bar{b} \to J/\psi X$ and $pp \to J/\psi X$ decays. In calibration studies, events with $B^\pm \to J/\psi K^\pm$ exclusive decays were also simulated. The MC samples use the A14 set of parameter values and the CTEQ6L1 parton distribution functions, [145]. The detector response was simulated using the ATLAS simulation framework based on Geant4 [49]. The MC events were weighted to reproduce the same number of pp interactions per bunch crossing (pile-up) and trigger conditions as occur in data.

6.2 Reconstruction and candidate selection

Events containing the $B_s^0 \to J/\psi(\mu^+\mu^-)\phi(K^+K^-)$ decay candidates must pass the trigger selections, and must contain at least one reconstructed primary vertex, PV, with at least one pair of opposite charged muon candidates. A minimum of four ID tracks is imposed to define a PV. Muon candidates are reconstructed with both ID and MS; the parameters are obtained exclusively from the ID measurement, as it dominates the precision of their measurement in the p_T range required. Muon candidates must either meet the "tight" or "low-p_T" criteria, as previously described in Section 3.5.2.2. Muon track pairs are refitted to a common vertex, provided they meet a quality of fit requirement based on $\chi^2/N_{\text{dof}} < 10$. To account for the different mass resolutions achievable in different regions of the detector, the J/ψ candidates are divided into three subsets depending on the pseudorapidities of the muons.

1. The first subset: both muons have $|\eta| < 1.05$, as these values correspond to the edges of the barrel part of the Muon Spectrometer.

2. The second subset: one muon has $1.05 < \eta < 2.5$ and the other muon has $|\eta| < 1.05$.

3. The third subset: contains candidates where both muons have $1.05 < \eta < 2.5$.

The J/ψ mass and its resolution are extracted for the three subsets with a maximum likelihood fit. In each case, the signal region is defined symmetrically around the

fitted mass to retain 99.7% of the J/ψ candidates. The choice for a symmetric distribution is justified by the J/ψ decay width being of the keV, which is negligible when compared with the detector resolution, which is typically $40 - 70$ MeV.

All pairs of oppositely charged tracks that have $p_T > 1$ GeV, and $\eta < 2.5$ and are not identified as muons or electrons are used to reconstruct candidates for the decay $\phi \to K^+K^-$. Candidates for $B_s^0 \to J/\psi(\mu^+\mu^-)\phi(K^+K^-)$ decays are selected by fitting the tracks for each combination of $J/\psi \to \mu^+\mu^-$ and $\phi \to K^+K^-$ to a common vertex and fitting the invariant mass calculated from the two muon tracks to the J/ψ mass. For the $\phi \to K^+K^-$ candidate, the invariant mass of the track pairs, using the charged kaon mass hypothesis, must fall within the interval 1.0085 GeV $< m(K^+K^-) <$ 1.0305 GeV. The interval is chosen using MC simulation and is selected to retain 98% of true $\phi \to K^+K^-$ decays. The Breit–Wigner width of the ϕ meson is 4.2 MeV, the interval chosen was ± 11 MeV, with the mass resolution of the $\phi(K^+K^-) \approx 2.4$ MeV. The range of interest is 11 MeV, which includes both the resonance of the K^+K^- decays and part of the non-resonance for the ${B_s}^0 \to J/\psi K^+K^-$ decays, this non-resonance is referred to as the S-wave. To obtain enough events with this S-wave contribution, 11 MeV was chosen, allowing for the determination of both the S-wave terms and the terms due to the $P - S$ wave interference. The window was restricted to limit the combinatorial background under K^+K^- and also under ${B_s}^0$ mass. A quadruplet of tracks is accepted for further analysis if the vertex has $\chi^2/N_{\rm dof} < 3$.

When more than one candidate in an event passes all selections, the B_s^0 candidate with the lowest $\chi^2/N_{\rm dof}$ is selected. A total of $5,434,606$ B_s^0 candidates are collected within the mass range $5150 - 5650$ MeV. This range is chosen to retain sufficient background events in the sidebands of the mass distribution to allow a precise determination of the properties of background events. Variations to the mass window choice show it to have a negligible systematic effect on the results.

As the mean number of interactions per bunch crossing is about 32, [146], it is necessary to identify the best candidate for the primary vertex. This identification

uses the three-dimensional impact parameter a_0, the minimum distance between each primary vertex candidate and the line extrapolated from the reconstructed B_s^0 meson candidate vertex in the direction of the B_s^0 momentum. The primary vertex with the smallest a_0 is chosen and used in the rest of the analysis.

The proper decay time, t, of each B_s^0 meson candidate is calculated from

$$t = \frac{L_{xy} m_b}{p_{T_b}} \tag{6.1}$$

where p_{T_b} is the reconstructed transverse momentum of the B_s^0 meson candidate and m_B denotes the mass of the B_s^0 meson, taken numerically as the world average. The transverse decay length, L_{xy}, is the displacement in the transverse plane of the B_s^0 meson decay vertex relative to the primary vertex, projected onto the direction of the B_s^0 transverse momentum, this is shown in Figure 6.1. To avoid biasing L_{xy}, the primary vertex position is recalculated after removing any track used in the B_s^0 meson candidate reconstruction. Figure 6.1 shows and interaction producing two light-flavour jets, and displays the relationship between the PV and the SV for L_{xy}.

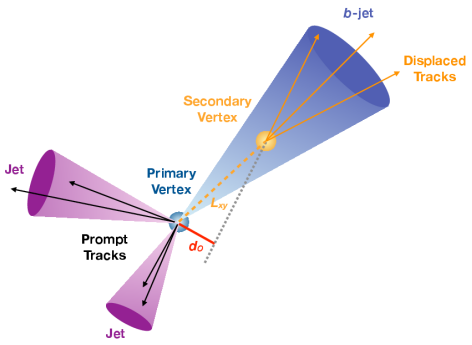

Figure 6.1: A schematic diagram of an interaction producing two light-flavour jets and one b-jet, shown in the transverse plane. The lifetime of b-hadrons corresponds to a transverse decay length, L_{xy}, and produces displaced tracks originating from a secondary vertex. The distance of closes approach of a displaced track to the primary vertex is defined as the transverse impact parameter, d_0, and typically is large for tracks originating from the decay of b-hadrons, [147].

6.3 A Foreword on Flavour Tagging

This analysis uses its own flavour tagging methods, which are different from the ATLAS flavour tagging that is typically used. This analysis team was asked by ATLAS management to use the traditional ATLAS flavour tagging in conjunction with the analysis-based tagging. The goal of the following sections is to introduce both the analysis particle anti-particle tagger, and the more usual b, c, or light quarks tagging. The initial idea was to just use the team's own tagging for the analysis, but after consultation with ATLAS management, it was requested that the analysis team verify that the "opposite hemisphere", shown in Figure 6.2, actually contained the b or $\bar{b}$ quark as outputted by the analysis tagger. The particle anti-particle tagger tags a physics object, then the traditional ATLAS tagger is used to tag b or c quarks. The traditional ATLAS tagger is introduced with a weaker working point than usual to keep the statistics for the analysis, and the traditional tagger confirms that there is a beauty quark in the opposite hemisphere. What matters most to

this analysis is the determination of particle or anti-particle when tagging; we are less concerned with the b or c hadron determination. For clarity, let us define the following:

- Particle Anti-Particle Tagging: The tagging method predominantly used in this analysis. Concerned, as the name suggests, with whether the candidate is a particle or an anti-particle
- Quark Flavour Tagging: The "typical" or "traditional" ATLAS quark flavour tagging, introduced to this analysis after consultation with ATLAS management.

Where possible, these two differing terms will be used to explain what type of flavour tagging is used and when. Sections 6.4 to 6.10 cover the Particle Anti-Particle tagging, while Section 6.11 covers the more typical ATLAS Quark Flavour Tagging.

6.4 Particle anti-particle tagging

This analysis relies on the identification of the flavour of the neutral B_s^0 meson at the point of its production. This uses a process known as "opposite-side-tagging" (OST), and is accomplished with information obtained from the other b-hadron produced from the $b\bar{b}$ pair of quarks. The OST algorithms are described in more detail in Section 6.6. The OST algorithms define discriminating variables that are sensitive to the quark flavour (b or $\bar{b}$) of the opposite-side b-hadron, based on electric charge information. The electric charge information involves a variable quantifying the weighted sum of the charge of tracks from the opposite side b-hadron, which is the bins in a charge cone, for more detail on charge cones see Equation 6.2.

The outcome of the algorithms is a probability that a particular signal B_s^0 meson candidate was produced as a meson or anti-meson, specifically relating to the production of the b or $\bar{b}$ quark. The algorithms are calibrated with data containing

$B^\pm \to J/\psi K^\pm$ candidate decays, as the charge of the kaon indicates if a b or $\bar{b}$ was produced, and hence if it was accompanied by a $\bar{b}$ or b at production. Due to the certainty of the decay products, inputting the calibration sample into the OST algorithm can verify the accuracy of the OST. The $B^\pm \to J/\psi K^\pm$ calibration sample also has the benefit that is has the same topology and similar kinematics to the B_s^0 signal sample in the main analysis. These OST algorithms are calibrated as a function of the discriminating variable, using yields of $B^\pm$ mesons extracted from fits to the data. Once calibrated, they are applied to the $B_s^0 \to J/\psi(\mu^+\mu^-)\phi(K^+K^-)$ candidates, and the resultant probability that each candidate was produced in a B_s^0 or $\bar{B_s^0}$ meson state is used in the maximum likelihood fit described in Section 6.12. The calibration procedure uses the complete Run 2 dataset, 139 fb^{-1} of proton-proton collision data.

6.5 Same-Side Tagging

Same-side Tagging, SST, is a technique used to determine the initial flavour of a neutral B_s^0 meson by examining particles produced alongside it during hadronisation. Hadronisation is a mechanism in which quarks and gluons in hard processes form the hadrons that are observed in the final state. Note that the focus is on the B_s^0 meson, but these methods can be extended to other B meson candidates. SST exploits quark conservation of the strong interaction, specifically the correlation between the B_s^0 meson's initial flavour and the flavour of nearby particles. During tagging, nearby particles get assigned to the B_s^0 meson so that the decay chain can be further analysed by the SST. When a strange quark is produced in fragmentation, an anti-strange quark will also be produced. The equal production of strange and anti-strange particles is leveraged, having found one strange quark, a search is carried out for a kaon containing the other strange quark. The decay products of this kaon are analysed, and will allow for separation of a B_s^0 meson and $\bar{B_s^0}$ meson. SST will search for kaons, which often involves data from the Transition Radiation Tracker

(TRT), such as the number of TRT hits.

Figure 6.2 displays the signal candidate for both the same side kaon as for the example of the SST, as well as displaying the same for OST.

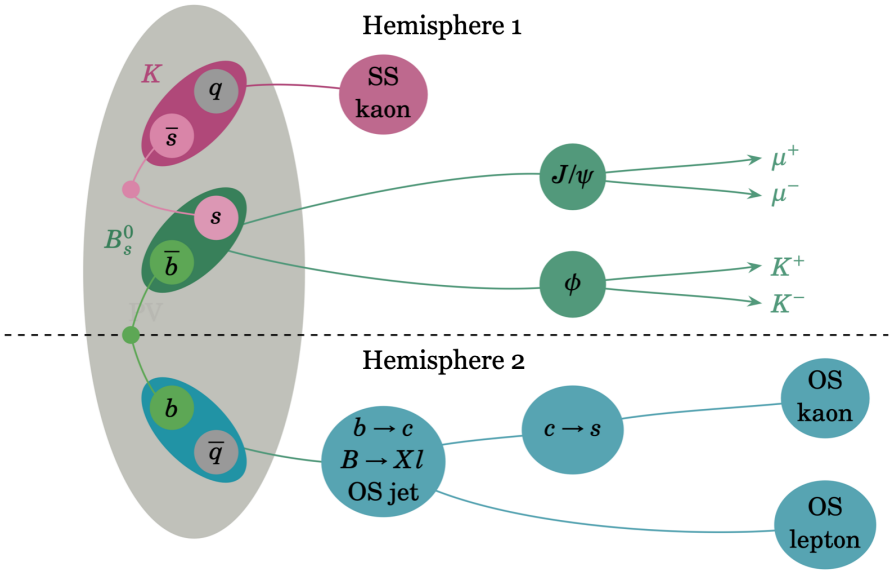

Figure 6.2: The schematic overview of the underlying principles of flavour tagging algorithms to infer the initial B_s^0 flavour. The horizontal dashed line displays the separation of hemispheres. Both algorithms for the same-side and opposite-side are shown. Figure taken from [79], Section 7.1.

6.6 Opposite-Side Tagging

A B_s^0 meson candidate is identified, typically through the decay products of the $J/\psi(\mu^+\mu^-)$ and $\phi(K^+K^-)$. OST is used to determine the initial flavour of the B_s^0 meson candidate, exploiting the correlated production of b and $\bar{b}$ quarks, achieved through focusing on the quark that does not participate in the signal process.

OST relies on semi-leptonic decays of the opposite-side b hadron. The charge of the observed lepton gives insight into the initial flavour of the b hadron with a positive lepton signalling an $\bar{b}$ quark, and therefore an $\bar{B}$ meson, while a negative lepton signals a b quark, resulting in a B meson on the signal side.

For the successful implementation of OST, fragmentation tracks associated with the opposite-side b-hadron must be reconstructible. If no tracks can be confidently assigned to this opposite-side meson, OST cannot be performed for that event.

6.7 Calibration using $B^{\pm} \to J/\psi K^{\pm}$ Event Selection

The $B^{\pm} \to J/\psi K^{\pm}$ decay can be used as a calibration tool for the opposite-sign tagger used in this analysis. Kinematically, the decay is very similar, but the crucial difference is that the correct states in the decay are known simply by recording the final decay state, as the charge of the kaon indicates if a b or $\bar{b}$ was initially produced. The certainty of the calibration sample's decay products allows for direct verification of the OST's output against the known particle identities. Calibration is done before applying it to the $B_s \to J/\psi\phi$ decay. Summarising, the calibration sample has a known decay chain, relating the kaon charge to that of the b or $\bar{b}$. Testing the OST with the calibration sample means the expected output is known, and used to verify the accuracy of the OST before it is applied to the uncertainty involved with the $B_s \to J/\psi\phi$ decay candidates.

The first step in the identification of $B^{\pm} \to J/\psi K^{\pm}$ decay candidates is the selection of J/ψ candidates from oppositely charged muon pairs forming a vertex for which the χ^2/N_{dof} of the fit is less than 5. Where 5 is the limit as the J/ψ candidate is being used in the ${B_s}^0$ vertex refitting. The vertex refitting uses the J/ψ muons, muons directly from the decay of the J/ψ meson, and the K^+ K^- tracks as well as the final PDG mass constraint [110]. After the B-vertex fit, the selection is narrowed to $\chi^2/N_{\text{dof}} < 3$. Each muon is required to have $p_T > 4$ GeV and $|\eta| < 2.5$. Dimuon candidates with invariant mass $2.8 < m(\mu^+\mu^-) < 3.4$ GeV, as determined from the re-fitted track parameters of the vertex, are retained for further analysis. An additional track is required to form the $B^{\pm}$ candidate. The mass of the dimuon pair is constrained to the J/ψ mass, and the additional track is assigned

the charged-kaon mass hypothesis. The additional track and the mass-constrained dimuon pair are combined using a vertex fit. A requirement on the proper decay time of the $B^{\pm}$ candidate of $t > 0.2$ ps is applied to suppress prompt background.

The tagging probabilities are determined from the B^{+} and B^{-} meson signal candidates in the charged B selection, as described in Section 6.6. These signal yields are derived from fits to the invariant mass distribution, $m(J/\psi K^{\pm})$, which are performed in intervals of cone charge Q_x. Two Gaussian functions with a common mean are used to describe the $B^{\pm} \to J/\psi K^{\pm}$ signal, one modelling the shorter lifetime kaon, one modelling the longer lifetime kaon. An exponential function is used to describe the combinatorial background. A hyperbolic tangent function is applied to parametrise the low-mass contribution from incorrectly or partially reconstructed b-hadron decays (denoted $B^{\pm} \to J/\psi X$). A Gaussian function is used to describe the $B^{\pm} \to J/\psi \pi^{\pm}$ contribution, with fixed parameters taken from simulation except in the case of the normalisation, which is a free parameter. The choice of Gaussian over a Briet-Wigner distribution is justified by the detector resolution being $\approx 30 - 40$ MeV, which is much bigger than the keV scale of the natural width of a decaying $J/\psi(\mu\mu)$. A fit to the overall mass distribution constrains the shapes of the signal and backgrounds. Subsequent fits are performed in the intervals of the tagging discriminating variables, separately for B^{+} and B^{-} meson candidates, with the normalisation and exponential slope parameters left free. Figure 6.3 shows the invariant mass distribution of $B^{\pm}$ candidates overlaid with the result of the fit to all selected candidates. The individual fit components for the signal and backgrounds are also shown.

6.8 Particle anti-particle tagging methods

Several methods are used to infer the flavour of the signal b-hadron at the point of production. They differ in their efficiency and discrimination power. The measured charge of the lepton ℓ, electron or muon, from the semileptonic decay of the b-hadron

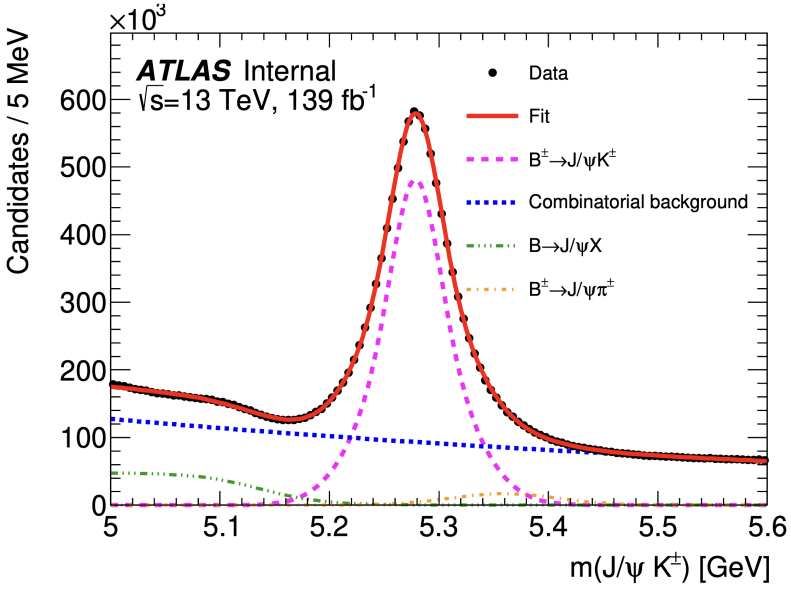

Figure 6.3: ATLAS internal result. The invariant mass distribution for selected $B^{\pm} \to J/\psi K^{\pm}$ candidates. Data are shown as points, and the overall result of the fit is given by the red curve. The signal component is described by the short-dashed magenta line. The contribution from the combinatorial background component is indicated by the blue dotted line, partially reconstructed b-hadron decays by the green dash-dot-dot line, and decays of $B^{\pm} \to J/\psi\pi^{\pm}$, where the pion is misassigned as a kaon, by the orange dash-dotted line.

provides strong discrimination; however, the $b \to \ell$ transitions are diluted through processes, such as B meson oscillations and cascade decays $b \to c \to \ell$, that can change the charge of the observed lepton. In the case of multiply lepton tagged events, the following order is used to select the OST method: Tight muon, electron, Low-p_T muon. If no lepton is present, tracks in a jet associated with the opposite-side b-hadron decay are used. The separation power of a lepton tagging method is enhanced by the use of a weighted sum of the charge of the tracks in a cone around the lepton or jet direction. The parameters applied, ε_{tag}, D_{tag} and T_{tag} in Section 6.11.5, are determined separately for each tagging method by optimising the tagging performance. The cone is defined for the volume $\Delta R = \sqrt{(\Delta\phi)^2 + (\Delta\eta)^2}$ around the lepton or jet direction, where ϕ is the azimuthal angle of the particle with respect to the track, and η is the pseudorapidity defined in Section 2.1.1. The weighted sum, or *cone charge*, Q_x, is defined according to Equation 6.2.

$$Q_x = \frac{\sum_i^{N \text{ tracks}} q_i \cdot (p_{\text{T}i})^\kappa}{\sum_i^{N \text{ tracks}} (p_{\text{T}i})^\kappa} \tag{6.2}$$

here $x = \{\mu, e, \text{jet}\}$ refers to muon, electron, and jet charge, respectively, and the summation uses the charge q_i and transverse momentum $p_{\text{T}i}$ of the selected tracks, including the lepton, satisfying method-dependent conditions defined below. The requirements on the tracks, on κ, is determined by an optimisation process, and ΔR depends on the OST method. The inverse transverse momentum, κ, is defined as (q/p_T) [148].

Two subcategories of charge cones are considered. The *discrete* category, Section 6.10.2, is used in the case where the cone charge is formed from one or more tracks of the same charge; this results in a cone charge of $Q_x = \pm 1$. The *continuous* category, Section 6.10.1, is used when more than one track is involved and the sum contains tracks of both negative and positive charges. In the continuous case, Q_x is divided into intervals within the range $-1 < Q_x < 1$ for each OST algorithm.

The probability $P(B|Q_x)$ that a signal B meson is produced in a state containing a $\bar{b}$-quark, given the value of the cone charge Q_x, is constructed. An equivalent

probability for the b-quark case is defined as $P(\bar{B}|Q_x)$. Using the $B^\pm$ calibration samples, the probability of Q_x, given the flavour of $B^\pm$, $P(Q_x|B^\pm)$ is defined for each tagging method as normalised number of $B^\pm$ events with given Q_x. The probability to tag a B_s^0 meson as containing a $\bar{b}$-quark is therefore given as:

$$P(B|Q_x) = \frac{P(Q_x|B^+)}{(P(Q_x|B^+) + P(Q_x|B^-))} \tag{6.3}$$

and correspondingly

$$P(\bar{B}|Q_x) = 1 - P(B|Q_x). \tag{6.4}$$

If there is no OST information available for a given B_s^0 meson, a probability of 0.5 is assigned to that candidate as there should be equal chance of the meson containing b and $\bar{b}$ quarks due to the expected equal production.

6.8.1 Muon tagging

At least one additional muon is required for muon-based tagging. It must have $p_T > 2.5$ GeV, $|\eta| < 2.5$, and $|\Delta z| < 5$ mm, where $|\Delta z|$ is the difference in z between the primary vertex and the longitudinal impact parameter, z_0, of the ID track associated with the muon. Muons are classified independently of the J/ψ selection criteria and kept if their identification quality selection working point is either Tight or Low-p_T; these categories are subsequently treated as distinct flavour tagging methods. Tight muons dominate the range of muon $p_T > 4$ GeV. The Low-p_T requirement typically identifies muons of $p_T < 4$ GeV. When multiple muons satisfy the selection criteria in one event, Tight muons are chosen over Low-p_T muons, as Tight muons are most likely muons from the B-signal. Within the same muon category, the muon with the highest p_T that passes the selections is used.

A muon cone charge variable, Q_μ, is calculated using Equation 6.2, with $\kappa = 1.1$ and the sum runs over the reconstructed ID tracks within a cone of size $\Delta R = 0.5$ around the muon direction. These tracks must have $p_T > 0.5$ GeV, $|\eta| < 2.5$, and $|\Delta z| < 5$ mm. Tracks associated with the decay of a signal B meson candidate are

excluded from the sum. In each interval of Q_μ, a fit to the $J/\psi K^\pm$ invariant mass spectrum is performed, and the number of signal events is extracted.

The distributions of the muon cone charge using $B^\pm$ signal candidates for Tight muons are shown in Figure 6.4. The corresponding distributions for Low-p_T muons are shown in Figure 6.5.

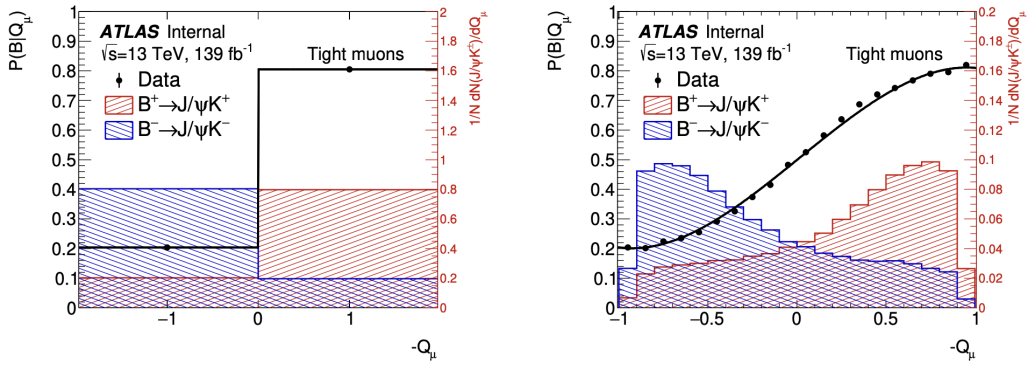

Figure 6.4: ATLAS internal result. Cone charge distributions, $-Q_\mu$, for Tight muons, shown for cases of discrete charge (left), and for the continuous distribution (right). For each plot, in red (blue), the normalised B^+ (B^-) cone charge distribution is shown (corresponding to the right axis scale). The negative value in $-Q_\mu$ is included to illustrate more B^+ like candidates with larger values on the horizontal axis (and smaller values for B^- like candidates). Superimposed is the distribution of the tagging probability, $P(B|Q_\mu)$, as a function of the cone charge, derived from a data sample of $B^\pm \to J/\psi K^\pm$ decays, and defined as the probability to have a B^+ meson (on the signal-side) given a particular cone charge Q_μ.

Figure 6.4 shows the expected number of J/ψ events per charge cone, for both the discrete (left plot) case and the continuous (right plot). These are useful figures given that the fitted parameterisation, shown in black, is used as the calibration curve for the tagger. For example, in Figure 6.4 if a charge cone has a charge value of 0.5 then the corresponding probability that the charge cone contains a B meson is ≈ 0.7. For that same charge cone of 0.5 it also has a normalised chance of containing a $B^+ \to J/\psi K^+$ event of ≈ 0.09, and a ≈ 0.03 chance of containing a

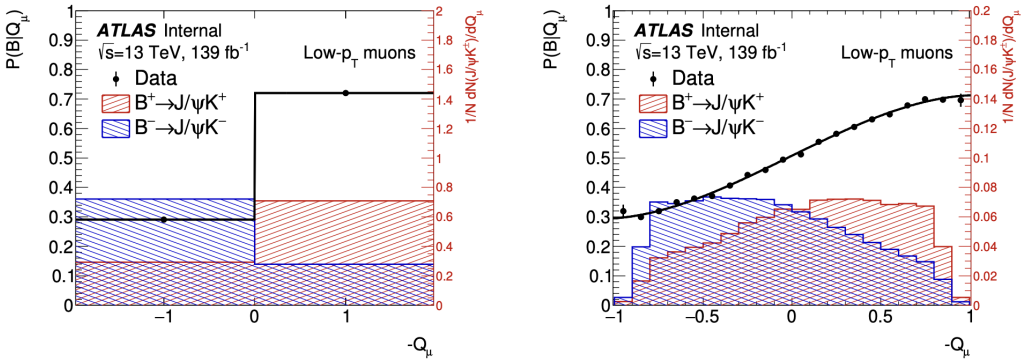

Figure 6.5: ATLAS internal result. Normalised cone charge distributions (shown against the right axis scale), $-Q_\mu$, for B^+ (B^-) events shown in red (blue) for Low p_T muons, for cases of discrete charge (left), and for the continuous distribution (right). The distribution of the tagging probability, $P(B|Q_\mu)$, is superimposed.

$B^- \to J/\psi K^-$.

6.8.2 Electron Tagging

Electron tagging is needed to correctly tag the electrons associated with the B meson candidates. Electrons are identified using ID and calorimeter information. Electrons must satisfy the Medium electron quality criteria [149], with $p_T > 2.5$ GeV. The ID track associated with the electron is required to have $|\eta| < 2.5$, and $|\Delta z| < 5$ mm. Electrons whose opening angle, ζ_b, between the signal B meson candidate momentum and the electron momentum is $\cos\zeta_b > 0.93$ are excluded in order to reject electrons from the signal-side decay. The opening angle is between the B meson candidates' momentum direction and electron momentum direction within the lab reference frame. This selection is equivalent to $\Delta R > 0.4$ rad, where $\Delta R = \Delta\phi + \Delta\eta$.

When more than one electron passes the selection, the electron with the highest p_T is chosen, as the lower p_T tracks are more likely to be fakes. Charged-particle tracks with $p_T > 0.5$ GeV, $|\eta| < 2.5$, and $|\Delta z| < 5$ mm, and within a cone of size $\Delta R = 0.5$ are used to form the electron cone charge Q_e, defined in Equation 6.2, with $\kappa = 1.0$. The resulting electron cone charge distributions and $P(B|Q_e)$ are shown in Figure 6.6.

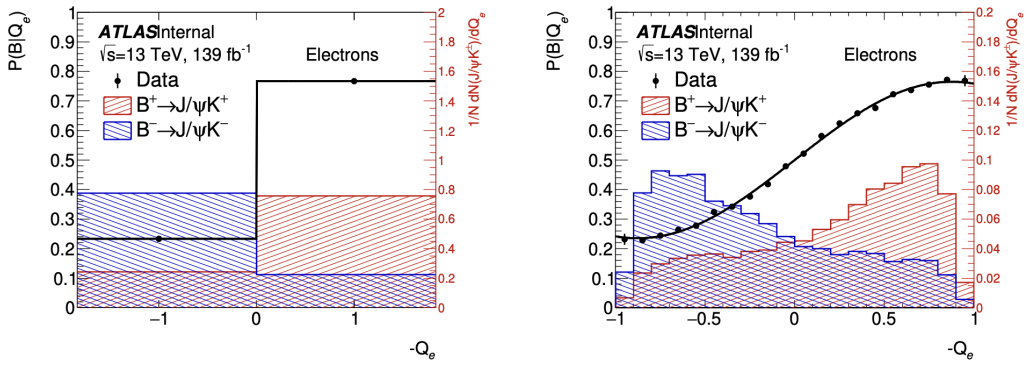

Figure 6.6: ATLAS internal result. Normalised cone charge distributions (shown against the right axis scale), $-Q_e$, for B^+ (B^-) events shown in red (blue) for electrons, for cases of discrete charge (left), and the continuous distribution (right). Superimposed is the distribution of the tagging probabilities, $P(B|Q_e)$.

6.8.3 Jet Tagging

In the absence of a muon or electron, a jet identified as containing a b-hadron is used. Jets are reconstructed from calorimetric information [150] using the anti-k_t algorithm [151, 152] with a radius parameter $R = 0.4$.The identification of a b-tagged jet uses a custom, ATLAS specific multivariate algorithm *MV2c10* [153], a BDT that combines the outputs of the low level tagging algorithms to output a classifier value. Jets are selected if the BDT classifier value exceeds 0.56, which maximises the tagging power of the calibration sample. If multiple jets are selected, the jet with the highest value of the BDT output classifier is used. Jets associated with the signal decay are not considered in this selection, where the signal decay is $B^\pm \to J/\psi K^\pm$ for the calibration sample and $B_s^0 \to J/\psi\phi$ decay for the fit to data.

Tracks within a cone of size $\Delta R = 0.5$ around the jet momentum axis are used to define a jet cone charge, Q_{jet}, using Eq. (6.2). In this case $\kappa = 1.1$. The sum runs over the tracks associated with the jet. Tracks must have $p_T > 0.5$ GeV, $|\eta| < 2.5$, and $|\Delta z| < 5$ mm. The sum excludes tracks with $\Delta R < 0.5$ between the track and the signal B meson candidate in order to reject the track from the signal-side decay.

Figure 6.7 shows the distribution of the opposite-side jet cone charge for $B^\pm$ signal candidates, together with the corresponding tagging probability, including $P(B|Q_{\text{jet}})$ parametrised by the black curve.

6.9 Particle anti-particle tagging performance

Three figure-of-merit terms are used to quantify and compare the performance of the analysis-specific tagging methods. They incorporate the fraction of events used by a given tagging method, the purity of the method, and the overall power of the method in the sample. The efficiency, ε_x, of an individual tagging method is defined as the number of signal events tagged by that method divided by the total number of signal events in the sample. The purity of a method, also called the dilution, is defined as $\mathcal{D}(Q_x) = 2P(B|Q_x) - 1$. The power is then defined as $T_x = \sum_i \varepsilon_{x\,i} \cdot \mathcal{D}^2(Q_{x\,i})$, where

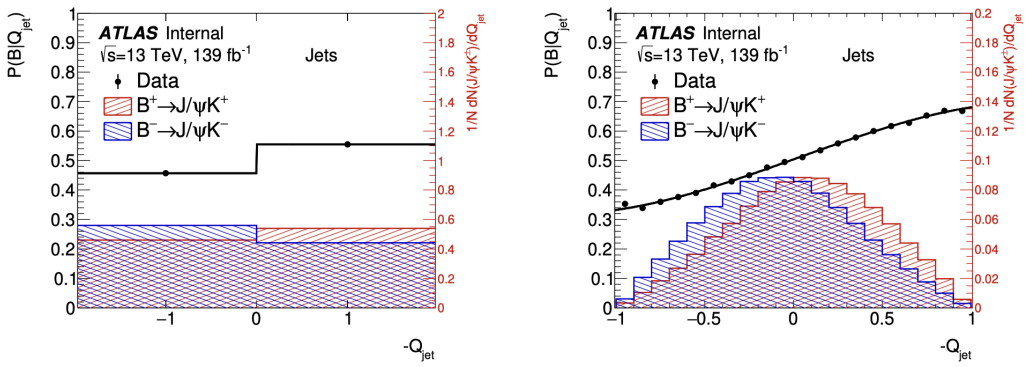

Figure 6.7: ATLAS internal result. Normalised cone charge distributions (shown against the right axis scale), $-Q_{\text{jet}}$, for B^+ (B^-) events shown in red (blue) for jets, for cases of discrete charge (left), and the continuous distribution (right). Superimposed is the distribution of the tag probability, $P(B|Q_{\text{jet}})$.

the sum is over the probability distribution in intervals of the cone charge variable. An effective dilution, $D_x = \sqrt{T_x/\varepsilon_x}$, is calculated from the measured tagging power and efficiency. These terms are introduced as a way to quantify the quality of the tagging and are not used directly in the fit code for tagging.

By definition, there is no overlap between lepton-tagged and jet-charge-tagged events. The overlap between events with a muon and events with an electron is about 0.6% of all tagged events. A summary of the tagging performance for each method and the overall performance on the $B^\pm$ sample is given in Table 6.1. All OST methods, tight muons, low-p_T muons, electrons and jet-charge tag, contribute to the tagging performance.

6.10 Using the particle anti-particle tag information in the B_s^0 fit.

The calibrations derived from the $B^\pm \to J/\psi K^\pm$ sample are used to determine the per-candidate probability $P(B|Q_x)$ that the B meson candidate was produced in the state B_s^0. Information from these calibrations is shown in Figures 6.4–6.7.

Tag method	ε_x [%]	D_x [%]	T_x [%]
Tight muon	4.341 ± 0.009	47.31 ± 0.14	0.972 ± 0.008
Electron	1.433 ± 0.005	46.96 ± 0.17	0.316 ± 0.002
Low-p_T muon	3.124 ± 0.007	29.53 ± 0.12	0.272 ± 0.004
Jet	12.144 ± 0.015	16.13 ± 0.03	0.316 ± 0.005
Total	21.043 ± 0.020	29.86 ± 0.04	1.876 ± 0.011

Table 6.1: Summary of the tagging performances for the different flavour tagging methods on the sample of $B^{\pm}$ signal candidates, as described in the text. Uncertainties shown are statistical only. The efficiency (ε_x) and tagging power (T_x) are each determined by summing over the individual bins of the cone charge distribution. The effective dilution (D_x) is obtained from the measured efficiency and tagging power. For the efficiency, effective dilution, and tagging power, the corresponding uncertainties are determined by combining the appropriate uncertainties in the individual bins of each charge distribution.

Because the distributions of $P(B|Q_x)$ from signal B_s^0 mesons and background data are typically different, separate probability density functions (PDFs) are necessary to describe them in the likelihood function. These PDFs are defined as $P_{\rm s}(P(B|Q_x))$ and $P_{\rm b}(P(B|Q_x))$, respectively. They are extracted using sideband subtraction on the B_s^0 candidate sample, where background PDFs are determined from the sideband regions and then applied to the signal region to obtain the signal PDF. The PDFs contain the fraction of events that are tagged with a particular method. Continuous events are then represented in the PDF by corresponding probability distributions, while discrete ones are assigned single probability values.

6.10.1 Continuous PDF

The parameterisations of the continuous PDF components for each OST method are defined in this section. The background probability distributions, $P_{\rm b}(P(B|Q_x))$, are described by the B_s^0 tag probability histograms of events selected in the sideband

regions, $5150 < m(J/\psi KK) < 5317$ MeV and $5417 < m(J/\psi KK) < 5650$ MeV.

For the signal probability distributions, $P_{\rm s}(P(B|Q_x))$, the B_s^0 tag probability histograms in the signal region, $5317 < m(J/\psi KK) < 5417$ MeV are selected. Background events in the signal region are parameterised by the histograms in sideband regions and subtracted from the signal probability distributions.

6.10.2 Discrete PDF

In the scenario no charged tracks are found around a tagged muon, there are only muons available, so the charge will be either positive or a negative, so the charge cone is said to be discrete. In some scenarios, the muon found will have the incorrect charge, as it has undergone a cascade decay, so the opposite of the B-hadron that produced it. When the cone charge is discrete, the fractions of events f_{+1} (f_{-1}) with cone charges $+1$ (-1) are determined separately for signal and background using events from the signal and sideband regions, respectively, of the B_s^0 mass distribution. The distribution can be seen in the left of Figure 6.4. The remaining fraction of events, $1 - f_{+1} - f_{-1}$, corresponds to the continuous parts of the distribution. Table 6.2 summarises the fractions f_{+1} and f_{-1} obtained from each tagging method for signal and background events.

Tag method	Signal		Background	
	f_{+1} [%]	f_{-1} [%]	f_{+1} [%]	f_{-1} [%]
Tight muon	6.8 ± 0.3	7.2 ± 0.3	4.61 ± 0.05	4.74 ± 0.05
Electron	19.3 ± 0.7	20.1 ± 0.7	17.0 ± 0.1	17.2 ± 0.1
Low-p_T muon	11.0 ± 0.3	11.2 ± 0.4	6.88 ± 0.07	7.40 ± 0.07
Jet	3.81 ± 0.11	3.78 ± 0.12	3.26 ± 0.03	3.37 ± 0.03

Table 6.2: Fractions f_{+1} and f_{-1} of events with cone charges of $+1$ and -1, respectively, for signal and background events and for the different tagging methods. Only statistical uncertainties are given.

Table 6.3 shows the fractions of signal and background events tagged using the different OST methods, found using a similar sideband-subtraction method.

Variations of the procedure described here are used to determine systematic uncertainties, see Section 6.13 related to possible deviations of the data from the selected fit models.

Tag method	Signal efficiency [%]	Background efficiency [%]
Tight muon	3.86 ± 0.04	3.06 ± 0.01
Electron	1.88 ± 0.03	1.56 ± 0.01
Low-p_T muon	2.93 ± 0.04	2.69 ± 0.01
Jet	12.1 ± 0.1	9.54 ± 0.01
Untagged	79.2 ± 0.2	83.16 ± 0.04

Table 6.3: Fractions of signal and background events tagged using the different methods. The efficiencies include both the continuous and discrete contributions. Only statistical uncertainties are quoted.

6.11 "Typical" ATLAS Flavour Tagging - Quark Flavour Tagging

To reiterate, this chapter now moves onto a different type of flavour tagging. The analysis is focused on particle-antiparticle tagging, which is described in the sections above. Described below are the more typical, or traditional, ATLAS flavour tagging techniques. These techniques are used as validation for this analysis's tagging methods.

6.11.1 ATLAS quark flavour tagging compared to this analysis' particle anti-particle tagging

Originally, this analysis did not use the "traditional" ATLAS flavour tagging; however, after consultation with ATLAS management, it was suggested that the analysis implement "traditional" tagging to verify that the opposite side really contained a b or $\bar{b}$ quark. This inclusion meant the tagging efficiency would now become $\approx 0.1\%$; meaning a lot of data would be rejected. The compromise was a specific, much looser selection so that our data was kept, harnessing the statistical power targeted for exploitation. This looser selection was suitable and confirmed that there are $b/\bar{b}$ candidates in the opposite hemisphere.

6.11.2 Quark Flavour Tagging within ATLAS

Once B_s^0 meson candidates have been identified, the flavour of the neutral B_s^0 meson at the point of production is needed. This is achieved through discerning the flavour of the hadronic jets. "Jets are clusters of energy deposits in the detector, grouped together to represent the original parton" [154] in a collision. "Jet flavour tagging enables the identification of jets originating from heavy-flavour quarks in proton-proton collisions" [155].

6.11.3 Quark Flavour Tagging Requirements

The requirements for quark flavour tagging are jet and sub-jet physics objects reconstructed within ATLAS, including the charged particle tracks and the primary vertices. First is discussion of the particle tracks.

6.11.3.1 Charged Particle Tracks

Charged particle tracks are reconstructed in the ID. For jet quark flavour tagging, only tracks with $p_T > 500$ MeV (the minimum for track reconstruction in Run 2) are used, with additional selection criteria used to reject fake and poorly measured

tracks. Charged pion tracking efficiency ranges from 90% for small $|\eta| < 1$ to 70% for the forward region $2.3 < \eta < 2.5$ of the detector for charged pions with $p_T > 4$ GeV [153]. Additional selection criteria for the reconstructed tracks are applied, maintaining high efficiency for charged particles, while rejecting tracks originating from pile-up.

6.11.3.2 Primary Vertex Reconstruction

Primary Vertex reconstruction can be done on an event-by-event basis which is important for $b-$tagging, as this sets the reference point for which tracks and vertex displacements are computed. The longitudinal vertex position resolution is about 30 μm for events with a high multiplicity of reconstructed tracks. The transverse resolution ranges from 10 to 20 μm, varying with the running conditions of the LHC which determine the beam-spot size, [153]. At least one PV is required per event, selected using the highest weighted sum of squares for the transverse momenta of all contributing tracks, including tracks that are not associated with a jet. Two key parameters are introduced, d_0, the transverse impact parameter, defined as the point of closest approach between the track and the PV in the transverse plane and z_0 the longitudinal impact parameter, defined as the longitudinal separation of the PV and the d_0 measurement point.

6.11.3.3 Hadronic Jets

Hadronic Jets are built from "particle flow objects" (PFOs) which are produced by the "particle flow algorithm" [156] and its offspring. These PFOs consist of the remaining calorimeter energy and tracks which are matched to the hard interaction, after the energy deposited in the calorimeter by all the charged particles is removed. Tracks and calorimeter cluster remnants form PFOs, which can be used as input for jet clustering. The better resolution of particle tracking in the ATLAS calorimeters and ID can be exploited through the use of PFOs. Jets are located through the anti-k_t algorithm, using radial constraints of $R = 0.4$ [151], which is implemented

in `FastJet`, [152] [157]. The reconstructed jet direction and transverse momentum are two important inputs for quark flavour tagging, so jets with $p_T < 20$ GeV, or $|\eta| \geq 2.5$ are not considered for jet flavour identification [157].

6.11.3.4 Tracks

Tracks are matched to jets using a maximum angular separation ΔR between track momenta and the jet axis. The maximum angular separation varies as a function of p_T jet, with low-p_T jets having wider ΔR and for high-p_T jets a comparatively narrower ΔR as higher-p_T b-hadron decay products are more collimated [157]. The jet axis determines the sign of the impact parameter, being negative if the intersection lies behind the primary vertex and positive if the intersection is in front of the PV [157]. Notably, negative d_0 values are unphysical "features" of detector resolution, as particles cannot decay before they are produced. Figure 6.8 has been adapted from Figure 4 from [158], and shows an event display, highlighting how the resolution error on the primary vertex can result in a secondary vertex being reconstructed behind (closer to the collision point) the primary vertex.

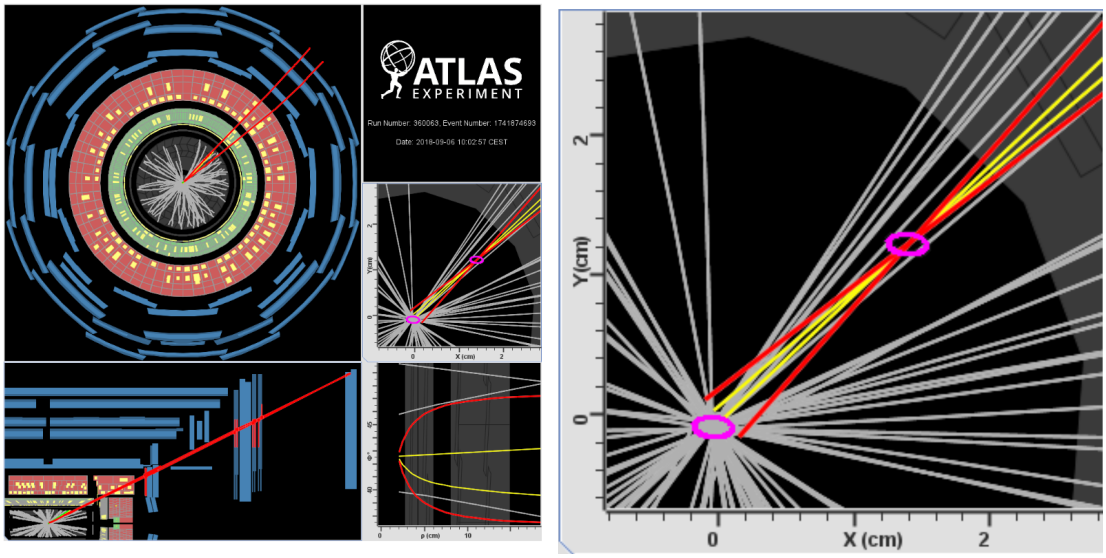

Figure 6.8: (Left) The full event display of a 2018 ATLAS proton proton collision at 13 TeV, showing a B^0 meson decay. The red lines represent muons, with the yellow lines the hadrons, the pink ellipses represent the primary and secondary vertex. (right) A zoomed display of the same event, highlighting the potential miscalculation of a secondary vertex behind a primary vertex [158].

6.11.3.5 Jet Flavour Labels

The flavour of a jet in simulation is determined by its hadron content. b-jets are jets that contain at least one weakly decaying b-hadron with $p_T \geq 5$ GeV within $\Delta R = 0.3$ of the jet axis [157]. If no b-hadrons are found, the same criteria are applied to search for c-hadrons and then τ-leptons, creating c-jets and τ-jets respectively, with remaining jets classified as light-flavour.

6.11.4 Tagging Parameters

Having introduced the requirements of quark flavour tagging, we now introduce tagging parameters, defining efficiency, dilution and tag power. The performance of a flavour-tagging algorithm is characterised by the probability, or efficiency, of correctly tagging a signal, ε.

The following tagging parameters are introduced to evaluate tagging performance, efficiency, dilution, and tag power. These parameters have the same name and function as in Section 6.9, but are reintroduced as defined by ATLAS to emphasize the distinction between the "traditional" ATLAS quark flavour tagging and the previous analysis specific particle-antiparticle tagging.

6.11.5 Tagging Efficiency, Dilution and Power

Beginning with efficiency, ε_{tag}, that can be defined as a function of the correctly tagged events, N_r, wrongly tagged events, N_w, and the total number of reconstructed $B^{\pm}$ candidates in the sample before tagging, $N_{B^{\pm}}$. The efficiency only equals 100% if every single b event has received a tagging decision, in practice, there are missed events which go untagged, which is neither correctly or incorrectly tagged. The reality of untagged events means $N_r + N_w < N_{B^{\pm}}$, which means the efficiency will not be 100%.

$$\varepsilon_{\text{tag}} = \frac{N_r + N_w}{N_{B^{\pm}}} \tag{6.5}$$

Wrongly tagged events happen given the possibility of $b \to c$ decays; if the

objects studied have undergone a quark flavour transition, this alters the final state of the muon, which is used to infer the original state of the b candidate. Expanding on this, if the b does decay into a c, the charge has flipped, and so, the muon charge changes, causing an incorrect determination of the original b candidate state. The purity of the tagger can be inferred through the dilution:

$$D_{\text{tag}} = \frac{N_r - N_w}{N_r + N_w} = 1 - 2\omega_{\text{tag}} \tag{6.6}$$

where ω_{tag} is the fraction of the wrongly tagged events with respect to the total number of tagged events. The highest purity has a dilution of 1, when there are no wrongly tagged events.

It is possible to combine both efficiency and purity into the tagging power, which is defined as:

$$P_{\text{tag}} = \sum_i \varepsilon_{\text{tag}}^{(i)} \left(D_{\text{tag}}^{(i)}\right)^2 \tag{6.7}$$

where the sum runs over each bin in the distribution. Tagging power is a figure of merit to compare the different tagging methods between experiments, and it is not used directly in the calibration of the B_s^0 sample.

6.12 Maximum Likelihood Fitting

An unbinned maximum likelihood fit is performed on the selected events in the B_s^0 sample to extract the parameter values of the $B_s^0 \to J/\psi\phi$ decay. The fit uses information about the reconstructed mass m, the measured proper decay time t, the measured mass uncertainty σ_m, the measured proper decay time uncertainty σ_t, the measured transverse momentum p_T, the tagging probability $P(B|Q_x)$, and the transversity angles, see Section 6.12.1, $\Omega = (\theta_T, \psi_T, \phi_T)$ of each B_s^0 decay candidate. The measured value of σ_t is obtained from the covariance matrix associated with the vertex fit for each candidate. The likelihood function is defined as a combination of

signal and background PDFs and described in Equation 6.8

$$\begin{aligned}\ln\ \mathcal{L} = \sum_{i=1}^{N} w_i \cdot \ln[& f_{\rm s} \cdot \mathcal{F}_{\rm s}(m_i, t_i, \sigma_{m_i}, \sigma_{t_i}, \Omega_i, P_i(B|Q_x), p_{{\rm T}_i}) + \\ & f_{\rm s} \cdot f_{B^0} \cdot \mathcal{F}_{B^0}(m_i, t_i, \sigma_{m_i}, \sigma_{t_i}, \Omega_i, P_i(B|Q_x), p_{{\rm T}_i}) + \\ & f_{\rm s} \cdot f_{\Lambda_b} \cdot \mathcal{F}_{\Lambda_b}(m_i, t_i, \sigma_{m_i}, \sigma_{t_i}, \Omega_i, P_i(B|Q_x), p_{{\rm T}_i}) + \\ & (1 - f_{\rm s} \cdot (1 + f_{B^0} + f_{\Lambda_b}))\mathcal{F}_{\rm bkg}[(m_i, t_i, \sigma_{m_i}, \sigma_{t_i}, \Omega_i, P_i(B|Q_x), p_{{\rm T}_i})].\end{aligned} \tag{6.8}$$

Here N is the number of selected candidates and w_i is a weighting factor to account for the trigger efficiency, see Section 6.12.3. The terms $\mathcal{F}_{\rm s}$, $\mathcal{F}_{B^0}$, $\mathcal{F}_{\Lambda_b}$, and $\mathcal{F}_{\rm bkg}$ are the PDFs modelling the signal, B^0 background, Λ_b background, and other background distributions, respectively. The term $f_{\rm s}$ is the fraction of signal candidates. The f_{B^0} and f_{Λ_b} terms are the fractions, calculated relative to the number of signal events, of backgrounds arising from, respectively, B^0 mesons and Λ_b baryons misidentified as B_s^0 candidates. These background fractions are fixed to their expectation values from the MC simulation, and variations are applied as part of the evaluation of the effects of systematic uncertainties. The mass, m_i, the proper decay time, t_i, and the decay angles, Ω_i, are the values obtained from each event, i, in the data. The signal PDF term, $\mathcal{F}_{\rm s}$, is described in Section 6.12.1, and the three background functions, $\mathcal{F}_{\rm bkg}$, $\mathcal{F}_{\Lambda_b}$, and $\mathcal{F}_{B^0}$, are described in Section 6.12.2.

6.12.1 Signal PDF

The PDF used to describe the signal events, $\mathcal{F}_{\rm s}$, is composed as

$$\begin{aligned}\mathcal{F}_{\rm s}(m_i, t_i, \sigma_{m_i}, \sigma_{t_i}, \Omega_i, P_i(B|Q_x), p_{{\rm T}_i}) = & P_{\rm s}(m_i|\sigma_{m_i}) \cdot P_{\rm s}(\sigma_{m_i}|p_{{\rm T}_i}) \cdot P_{\rm s}(t_i, \Omega_i|\sigma_{t_i}, P_i(B|Q_x)) \\ & \cdot P_{\rm s}(\sigma_{t_i}|p_{{\rm T}_i}) \cdot P_{\rm s}(P_i(B|Q_x)) \cdot A(\Omega_i, p_{{\rm T}_i}) \cdot P_{\rm s}(p_{{\rm T}_i}).\end{aligned}$$

The mass term $P_{\rm s}(m_i|\sigma_{m_i})$ is modelled as

$$P_{\rm s}(m_i|\sigma_{m_i}) \equiv \frac{1}{\sqrt{2\pi} S_m \sigma_{m_i}} \cdot {\rm e}^{\frac{-(m_i - m_{B_s})^2}{2(S_m \sigma_{m_i})^2}}. \tag{6.9}$$

The $P_{\rm s}(m_i|\sigma_{m_i})$ term uses per-candidate mass errors, σ_{m_i}, calculated for each $B_s^0 \to J/\psi\phi$ candidate from the covariance matrix associated with the four-track

vertex fit. The covariance matrix of tracking and vertexing contains 5 independent parameters for each track, and the B_s^0 vertex which is characterised by 4 parameters, the covariance matrix also contains errors for each of these parameters. This "grand" matrix, is used to calculate the errors of the invariant mass of the B_s^0 and the proper decay times, both of these depend on track momenta and their errors. Every measured candidate mass is convolved with a Gaussian function of width, σ_{m_i}, multiplied by a scale factor, S_m, which accounts for any mismeasurements. Both S_m and the mean value, m_{B_s}, the B_s^0 meson mass, are free parameters determined in the fit.

The probability terms $P_{\rm s}(\sigma_{m_i}|p_{{\rm T}_i})$, $P_{\rm s}(\sigma_{t_i}|p_{{\rm T}_i})$, and $P_{\rm s}(p_{{\rm T}i})$ account for differences between signal and background events in, respectively, the values of σ_{m_i}, the time error, and the $p_{{\rm T}_i}$ values. Their distributions are described by gamma functions using the method described in [159]. The tagging probability term for the signal $P_{\rm s}(P_i(B|Q_x))$ is described in Section 6.10.

The term $P_{\rm s}(t_i, \Omega_i|\sigma_{t_i}, P_i(B|Q_x))$ is a joint PDF for the decay time, t, and the transversity angles, Ω, for the $B_s^0 \to J/\psi\phi$ decay. Ignoring detector effects, the distribution for the time, t, and the angles, Ω, is given by the differential decay rate [160]:

$$\frac{{\rm d}^4\Gamma}{{\rm d}t\ {\rm d}\Omega} = \sum_{k=1}^{10} \mathcal{O}^{(k)}(t) g^{(k)}(\theta_T, \psi_T, \phi_T).$$

Here the $\mathcal{O}^{(k)}(t)$ are time-dependent functions corresponding to the contributions of amplitudes A_0, $A_{||}$, $A_\perp$, and A_S, and their interference terms, and the $g^{(k)}(\theta_T, \psi_T, \phi_T)$ are the angular functions. The time-dependent and angular functions of the transversity angles are shown in Table 6.4. The expressions for the time-dependent functions for B_s^0 and $\bar{B_s^0}$ have the same structure with a sign reversal in the terms containing Δm_s.

Parameter, $A_\perp(t)$, is the time-dependent amplitude for the CP-odd final state configuration, while, $A_0(t)$, and, $A_\parallel(t)$, correspond to CP-even final state configurations. The amplitude, $A_S(t)$, gives the contribution from the CP-odd non-

k	$g^{(k)}(\theta_T, \psi_T, \phi_T)$	$A^{(k)}$	$T^{(k)}(t)$	meaning of δ_k
1	$2\cos^2\psi_T(1-\sin^2\theta_T\cos^2\phi_T)$	$\frac{1}{2}\lvert A_0(0)\rvert^2$	$\left(1+\frac{2\lvert\lambda\rvert}{1+\lvert\lambda\rvert^2}\cos\right)\mathrm{e}^{-\Gamma_{\mathrm{L}}^{(s)}t}+\left(1-\frac{2\lvert\lambda\rvert}{1+\lvert\lambda\rvert^2}\cos\right)\mathrm{e}^{-\Gamma_{\mathrm{H}}^{(s)}t}$ $\pm 2\mathrm{e}^{-\Gamma_s t}\left(\frac{2\lvert\lambda\rvert}{1+\lvert\lambda\rvert^2}\sin(\Delta m_s t)\sin\phi_s+\frac{1-\lvert\lambda\rvert^2}{1+\lvert\lambda\rvert^2}\cos(\Delta m_s t)\right)$	
2	$\sin^2\psi_T(1-\sin^2\theta_T\sin^2\phi_T)$	$\frac{1}{2}\lvert A_\parallel(0)\rvert^2$		
3	$\frac{1}{\sqrt{2}}\sin 2\psi_T\sin^2\theta_T\sin 2\phi_T$	$\frac{1}{2}\lvert A_0(0)\rvert\lvert A_\parallel(0)\rvert\cos\delta_{\parallel}$		
4	$\sin^2\psi_T\sin^2\theta_T$	$\frac{1}{2}\lvert A_\perp(0)\rvert^2$	$\left(1-\frac{2\lvert\lambda\rvert}{1+\lvert\lambda\rvert^2}\cos\right)\mathrm{e}^{-\Gamma_{\mathrm{L}}^{(s)}t}+\left(1+\frac{2\lvert\lambda\rvert}{1+\lvert\lambda\rvert^2}\cos\right)\mathrm{e}^{-\Gamma_{\mathrm{H}}^{(s)}t}$ $\mp 2\mathrm{e}^{-\Gamma_s t}\left(\frac{2\lvert\lambda\rvert}{1+\lvert\lambda\rvert^2}\sin(\Delta m_s t)\sin\phi_s-\frac{1-\lvert\lambda\rvert^2}{1+\lvert\lambda\rvert^2}\cos(\Delta m_s t)\right)$	
5	$\frac{2}{3}\left(1-\sin^2\theta_T\cos^2\phi_T\right)$	$\frac{1}{2}\lvert A_S(0)\rvert^2$		
6	$\frac{1}{3}\sqrt{6}\sin\psi_T\sin 2\theta_T\cos\phi_T$	$\frac{1}{2}\alpha\lvert A_S(0)\rvert\lvert A_\perp(0)\rvert\sin(\delta_\perp-\delta_S)$		
7	$-\sin^2\psi_T\sin 2\theta_T\sin\phi_T$	$\frac{1}{2}\lvert A_\parallel(0)\rvert\lvert A_\perp(0)\rvert$	$\left(\mathrm{e}^{-\Gamma_{\mathrm{L}}^{(s)}t}-\mathrm{e}^{-\Gamma_{\mathrm{H}}^{(s)}t}\right)\frac{2\lvert\lambda\rvert}{1+\lvert\lambda\rvert^2}\cos\delta_k\sin$ $+\frac{1}{2}\left(\mathrm{e}^{-\Gamma_{\mathrm{L}}^{(s)}t}+\mathrm{e}^{-\Gamma_{\mathrm{H}}^{(s)}t}\right)\frac{1-\lvert\lambda\rvert^2}{1+\lvert\lambda\rvert^2}\sin\delta_k$ $\pm 2\mathrm{e}^{-\Gamma_s t}\left(\sin\delta_k\cos(\Delta m_s t)-\frac{2\lvert\lambda\rvert}{1+\lvert\lambda\rvert^2}\cos\delta_k\cos\phi_s\sin(\Delta m_s t)\right)$	$\delta_7=\delta_\perp-\delta_{\parallel}$
8	$\frac{1}{\sqrt{2}}\sin 2\psi_T\sin 2\theta_T\cos\phi_T$	$\frac{1}{2}\lvert A_0(0)\rvert\lvert A_\perp(0)\rvert$		$\delta_8=\delta_\perp$
9	$\frac{1}{3}\sqrt{6}\sin\psi_T\sin^2\theta_T\sin 2\phi_T$	$\frac{1}{2}\alpha\lvert A_S(0)\rvert\lvert A_\parallel(0)\rvert$		$\delta_9=\frac{\pi}{2}-(\delta_{\parallel}-\delta_S)$
10	$\frac{4}{3}\sqrt{3}\cos\psi_T\left(1-\sin^2\theta_T\cos^2\phi_T\right)$	$\frac{1}{2}\alpha\lvert A_0(0)\rvert\lvert A_S(0)\rvert$		$\delta_{10}=\frac{\pi}{2}+\delta_S$

Table 6.4: The ten time-dependent functions, $\mathcal{O}^{(k)}(t)=A^{(k)}T^{(k)}(t)$ and the functions of the transversity angles $g^{(k)}(\theta_T,\psi_T,\phi_T)$. The amplitudes $|A_0(0)|^2$ and $|A_\parallel(0)|^2$ are for the CP-even components of the $B_s^0\to J/\psi\phi$ decay, $|A_\perp(0)|^2$ is the CP-odd amplitude; they have corresponding strong phases δ_0, $\delta_\parallel$ and $\delta_\perp$. By convention, δ_0 is set to be zero. The S-wave amplitude $|A_S(0)|^2$ gives the fraction of $B_s^0\to J/\psi K^+K^-(f_0)$ and has a related strong phase δ_S. The factor α is described in the text of Section 6.12.1. The $\pm$ and $\mp$ terms denote two cases: the upper sign describes the decay of a meson that was initially a B_s^0 meson, while the lower sign describes the decays of a meson that was initially $\bar{B_s^0}$

resonant $B_s^0 \to J/\psi K^+K^-$ S-wave state [161], which includes the f_0 meson.

The amplitudes are parameterised by $|A_j|e^{i\delta_j}$, where $j = \{0, ||, \perp, S\}$, with $\delta_0 = 0$. They are normalised such that $|A_0(0)|^2 + |A_\perp(0)|^2 + |A_\parallel(0)|^2 = 1$. The amplitude, $|A_\perp(0)|$, is determined according to this condition, while the remaining three amplitudes are free parameters of the fit. The phase difference between $A_S(0)$ and $A_0(0)$ at the K^+K^- resonance peak is denoted by δ_S. The value, $|A_S|^2$, gives the ratio of non-resonant yield to resonant yield in the interval of $m(K^+K^-)$ used in the analysis. In the sum over the mass interval, the interference terms are corrected by a factor $\alpha = 0.51 \pm 0.02$ that takes into account the mass-dependent differences in absolute amplitude and phase between the resonant and S-wave amplitudes. The correction is based on the Breit-Wigner description of the resonance and on the assumption that A_S is uniform. The uncertainty (see Section 6.13) in the value of α has been calculated using the Flatté parameterisation [162].

The angles are defined as follows:

- θ_T, the angle between $\vec{p}(\mu^+)$ and the normal to the x–y plane, in the J/ψ meson rest frame;
- ϕ_T, the angle between the x-axis and $\vec{p}_{xy}(\mu^+)$, the projection of the μ^+ momentum in the x–y plane, in the J/ψ meson rest frame; and
- ψ_T, the angle between $\vec{p}(K^+)$ and $-\vec{p}(J/\psi)$ in the ϕ meson rest frame.

Figure 6.9 shows these three angles, θ_T, ϕ_T, and ψ_T.

The PDF describing the $B_s^0 \to J/\psi\phi$ decay is invariant under the following simultaneous transformations, as was derived in [164]

$$\{\phi_s, \Delta\Gamma_s, \delta_\perp, \delta_\parallel\} \to \{\pi - \phi_s, -\Delta\Gamma_s, \pi - \delta_\perp, 2\pi - \delta_\parallel\}. \tag{6.10}$$

Since $\Delta\Gamma_s$ was determined to be positive [165], there is a unique solution left.

The PDF term $P_s(t_i, \Omega_i|\sigma_{t_i}, P_i(B|Q_x))$ takes into account the lifetime resolution, so each time element is smeared with a Gaussian function. This smearing is performed numerically on an event-by-event basis. The width of the Gaussian

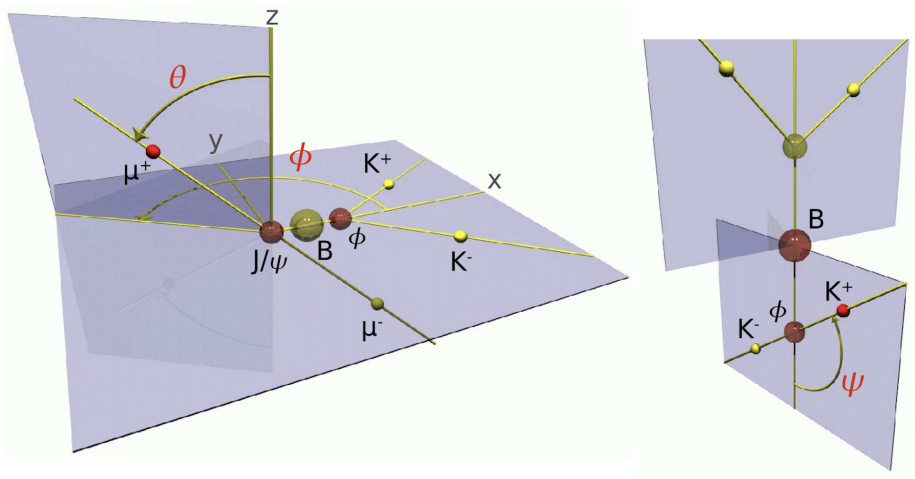

Figure 6.9: The transversity basis: defined in terms of the angles θ and ϕ in the J/ψ rest frame (left) and ψ in the ϕ meson rest frame (right), taken from [163].

function is the proper decay time uncertainty, measured for each event and multiplied by a scale factor to account for any mismeasurements. The average value of this uncertainty for signal events is 64 fs which is the mean value of time error for signal candidates derived from the fit shown in the Figure 6.10.

The angular acceptance of the detector and the kinematic cuts on the angular distributions are included in the likelihood function through the acceptance function $A(\Omega_i, p_{\mathrm{T}i})$. It is calculated using a four-dimensional binned acceptance method, applying an event-by-event efficiency correction according to the transversity angles and the p_T of the candidate. The angular acceptance is influenced by the p_T of the B_s^0 candidate, and therefore it is binned in p_T.

The acceptance is calculated from the $B_s^0 \to J/\psi\phi$ MC events with weighting to account for imperfect re-creation of the p_T and η distributions for B_s^0 found in the data. The MC events are re-weighted to account for the differences in the 2D plots for p_T and η distributions for the B_s^0 candidates between data and MC. In the likelihood function, the acceptance-binned distribution is multiplied by the time- and angle-dependent PDF describing the $B_s^0 \to J/\psi\phi$ decays. As both the acceptance and time- and angle-dependent decay PDFs depend on the transversity angles, they are normalised together, numerically, during the likelihood fit. The

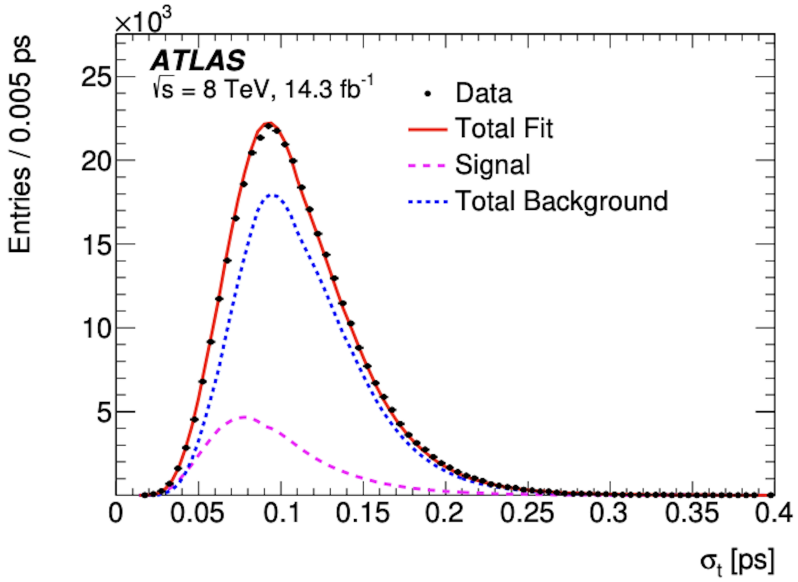

Figure 6.10: The proper decay time uncertainty distributions for data (black), and the fits to the background (blue) and the signal (purple) contributions. The total fit is shown as a red curve, Figure 6 from [132].

PDF is normalised over the entire B_s^0 mass range, $5150 - 5650$ MeV.

6.12.2 Background PDF

The background PDF is formed as

$$\begin{aligned}\mathcal{F}_{\text{bkg}}(m_i, t_i, \sigma_{t_i}, \Omega_i, P_i(B|Q_x), p_{\text{T}_i}) &= P_{\text{b}}(m_i) \cdot P_{\text{b}}(t_i|\sigma_{t_i}) \cdot P_{\text{b}}(P_i(B|Q_x)) \\ &\cdot P_{\text{b}}(\Omega_i) \cdot P_{\text{b}}(\sigma_{m_i}|p_{\text{T}_i}) \cdot P_{\text{b}}(\sigma_{t_i}|p_{\text{T}_i}) \cdot P_{\text{b}}(p_{\text{T}_i}).\end{aligned}$$

The background mass distribution, $P_{\text{b}}(m_i)$, is modelled by an exponential function plus a constant term. The proper decay time function $P_{\text{b}}(t_i|\sigma_{t_i})$ is parameterised as a prompt peak modelled by a Gaussian distribution, two positive-time exponential functions, and a negative-time exponential function. The prompt peak models the combinatorial background events, which populate around zero in the lifetime distribution. The two positive-time exponential functions represent a fraction of longer-lived backgrounds involving non-prompt J/ψ mesons, combined either by chance with prompt hadronic tracks from the primary vertex, or with hadrons

from the same B or D meson decay. The negative-time exponential function takes into account events with poor vertex resolution. These functions are smeared with the same resolution function that is used for the signal decay time-dependence. The probability terms $P_{\rm b}(\sigma_{m_i}|p_{{\rm T}_i})$, $P_{\rm b}(\sigma_{t_i}|p_{{\rm T}_i})$, and $P_{\rm b}(p_{{\rm T}_i})$, represented as gamma functions, are described in [159]. The tagging probability term for background events $P_{\rm b}(P_i(B|Q_x))$ is described in Section 6.10.

The shape of the background angular distribution, $P_{\rm b}(\Omega_i)$, is dominated by detector and kinematic acceptance effects and described by Legendre polynomial functions:

$$
\begin{aligned}
Y_l^m(\theta_T) &= \sqrt{\frac{2l+1}{4\pi}}\sqrt{\frac{(l-m)!}{(l+m)!}}\,P_l^{|m|}(\cos\theta_T) \\
P_k(x) &= \frac{1}{2^k k!}\frac{{\rm d}^k}{{\rm d}x^k}(x^2-1)^k \\
\mathscr{P}_{\rm b}(\theta_T,\psi_T,\phi_T) &= \sum_{k=0}^{14}\sum_{l=0}^{14}\sum_{m=-l}^{l}
\begin{cases}
a_{k,l,m}\sqrt{2}Y_l^m(\theta_T)\cos(m\phi_T)P_k(\cos\psi_T) & \text{if } m>0 \\
a_{k,l,m}\sqrt{2}Y_l^{-m}(\theta_T)\sin(m\phi_T)P_k(\cos\psi_T) & \text{if } m<0 \\
a_{k,l,m}\sqrt{2}Y_l^0(\theta_T)P_k(\cos\psi_T) & \text{if } m=0
\end{cases}
\end{aligned}
\tag{6.11}
$$

The coefficients, $a_{k,l,m}$, are adjusted to give the best fit to the angular distributions for events in the sidebands of the B_s^0 mass distribution. These parameters are then fixed in the fit to the signal region, using the likelihood function defined in Equation 6.8. The B_s^0 mass interval used for the background fit ranges from 5150 to 5650 MeV, excluding the signal mass region $|(m(B_s^0) - 5366| < 0.110$ MeV. Higher-order Legendre polynomial functions were tested, and differences are taken into account as a systematic uncertainty.

$B_d^0 \to J/\psi K^{*0}$ and $\Lambda_b \to J/\psi p K^-$ candidates misreconstructed as $B_s^0 \to J/\psi\phi$ candidates are represented in the fit through the $\mathcal{F}_{B^0}$ and $\mathcal{F}_{\Lambda_b}$ terms in the PDF function. The fractions of these contributions, $f_{B^0} = (4.5 \pm 0.5)\%$ and $f_{\Lambda_b} = (2.1 \pm 0.6)\%$, are estimated relative to the number of $B_s^0 \to J/\psi\phi$ signal candidates. They

are evaluated from MC simulation using production cross sections and branching fractions from the following references [141, 166, 167, 168, 169, 170]. The shapes of the mass and transversity angle distributions are derived from MC-simulated events. Information from [171] is used to model the three-dimensional angular distributions of the $B_d^0 \to J/\psi K^{*0}$ decay channel and its conjugate. The angular distributions for the $\Lambda_b \to J/\psi p K^-$ decay and its conjugate are considered to be flat. These distributions are sculpted by detector acceptance effects and then described by Legendre polynomial functions as in Equation 6.11. The B_d^0 and Λ_b lifetimes are represented in the fit by exponential terms, scaled by the ratio of the masses of B_d^0 with respect to B_s^0, or of Λ_b with respect to B_s^0, respectively; the lifetimes and masses are taken as the world averages [141]. The contributions of the S-wave $B_d^0 \to J/\psi K\pi$ decays and their interference with the P-wave $B_d^0 \to J/\psi K^{*0}$ decays are included in the PDF of the fit by using parameters reported in [171].

6.12.3 Proper decay time dependence of the muon trigger efficiency

An inefficiency at large values of the proper decay time arises due to trigger-matched muons with high values of transverse impact parameter, as these are strongly affected by the tracking acceptance. Trigger matched muons are when a muon identified by the trigger is matched with a reconstructed muon. This inefficiency is estimated by comparing the $B_s^0 \to J/\psi\phi$ proper decay time distributions of MC simulated events before and after applying the trigger selection. To account for this inefficiency in the fit, the events are reweighted by a factor w defined as

$$w = p_0 \cdot [1 - p_1 \cdot (\mathrm{Erf}((t - p_3)/p_2) + 1)]. \tag{6.12}$$

Here, Erf denotes the error function and p_0, p_1, p_2, and p_3 are parameters determined in the fit to MC events, $p_{0,1,2,3}$, are phenomenology parameters. No significant bias or inefficiency due to offline track reconstruction, vertex reconstruction, or track quality selection criteria is observed.

6.12.4 Summary of the fit parameters

The parameters of physical interest in the joint PDF of proper decay time and decay angles are:

- the CP interference parameter, λ, and CP-violating phase ϕ_s;
- the average decay width, Γ_s, and decay width difference, $\Delta\Gamma_s$;
- the mass difference, Δm_s;
- the size of the CP-state amplitudes at $t = 0$, as given by $|A_\parallel(0)|^2$, $|A_\perp(0)|^2$ and $|A_0(0)|^2$ and their corresponding strong phases $\delta_\parallel$, $\delta_\perp$ and δ_0;
- the size of the S-wave amplitude at $t = 0$, as given by $|A_S(0)|^2$ and the corresponding strong phase, δ_S.

The size of the amplitude $|A_\perp(0)|^2$ is constrained by the normalisation condition, and the phase, δ_0, is set to zero.

The likelihood function also includes the nuisance parameters f_s for the B_s^0 signal fraction, parameters describing the invariant mass and decay time-angular distributions of combinatorial background events, and the scale factors of the mass and decay time uncertainties. Other nuisance parameters in this analysis include acceptance functions, parametrisations of the angles of background channels $B_d \to J/\psi K^{*0}$ and $\Lambda_b \to J/\psi p K^-$ and their fractions f_{B^0} and f_{Λ_b}, the PDFs of time error distributions $P(\sigma_{t_i}|p_{\mathrm{T}_i})$, mass error distributions $P(\sigma_{m_i}|p_{\mathrm{T}_i})$, p_{T} distributions $P(p_{\mathrm{T}_i})$, and tagging parameters and calibrations. The values of these parameters are fixed in the fit to the values extracted from the B_s^0 mass signal and sideband regions or from MC simulations. A systematic uncertainty is assigned based on variations of the nuisance parameters, affecting the measured parameters of interest.

6.13 Systematic Uncertainties

The following contributions to the total systematic uncertainty are considered.

- **Particle anti-particle tagging:** Uncertainties in the fit parameters due to the flavour tagging procedure have both statistical and systematic contributions. The statistical uncertainty due to the size of the sample of $B^\pm \to J/\psi K^\pm$ decays is included in the overall statistical uncertainty. The systematic uncertainty arising from the precision of the OST calibration is estimated by varying the models used to parameterise $P(B|Q_x)$ as a function of the cone charge. Details of the cone charge are given in Section 6.8 and Equation 6.2. Each of the functions used by default (a third-order polynomial for muons and a sinusoid for electrons) is replaced by a linear function, a fifth-order polynomial, or two third-order polynomials that describe the positive and negative regions and have common constant and linear terms, but independent quadratic and cubic terms. The B_s^0 fit is repeated using each alternative model. The largest deviation from the nominal fit is assigned as the systematic uncertainty.

  To quantify any possible difference between the performance of the opposite side taggers for $B^\pm$ and B_s^0 events, calibration curves are derived from simulated samples of $B^\pm$ and B_s^0 signals. Variations between the curves from these simulated samples are propagated to the calibration curves derived from the data. The differences in the parameter values between the nominal fit and that with the varied calibration curves are included in the systematic uncertainty. The MC was tuned to data, and the remaining differences between data and MC were propagated as systematic uncertainties.

  Potential dependence on the pile-up distribution is assigned as another systematic contribution. The calibration data are divided into subsets of approximately equal size according to the pile-up profile of the event. Separate calibrations are made for each of these subsets. The B_s^0 fit is repeated using the calibrations corresponding to the pile-up profile of that event, and variations of the parameters of interest with respect to the nominal value are taken as the systematic uncertainty. The effect of parameterisation variations is also

applied to the terms $P_{\rm b}(P(B|Q_x))$ and $P_{\rm s}(P(B|Q_x))$. The resulting changes in the parameter values of the B_s^0 fit are similarly included in the systematic uncertainties.

- **Angular acceptance method:** The combined angular acceptance of the detector and kinematic cuts, $A(\Omega_i, p_{\mathrm{T}_i})$, is calculated from a binned fit to MC simulated data. Alternative acceptance functions are calculated with different bin central values and widths to estimate the systematic uncertainty introduced by the choice of binning.

- **ID alignment:** The effects of residual misalignments of the ID [172], upon the B_s^0 proper-decay time and p_T, through the fit parameters, are included in the systematic uncertainties.

- **Trigger efficiency:** To correct for the proper decay time dependence of trigger inefficiencies, the events are reweighted according to Equation 6.12. An alternative fit is performed using different binning choices in the MC sample that is used to determine the efficiency. These systematic effects are found to be negligible.

- **Best candidate selection:** Approximately 5% of events contain multiple candidates after all requirements are applied as is observed in the data. The candidate with the lowest $\chi^2/N_{\rm dof}$ from the B_s^0 vertex fit is selected. The systematic uncertainty associated with this selection is determined by creating an equivalent sample in which the candidate is selected randomly. This random choice, not targeting the best B_s^0 candidates, would slightly increase the level of combinatorial background.

- **Background angular distribution:** The shape of the background angular distribution, $P_{\rm b}(\theta_T, \varphi_T, \psi_T)$, is described by the fourteenth-order Legendre polynomial functions, given in Equation 6.11. These are replaced by higher-order Legendre polynomial functions, and the changes in the fit parameter

values relative to the default fit are taken as systematic uncertainties.

The background angular distribution shapes are determined primarily by detector and kinematic acceptance effects. As they are sensitive to the p_T of the B_s^0 meson candidate, the parameterisation using the Legendre polynomial functions is performed in six p_T intervals: 10–15 GeV, 15–20 GeV, 20–25 GeV, 25–30 GeV, 30–35 GeV and >35 GeV. The systematic uncertainties due to the choice of p_T intervals are estimated by repeating the fit after changing these intervals by 1 GeV and 2 GeV. The largest associated changes in the fit results are assigned as the systematic uncertainties.

- **B_d^0 background:** Contamination from $B_d^0 \to J/\psi K^{*0}$ events misreconstructed as $B_s^0 \to J/\psi/\phi$ events is presented in the PDF of the fit. Uncertainties in the $B_d^0 \to J/\psi K^{*0}$ fraction, the B_d^0 lifetime and the shapes of transversity angles are taken into account to determine the systematic uncertainties. In the MC events, the angular distributions of the $B_d^0 \to J/\psi K^{*0}(K^+\pi^-)$ decays are shaped according the parameters measured in [173]. The uncertainties of these parameters published in [173] are used to determine systematic uncertainties in our fit.

- **Λ_b background:** The effect of $\Lambda_b \to J/\psi p K^-$ events misreconstructed as $B_s^0 \to J/\psi/\phi$ events is represented in the fit. The effects of the uncertainties in the $\Lambda_b \to J/\psi p K^-$ fraction f_{Λ_b}, and of the shapes of the distributions of the mass, transversity angles, and lifetime, are included, as are the effects of the uncertainties in the $\Lambda_b \to J/\psi\Lambda^*$ branching ratios used to reweight the generated MC sample.

- **Mass and lifetime modelling:** The systematic uncertainty related to the signal B_s^0 mass model is estimated by adding a second Gaussian function to the default model in Equation 6.9. The second function has the same structure as the first Gaussian function but a different scale factor, S_m^1, which is an additional free parameter of the fit. The consequent changes in the parameter

values returned by the fit are negligible.

The sensitivity of the part of the fit model related to the lifetime is tested in two ways. The signal and background lifetime uncertainties are sensitive to the choice of p_T bins in which the relative contributions of these two components are evaluated. The fit is repeated for different intervals of p_T binning. Similarly, the signal and background lifetime uncertainties are sensitive to the determination of the signal fraction. The fit is repeated for alternative choices of this fraction within one standard deviation of its uncertainty. The consequent differences are included in the systematic uncertainty.

- **S-wave phase modelling**: The model for interference between the $B_s^0 \to J/\psi\phi(K^+K^-)$ and the S-wave $B_s^0 \to J/\psi\, K^+K^-$ is corrected by a factor $\alpha = 0.51 \pm 0.02$ to account for the mass-dependent differences in absolute amplitude and phase between the resonant and S-wave amplitudes. The uncertainty in α is due to uncertainties in the differential cross sections. These are evaluated by comparing the difference between a Breit-Wigner and a Flatté parametrisation [162] for the resonance, and by assessing the phase space dependence of the continuum amplitude. All of this includes the effects of the uncertainties in the detector mass scale and mass resolution. The effect of the uncertainty in α is estimated by repeating the fit for revised values of $\alpha = 0.51 + 0.02$ and $\alpha = 0.51 - 0.02$. The variations of the parameter values relative to those from the default fit using the central value of α are included in the systematic uncertainties.

- **Limitations of the data fit model:** To test the stability of the results, pseudo-experiments are conducted using the default model in both the generation and the fit. Systematic uncertainties are determined from the mean of the pull distributions of the pseudo-experiments scaled by the statistical uncertainty of that parameter in the fit to data. In total 193 repeating toy pseudo-experiments were produced, as described in [174]. The observed

deviations are included in the systematic uncertainties.

The systematic uncertainties are listed in Table 6.5. For each parameter, the total systematic uncertainty is obtained by adding all the contributions in quadrature. Correlations between physical parameters due to the systematic variations have been estimated from scatter diagrams, collecting all the systematic deviations for each pair of parameters. In this case, each variable is plotted against one another in a 2D plot, with each point represents one systematic test and then a correlation coefficient is calculated. The estimations found that the uncertainties can be considered as uncorrelated with the only exception is systematics due to the limitation of the data fit model, which has shown correlations from the pseudo-experiments and is thus treated separately.

6.14 Results

The results shown in this section are preliminary, subject to change, and should not be taken as final values. The work by the "BsJPsiPhi" team is ongoing, and these results will change before official publication.

6.14.1 Fit results

The results of the likelihood fit are shown in Table 6.6. At a luminosity of 139 fb^{-1}, the total number of B_s^0 meson candidates is $838,560 \pm 980$. The fitted value of the B_s^0 mass agrees with the world average value, [141]. Fit projections, including ratio plots, are shown in Figure 6.11 for the mass and proper decay time and in Figure 6.12 for the angles. The ratio plots show the difference between each data point and the total fit line divided by the statistical and systematic uncertainties summed in quadrature (σ) for that point. The deviations of ratio plots are within 2σ, which shows that the total uncertainties cover any discrepancy between data and the fit model. The lower left ratio plot in Figure 6.11 looks oscillatory, but as these oscillations are within one sigma, they are not meaningful. The background

	ϕ_s [mrad]	$\Delta\Gamma_s$ [ns^{-1}]	Γ_s [ns^{-1}]	Δm_s [ns^{-1}]	$\lvert\lambda\rvert$ [10^{-3}]	$\lvert A_\parallel(0)\rvert^2$ [10^{-3}]	$\lvert A_0(0)\rvert^2$ [10^{-3}]	$\lvert A_S(0)\rvert^2$ [10^{-3}]	$\delta_\perp$ [mrad]	$\delta_\parallel$ [mrad]	$\delta_\perp - \delta_\parallel$ [mrad]
Tagging:											
Calibration	17	0.1	0.2	58	3.8	0.1	< 0.1	0.1	120	3.5	0.6
Simulation differences	7.2	< 0.1	0.4	7.9	0.7	0.2	0.1	0.2	21	8.5	2.4
Tag probability modelling	0.9	< 0.1	< 0.1	0.4	< 0.1	< 0.1	< 0.1	< 0.1	2.4	1.3	1.0
Acceptance	0.1	0.3	< 0.1	1.5	0.2	0.3	0.1	0.4	4.1	3.4	3.6
ID alignment	0.3	< 0.1	0.7	12	0.1	< 0.1	< 0.1	< 0.1	3.7	0.1	0.2
Best candidate selection	0.2	0.3	0.8	7.8	0.9	0.1	0.2	0.7	12	0.7	7.2
Background angles model:											
Choice of fit function	0.4	0.1	< 0.1	2.9	0.8	0.2	< 0.1	0.4	6.1	0.2	3.5
Choice of p_T bins	0.4	0.3	0.1	0.3	0.3	0.1	0.2	0.3	6.8	10	2.6
Choice of mass interval	0.3	0.2	0.1	0.4	0.5	0.1	0.2	0.9	0.5	2.8	7.2
Dedicated backgrounds:											
B_d^0	1.2	< 0.1	< 0.1	1.0	0.4	0.2	0.1	1.1	5.2	7.2	7.0
Λ_b	0.3	0.2	0.1	1.2	0.4	0.3	0.5	0.9	4.7	9.5	5.6
Fit model:											
Mass resolution	1.2	0.5	0.4	0.7	0.5	0.1	< 0.1	1.3	2.8	5.4	6.2
Mass background model	0.4	< 0.1	< 0.1	0.5	0.1	< 0.1	< 0.1	< 0.1	0.4	2.9	0.2
Mass errors fit-model	1.4	< 0.1	0.3	4.6	0.5	0.6	0.8	2.0	7.2	8.3	21
Time res. sig frac	0.3	1.2	0.3	0.4	0.3	0.3	0.4	0.1	6.7	12	0.8
Time res. p_T bins	0.9	0.1	0.3	1.5	0.8	0.6	0.7	1.1	14	21	5.5
Time res. mass window	1.3	0.7	< 0.1	0.2	0.7	0.2	0.2	0.2	5.4	7.2	0.9
S-wave phase	0.2	0.1	< 0.1	0.8	< 0.1	0.1	< 0.1	0.1	1.6	3.0	12
Model limitation	4.6	< 0.1	0.1	2.3	0.6	1.2	0.9	2.7	7.5	12	19
Time eff corrections	0.8	0.1	0.2	0.8	< 0.1	< 0.1	< 0.1	< 0.1	1.1	0.4	0.1
Total	**20**	**1.6**	**1.1**	**61**	**4.4**	**1.7**	**1.6**	**4.3**	**130**	**35**	**35**

Table 6.5: Summary of systematic uncertainties assigned to the physical parameters of interest. For each parameter, the systematic uncertainties have been symmetrised.

modelling was studied and the small bumps were not associated with the alternative models, so these oscillations are said to be coincidence.

While for most of the physics parameters, including ϕ_s, $\Delta\Gamma_s$, Γ_s and Δm_s, the fit determines a single solution with a Gaussian behaviour of the projection of the log-likelihood, see Figure 6.14, for the strong-phases $\delta_\parallel$, and $\delta_\perp$ two well separate local maxima of the likelihood are found, and shown in solution (a) and (b) in Table 6.6. The difference in $-2\Delta\ln(\mathcal{L})$ between the two solutions is 0.6 which favours solution (a) but cannot rule out solution (b), more detail in Section 6.14.2 on the two-fold behaviour of the likelihood in the strong phases. This two fold behaviour is the result of an approximate symmetry of the signal PDF. The effects on the other variables are small for the parameters $\delta_\perp - \delta_S$ and $|\lambda|$ - the projection of the two solutions shows a large overlap in the $\pm 1\sigma$ range. The effect is completely negligible for all other variables, for which the fit values and uncertainty ranges overlap accurately.

The correlation parameter between statistical total uncertainties have been computed for both maxima of the likelihood, and are provided in Tables 6.7 and 6.8 for solution (a) and in Tables 6.9 and 6.10 for solution (b). Tables 6.7 and 6.9 introduce the term "statistical correlation", which are the correlations directly obtained from the likelihood fit to data, meaning there are no systematics considered at that point.

Parameter	Value	Statistical uncertainty	Systematic uncertainty
ϕ_s [rad]	-0.069	0.030	0.020
$\Delta\Gamma_s$ [ps^{-1}]	0.0620	0.0034	0.0016
Γ_s [ps^{-1}]	0.6695	0.0011	0.0011
Δm_s [ps^{-1}]	17.889	0.060	0.061
$\lvert A_\parallel(0)\rvert^2$	0.2249	0.0014	0.0017
$\lvert A_0(0)\rvert^2$	0.5079	0.0010	0.0016
$\lvert A_S(0)\rvert^2$	0.0225	0.0024	0.0043
Solution (a)			
$\lvert\lambda\rvert$	0.990	0.010	0.004
$\delta_\perp$ [rad]	3.00	0.11	0.13
$\delta_\parallel$ [rad]	2.91	0.03	0.04
$\delta_\perp - \delta_S$ [rad]	-0.30	0.04	0.04
Solution (b)			
$\lvert\lambda\rvert$	0.995	0.010	0.004
$\delta_\perp$ [rad]	3.23	0.11	0.13
$\delta_\parallel$ [rad]	3.36	0.03	0.04
$\delta_\perp - \delta_S$ [rad]	-0.29	0.04	0.04

Table 6.6: Fitted values for the physical parameters of interest with their statistical and systematic uncertainties. For variables $|\lambda|$, $\delta_\perp$ and $\delta_\parallel$ the values are given for the two solutions (a) and (b). The difference in $-2\Delta\ln(\mathcal{L})$ between solution (b) and (a) is 0.6. For the rest of the variables, the values for the two minima are consistent. The same is true for statistical and systematic uncertainties of all variables.

	$\Delta\Gamma_s$	Γ_s	Δm_s	$\lvert\lambda\rvert$	$\lvert A_\parallel(0)\rvert^2$	$\lvert A_0(0)\rvert^2$	$\lvert A_S(0)\rvert^2$	$\delta_\parallel$	$\delta_\perp$	$\delta_\perp - \delta_S$
ϕ_s	−0.05	0.01	0.18	−0.02	−0.01	0.00	0.00	0.01	0.18	0.01
$\Delta\Gamma_s$	1	−0.59	−0.02	0.00	0.09	0.09	0.05	−0.03	−0.03	0.02
Γ_s		1	0.01	0.00	−0.12	−0.04	0.07	0.07	0.02	0.03
Δm_s			1	−0.23	0.01	0.00	0.01	−0.01	0.74	0.00
$\lvert\lambda\rvert$				1	−0.01	0.00	0.00	0.03	−0.27	0.01
$\lvert A_\parallel(0)\rvert^2$					1	−0.34	−0.11	−0.45	−0.06	−0.06
$\lvert A_0(0)\rvert^2$						1	0.26	0.08	0.01	0.09
$\lvert A_S(0)\rvert^2$							1	0.30	0.06	0.35
$\delta_\parallel$								1	0.14	0.13
$\delta_\perp$									1	0.05

Table 6.7: Statistical correlations between the physical parameters of interest, obtained from the fit for the solution (a).

	$\Delta\Gamma_s$	Γ_s	Δm_s	$\lvert\lambda\rvert$	$\lvert A_\parallel(0)\rvert^2$	$\lvert A_0(0)\rvert^2$	$\lvert A_S(0)\rvert^2$	$\delta_\parallel$	$\delta_\perp$	$\delta_\perp - \delta_S$
ϕ_s	−0.03	0.10	0.41	−0.09	0.01	0.07	0.04	0.04	0.43	0.03
$\Delta\Gamma_s$	1	−0.36	0.01	−0.02	0.11	−0.01	0.01	0.10	0.03	0.04
Γ_s		1	0.12	0.03	−0.14	0.18	0.26	−0.02	0.05	0.20
Δm_s			1	−0.37	0.05	0.04	0.02	0.07	0.86	0.01
$\lvert\lambda\rvert$				1	−0.04	0.01	0.03	−0.04	−0.39	0.01
$\lvert A_\parallel(0)\rvert^2$					1	−0.49	−0.24	0.07	0.06	−0.15
$\lvert A_0(0)\rvert^2$						1	0.47	−0.30	0.00	0.25
$\lvert A_S(0)\rvert^2$							1	−0.03	0.02	0.46
$\delta_\parallel$								1	0.21	0.03
$\delta_\perp$									1	0.03

Table 6.8: Total correlations obtained by the combination of statistical correlations from the fit and estimated correlations from systematic uncertainties for the solution (a).

	$\Delta\Gamma_s$	Γ_s	Δm_s	$\lvert\lambda\rvert$	$\lvert A_\parallel(0)\rvert^2$	$\lvert A_0(0)\rvert^2$	$\lvert A_S(0)\rvert^2$	$\delta_\parallel$	$\delta_\perp$	$\delta_\perp - \delta_S$
ϕ_s	−0.049	0.005	0.116	0.041	−0.003	−0.001	0.000	0.003	0.101	−0.000
$\Delta\Gamma_s$	1	−0.582	−0.009	−0.012	0.087	0.089	0.050	0.032	−0.004	0.019
Γ_s		1	0.006	−0.003	−0.123	−0.041	0.083	−0.085	−0.008	0.027
Δm_s			1	−0.225	−0.000	0.005	0.029	−0.007	0.746	0.013
$\lvert\lambda\rvert$				1	0.027	−0.020	−0.077	0.056	−0.255	−0.038
$\lvert A_\parallel(0)\rvert^2$					1	−0.340	−0.159	0.511	0.075	−0.067
$\lvert A_0(0)\rvert^2$						1	0.267	−0.097	−0.010	0.092
$\lvert A_S(0)\rvert^2$							1	−0.352	−0.027	0.336
$\delta_\parallel$								1	0.142	−0.120
$\delta_\perp$									1	0.017

Table 6.9: Statistical correlations between the physical parameters of interest, obtained from the fit for the solution (b).

	$\Delta\Gamma_s$	Γ_s	Δm_s	$\lvert\lambda\rvert$	$\lvert A_\parallel(0)\rvert^2$	$\lvert A_0(0)\rvert^2$	$\lvert A_S(0)\rvert^2$	$\delta_\parallel$	$\delta_\perp$	$\delta_\perp - \delta_S$
ϕ_s	−0.031	0.089	0.349	−0.013	0.003	0.062	0.036	0.005	0.351	0.032
$\Delta\Gamma_s$	1	−0.328	0.005	−0.031	0.137	−0.003	0.012	0.124	0.027	0.043
Γ_s		1	0.099	0.033	−0.177	0.179	0.244	−0.116	0.021	0.193
Δm_s			1	−0.330	0.034	0.043	0.035	0.013	0.842	0.024
$\lvert\lambda\rvert$				1	0.005	0.006	−0.018	0.011	−0.354	−0.027
$\lvert A_\parallel(0)\rvert^2$					1	−0.333	−0.176	0.601	0.108	−0.128
$\lvert A_0(0)\rvert^2$						1	0.536	−0.350	−0.011	0.277
$\lvert A_S(0)\rvert^2$							1	−0.269	−0.010	0.451
$\delta_\parallel$								1	0.163	−0.103
$\delta_\perp$									1	0.020

Table 6.10: Total correlations obtained by the combination of statistical correlations from the fit and estimated correlations from systematic uncertainties for the solution (b).

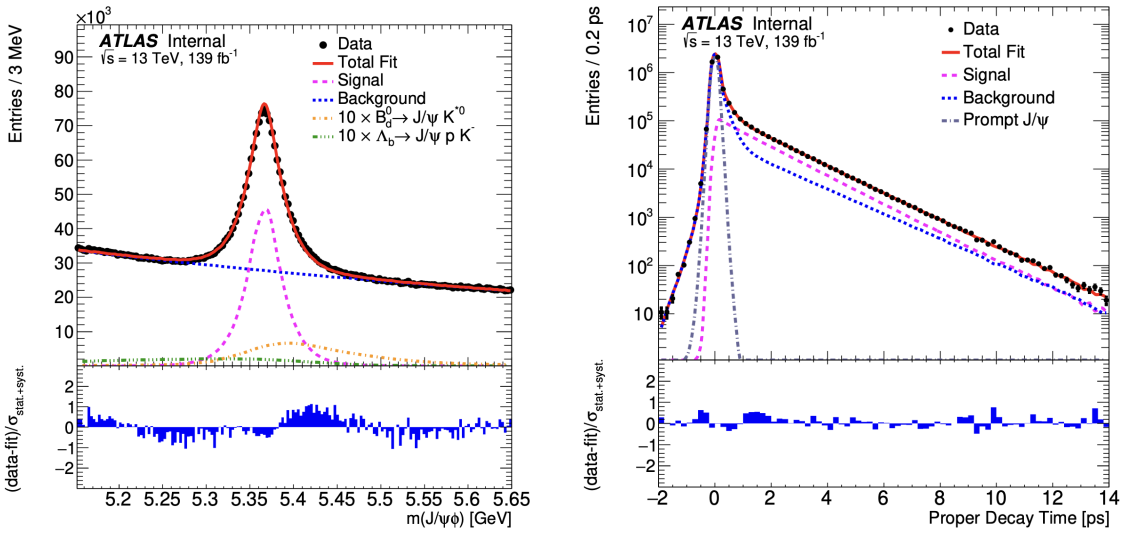

Figure 6.11: ATLAS internal result. (Left) Mass fit projection for the $B_s^0 \to J/\psi\phi$ sample. The red line shows the total fit, the short-dashed magenta line shows the $B_s^0 \to J/\psi\phi$ signal component, the combinatorial background is shown as the blue dotted line, the orange dash-dotted line shows the $B_s^0 \to J/\psi K^{*0}$ component, and the green dash-dot-dot line shows the contribution from $\Lambda_b \to J/\psi p K^-$ events. (Right) Proper decay time fit projection for the $B_s^0 \to J/\psi\phi$ sample. The red line shows the total fit, while the short-dashed magenta line shows the total signal. The total background is shown as a blue dotted line, and a long-dashed grey line shows the prompt J/ψ background component. A ratio plot reporting the difference between each data point and the total fit line, divided by the statistical and systematic uncertainties summed in quadrature of that point, is shown at the bottom of each figure.

6.14.2 Fit to strong phases

The results shown in Table 6.6 show the determination of the likelihood fit, with well-separated values for the strong phases $\delta_{\parallel}$ and $\delta_{\perp}$. Figure 6.13, shows the result of the 2D log-likelihood scan in both the $\delta_{\parallel}$ and $\delta_{\perp}$ planes, revealing two minima, the first at $(\delta_{\parallel} = 2.91, \delta_{\perp} = 3.00)$ and the second at $(\delta_{\parallel} = 3.37, \delta_{\perp} = 3.23)$. Introducing the difference in the likelihoods, between solution (a) and (b), as $-2\Delta\ln(\mathcal{L})$, the minima are represented by two-dimensional contours at levels of $-2\Delta\ln(\mathcal{L}) = 2.30, 6.18, 11.83$. $-2\Delta\ln(\mathcal{L}) = 2(\ln(\mathcal{L}^i) - \ln(\mathcal{L}^a))$ is the difference between the likelihood values $(\mathcal{L}^i)$ of the fit in which the two strong phases are fixed to the values shown on the horizontal and vertical axes. $(\mathcal{L}^a)$ is the likelihood value of the default fit for the solution (a).

The source of this duality is an approximate symmetry in the signal PDF. The strong phases are determined by the six interference terms. Four of the terms in Table 6.4 ($k = 3, 6, 7$ and 9), are invariant under the following transformation:

$$\{\delta_{\parallel}, \delta_{\perp}, \delta_{\S}\} \rightarrow \{-\delta_{\parallel}, \delta_{\perp} + 2(\pi - \delta_{\parallel}), \delta_{\S} + 2(\pi - \delta_{\parallel})\}. \tag{6.13}$$

For terms ($k = 8$ and 10) in Table 6.4, they break the symmetry, and the symmetry breaking is proportional to $\pi - \delta_{\parallel} \approx 0.23$, with the value from data. The local maxima satisfy Equation 6.13 very accurately for $\delta_{\parallel}$ and δ_S, with a deviation of 2.1σ for $\delta_{\perp}$. This deviation is calculated neglecting the systematic uncertainties and assuming a full correlation of the statistical uncertainties, meaning all existing symmetries of this decay are included in the PDF which obtains a conservative (over)estimate of the errors. The value of $-2\Delta\ln(\mathcal{L}) = 0.6$ favours solution (a) but cannot rule out solution (b). The two-fold nature of this likelihood maxima has a minor effect on the λ parameter, but a negligible effect on all other variables.

Figure 6.14 shows the 1D likelihood scans on four (Γ_s, $\Delta\Gamma_s$, ϕ_s, and Δm_s) of the other parameters, for each solution (a) and (b). For the remaining five parameters, please see AppendixC.1. In Figure 6.14, while all of solution (a) is lower, it is not possible to rule out solution (b), as the difference in $-2\Delta\ln\mathcal{L} =$

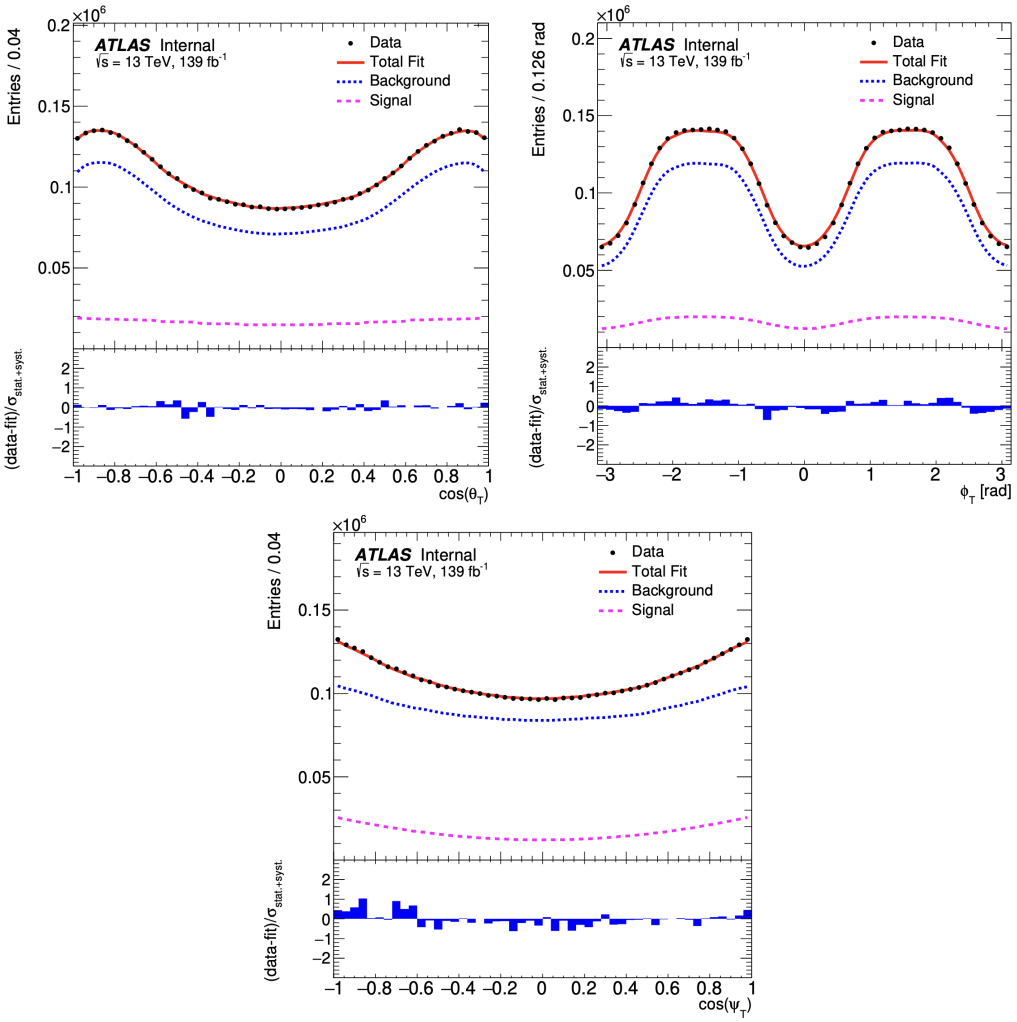

Figure 6.12: ATLAS internal result. Fit projections for the transversity angles ϕ_T (top left), $\cos\theta_T$ (top right) and $\cos\psi_T$ (bottom). In all three plots, the red solid line shows the total fit, the $B_s^0 \to J/\psi\phi$ signal component is shown by the magenta dashed line, and the blue dotted line shows the contribution of all background components. A ratio plot reporting the difference between each data point and the total fit line, divided by the statistical and systematic uncertainties summed in quadrature of that point, is shown at the bottom of each figure.

0.6. There are asymmetries in the curves, but these are small compared to the corresponding statistical uncertainties of the physical variables for which the scan is done. Therefore, symmetric statistical uncertainties are quoted.

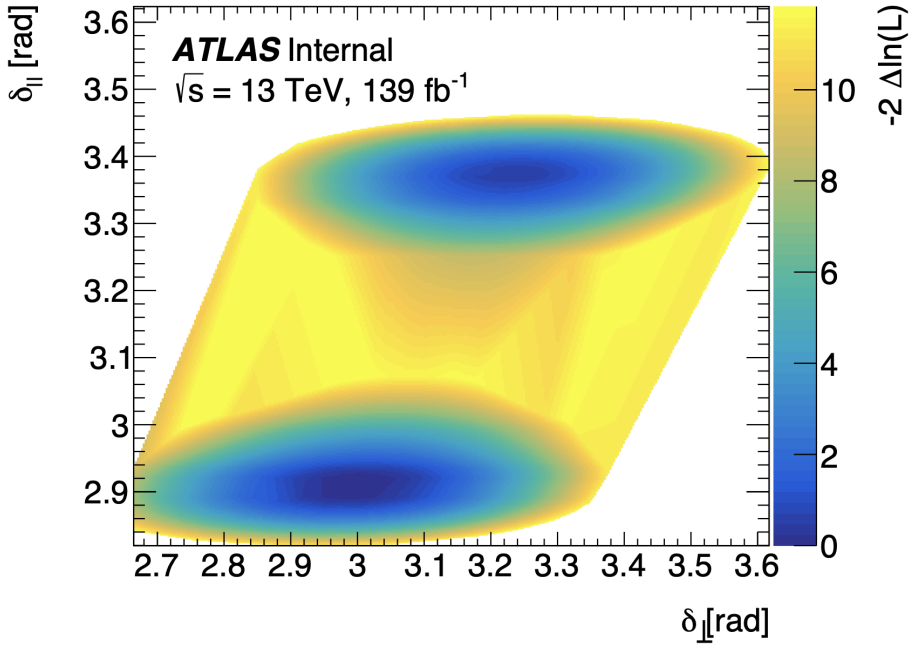

Figure 6.13: ATLAS internal result. The 2D log-likelihood scan in the $\delta_{||}$, $\delta_{\perp}$ plane in 3σ contours. The variable on vertical axis, $2\Delta\ln(\mathcal{L}) = 2(\ln(\mathcal{L}^G) - \ln(\mathcal{L}^i))$, is a difference between the likelihood values of a default fit, $(\mathcal{L}^G)$, and of the fit in which the physical parameter is fixed to a value shown on horizontal axis, $(\mathcal{L}^i)$. $2\Delta\ln(\mathcal{L}) = 1$ corresponds to the estimated 1σ confidence level.

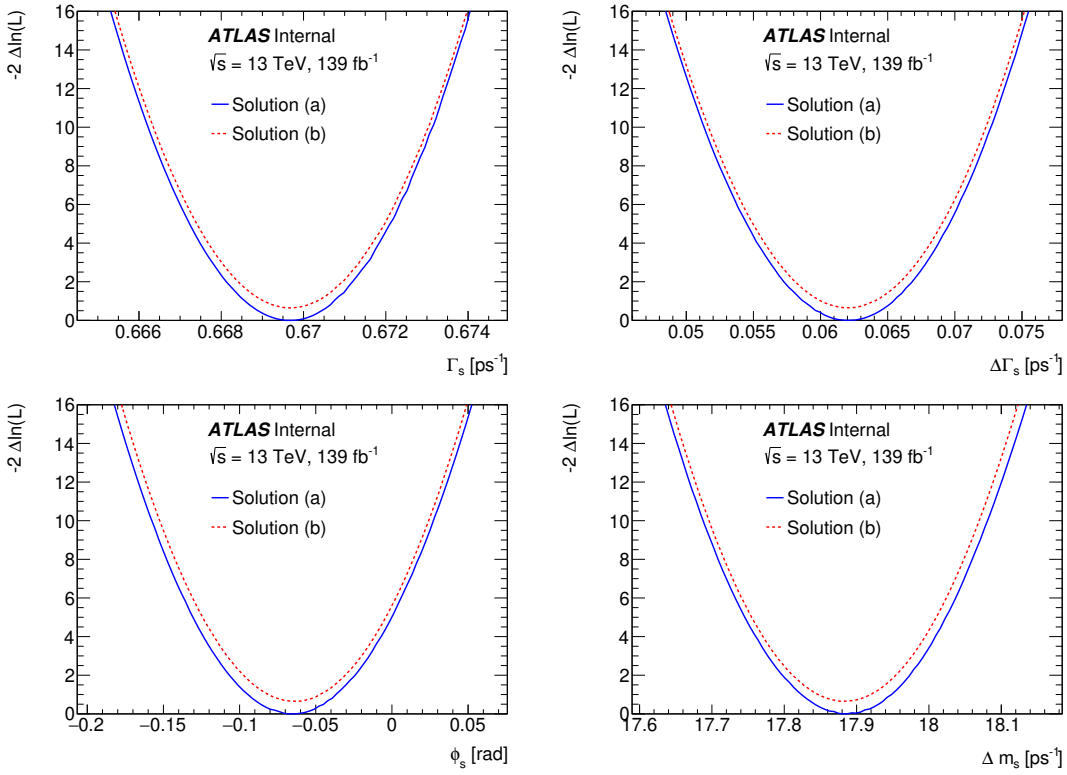

Figure 6.14: ATLAS internal result. 1D log-likelihood scans of four (Γ_s, $\Delta\Gamma_s$, ϕ_s, and Δm_s) of the remaining variables of the fit for the primary minimum (blue) and the secondary minimum (red). The variable on vertical axis, $2\Delta\ln(\mathcal{L}) = 2(\ln(\mathcal{L}^G) - \ln(\mathcal{L}^i))$, is a difference between the likelihood values of a default fit, $\mathcal{L}^G$, and of the fit in which the physical parameter is fixed to a value shown on horizontal axis.

6.14.3 Comparison of the measurements with the other experiments

In Figures 6.15 and 6.16, the comparison of the Δm_s and Γ_s values from the fit is shown in comparison with previous measurements. Figure 6.17, is a two-dimensional comparison plot in the $\phi_s - \Delta\Gamma_s$ plane, the figure compares this ATLAS result, the previous Partial Run 2 result with data from 2015 - 2017, [121], the CMS results [133], and the LHCb results, [134]. The contours are obtained by interpreting each result as a two-dimensional Gaussian probability distribution in the given plane. The statistical and systematic uncertainties are combined in quadrature, and correlations are taken into account in the construction of the contours. The recent SM prediction [126, 128] is shown in the figure as a very thin, line like black rectangle, with the width being the uncertainty in ϕ_s and the height being the uncertainty in $\Delta\Gamma$.

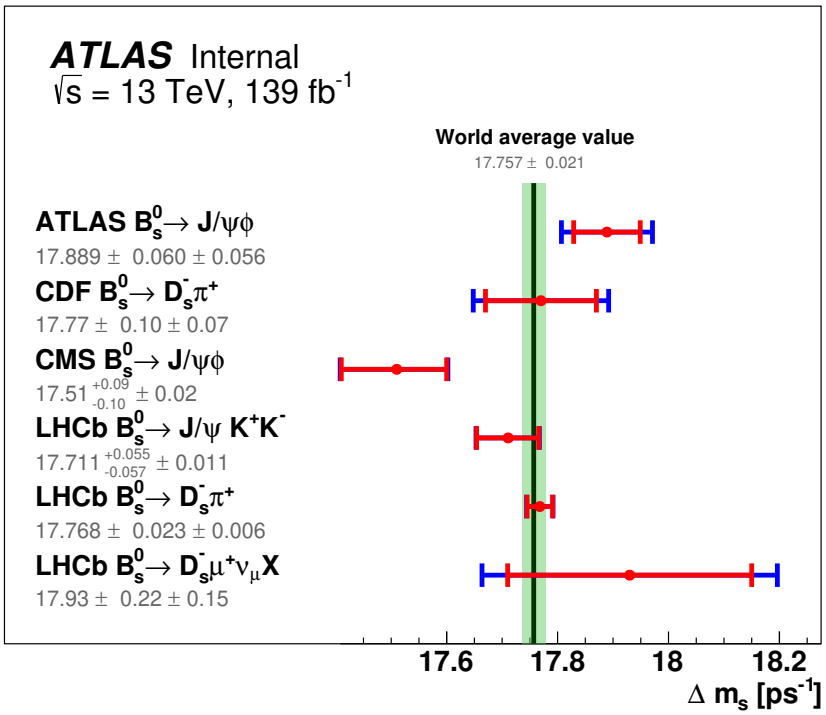

Figure 6.15: ATLAS internal result. Comparison of the mass difference Δm_s of the B_s^0 meson eigenstates of the ATLAS Run 2 results with LHCb [142, 143], CDF [144], CMS [133] results and the world average value (PDG value) [141]. Red lines are statistical uncertainties, and blue lines are the sum of statistical and systematic uncertainties. The green area is the uncertainty of the world's average value.

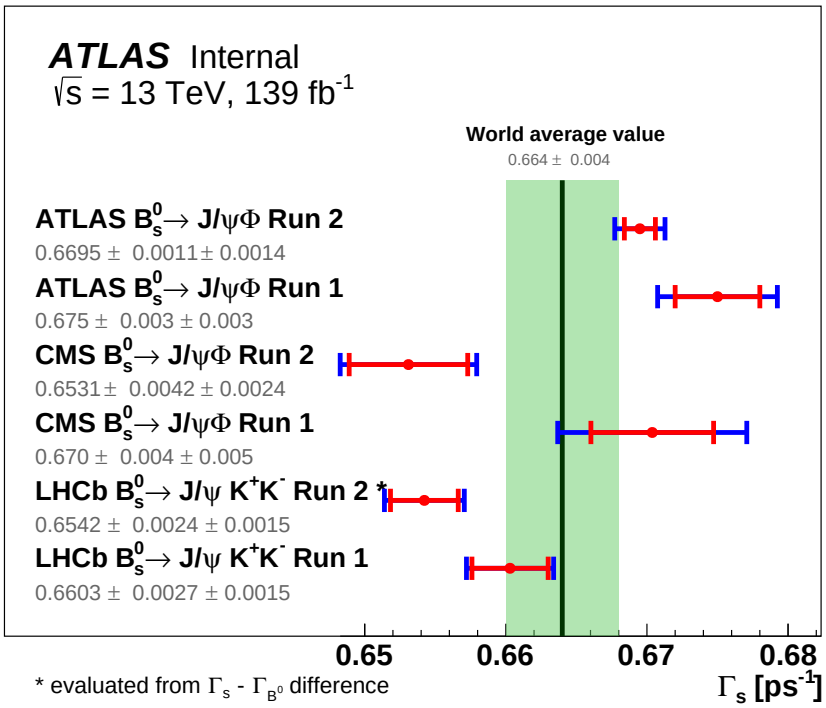

Figure 6.16: ATLAS internal result. Comparison of the average decay width Γ_s of the B_s^0 meson eigenstates of the ATLAS Run 2 results with ATLAS Run 1 [132], LHCb [131, 134], CMS [133, 175] results and the the world average value (PDG value) [141]. Red lines are statistical uncertainties, and blue lines are the sum of statistical and systematic uncertainties. The green area is the uncertainty of the world's average value. Since the LHCb Run 2 is measuring the $\Gamma_s - \Gamma_{B^0}$, the Γ_s value is evaluated using the world average value of Γ_{B^0}.

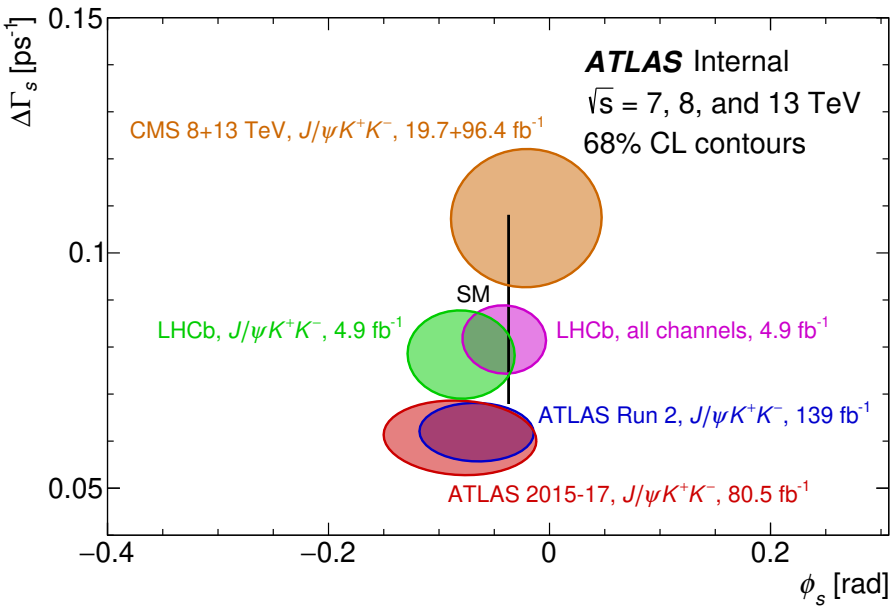

Figure 6.17: ATLAS internal result. Two-dimensional constraints on the values of ϕ_s and $\Delta\Gamma_s$ at the 68% confidence level for this ATLAS result (blue), the previous ATLAS result [136] (red), the CMS result [133] (orange), and LHCb results [134] (green and purple). The Standard Model prediction [126, 128] is shown as a very thin black rectangle, with the width and height defined by the respective uncertainties. In all contours, the statistical and systematic uncertainties are combined in quadrature. For the ATLAS 2015-2017 result, only the statistical correlation is available.

6.15 Personal Contribution to the analysis

My personal contribution to the analysis comes after the results section. Sections 6 to 6.14 are setting the metaphorical scene for my work, these sections provide the backbone for where my work comes to the forefront. My work involved investigating issues that arose during the analysis before I joined the team. My work aims to build on the previous analysis in preparation for both an improved version of Sections 6 to 6.14 and future work towards Run 3 analyses and beyond.

6.16 Evaluating the mass sideband choice

When creating a multi-parameter fit function for a physics analysis, there are many factors to consider, one of which is the signal vs background rejection. For good background rejection, a thorough understanding of the background and background signals is necessary. By testing the fit produced in Section 6.12, outside the fit's intended range, a deeper appreciation for the underlying background physics is gained.

6.16.1 Introduction to the Punzi methodology

There are pitfalls with the use of "templates" when unbinned likelihood fits are used within physics [176]. Summarising, the choice of template is paramount to an analysis's success, the template must be appropriate for the resolution of events and the type of events, i.e. signal or background, so it is fair that the fit in Section 6.12 is scrutinised.

Following the example presented by Punzi in [176], if there are two types of events, A and B, that can occur, suppose f is the fraction of type-A events, then the probability of a generic event being type-A is f. The goal is to extract a measurement of, f, from a given dataset, we measure the observable, x, with the

following probability distributions:

$$\begin{aligned} p(x|A) &= N(0,\sigma) \\ p(x|B) &= N(1,\sigma) \end{aligned} \tag{6.14}$$

where σ is a known constant and $N(\mu,\sigma)$ is the Normal distribution. This problem is solved using an "unbinned Likelihood fit". We maximise the Likelihood function:

$$L(f) = \prod_i fN(x_i,0,\sigma) + (1-f)N(x_i,1,\sigma) \tag{6.15}$$

with respect to the required parameter f.

Introducing a constraint that the resolution of the parameter x is not constant, so that each event x_i comes with an individual value of σ, σ_i. The common approach, and pitfall, would be to modify the likelihood function as follows:

$$L(f) = \prod_i fN(x_i,0,\sigma_i) + (1-f)N(x_i,1,\sigma_i) \tag{6.16}$$

After testing and upon further consideration, it is revealed that there are two observables in each observation, the pair of values (x_i,σ_i), which means the Likelihood function must now be written on the probability distribution of the pair, and remembering that

$$p(x_i,\sigma_i|X) = p(x_i|\sigma_i X)p(\sigma_i|X) \tag{6.17}$$

it is possible to write the correct expression of the Likelihood function for this problem.

$$L(f) = \prod_i fN(x_i,0,\sigma)p(\sigma_i|A) + (1-f)N(x_i,1,\sigma_i)p(\sigma_i|B) \tag{6.18}$$

Whenever you include σ_i in your Likelihood expression, even just for one class of events, you must also account for its distribution, this must be done for all event classes. For every problem, there is only one correct expression for the Likelihood, and it is critical to verify in every case that the expression used is the right one [176].

Imagine a scenario in which only photons are detected, and the photon has an energy resolution depending on where it hit the detector pixel, if it hits the centre of the pixel it has an uncertainty of U_a but if it hits the edge of the detector pixel, there is an uncertainty U_b, where $U_b > U_a$. In the scenario, all photons are treated the same, with some constant uncertainty on the energy resolution U_{const}, and the better resolution of events that hit the edge of the pixel is overlooked.

To summarise, there are systematic biases that can occur in unbinned maximum likelihood fits when the resolution or probability density functions are dependent on event-specific observables. Once identified, appropriate templates must be implemented to ensure unbiased parameter estimation.

6.16.2 Limitations of Punzi modelling

Punzi and the methodology described in Section 6.16.1 highlight the pitfalls of suggesting a plausible, but incorrect likelihood function that gives a biased result. This bias has been tested and is surprisingly large, and will overestimate the fraction of events corresponding to the peak with better resolution.

Another limitation occurs in the case of particle physics, momentum spectra of differing particles can be different, and as such, even at a constant resolution, the Punzi bias can arise. It can be possible to discern between two particle types if their momentum distributions are different enough, purely on their momentum distributions, without use of the detector particle identifier. This is done through parametric forms of momentum distributions of the particles, with parameter choice determined by the data analysed, [177].

6.16.3 Systematic tests of the mass sideband choice

The creation of two alternative functional forms used to model the background has resulted into an investigation into the suitability of the nominal range of 5150 MeV to 5650 MeV.

As discussed in Sections 6.2 and 6.12.1, the fit runs for a $m_{B_s^0}$ range of 5150 MeV to 5650 MeV, covering the mass peak around 5366 MeV and a signal region of ±150 MeV. To determine whether an event is background or signal, the Punzi background control method is used. The original Punzi is for the same $m_{B_s^0}$ range 5150 MeV to 5650 MeV as the maximum likelihood fit. The total $m_{B_s^0}$ range of 5000 to 5800 MeV is limited by the High Level Trigger (HLT) bandwidth constraints. Studies at the start of Run 2 showed that extending beyond this range would introduce background events with properties too dissimilar from the B_s^0 to be useful for the analysis.

The majority of the background comes from combinations of the J/ψ produced in any B-hadron decay and direct from J/ψ production in p-p collisions, combined with two random tracks that give the combined mass within the region considered. The additional, smaller backgrounds come from kinematic reflections of processes such as the $\Lambda_b \to J/\psi p K^-$ and $B_d^0 \to J/\psi K^{*0}$, that contribute differently to the left sideband compared to the right sideband. Figure 6.18 is the mass distribution used in this analysis.

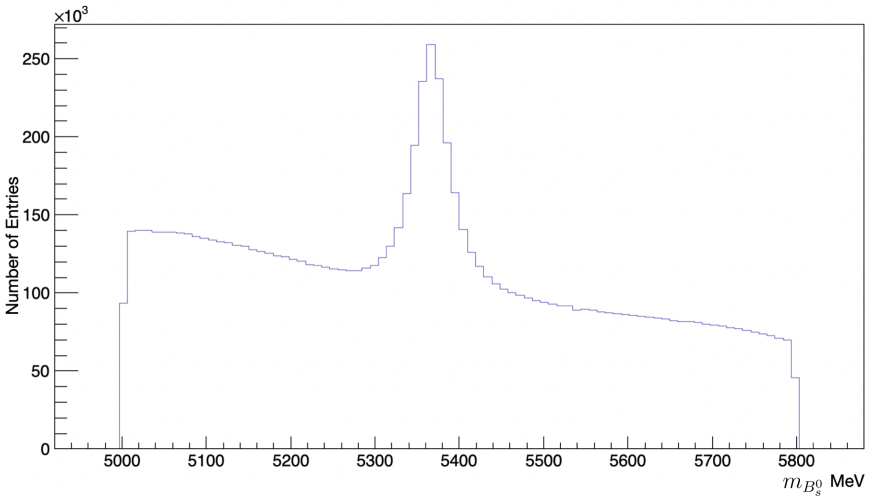

Figure 6.18: A histogram of $m_{B_s^0}$ candidates available within the data files ranging from $5000 - 5800$ MeV, with the sidebands being $5000 - 5216$ MeV and $5516 - 5800$MeV, and the signal region to be 5216 MeV $\leq m_{B_s^0} \leq$ 5516 MeV.

When investigating the effects of Punzi models on the fit parameters of this analysis, specifically Γ, there were two updated Punzi models created to compare with the original default one used before, as shown in Table 6.11.

Punzi model version	**Original Punzi**	**Wider Punzi**	**Refined Punzi**
Mass Range (MeV)	5150–5650	5100–5736	5150–5650

Table 6.11: A table highlighting the differences between the Punzi models used. All Punzi models were intended to run over the 5150–5650 MeV range.

These new Punzis were then tested through the changing of the mass fitting window, so while still using all of the 5000 MeV $< m_B <$ 5800 MeV mass window available, instead the fitted regions for these new Punzis were moved from the their designed, or desired, fitting regions to test their behaviour outside of their intended mass ranges. This meant the performance of the Punzis could be compared outside of their normal operating mass window and indeed the last used mass fit window of 5150 MeV $< m_B <$ 5650 MeV. This choice was motivated by a similar study undertaken by the ATLAS collaboration, [178], so the fitting algorithm must be able to fit well in the region required, but not hyper-specialised for that specific mass range, wherein accidental over-fitting biases may occur. These tests can partially account for the volatility of the backgrounds outside of the signal region. Table 6.12 shows some results from the fits carried out, focusing on the Γ parameter, as that is the most important parameter for this analysis.

In Table 6.12, the results of six different fits are shown for various mass ranges; these six are compared to a seventh stable "default" from before the Punzi investigation took place. This "default" was made using the same original Punzi as on trial here, but there were minor differences to the procedure of the fits being run, and root version updates, which we believe account for the difference between the "default" and the "nominal range" fit runs. The values in this table have been rounded to five decimal places, but the full values from the run logs were used for the pseudo significance calculation; this is true for Tables 6.12, 6.13, 6.14, and

6.15. In Tables 6.12 to 6.15 the metric of (test - default)/stat err (default) is used as a pseudo significance, and is not genuine mathematical significance. Hereafter, the term significance means this pseudo significance.

Default Punzi							
Parameters	Default	L-20	L+20	L+20, R-34	Nominal Range	L+50, R-86	R+30
Mass Fit Window (MeV)	5150 - 5650	5130 - 5650	5170 - 5650	5170 - 5616	5150 - 5650	5200 - 5564	5150 - 5680
Γ (ps^{-1})	0.66967	0.67029	0.66923	0.66993	0.66967	0.67079	0.66932
$\delta\Gamma$ (ps^{-1})	0.00110	0.00110	0.00108	0.00112	0.00109	0.00111	0.00108
(test - default) / stat err (default)	N/A	0.55797	-0.40837	0.23659	-0.00174	1.01158	-0.31929

Table 6.12: Analysis of the decay width parameter, Γ, including the error of that decay width, $\delta\Gamma$, for Default Punzi across multiple mass fitting windows, outside of the designed fit window of the Default Punzi.

As can be seen from Table 6.12, there is good agreement across the "default" and the "nominal range" fits, which is expected, with the only differences seen very small and thus attributed to ROOT version differences, [48]. Generally, as the mass fitting range moves, the Γ parameter is not changed much, which is good, showing that the fitting code does not over-fit the signal region. The smaller changes ($\pm$30 MeV) to either the upper or lower limits causing little change (< 0.5 significance), the only "mildly significant" change is when cutting into the Punzi range by > 50 MeV, where "mildly significant" is in quotation marks as it is comparatively more significant but still not actually significant.

The same fit performances were examined for the alternative wider ranged Punzi, with 5100 MeV $< m_B <$ 5736 MeV mass range, seen in Table 6.13. From Table 6.13, the updated Punzi performs worse with all mass ranges, giving a larger Γ than the default. Evaluating the significances as way of measuring performance, given that all of the significances are larger for the updated Punzi than the Default Punzi, we can conclude that this updated wider Punzi is not ideal for the analysis, and should not be carried forward.

The third and final Punzi test was an updated version of the default, spanning the same mass range, $5150 < m_B < 5650$ MeV. This is displayed in Table 6.14; from

updated Punzi, $5100 < m_B < 5736$ MeV							
Parameters	Default	L-20	L+20	L+20, R-34	Nominal Range	L+50, R-86	R+30
Mass Fit Window (MeV)	5150 - 5650	5130 - 5650	5170 - 5650	5170 - 5616	5150 - 5650	5200 - 5564	5150 - 5680
Gamma (ps^{-1})	0.66967	0.67247	0.67139	0.67177	0.67186	0.67079	0.67150
Gamma Error (ps^{-1})	0.00110	0.00112	0.00111	0.00112	0.00109	0.00111	0.00111
(test - default) / stat err (default)	N/A	2.54072	1.55733	1.90735	1.98601	1.01158	1.65732

Table 6.13: Analysis of the decay width parameter, Γ, including the error of that decay width, $\delta\Gamma$, for updated, wider Punzi across multiple mass fitting windows, outside of the designed fit window of the updated Punzi.

this, the Γ values are similar to the default Punzi, arguably on par generally, but there is a larger range of significance values in the updated default Punzi. This led to further investigation into the suitability of the updated default Punzi, looking to solidify whether this was a worthwhile transition from the older default to the updated default Punzi. This is explored more in Table 6.15.

updated default Punzi, $5150 < m_B < 5650$ MeV								
Parameters	Default	L-20	L+20	L+20, R-34	Nominal Range	R-20	L+50, R-86	R+30
Mass Fit Window (MeV)	5150 - 5650	5130 - 5650	5170 - 5650	5170 - 5616	5150 - 5650	5150 - 5630	5200 - 5564	5150 - 5680
Gamma (ps^{-1})	0.66967	0.67066	0.66950	0.66993	0.67006	0.67032	0.67043	0.66962
Gamma Error (ps^{-1})	0.00110	0.00112	0.00111	0.00112	0.00112	0.00112	0.00112	0.00111
(test - default) / stat err (default)	N/A	0.89857	-0.15964	0.23659	0.35218	0.59069	0.68804	-0.04719

Table 6.14: Analysis of the decay width parameter, Γ, including the error of that decay width, $\delta\Gamma$, for the new updated Default Punzi across multiple mass fitting windows, outside of the designed fit window of the new updated Default Punzi.

Before reviewing Table 6.15, there are some incomplete fits shown in this table. This is because the fits were seen to converge and run successfully enough to an appropriate precision needed for this study. The unfinished fits are "L-35", "L-25", "L-25, R+35"; these results are still shown as they give an indication of the behaviour of the fit outside of the normal window. From Table 6.15, the performance of the updated Punzi can be evaluated, with the updated Punzi performing well for the fits that finished, and the fits that did not complete, showed reasonably "in"significant results, with the highest significance value being 1.28.

updated default Punzi, $5150 < m_B < 5650$ MeV further investigation									
Parameters	Default	L-50, R+86	R-30	L-35	L-25	L+25	L+35	L-35, R+35	L-50, R+150
Mass Fit Window (MeV)	5150 - 5650	5100 - 5736	5150 - 5620	5115 - 5650	5125 - 5650	5175 - 5650	5185 - 5650	5115 - 5615	5100 - 5800
Gamma (ps^{-1})	0.66967	0.67040	0.67046	0.67108	0.67085	0.66939	0.66910	0.67165	0.66912
Gamma Error (ps^{-1})	0.00110	0.00109	0.00112	0.00113	0.00113	0.00111	0.00111	0.00105	0.00110
(test - default) / stat err (default)	N/A	0.66700	0.71552	1.28545	1.07273	-0.25508	-0.52060	0.51000	-0.49667

Table 6.15: Analysis of the decay width parameter, Γ, including the error of that decay width, $\delta\Gamma$, for the new updated Default Punzi across more mass fitting windows designed for closer scrutiny with the default Punzi, outside of the designed fit window of the new updated Default Punzi.

6.16.4 Sideband Systematic Conclusion

The ideal Punzi model to be used going forward is the updated Default Punzi, it behaves more robustly outside the intended mass fit range. However, due to the rewriting of the code that would be necessary, along with the subsequent update to the overall uncertainty and systematics, this has not been included for the next iteration, the Full Run 2 paper, but is under consideration for the Run 3 analysis.

6.17 Using sPlot and sWeight for background rejection

sPlot is a statistical technique for untangling distributions through statistical methods, referring to the original paper in which sPlot was introduced, sPlot can separate contributions of different sources to the distributions of data samples within a variable [179]. sPlot is a powerful technique that provides background rejection through the exploitation of correlations between event variables. sPlot allows for reconstruction of distributions for a control variable, independently for each type of event, without making use of any prior knowledge on this variable. sPlot is able to separate a complicated background into its constituent physical processes, as well as isolate the signal. This technique is well-suited for particle physics applications, as often, mass or other variables and their distributions are recorded from a mixture

of sources, and as such, background rejection and signal acceptance are crucial for insight.

sPlot can crudely be broken down into four steps as follows,

1. A choice of discriminant variable, for example invariant mass, which is applicable for this analysis, and assume the data taken is of several components, a signal and multiple backgrounds.

2. Model the Probability Density Function, PDF, for each component with respect to the discriminant variable and any other relevant observable variables, eg angular acceptance.

3. Perform a global fit of the sum of these PDFs to your data, determining the fractional contribution, sometimes referred to as yields, of each component.

4. sPlot calculates "sWeights" for each event in your dataset. These are effectively probabilities for an event to belong to a certain PDF, which aids the classification of background or signal. Moreover, it is a probability that a specific event belongs to the signal or other dataset species, given the event's position in the discriminant variable and the overall PDF fit.

6.17.1 An introduction to sWeights

sWeights are probabilities calculated from the covariant matrix. The main idea is that events in regions dominated by signal will earn higher signal sWeights, and vice versa for background region events gaining higher background sWeights. Note that the original distribution can be made up of more subsets, species of data, than the signal and background used here. For example, in B physics experiments, the background is often made up of multiple sources, and each source of background would be considered a species, as well as the signal. For simplicity, this section continues with an example using just signal and background.

6.17.2 sPlot

This subsection is largely inspired by [180] Chapter 6, Section 6.2. For a complete breakdown of the technique, see the original sPlot paper, [179] and the ROOT documentation [48].

The aim of sPlot is to reconstruct the constituent distributions of a sample for all subsets, species, crucially, without using any prior knowledge of them and using only the distribution of discriminating variables. For simplicity of this example, only one discriminating variable is considered. sWieghts are calculated for each species, to obtain a specific species distribution, the histogram beins are filled with sWeights of corresponding species as weighting factors for each event in the control variables, [180].

Following the example on the ROOT sPlot webpage, consider a data sample in which, are merged, several species of events. The species of events represent various signal components and background components, with all the species together accounting for the data sample. The terms within the log-Likelihood are:

- N: the total number of events in the data sample.
- N_s: the total number of species of events populating the data sample.
- N_i: the number of events expected on average for the i^{th} species.
- $f_y(y_e)$: the value of the PDFs of the discriminating variable y for the i^{th} species and for event e.
- x: is the set of control variables which, by definition, do not appear in the expression of the Likelihood function $\mathcal{L}$.

Now the extended log-Likelihood is:

$$\mathcal{L} = \sum_{e=1}^{N} \ln \left\{ \sum_{i=1}^{N_s} N_i f_i(y_e) \right\} - \sum_{i=1}^{N_s} N_i \tag{6.19}$$

From this expression, after maximisation of $\mathcal{L}$ with respect to N_i parameters, a weight can be computed for every event and for each species, in order to obtain later the true distribution $M_i(x)$ of a variable.

If it is one of the species present in the data sample, the weight for this species is defined by Equation 6.20, seen later, for now, a simple example is provided. If the data is fixed to be entirely signal or background, i.e. there are two species, there will be two sWeights calculated: one for signal, one for background. To get the distribution for a control variable, such as the signal distribution, the histogram is filled with signal sWeights as weighting factors, allowing the determination of the signal distribution. The formula for the calculation of sWeights is,

$$ {}_s\mathcal{P}_n(y_e) = \frac{\sum_{j=1}^{N_S} \boldsymbol{V}_{nj} f_j(y_e)}{\sum_{k=1}^{N_S} N_k f_k(y_e)}. \tag{6.20} $$

where N is the total number of events in your sample, N_s is the number of species, subsets, in your data sample, N_i is the number of events expected on the average for the i^{th} species, y is the set of discriminating variables, f_n is the PDF of discriminating variables for the n^{th} species, $f_i(y_e)$ denotes the value taken by the PDFs f_i for event e, x denotes the set of control variables, $V_{n;j}$ are covariance matrix elements, so that where ${}_s\mathcal{P}_n(y_e)$ is the sWeight for discriminating variable y, of species n and event e.

It is possible to perform a simultaneous maximum likelihood fit to the discriminating variable so that the total number of species within a sample is calculated, which in turn gives the total number of events N_i per species.

To obtain the covariance matrix elements, the second derivative of the likelihood function is calculated with respect to the parameters at the central values, which yields the inverse covariant matrix elements. The covariance matrix can be obtained by taking the inverse of the matrix given in Equation 6.21

$$ V_{nj}^{-1} = \frac{\partial^2(-\mathcal{L})}{\partial N_n \partial N_j} = \sum_{n=1}^{N_s} \frac{f_n(y_e) f_j(y_e)}{(\sum_{k=1}^{N_s} N_k f_k(y_e))^2}. \tag{6.21} $$

Using Equation 6.20, the sWeights for each species is achieved, which can be used in filling the histogram bins to obtain the distributions of the control variables for

each species. The total number of events of a given species provided by the fit is equivalent to the sum of the weights of all events for that given species. It is possible to calculate the uncertainty per bin for the sWeights through the following Equation, 6.22.

$$\sigma[N_n \, s\tilde{M}_n(x)\delta x] = \sqrt{\sum_{e \subset \delta x} ({}_sP_n)^2} \tag{6.22}$$

For Equation 6.22, $\tilde{M}$ is the x (the control variable) distribution and the sum $\sum_{e \subset \delta x}$ runs over the $N_{\delta x}$ events for which x_e (i.e. the value taken by the variable x for event e) lies in the x bin centred on $\bar{x}$ and of total width δx. More detailed information about sPlot can be found in [179] and [180].

6.17.2.1 Sideband subtraction

In these sPlot investigations, my contribution was to test and compare the finalised sPlot models rather than to create the sPlot parameter optimisations. The optimisations were run year by year and split into signal region and sidebands as seen in Figure 6.19, where a m_B distribution has been annotated to roughly show the apparent regions. Figure 6.19 demonstrates the Signal Region, SR, and the Sideband region(s), sb, which are later relied upon for the two varying sPlot fit results.

Figure 6.21 shows the differences between the original fit results and the current, altered to include Signal Region sPlot regions. Before examining Figure 6.21, the naming convention needs to be explained for clarity so readers can deduce what is being shown. There are four different types of fit investigated in this work. These are as follows

1. `ATLAS Partial Run 2`

   This is the default fit from the previous version of this analysis, [121], using data from 2015 to 2017. Fit 1 had 9 parameters and was applied to a partial Run 2 data set.

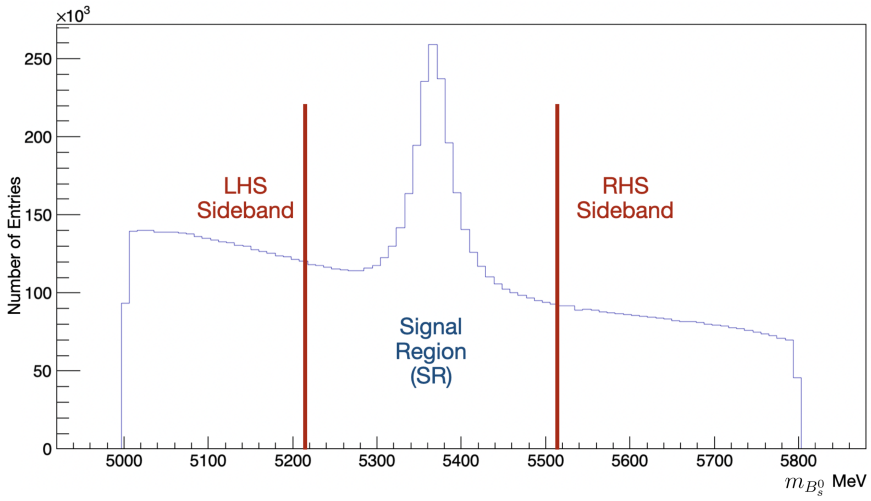

Figure 6.19: Full $m_{B_s^0}$ distribution, annotated with the approximate region cuts for the signal region and the sidebands.

2. `data_2015_old_punzi`

   This involves the previously run 2015 data, where "old_punzi" denotes the original Punzi being used, not the updated sPlot Punzi. Here, 2015 is just one of the several different years' worth of data available. The old punzis used sideband subtraction, not the sPlot technique.

3. `fit2_data_SR_2015`

   This uses the new, updated sPlot Punzi for 2015, for the signal region only. Again, 2015 is just one of the several different years' worth of data available.

4. `fit2_data_sb_2015`

   This displays the new, updated sPlot Punzi for 2015, for the sidebands only. Again, 2015 is just one of the several different years' worth of data available.

Sideband subtraction is a method to deal with the background uncertainty in experiments. In simple terms, this is when the signal region out is cut out, as shown in Figure 6.19, it is possible to model the sidebands as an approximation for the background. Extrapolating the background assuming it is linear, achieves a line of

best fit seen in Figure 6.20, which can then be used as a background estimation in the signal region. Linear is the best method for visualisation, yet primitive; it is possible to refine sideband subtraction with the use of other polynomials.

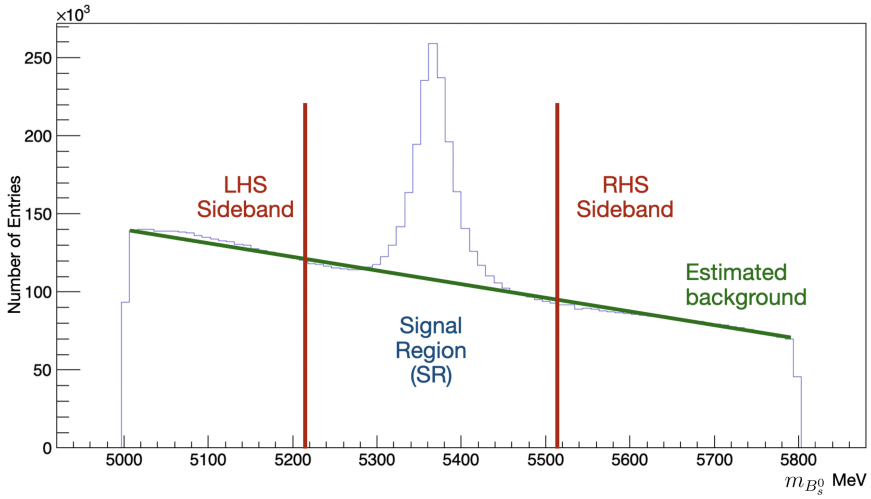

Figure 6.20: Full m_B distribution, edited to show a linear example of the sideband subtraction background estimation method.

6.17.2.2 sPlot Results

With the sideband extraction explained, reviewing the results begins with Figure 6.21, the fit results are very consistent across the altered sPlot SR and the plain original fit, making very minimal difference to the overall result. This can also be demonstrated for the sidebands, as seen in Figure 6.22. This time, there is more of an impact on the Γ parameter, but this is affecting mostly the background region, a region in which the Γ should be noticeably different from the signal region, given the sidebands are made up from different source signals. Here it is important to note a feature of the plotting code, as it is a log likelihood function, it can sometimes close in on a local minima not a global minima, this was suspected to be the case for "fit2_data_sb_2018", given the vast difference in Γ value, comparing 0.5115 ps^{-1} to the more typical 0.67± 0.2 ps^{-1} seen in Figures 6.21 to 6.23. However, after the investigation into this result seen in Appendix B.1, it was found that the fit failed

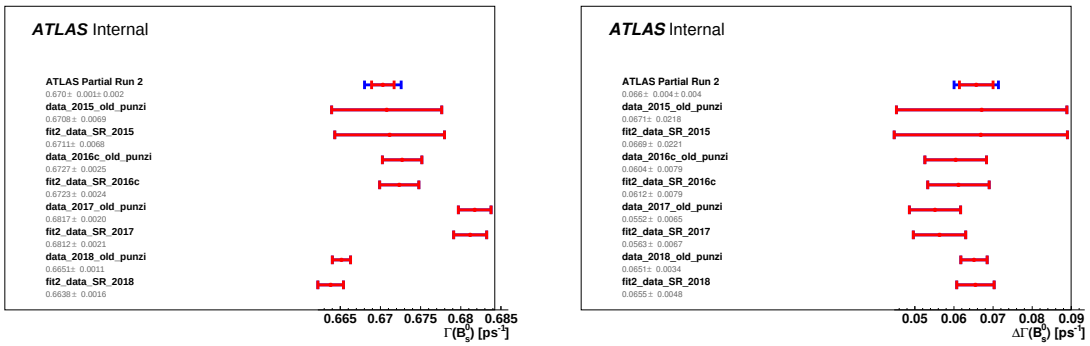

(*a*) Γ (*b*) ΔΓ

Figure 6.21: (*a*) Comparison of Γ distributions for the signal region against the previously run fits for different sub data samples from 2015 to 2018.
(*b*) Comparison of ΔΓ distributions for the signal region against the previously run fits for different sub data samples from 2015 to 2018.

and the result is erroneous; it has been kept in these plots for completeness, as the methodology was the same between each fit and adding in new sPlot Punzis for the fits. The erroneous result is also seen in Figure 6.22, as it plots the same fit result.

For completeness, displayed in Figure 6.23 is the comparison of simply the signal region and the sidebands. The typical trend from this figure is that the sideband is made up of mostly smaller decay width particles and not the desired B_s^0 meson, apart from for the 2016a sample, in which it appears the sidebands are dominated by events that have a higher decay width than the full sample.

Given the minimal improvement of the sPlot technique on the overall Γ result, sPlot was not taken further and was not included in the overall analysis. Another reason behind this decision was the knock-on effects on the systematics and having to update the complex calculations, so a cost-benefit analysis was undertaken, in which it was concluded to stick with the current model.

The analysis team is aware of and investigating the differences between the data from 2017 and 2018, seen in Figures 6.21, 6.22, and 6.23. This difference is due to multiple things, mainly stemming from an issue with the trigger menus. The

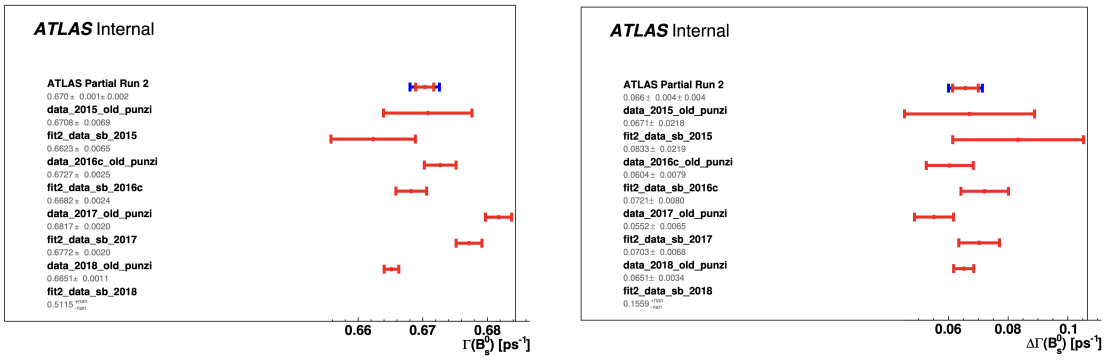

(*a*) Γ (*b*) ΔΓ

Figure 6.22: (*a*) Comparison of Γ distribution for the sidebands against the previously run fits for different sub data samples from 2015 to 2018.
(*b*) Comparison of ΔΓ distribution for the sidebands against the previously run fits for different sub data samples from 2015 to 2018.

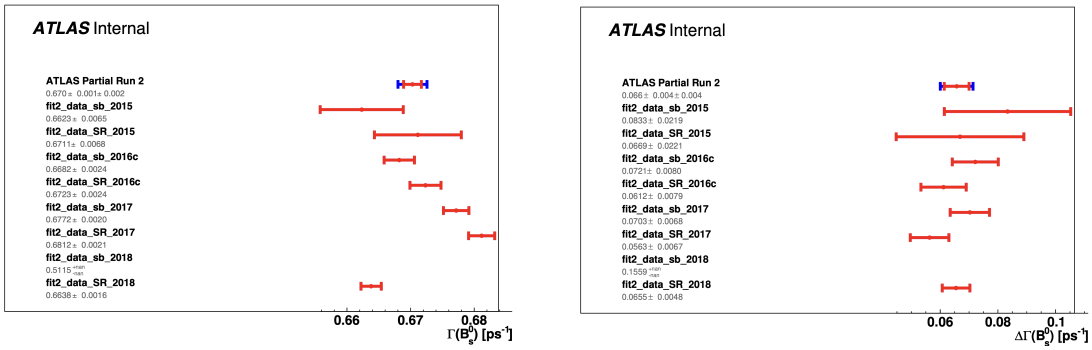

(*a*) Γ (*b*) ΔΓ

Figure 6.23: (*a*) Comparison of Γ distributions for the signal region against sideband fits for different sub data samples from 2015 to 2018.
(*b*) Comparison of ΔΓ distributions for the signal region against the sideband fits for different sub data samples from 2015 to 2018.

data taking period of 2016a was short and declared not fit for use in to the data by ATLAS, this was due to several issues at the start of 2016 with data taking, and so it was not used in the fit. For 2018, there was a new trigger algorithm introduced, dedicated to select events from $\mu\mu\phi(KK)$. This algorithm was rejected events within the opening angle of $\mu^+K^+ < 0.04$ rad and $\mu^-K^- < 0.04$ rad. This cut in the 2018 dataset meant that the $B_s^0 \to J/\psi\phi$ events were biased, this bias has been corrected for application of a specific 4D acceptance correction. This has not been done within the time frame of this thesis, and has been completely removed for Run 3 data taking. There were also inefficiencies within the Punzi method for both of these years, with [121] using Punzis with sideband subtraction, and this analysis using sPlot in conjunction with Punzis. Both of these approaches are used to disentangle the signal from the background across variables. In the previous analysis, Punzi was applied in one dimension, but it is possible to construct Punzis in two dimensions; this has yet to be completed for the updated analysis, but is being done as a result of the work presented in this thesis for the latest version of the analysis.

6.18 Study of mass-time correlations in B_s^0 meson background

In previous iterations of this analysis, and the current ongoing analysis, there have been several attempts to enhance understanding and modelling of the background; inevitably and unfortunately, compromises are made either as an analysis team pushes for publication or is simply suffering from a lack of resources. Within this section, insight into the combinatorial background and prompt J/Ψ background is gained through investigating the underlying parameters that were previously assumed to have a low impact on the overall background.

The previous version of this analysis [121] did not account for a mass dependence for some fit parameters, the mass dependence was assumed constant. Within this

section, an analysis of four fit result parameters takes place to discern if it is reasonable to assume constant distribution across the mass range, or if there needs to be an update to the method to account for the mass dependence. The fit result parameters under close scrutiny are f_{prompt}, $f_{indirect}$, τ_{fast} and τ_{slow}. First, defining f_{prompt} is the fraction of prompt J/ψ mesons in the mass sample, and likewise $f_{indirect}$ is the fraction of indirect J/ψ mesons in the mass sample. Within the data sample, there are two classifications of J/ψ mesons:

1. prompt J/ψ: these are also known as direct J/ψ, these are background events created by a combination of J/ψ produced in proton-proton interactions, combined with two random tracks, that pass $\phi(KK)$ selections.

2. non-prompt J/ψ: these are also known as indirect J/ψ; these are background events that are formed of J/ψ produced in a decay of any B-hadron; combined with two tracks - that can be a random track, or tracks from b-hadrons.

With the two types of J/ψ mesons defined, the importance of understanding the fraction of each throughout the mass range is seen. The background composition will inevitably be made up of some proportion of f_{prompt} and $f_{indirect}$. Understanding if this fractional composition changes as a function of mass is crucial to gaining a fuller understanding of the background, to check whether the previous assumption of no mass dependence was suitable.

There are two more parameters under investigation which are the τ_{fast} and τ_{slow}, both of which are decay lifetimes used in modelling the background within the fit, specifically not the prompt J/ψ background. The background is modelled by two exponentials, both decaying quickly, but one faster than the other comparatively, hence we have τ_{fast} for the fast decaying background component and τ_{slow} for the slower decaying background component. The mass dependence of these parameters was not investigated in the previous version of this analysis [121]. However, a similar study was performed in the B_d^0 lifetime measurement [178]. The approach

used here is detailed in Section E.7 ("Mass-Time Correlation systematics") of the B_d^0 paper [178].

Figure 6.24 shows the proper decay time fit projection for the $B_s^0 \to J/\psi\phi$ sample and shows the background components in the fit. The blue line is applicable to this investigation, as the right-hand side of the peak is made up of two exponents, specifically one fast decaying and one more steady decaying exponent, these are directly related to τ_{fast} and τ_{slow}.

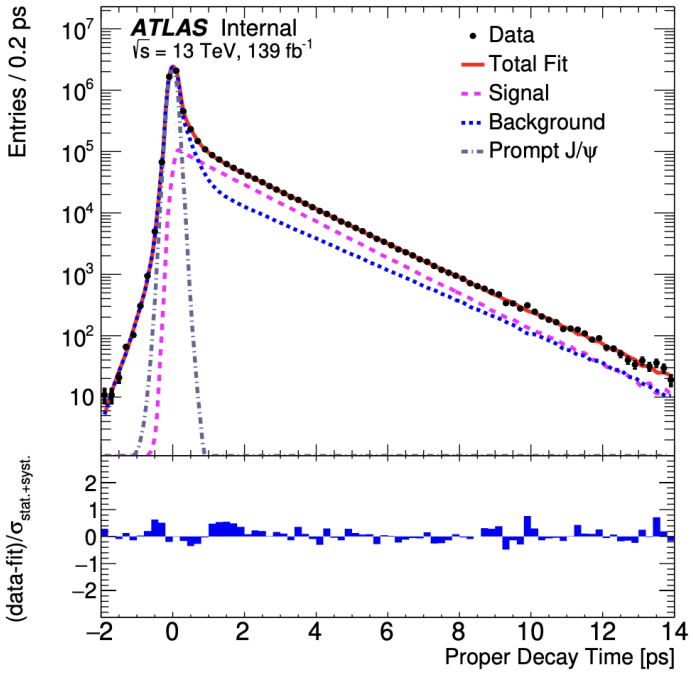

Figure 6.24: Proper decay time fit projection for the $B_s^0 \to J/\psi\phi$ sample. The red line shows the total fit, while the short-dashed magenta line shows the total signal. The total background is shown as a blue dotted line, and a long-dashed grey line shows the prompt $J/\psi\phi$ background component. A ratio plot reporting the difference between each data point and the total fit line divided by the statistical and systematic uncertainties summed in quadrature ($\sigma_{stat.+syst.}$)of that point is shown at the bottom of the figure. Figure taken from [121].

Figure 6.24 has negative decay times, which at first seems nonsensical; quite rightly, there is no known physical process with a negative proper decay time, but it

is actually a feature of the detector and how the data is extracted. Looking at the grey dashed line in Figure 6.24, the prompt J/ψ production, it is known that prompt J/ψ mesons are produced from the proton-proton interaction and the fragmentation at the collision point, then they decay; they cannot decay before they are made. In a perfect world, the ATLAS detector would have infinite precision, and measurement of the prompt J/ψ mesons would look like a delta function. Unfortunately, this is not a perfect world; there is finite precision on the detector. If the precision were worse, this would be a wider peak; if the precision were better, it would be a narrower peak.

Further details of the event selection are given in Section 3 "Reconstruction and candidate selection" of [121]. A short summary of the reconstruction is that a secondary vertex (SV) is identified with the correct characteristics, this is then assigned to a primary vertex (PV), the distance between the SV and the PV, L_{xy} is related to the proper decay time, t, through the Equation 6.23.

$$t = \frac{L_{xy} m_B}{p_{T_B}} \tag{6.23}$$

where the proper decay time, t, of each B_s^0 meson candidate is estimated using the reconstructed transverse momentum of the B_s^0 meson candidate, p_{T_B}, using m_B the mass of the B_s^0 meson candidate, taken numerically as the world average [141] and the transverse decay length L_{xy} is the displacement in the transverse plane of the B_s^0 meson decay vertex relative to the primary vertex, projected onto the direction of the B_s^0 transverse momentum. In the event that the primary vertex matched to the secondary vertex is in front of the secondary vertex, L_{xy} is negative, and thus negative decay times are achieved.

This smearing can be defined as the difference between the true actual value of the measured parameter and the measured value. Smearing is caused by the finite precision of the ATLAS detector, and as such, a measured event will have associated uncertainties as a direct result of the detector characteristics. The main source of smearing is the detector precision and associated uncertainties.

To combat smearing, a de-smearing correction factor is applied. This factor

is derived by processing MC events through the detector simulation software and comparing the reconstructed lifetimes with the known MC truth values, allowing the smearing effect to be quantified.

Within this analysis, smearing is performed on an event-by-event basis in which the width of the Gaussian function is the proper decay time, measured for each event and multiplied by a scale factor to account for any mismeasurements. De-smearing is described in more detail in [121].

6.18.1 Mass-time correlations in B_s^0 meson background results

Within the analysis, there is the available mass region 5000 MeV $< m_{B_s^0} <$ 5800 MeV, which is seen in Figure 6.19. The mass region is centred around the signal region which is defined around the mass peak of 5366 ± 150 MeV. This allows for the sidebands to be defined, the left hand side, *LHS* sideband, $m_{B_s^0} < 5216$ MeV and the right hand side *RHS* sideband 5516 MeV $< m_{B_s^0}$. Typically the fitting code runs from 5150 MeV $< m_{B_s^0} <$ 5650 MeV, but this is changed to specific regions to gain insight into the mass dependence of f_{prompt}, $f_{indirect}$, τ_{fast} and τ_{slow}. By changing the limits of the fit to isolate a specific region, it is possible to examine the makeup of the events within this specific region. Beginning with an initial study, looking at a default fit, the LHS and the RHS, and comparing the four target parameters, we get the following Table 6.16:

		LHS, $m_{B_s^0} < 5216$ MeV		5000 MeV $< m_{B_s^0} <$ 5800 MeV		*RHS*, 5516 MeV $< m_{B_s^0}$	
Parameter	units	value	error	value	error	value	error
τ_{fast}	ps	0.2541	0.0016	0.2075	0.0487	0.1844	0.0009
τ_{slow}	ps	1.6734	0.0088	1.5135	0.1491	1.5156	0.0113
f_{prompt}	N/A	0.5707	0.0029	0.5011	0.1160	0.6813	0.0024
$f_{indirect}$	N/A	0.3102	0.0020	0.5154	0.0785	0.1351	0.0012

Table 6.16: A comparison of f_{prompt}, $f_{indirect}$, τ_{fast} and τ_{slow} across three mass fitting regions.

From Table 6.16, it is seen that τ_{fast} and τ_{slow} are both larger on the LHS, in the lower mass region, while there is more direct background in the higher mass region on the RHS. Additionally, f_{prompt} increases by about 0.11 when compared with the value from the low mass sideband to the higher mass sideband, while $f_{indirect}$ decreases by about 0.16, over half its original value. This is evidence enough to further divide these regions of interest to try to see what is happening in each of the sidebands and, moreover, in the available mass window as a whole. Now seven new regions of interest are defined, three in the LHS and four in the RHS, as follows:

1. L1: 5018 MeV $< m_{B_s^0} <$ 5084 MeV
2. L2: 5084 MeV $< m_{B_s^0} <$ 5150 MeV
3. L3: 5150 MeV $< m_{B_s^0} <$ 5216 MeV
4. R1: 5518 MeV $< m_{B_s^0} <$ 5584 MeV
5. R2: 5584 MeV $< m_{B_s^0} <$ 5650 MeV
6. R3: 5650 MeV $< m_{B_s^0} <$ 5716 MeV
7. R4: 5716 MeV $< m_{B_s^0} <$ 5782 MeV

These are seven ranges that each incrementally change by 66 MeV, beginning from the signal fringe of the sideband outwards, getting further from the signal region. An extra 2 MeV has been added to the RHS as this would achieve equal widths for all the tested bins. For clarity within the tables, regions will be referred to by their shortened names, eg L1, not the full mass ranges. The results of the left hand side regions are shown in Table 6.17 and the right hand side regions are shown in Table 6.18.

Within Tables 6.17 and 6.18, a trend is observed for all four parameters, shifting with respect to mass; this is best seen in Figure 6.25. While assuming a linear relationship between mass and these four parameters is perhaps an oversimplification, it is appropriate for the aim of this study, with the goal to

		L1		L2		L3	
Parameter	units	value	error	value	error	value	error
τ_{fast}	ps	0.2930	0.0018	0.2730	0.0017	0.2542	0.0016
τ_{slow}	ps	1.7408	0.0082	1.7174	0.0084	1.6735	0.0088
f_{prompt}	N/A	0.5385	0.0026	0.5567	0.0027	0.5707	0.0028
$f_{indirect}$	N/A	0.3463	0.0020	0.3292	0.0020	0.3102	0.0020

Table 6.17: A comparison of the four fitting parameters, f_{prompt}, $f_{indirect}$, τ_{fast} and τ_{slow} across the three left sideband mass regions of interest.

		R1		R2		R3		R4	
Parameter	units	value	error	value	error	value	error	value	error
τ_{fast}	ps	0.1877	0.0013	0.1804	0.0012	0.1722	0.0012	0.1626	0.0012
τ_{slow}	ps	1.5077	0.0146	1.5249	0.0186	1.4690	0.0223	1.3979	0.0252
f_{prompt}	N/A	0.6739	0.0034	0.6897	0.0035	0.7024	0.0036	0.7075	0.0037
$f_{indirect}$	N/A	0.1571	0.0018	0.1087	0.0016	0.0793	0.0015	0.0638	0.0014

Table 6.18: A comparison of the four fitting parameters, f_{prompt}, $f_{indirect}$, τ_{fast} and τ_{slow} across the four right sideband mass regions of interest.

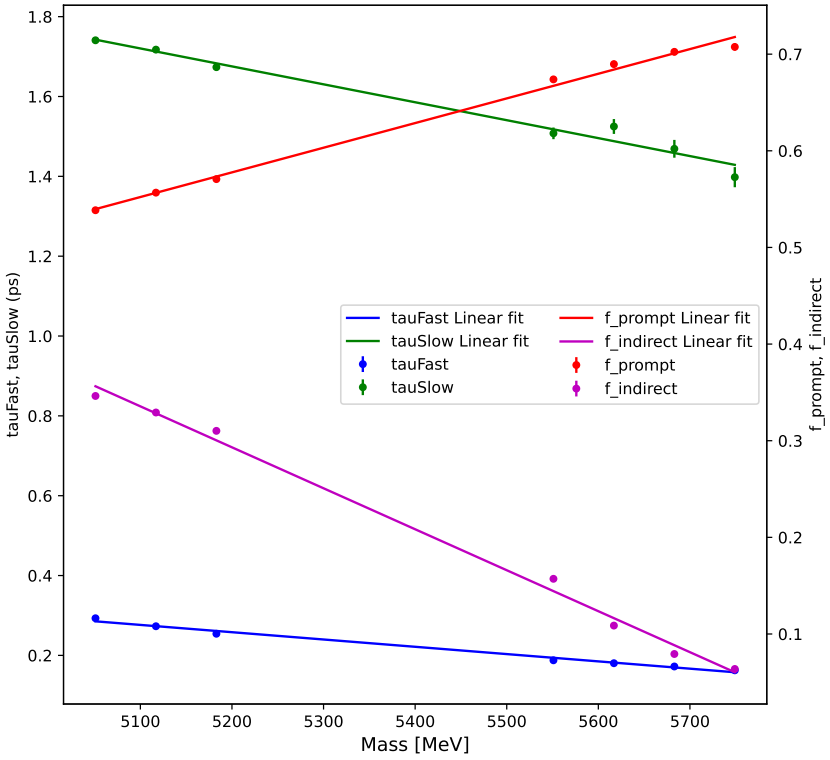

Figure 6.25: A comparison plot of the four fit parameters f_{prompt}, $f_{indirect}$, τ_{fast} and τ_{slow} as a function of mass across seven mass regions of interest. Linear fits (solid lines) are shown for each parameter. The left vertical axis corresponds to τ_{fast} and τ_{slow} values, while the right vertical axis displays f_{prompt}, $f_{indirect}$ values.

determine whether a mass dependence exists at all. A linear model provides the most straightforward approach to answer whether there is a mass dependence and is appropriate for finding "if" there is a mass dependence.

There is a mass dependence for all of the parameters investigated f_{prompt}, $f_{indirect}$, τ_{fast} and τ_{slow}. Reading out the slope and intercept, it is possible to get a rudimentary estimate for the mass relationship of these parameters, displayed in Table 6.19.

In short, all four of the parameters have a mass dependence, looking at both

Parameter	Units	Slope	Slope Error	Intercept	Intercept Error
τ_{fast}	ps	-1.827E-04	8.301E-06	1.208E+00	4.506E-02
τ_{slow}	ps	-4.493E-04	3.193E-05	4.012E+00	4.506E-02
f_{prompt}	N/A	2.551E-04	8.609E-06	-7.490E-01	4.674E-02
$f_{indirect}$	N/A	-8.240E-04	1.409E-05	2.498E+00	7.646E-02

Table 6.19: A comparison of τ_{fast}, τ_{slow}, f_{prompt} and $f_{indirect}$ across the four right sideband regions.

Figure 6.25 and Table 6.19.

It is expected that both of the τ parameters will be directly affected by mass, as mass is directly related to the lifetime of particles, with heavier particles having shorter lifetimes. This is supported by Equation 6.23, where the mass of the B_s^0 meson candidate relates to the proper decay time linearly. There is also an inverse mass dependence on the transverse momentum of the B_s^0 meson candidate. Given that the majority of the momentum will be in the longitudinal plane, it is evident that there is an expected mass dependence of the proper decay time. This is supported in Figure 6.25 and Table 6.19 with both of the τ parameters having mass dependence. As expected, τ_{fast} shows less mass dependence than τ_{slow} because τ_{fast} models faster decaying particles and prompt background within a narrower mass window. While the τ_{slow} model models the longer lifetime background, which will encompass a greater range of lifetimes, and as such will have a higher mass dependence, this again is supported by Figure 6.24. So the question now shifts, becoming, "how much are the τ parameters affected by mass?", and "would accounting for this affect make a tangible difference to the overall Γ result?".

There is less substantial support for the expectation of the mass dependence of f_{prompt} and $f_{indirect}$ than that of the τ parameters. Despite a less mathematical foundation, it is still possible to have an expectation for the distribution of f_{prompt} and $f_{indirect}$ based on their physical interpretation. Firstly, an inverse relationship between f_{prompt} and $f_{indirect}$; this is logical as fractional measurements are being

observed, so if one fraction of a whole increases, the other must decrease. Secondly, it is expected that there are higher f_{prompt} values in higher mass regions because f_{prompt} is defined as direct production from high-energy proton-proton collisions and fragmentation processes. These energetic processes are more likely to generate higher-mass particles. While it is expected that the signal region is dominated by signal, the mass region as a whole is less understood, with the sidebands containing background processes that interfere with the physics goals of the analysis.

Examining Figure 6.25, as predicted, f_{prompt} does increase in the higher mass regions, and the relationship is somewhat inversely proportional to $f_{indirect}$. This relationship is not directly inversely proportional, as from Table 6.19, the gradients are not simply the negative of each other. Notably, the $f_{indirect}$ decreases approximately four times quicker than f_{prompt} increases. Suggesting that what was measured does not match the current understanding and needs to be better understood specifically within the higher mass regions. This is supported by the sum of f_{prompt} and $f_{indirect}$, with the LHS sum being roughly 0.88, while on the RHS it is only 0.80, leaving an additional 8% of the background unaccounted for between these two parameters.

6.19 Conclusions and Future Work

To conclude, while there is a mass dependence seen in all of the four examined parameters, f_{prompt}, $f_{indirect}$, τ_{fast} and τ_{slow}, given the time constraints of the PhD, it was not possible to pursue this further. This will continue to be examined by the ATLAS collaboration along, along with addressing "what type of mass dependence is present?" and "how much will this affect the overall Γ result?". Both questions are important in the context of the wider research, isolating an accurate Γ allows for more precise determination of CP-violation.

The analysis in this section focuses on the ATLAS Run 2 dataset. Also underway by the analysis team is the Run 2 with partial Run 3 dataset analysis. The addition

of the partial Run 3 dataset introduces new technical challenges of its own; again, the consistency of the year-on-year datasets will need to be evaluated. The addition of more data should also increase the statistics available to the analysis team, with Run 2 having a recorded luminosity of 147 fb^{-1}, and Run 3 has already, as of January 2025, recorded 183 fb^{-1}. As mentioned in Section 2.2, with a higher luminosity, there are more collisions taking place, which results in more data with an increased number of rare processes.

A new tagger will be introduced for the partial Run 3 analysis. This tagger will exploit the same-side tagging, used in combination with the already implemented opposite-side tagging; this should increase the total number of B meson candidates available to the analysis. The motivation for this is to increase the precision on ϕ_s, the parameter which is the CP phase and hopefully sensitive to new physics.

Chapter 7

ATLAS Qualifying Project: Large Radius Tracking systematics based off Inner Detector material map variations

This chapter highlights the work undertaken for my ATLAS authorship qualifying project (AQP), for that internal note, see [181].

7.1 AQP Motivation

Within the ATLAS detector, over the course of its lifetime and indeed the duration of the data taking, there is a build-up of material on the detector; mass deposits from the collisions mean material can be dumped onto the detector. Simply, with more material in the detector volume, the mechanics of interactions change; as such, a precise understanding of the detector material map is crucial. Another of the potential areas for uncertainty surrounding the material map, is the engineering tolerances, the pieces of the detector are made to a certain tolerance, but across the whole detector with "over 92 million pixels and almost 2000 detector elements" and

"over 4,000 modules of 6 million 'micro-strips' of silicon sensors" [182] among other high volume detector components these uncertainties can add up.

This qualification task produced a combined performance (CP) tool that takes the input of a 2D histogram comparing the production radius against the $|\eta|$ as an output from the Athena python package, `runIDPVM.py`. The 2D output histogram should be processed by the tracking recommendations plotting code, which will rebin it based on what the user needs.

7.2 AQP Description

The AQP, was defined as follows: the uncertainty on the ID material needs to be evaluated for *Large Radius Tracking* (LRT) tracks in release 22. Release 22 was the updated internal software release for ATLAS in January 2022 when the AQP was set. This complements the study of V0 decays. This update to the uncertainty on the ID material is a straightforward comparison of the efficiency derived from MC (via ID Phys Val monitoring) from several samples. This study is on the critical path for the first LRT track reconstruction efficiency systematic [183].

7.3 ATLAS Inner Detector

This section touches on the specifics of the Inner Detector (ID) for the AQP and reiterates points from Chapter 2. The ATLAS detector has undergone upgrades for Run 3; however, the ID has not changed significantly compared with Run 2. Once sufficient data has been accumulated from Run 3, the material budget will be specified more precisely using data-driven methods, as this is only an MC comparison. The inner detector is used to measure the momentum of charged particles, its η - ϕ coverage includes the full azimuthal $-\pi < 0 < \pi$ radians and the pseudorapidity range $|\eta| < 2.5$. The inner detector uses a silicon pixel detector (Pixel), a silicon microstrip tracker (SCT) and a transition radiation tracker (TRT).

For Run3, there were only minor upgrades to the ID, as ATLAS already had a major change of the ID in 2015, by introducing the innermost pixel layer, the Insertable B Layer (IBL).

7.4 ATLAS Inner Detector Tracking

The following paragraphs are an excerpt from the ATLAS NOTE titled "Improved Track Reconstruction Performance for Long-lived Particles in ATLAS", [184], which aptly describes ATLAS Tracking and the need for Large Radius Tracking. The standard ATLAS track reconstruction algorithm is optimized for reconstructing tracks that originate in the vicinity of the primary interaction point (IP), and is not efficient for reconstructing tracks that are displaced by more than 5 mm from the IP due to tight selections placed on the transverse and longitudinal impact parameters. Thus, to reconstruct displaced tracks originating from the decays of long-lived particles (LLPs), a secondary large-radius tracking (LRT) algorithm [185] is used, which improves the ATLAS track reconstruction efficiency for a larger particle lifetime range.

The LRT reconstruction is performed after the standard ATLAS track reconstruction, taking as input the hits that are unassociated with standard tracks. It follows the same reconstruction strategy as the standard tracking, but with modified selections that are tuned to achieve improved performance for reconstructing displaced particles, most notably on the maximally allowed values of the transverse and longitudinal impact parameters ($d0$ and $z0$). With relaxed selection cuts of 300 mm on $|d_0|$ and 500 mm on $|z_0|$, the LRT algorithm can reconstruct charged particles at efficiencies greater than 75% for production radii of 300 mm or less.[184].

7.5 Two Processes

As described in Section 7.2, there are multiple samples needed to undertake this AQP. There were two physics processes used within the Monte Carlo samples used. The first was a Higgs to Axial Axial (HAA) decay chain, decaying hadronically. This would be most suitable for the study, as this study involves the inner detector where hadronic decays most commonly happen. The particles were generated with a decay distance: $c\tau = 100$ mm, allowing efficient study of LRT tracking performance.

Also available was a Heavy Neutral Lepton (HNL) sample, in which heavy neutral leptons decay with $c\tau = 100$ mm while there are also direct muons from W, which would be covered by standard tracking. The complete list of samples used is given in Appendix D.1.

7.6 Material Maps

To further the requirements of this AQP, there are also different material maps needed to accurately model the material variations. The material maps are as follows:

- **Nominal:** The current understanding of how much material is in the Inner Detector.
- **+5% Overall:** The nominal sample is now contains 5% more material.
- **+10% IBL:** The Insertable B-Layer has 10% more material than the nominal sample.
- **+25% PP0:** The PP0 corresponds to the Patch Panel 0, which in this model has 25% more material than the nominal sample.
- **QGSP_BIC:** This is an alternative physics model split into two parts. The "QGSP" refers to applying the Quark Gluon String model, which is used for high-energy interactions of protons, neutrons, pions, kaons and nuclei. The

"BIC" portion of the name refers to an extension of the QGSP, in which Geant4 [49] uses binary cascades for primary protons and neutrons with energies below 10 GeV. This model uses the same detector geometry as the nominal sample.

Now, with the two physics samples and the five material map variations, the material budget study was undertaken.

7.7 Production of the systematics

The five Monte Carlo datasets available were processed by `runIDPVM.py`, producing output files for analysis. `runIDPVM.py` is a python Athena program designed for inner detector physics validation.

7.7.1 Example command ran

An example of a command run in `runIDPVM.py` is as follows

```
runIDPVM.py --filesInput " /path/to/your/input/file/AOD.root "
--doLargeD0Tracks --doMergedLargeD0Tracks --ancestorIDList 36
--outputFile output_file_name.root
```

This code has been split from one line into three lines, so when running this command, please make sure to run it all on one line. To explain the command in more detail, the following flags:

- `--filesInput`

  Specify the input file(s) location. To use multiple input files within the same directory, the * wildcard is available.

- `--doLargeD0Tracks`

  This flag turns on LRT, which is not on by default. This allows large d_0 tracks to be included in the output.

- `--doMergedLargeD0Tracks`

  Produces the Merged tracks container, including both Nominal and LRT reconstructed tracks.

- `--ancestorIDList`

  Is the Particle Data Group Identification (PDGID) [186] of the mother particle, from which the decay then happens. The PDG is an international collaboration which complies and reanalyses published particle physics results and theories. Where 36 is the ancestor identification for the HAA sample and 50 is the ancestor identification for the HNL sample, with an incorrect ancestor identification, the reconstruction will not work.

- `--outputFile`

  Is the name of the output file and location, `runIDPVM.py` produces .root output files.

Whilst there are a multitude of other potential flags, those listed are the ones used in this material budget. All available MC samples were used in this study. Details of the samples are given in Appendix D.1.

7.7.2 Determination of Systematic and Uncertainties

Two main equations were used, the first is Equation 7.1. which takes the track reconstruction efficiency for each variation (+5% Overall, +10% IBL, +25% PP0, and QGSP_BIC) and compares it to the nominal sample for the chosen parameter. Note that the error in track reconstruction efficiency is propagated using the python uncertainties package [187], which becomes the error on total systematic uncertainty.

$$\text{Systematic}_i = 1 - \frac{\text{Variation}_i}{\text{Nominal}} \tag{7.1}$$

Equation 7.2 shows how the systematic for each sample was added for a Total Systematic Uncertainty, where the subscripts denote different variation samples

being used.

$$\text{Total Systematic Uncertainty} = \sqrt{\text{Sys}_i{}^2 + \text{Sys}_j{}^2 + \text{Sys}_k{}^2 + \text{Sys}_l{}^2} \tag{7.2}$$

7.8 AQP Results

Systematics due to uncertainties of material maps and hadron interaction modes were studied for LRT. The following plots have been prepared using LRT. One dimensional efficiencies and systematics are produced for the following list of variables: pt, eta, abs_eta, mu, phi, d0, abs_d0, z0, abs_z0, R, Z, mu, ext_d0, abs_ext_d0, ext_Z0, abs_ext_Z0, prodR, prodZ, ext_prodZ, pt_log. The English spelling for the Greek symbols has been used, as this is how they appear within the code.

7.8.1 2D Efficiencies and Systematics

The first figure, Figure 7.1, shows the nominal material map LRT track reconstruction efficiency per bin in the 2D production radius vs η. Looking at the extremities in η, the range has been extended past 2.5 to 3; this was a change consciously made within the code. The extension of η was done to check that the systematic uncertainties were not diluted due to statistics in a low event phase space. Looking at the first increment, up to 25 mm, in production radius, the LRT tracking takes over past 5 mm, where a lot of tracks are, so LRT performs poorly below 5 mm. This has an overall effect on the track reconstruction efficiency in this section of the plot. It would be expected that a 5 mm $\rightarrow$ 25 mm bin would have a higher track reconstruction efficiency than the full 0 mm $\rightarrow$ 25 mm bin. However, given the scale of this plot in production radius, a 5 mm bin would not be visually coherent.

The most effective track reconstruction region is between $-1.5\eta \rightarrow 1.5\eta$. This is due to the higher number of tracks in this region, as well as the LRT being in its "most comfortable" state, being mostly what the LRT is specifically designed for. Generally, the higher the production radius, the lower the track reconstruction

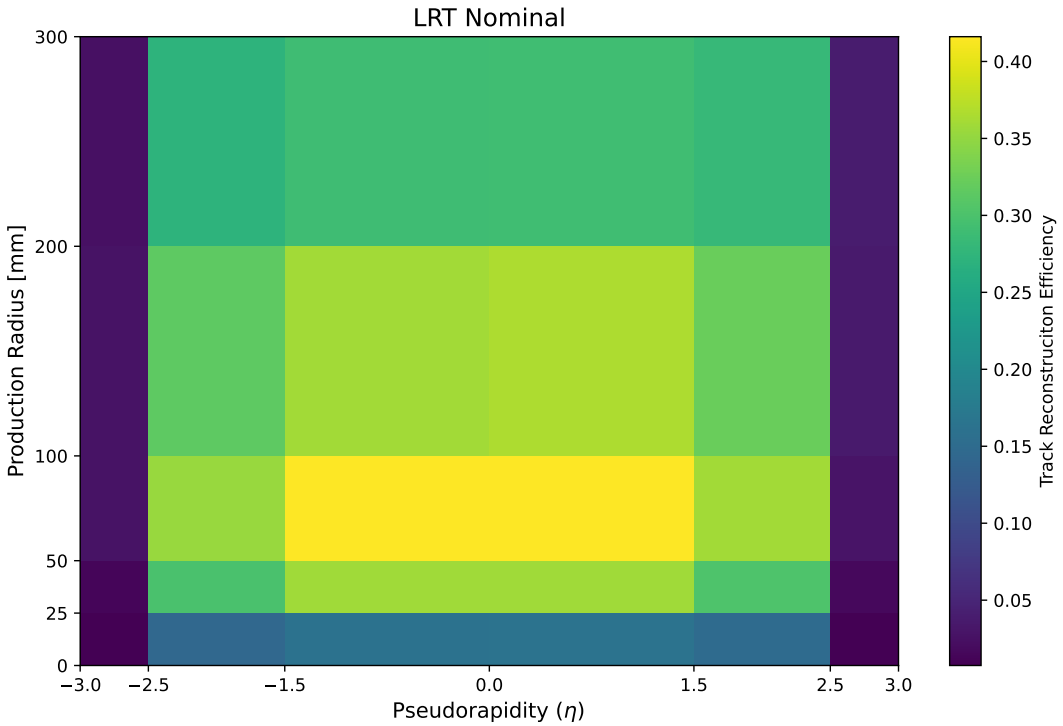

Figure 7.1: Nominal Material Map 2D LRT track reconstruction efficiency.

efficiency; similarly, the higher the η value, the worse the performance of track reconstruction.

There are also the four material map variations, so the four plots in Figure 7.2, are the ratio plots, referring back to Equation 7.1. Here, it is possible to draw a comparison on performance relative to the nominal tracking, so the alternative geometry will show negative values when the variation outperforms the nominal, conversely, positive values when the nominal geometry performs better.

The four variations in Figure 7.2 are used and combined using Equation 7.2 to create a final systematic map, shown in Figure 7.3.

Figure 7.3 is a collection of the total systematic uncertainty for the production radius vs η phase space. The total systematic is calculated using Equation 7.2 and the errors are propagated through using the python uncertainties package [187]. The majority of this plot is close to zero in value; this is a good thing, suggesting that there is little difference in the material maps. Given this is non-zero, it may be

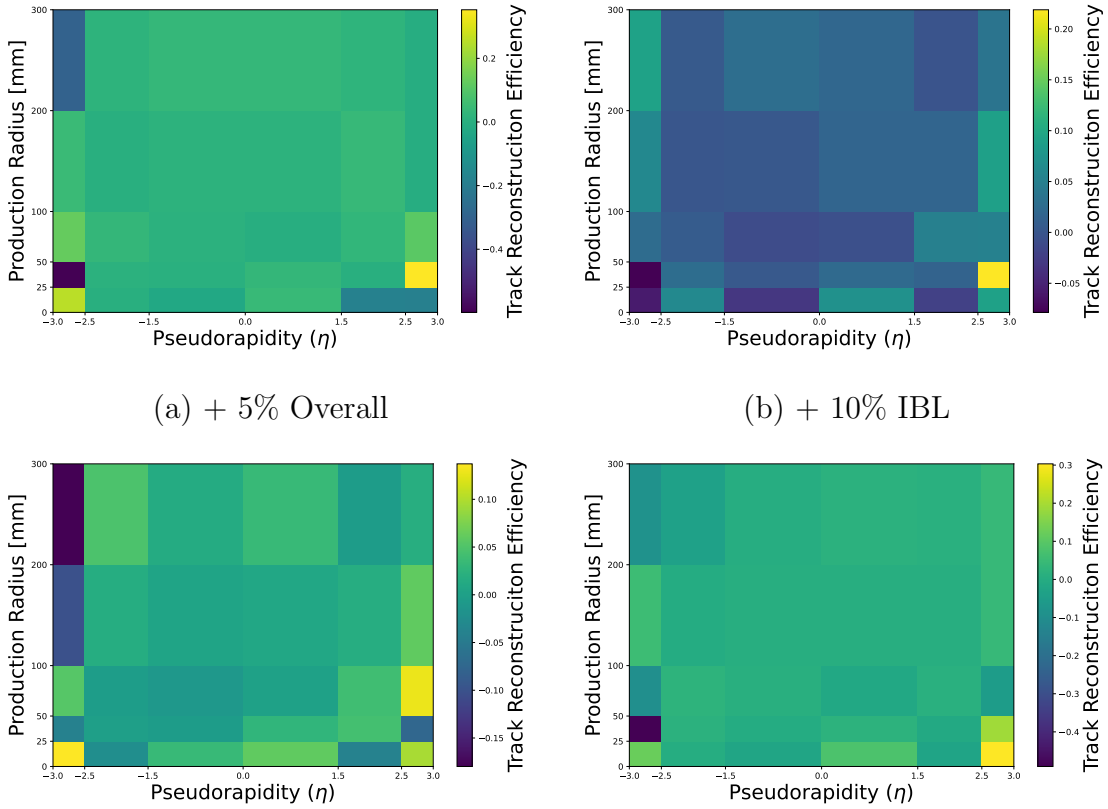

(a) + 5% Overall

(b) + 10% IBL

(c) + 25% PP0

(d) QGSP_BIC

Figure 7.2: 1-Ratio plot using Equation 7.1, LRT track reconstruction efficiency ratio, plots for all of the 4 material maps described in Section 7.6.

useful for users.

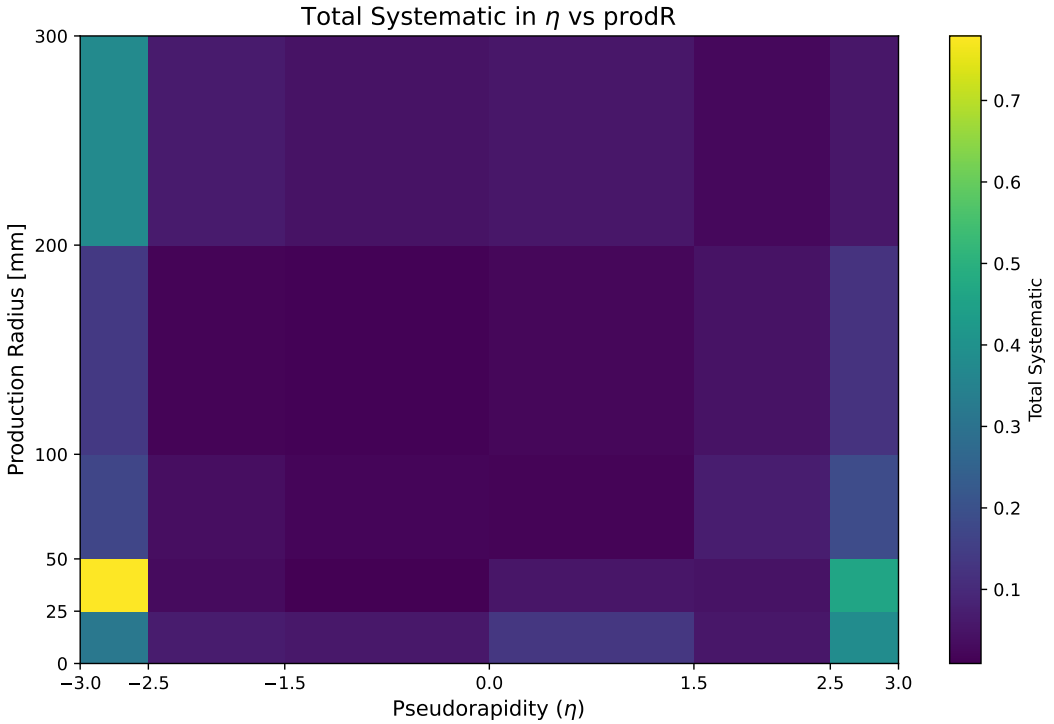

Figure 7.3: A total systematic uncertainty for the *prodR_vs_η*, with the errors propagated through coming from the original error in track reconstruction efficiency.

7.8.2 1D Efficiencies and Systematics

Users can also gain insight from the 1D plots from runIDPVM.py, as described in Section 7.9. Figure 7.4 is an example of a 1D Efficiency plot produced with the corresponding systematic for $|\eta|$. In Figure 7.4, part *a* (LHS) is the track reconstruction efficiency as a function of $|\eta|$, and part *b* (RHS) shows the appropriate systematic, calculated with Equation 7.1. As expected, the higher the $|\eta|$ value, the lower track reconstruction efficiency, this is due to both the low statistics and the fact that the higher the η value the more crowded the tracks in the detector are, so it is easier for the LRT algorithm to incorrectly reconstruct a track at this extreme. Similarly, there is more divergence between material maps with the increasing $|\eta|$ value; this is perhaps due to the nature of the material maps diverging in this area.

Figure 7.5 part *a* (LHS) is the track reconstruction efficiency as a function of

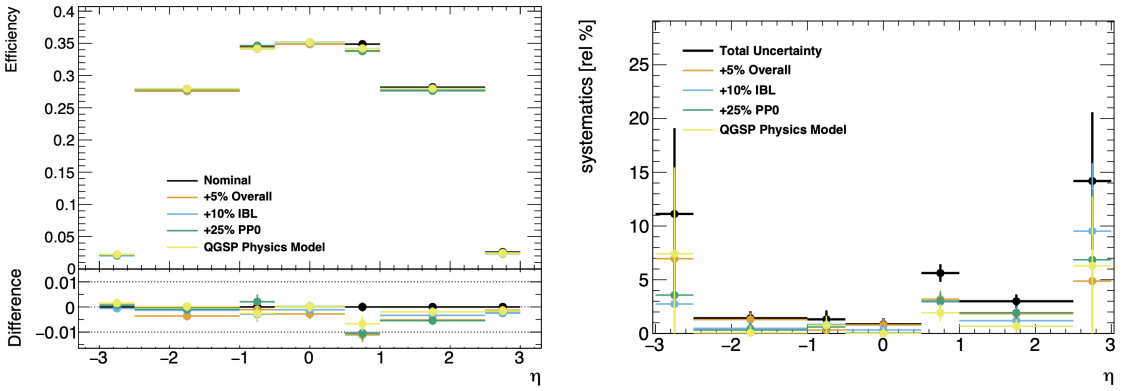

(a) Track Reconstruction Efficiency

(b) Systematic Uncertainty

Figure 7.4: Track Reconstruction Efficiency and Systematic due to material map variations for η.

production radius and part *b* (RHS) shows the appropriate systematic, calculated with Equation 7.1. With very small production radii, there are a lot of processes going on in such a concentrated area of the detector. As such, the reconstruction efficiency is not optimal as the algorithm is overloaded. As the tracks become less concentrated around 50 mm (roughly the end of the B-Layer), there is an increase in the track reconstruction efficiency, peaking at 75 mm before falling off. This decline is expected given the sparsity of events with large production radii.

Figure 7.6 part *a* (LHS) is the track reconstruction efficiency as a function of d_0 and part *b* (RHS) shows the appropriate systematic, calculated with Equation 7.1. LRT is by definition used when $d_0 > 5$ mm, so it is expected that the first bin is dominated by the poor handling of the tracks below 5 mm. The LRT performs best early on in d_0, as this is where the majority of use cases will be and thus is more optimised for this space. As with previous parameters, the LRT track reconstruction struggles with the larger parameter space, in this instance for large d_0. The systematic uncertainty is dominated by the divergence of material maps with agreement around 5% up until 100 mm.

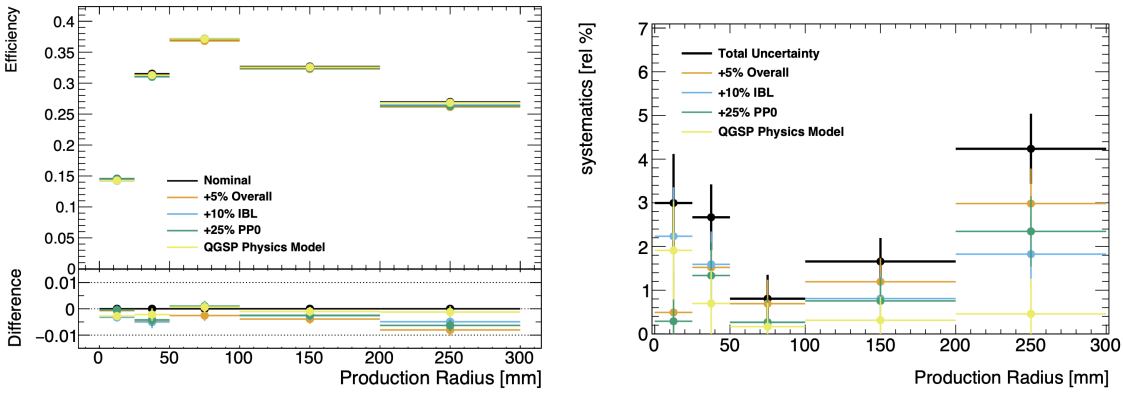

(a) Track Reconstruction Efficiency (b) Systematic Uncertainty

Figure 7.5: Track Reconstruction Efficiency and Systematic due to material map variations for production radius.

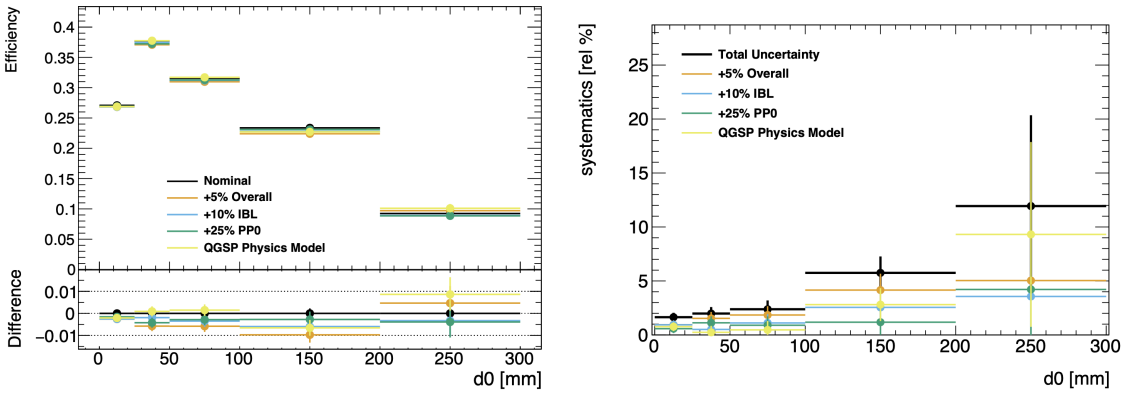

(a) Track Reconstruction Efficiency (b) Systematic Uncertainty

Figure 7.6: Track Reconstruction Efficiency and Systematic due to material map variations for d_0.

7.9 Material Map Study Conclusion

This study has evaluated the uncertainty on the inner detector material for LRT tracks in Release 22. To characterise the effect of material map variations, a comprehensive systematic evaluation was performed and made available to the ATLAS collaboration.

Systematics due to uncertainties of material maps and hadron interaction modes were studied. Combined systematics values and their respective errors are provided in terms of two-dimensional maps across various parameter spaces: $|\eta|$ vs. extended production radius, $|\eta|$ vs. production radius, $|d_0|$ vs. $|\eta|$, $|\eta|$ vs. p_{T}, η vs. production radius, η vs. extended production radius, d_0 vs. η, extended_d_0 vs. η, extended_$|d_0|$ vs. η, and extended_$|d_0|$ vs. $|\eta|$. Additionally, one-dimensional systematic plots are available, providing values for individual types of material uncertainties. These tools have been designed to allow users to apply them to their own datasets and derive their parameter-specific systematics of choice.

The framework has been integrated into Athena as part of the tracking recommendations package and is available to ATLAS users through the ATLAS Git pages [47]. This systematic evaluation provides ATLAS users with the necessary tools to successfully account for inner detector material uncertainties in their analyses, specifically when involving LRT tracks where material effects can have significant impact on tracking performance.

Chapter 8

Conclusions and Further Work

In this thesis, four main investigations took place, three in Chapter 6 surrounding CP violation in the $B_s^0 \to J/\psi\phi$ decay channel, specifically Evaluating the mass sideband choice, 6.16, Using sPlot and sWeight for background rejection, 6.17 and a Study of mass-time correlations in B_s^0 meson background 6.18, and one in Chapter 7 around the systematics in large radius tracking due to material map variations. Each investigation will be discussed chronologically as they appeared in the thesis and summarised before a discussion of possible future directions for this work.

8.0.1 Mass sideband investigation

The first investigation was evaluating the mass sideband choice in Section 6.16. Using three Punzi models the mass fit limits of each Punzi model were tested outside their projected use range. The performance of these models outside their intended range was investigated to avoid overspecialising the Punzi models to the data and ensuring they could correctly account for signal and multiple backgrounds. There was varying performance shown between the models, indicating sufficient change between them, while still all being able to be used for their intended purpose.

Evaluating the performance of these three models, it was found that the refined Punzi would be the most suitable model for the analysis. However due to the introduction of new systematic uncertainties with a new model, this refined Punzi

was not used for this analysis, but will be used in future analyses.

The work presented in this section has lead to a wider investigation about the suitability of Punzis, including introducing 2D Punzi models which could aid the $B_s^0 \to J/\psi\phi$ analysis in future.

8.0.2 sPlot as a background rejection method

The second investigation was using sPlot as an updated background rejection method, as described in Section 6.17. sPlot is a statistical technique for untangling distributions through statistical methods. This could be suitable for a mass distribution as there are multiple sources of events and being able to statistically disentangle these would improve the systematics around the result.

Tests and comparisons were made across multiple dataset as the goal was to improve performance and refine the measurement of the Γ parameter. sPlot was found to provide minimal improvement to the Γ result, as with the Punzi method, it was rejected, due to the increased workload with the time investment needed to overhaul the systematic uncertainty calculations not deemed worthwile with the pressures of publication deadlines. sPlot is under consideration for inclusion within the further analyses of this work.

8.0.3 Mass-time correlations

The third investigation was into mass-time correlations surrounding currently unfitted parameters in the main maximum likelihood fit as discussed in Section 6.12, and the investigation outlined in Section 6.18. Often within particle physics analyses, there are compromises around computation time with accurate modelling and marginal gains. One such example is the improved number of fitted parameters going from 9 parameters in the partial Run 2 iteration of the $B_s^0 \to J/\psi\phi$ analysis to the 11 fitted parameters for the Full Run 2 analysis. There are many more parameters involved in a fit, assumed constant or mass-independent, including f_{prompt}, $f_{indirect}$, τ_{fast} and τ_{slow} parameters.

This investigation split the background distribution into seven mass regions, three on the lower mass LHS, and four on the higher mass RHS, the asymmetric three vs four was due to the signal region not being directly in the centre of the mass window available. It was found that all four parameters display a mass dependence and will be further investigated for the overall impact on the Γ parameter.

8.0.4 $B_s^0 \to J/\psi\phi$ investigations

The CP violation present in the $B_s^0 \to J/\psi\phi$ decay is motivation for the work performed in this thesis. Investigating CP violation can help understanding the matter-antimatter asymmetry seen within the universe.

The the $B_s^0 \to J/\psi\phi$ decay is known to involve CP violation so could be a good source for this phenomena. Precise measurement of the Γ parameter enables accurate determination of the B_s^0 meson lifetime, a crucial step toward better isolating CP violation and potentially unlocking new theories or mechanisms that can explain the matter-antimatter asymmetry.

8.1 Systematic uncertainty due to material map variations at ATLAS

There are systematic uncertainties within the ATLAS experiment relating to the (mis)modelling of the material maps. The uncertainty of the model stems from the engineering tolerances and the constant bombardment of high energy particles resulting in both material deposits and breakages.

Four variations of the material map were compared to the nominal material map. This resulted in the creation of a performance tool that can be used by ATLAS analysts to calculate material map variations for their specific analysis. This work was part of the wider push within the ATLAS collaboration to improve involvement with Combined-Performance tasks from users and not just to focus on analysis work.

This work used ATLAS software release 22, which at the time was the current release. This systematic uncertainty must be updated for each subsequent software release.

Appendix A

Complete list of Triggers for the analysis

A.1 ATLAS Triggers used in the analysis

Below is a list of the specific ATLAS triggers ued in the $B_s^0 \to J/\psi\phi$ analysis. These triggers are split between each year, although 2016 has been split into multiple sections due to the trigger menu issues mentioned in Section 6.17.2.2 of Chapter 6.

2015 Data:

HLT_2mu4_bJpsimumu_noL2

HLT_mu6_mu4_bBmumuxv2

HLT_mu18_2mu0noL1_JpsimumuFS

Data 2016 Main Stream Early runs:

HLT_mu6_mu4_bBmumuxv2

HLT_2mu6_bBmumuxv2

HLT_mu10_mu6_bBmumuxv2

HLT_mu20_2mu0noL1_JpsimumuFS

HLT_mu10_mu6_bJpsimumu

HLT_mu6_mu4_bJpsimumu

Data 2016 Main Stream Late runs:

HLT_2mu4_bJpsimumu_L1BPH_2M8_2MU4

HLT_2mu10_bBmumuxv2

HLT_2mu6_bBmumux_BsmumuPhi_L1BPH_2M9_2MU6_BPH_2DR15_2MU6

HLT_mu20_2mu0noL1_JpsimumuFS

HLT_2mu6_bBmumuxv2

HLT_mu6_mu4_bBmumuxv2

HLT_mu10_mu6_bBmumuxv2

HLT_3mu4_bDimu

HLT_mu20_nomucomb_mu6noL1_nscan03

HLT_mu6_mu4_bJpsimumu_L12MU4_B

HLT_mu4_mu4_idperf_bJpsimumu_noid

HLT_3mu6_msonly

HLT_2mu6_bDimu

HLT_mu6_mu4_bBmumux_BsmumuPhi_L1BPH_2M8_MU6MU4_BPH_0DR15_MU6MU4

HLT_mu20_2mu4_JpsimumuL2

HLT_mu6_mu4_bJpsimumu

HLT_2mu4_bBmumux_BsmumuPhi_L1BPH_2M8_2MU4

Data 2016 delayed stream:

HLT_mu6_mu4_bBmumuxv2_delayed

HLT_2mu6_bBmumuxv2_delayed

HLT_mu6_mu4_bBmumux_BsmumuPhi_delayed_L1BPH_2M8_MU6MU4_BPH_0DR15_MU6MU4

HLT_2mu4_bBmumux_BsmumuPhi_delayed_L1BPH_2M8_2MU4

HLT_mu6_mu4_bBmumux_BsmumuPhi_delayed

HLT_mu6_2mu4_bJpsi_delayed

HLT_mu6_nomucomb_2mu4_nomucomb_delayed_L1MU6_3MU4

HLT_mu6_mu4_bJpsimumu_delayed

Data 2017 Main and delayed stream:

HLT_mu6_mu4_bBmumux_BsmumuPhi_L1BPH_2M9_MU6MU4_BPH_0DR15_MU6MU4

HLT_mu11_mu6_bDimu

HLT_2mu6_bJpsimumu_L1BPH_2M9_2MU6_BPH_2DR15_2MU6

HLT_mu20_2mu2noL1_JpsimumuFS

HLT_3mu4_bDimu

HLT_2mu6_bBmumuxv2_L1LFV_MU6

HLT_mu11_2mu4noL1_bNocut_L1MU11_2MU6

HLT_mu22_mu8noL1

HLT_2mu6_bJpsimumu

HLT_mu20_2mu4_JpsimumuL2

HLT_2mu4_mu3_mu2noL1_bNocut_L13MU4

HLT_mu6_mu4_bBmumuxv2

HLT_2mu4_invm1_j20_xe40_pufit_2dphi10_L12MU4_J20_XE30_DPHI_J20s2XE30

HLT_3mu4

HLT_3mu6_msonly

HLT_2mu14

Data 2018 Main and delayed stream:

HLT_mu6_mu4_bBmumux_BsmumuPhi_L1BPH_2M9_MU6MU4_BPH_0DR15_MU6MU4

HLT_2mu4_bBmumux_BsmumuPhi_L1BPH_2M9_2MU4_BPH_0DR15_2MU4

HLT_2mu6_bJpsimumu_L1BPH_2M9_2MU6_BPH_2DR15_2MU6

HLT_2mu6_bBmumuxv2_L1LFV_MU6

HLT_2mu6_bBmumux_BsmumuPhi_L1BPH_2M9_2MU6_BPH_2DR15_2MU6

HLT_2mu6_bBmumux_BpmumuKp_L1BPH_2M9_2MU6_BPH_2DR15_2MU6

HLT_mu11_mu6_bDimu

HLT_mu11_mu6_bBmumuxv2

HLT_mu11_mu6_bDimu_L1LFV_MU11

HLT_mu11_mu6_bBmumuxv2_L1LFV_MU11

HLT_mu11_mu6_bJpsimumu

HLT_mu11_mu6_bJpsimumu_L1LFV_MU11

HLT_mu6_mu4_bJpsimumu_Lxy0_L1BPH_2M9_MU6MU4_BPH_0DR15_MU6MU4

HLT_2mu6_bJpsimumu_Lxy0_L1BPH_2M9_2MU6_BPH_2DR15_2MU6

HLT_mu11_mu6_bBmumux_BpmumuKp

HLT_mu11_mu6_bBmumux_BpmumuKp_L1LFV_MU11

HLT_mu11_mu6_bDimu_Lxy0

HLT_mu11_mu6_bDimu_Lxy0_L1LFV_MU11

HLT_mu11_mu6_bJpsimumu_Lxy0

HLT_mu11_mu6_bJpsimumu_Lxy0_L1LFV_MU11

Appendix B

Checking the validity of the Γ Fitting

B.1 Checking the validity of the Γ Fitting

Continuing from Section 6.17.2.1 and to briefly summarise, the "fit2_data_sb_2018" fit result found a local minima and not a global minima, this is evidenced by the following figures which introduce the $\Delta\Gamma$ parameter which compares the difference between the two lifetimes, and the Γ_{L-H} parameter which introduces a comparison between the light mass state and the heavy mass state.

From both of these figures, the "fit2_data_sb_2018" is result highlighted, compared to the more normal fitted results. For Figure B.1 the error values in the figure are "nan" supporting the idea that this is an error in the function of the fitting code. As for Figure B.2, probably the best evidence for the failure of the fitting code, demonstrated in the plot is both the heavy state decay width on the left and the light state decay width on the right. Given the light state decay width is actually smaller than the smallest alternative heavy state decay width, the conclusion is that either the fit found a local minima and thus incorrectly finished the fit, or the fit generally failed. This can be investigated further by examining the log file. The first cause for concern is the sheer size of the log file, with it being

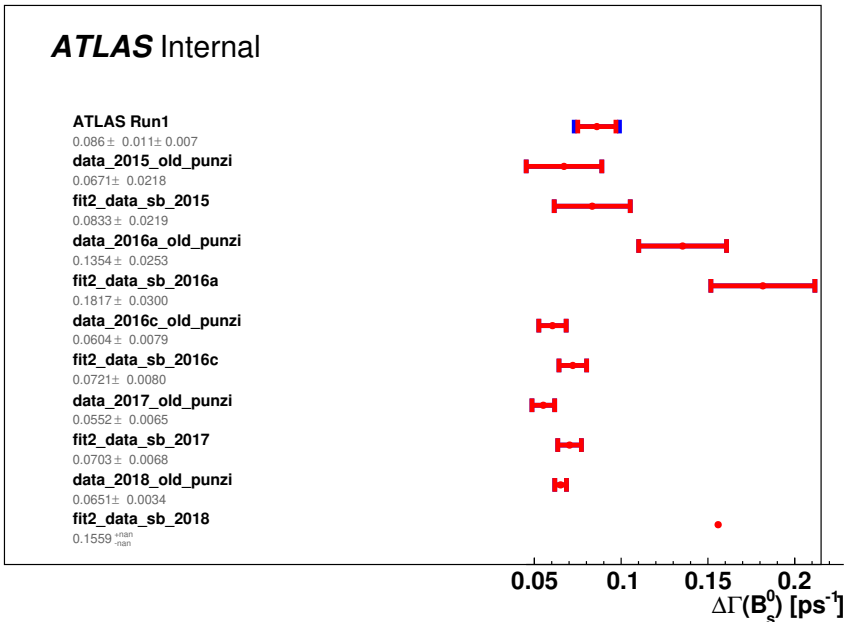

Figure B.1: ATLAS internal result. Comparing $\Delta\Gamma$ parameter fit results for the sideband fits against the previously ran fits for different sub data samples form 2015 to 2018.

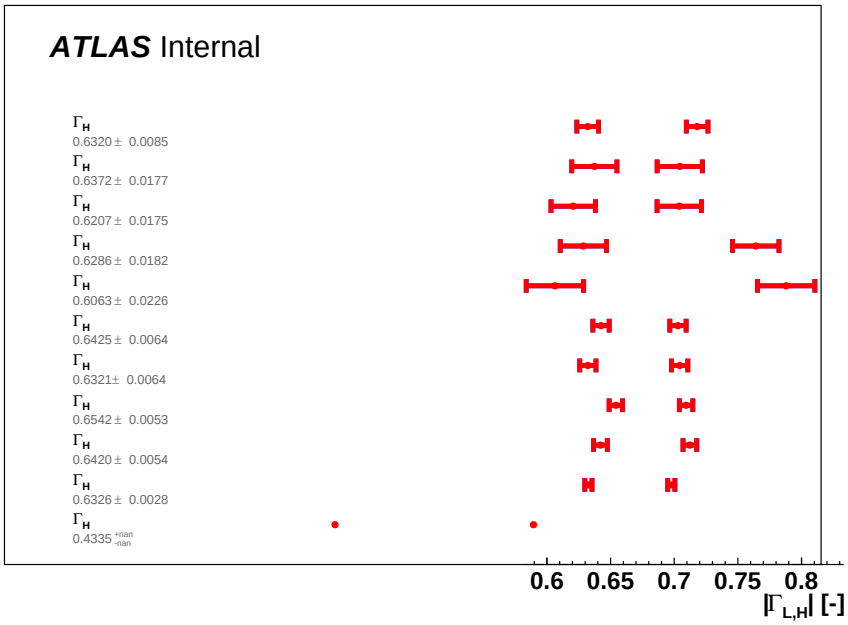

Figure B.2: ATLAS internal result. Comparing Γ_{L-H} parameter fit results for the sideband fits against the previously ran fits for different sub data samples form 2015 to 2018.

121 MB compared to the more typical 0.5 MB. The fit results and final outputs are examined in the table B.1 below.

fit2_data_sb_2018 fit results from the log file	
Fit status	(0) CALL LIMIT
Hesse status	(0) not run
fcn:	-inf

Table B.1: results from the fit2_data_sb_2018 fit log file.

Reviewing the table, it is clear to see that the fit did not work at all, and hence the anomalous result is in fact erroneous.

Appendix C

1D log-likelihood scans

C.1 Five Renaming Variables for the 1D log-likelihood scans

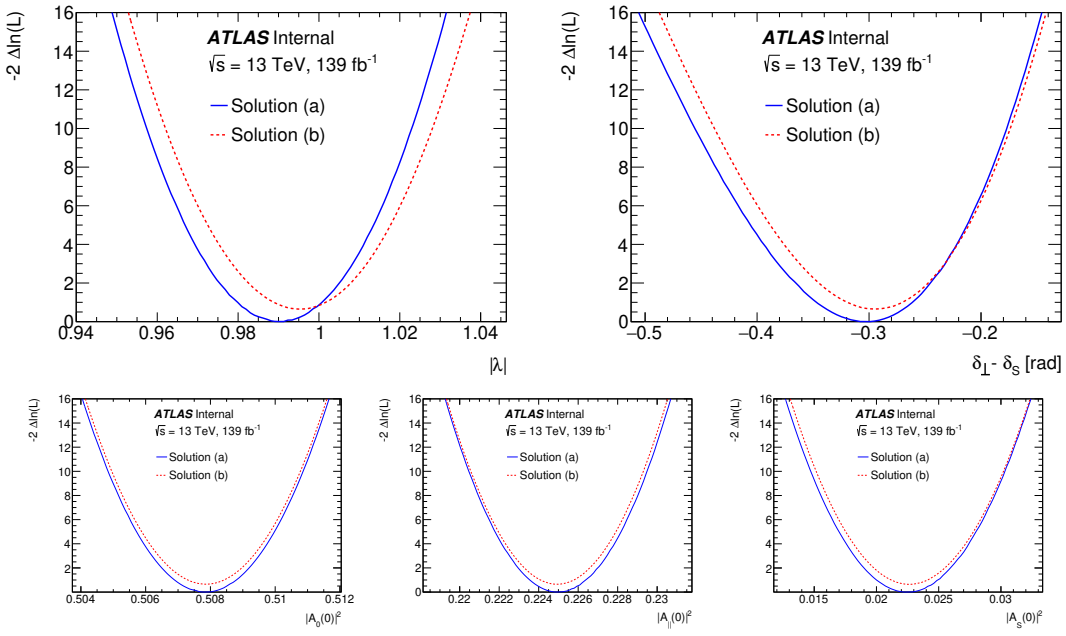

Figure C.1: ATLAS internal result. 1D log-likelihood scans of the remaining five variables of the fit ($|\lambda|$, $\delta_{\parallel} - \delta_{\perp}$, A_0, $A_{\parallel}$, and A_s) for the primary minimum (blue) and the secondary minimum (red). The variable on vertical axis, $2\Delta\ln(\mathcal{L}) = 2(\ln(L^G) - \ln(L^i))$, is a difference between the likelihood values of a default fit, L^G, and of the fit in which the physical parameter is fixed to a value shown on horizontal axis.

Appendix D

AQP: Full list of Samples

Below is a complete list of the MC simulation files used in the material map systematic uncertainty study. These were produced by the ATLAS MC Production team and were processed for this specific use case.

D.1 HAA samples used

D.1.1 HAA Nominal

```
mc20_13TeV.312939.PowhegPythia8EvtGen_ZH_H125_a35a35_4b_ctau100.reco
↪ n.AOD.e7962_e5984_s3126_r13051_r13474/AOD.29256833._000001.pool.
↪ root.1
mc20_13TeV.312939.PowhegPythia8EvtGen_ZH_H125_a35a35_4b_ctau100.reco
↪ n.AOD.e7962_e5984_s3126_r13051_r13474/AOD.29256833._000002.pool.
↪ root.1
mc20_13TeV.312939.PowhegPythia8EvtGen_ZH_H125_a35a35_4b_ctau100.reco
↪ n.AOD.e7962_e5984_s3126_r13051_r13474/AOD.29256833._000003.pool.
↪ root.1
mc20_13TeV.312939.PowhegPythia8EvtGen_ZH_H125_a35a35_4b_ctau100.reco
↪ n.AOD.e7962_e5984_s3126_r13051_r13474/AOD.29256833._000004.pool.
↪ root.1
```

```
mc20_13TeV.312939.PowhegPythia8EvtGen_ZH_H125_a35a35_4b_ctau100.reco
↪ n.AOD.e7962_e5984_s3126_r13051_r13474/AOD.29256833._000005.pool.
↪ root.1
mc20_13TeV.312939.PowhegPythia8EvtGen_ZH_H125_a35a35_4b_ctau100.reco
↪ n.AOD.e7962_e5984_s3126_r13051_r13474/AOD.29256833._000006.pool.
↪ root.1
mc20_13TeV.312939.PowhegPythia8EvtGen_ZH_H125_a35a35_4b_ctau100.reco
↪ n.AOD.e7962_e5984_s3126_r13051_r13474/AOD.29256833._000007.pool.
↪ root.1
mc20_13TeV.312939.PowhegPythia8EvtGen_ZH_H125_a35a35_4b_ctau100.reco
↪ n.AOD.e7962_e5984_s3126_r13051_r13474/AOD.29256833._000008.pool.
↪ root.1
mc20_13TeV.312939.PowhegPythia8EvtGen_ZH_H125_a35a35_4b_ctau100.reco
↪ n.AOD.e7962_e5984_s3126_r13051_r13474/AOD.29256833._000009.pool.
↪ root.1
mc20_13TeV.312939.PowhegPythia8EvtGen_ZH_H125_a35a35_4b_ctau100.reco
↪ n.AOD.e7962_e5984_s3126_r13051_r13474/AOD.29256833._000010.pool.
↪ root.1
mc20_13TeV.312939.PowhegPythia8EvtGen_ZH_H125_a35a35_4b_ctau100.reco
↪ n.AOD.e7962_e5984_s3126_r13051_r13474/AOD.29256833._000011.pool.
↪ root.1
mc20_13TeV.312939.PowhegPythia8EvtGen_ZH_H125_a35a35_4b_ctau100.reco
↪ n.AOD.e7962_e5984_s3126_r13051_r13474/AOD.29256833._000012.pool.
↪ root.1
mc20_13TeV.312939.PowhegPythia8EvtGen_ZH_H125_a35a35_4b_ctau100.reco
↪ n.AOD.e7962_e5984_s3126_r13051_r13474/AOD.29256833._000013.pool.
↪ root.1
```

```
mc20_13TeV.312939.PowhegPythia8EvtGen_ZH_H125_a35a35_4b_ctau100.reco⌋
↪ n.AOD.e7962_e5984_s3126_r13051_r13474/AOD.29256833._000014.pool.⌋
↪ root.1
mc20_13TeV.312939.PowhegPythia8EvtGen_ZH_H125_a35a35_4b_ctau100.reco⌋
↪ n.AOD.e7962_e5984_s3126_r13051_r13474/AOD.29256833._000015.pool.⌋
↪ root.1
mc20_13TeV.312939.PowhegPythia8EvtGen_ZH_H125_a35a35_4b_ctau100.reco⌋
↪ n.AOD.e7962_e5984_s3126_r13051_r13474/AOD.29256833._000016.pool.⌋
↪ root.1
mc20_13TeV.312939.PowhegPythia8EvtGen_ZH_H125_a35a35_4b_ctau100.reco⌋
↪ n.AOD.e7962_e5984_s3126_r13051_r13474/AOD.29256839._000001.pool.⌋
↪ root.1
mc20_13TeV.312939.PowhegPythia8EvtGen_ZH_H125_a35a35_4b_ctau100.reco⌋
↪ n.AOD.e7962_e5984_s3126_r13051_r13474/AOD.29256839._000002.pool.⌋
↪ root.1
mc20_13TeV.312939.PowhegPythia8EvtGen_ZH_H125_a35a35_4b_ctau100.reco⌋
↪ n.AOD.e7962_e5984_s3126_r13051_r13474/AOD.29256839._000003.pool.⌋
↪ root.1
mc20_13TeV.312939.PowhegPythia8EvtGen_ZH_H125_a35a35_4b_ctau100.reco⌋
↪ n.AOD.e7962_e5984_s3126_r13051_r13474/AOD.29256839._000004.pool.⌋
↪ root.1
mc20_13TeV.312939.PowhegPythia8EvtGen_ZH_H125_a35a35_4b_ctau100.reco⌋
↪ n.AOD.e7962_e5984_s3126_r13051_r13474/AOD.29256853._000001.pool.⌋
↪ root.1
mc20_13TeV.312939.PowhegPythia8EvtGen_ZH_H125_a35a35_4b_ctau100.reco⌋
↪ n.AOD.e7962_e5984_s3126_r13051_r13474/AOD.29256853._000002.pool.⌋
↪ root.1
```

```
mc20_13TeV.312939.PowhegPythia8EvtGen_ZH_H125_a35a35_4b_ctau100.reco
↪ n.AOD.e7962_e5984_s3126_r13051_r13474/AOD.29256853._000003.pool.
↪ root.1
mc20_13TeV.312939.PowhegPythia8EvtGen_ZH_H125_a35a35_4b_ctau100.reco
↪ n.AOD.e7962_e5984_s3126_r13051_r13474/AOD.29256853._000004.pool.
↪ root.1
mc20_13TeV.312939.PowhegPythia8EvtGen_ZH_H125_a35a35_4b_ctau100.reco
↪ n.AOD.e7962_e5984_s3126_r13051_r13474/AOD.29256853._000005.pool.
↪ root.1
mc20_13TeV.312939.PowhegPythia8EvtGen_ZH_H125_a35a35_4b_ctau100.reco
↪ n.AOD.e7962_e5984_s3126_r13051_r13474/AOD.29256853._000006.pool.
↪ root.1
mc20_13TeV.312939.PowhegPythia8EvtGen_ZH_H125_a35a35_4b_ctau100.reco
↪ n.AOD.e7962_e5984_s3126_r13051_r13474/AOD.29256853._000007.pool.
↪ root.1
mc20_13TeV.312939.PowhegPythia8EvtGen_ZH_H125_a35a35_4b_ctau100.reco
↪ n.AOD.e7962_e5984_s3126_r13051_r13474/AOD.29256853._000008.pool.
↪ root.1
mc20_13TeV.312939.PowhegPythia8EvtGen_ZH_H125_a35a35_4b_ctau100.reco
↪ n.AOD.e7962_e5984_s3126_r13051_r13474/AOD.29256853._000009.pool.
↪ root.1
mc20_13TeV.312939.PowhegPythia8EvtGen_ZH_H125_a35a35_4b_ctau100.reco
↪ n.AOD.e7962_e5984_s3126_r13051_r13474/AOD.29256853._000010.pool.
↪ root.1
mc20_13TeV.312939.PowhegPythia8EvtGen_ZH_H125_a35a35_4b_ctau100.reco
↪ n.AOD.e7962_e5984_s3126_r13051_r13474/AOD.29256853._000011.pool.
↪ root.1
```

```
mc20_13TeV.312939.PowhegPythia8EvtGen_ZH_H125_a35a35_4b_ctau100.reco
↪ n.AOD.e7962_e5984_s3126_r13051_r13474/AOD.29256853._000012.pool.
↪ root.1
mc20_13TeV.312939.PowhegPythia8EvtGen_ZH_H125_a35a35_4b_ctau100.reco
↪ n.AOD.e7962_e5984_s3126_r13051_r13474/AOD.29256853._000013.pool.
↪ root.1
mc20_13TeV.312939.PowhegPythia8EvtGen_ZH_H125_a35a35_4b_ctau100.reco
↪ n.AOD.e7962_e5984_s3126_r13051_r13474/AOD.29256853._000014.pool.
↪ root.1
mc20_13TeV.312939.PowhegPythia8EvtGen_ZH_H125_a35a35_4b_ctau100.reco
↪ n.AOD.e7962_e5984_s3126_r13051_r13474/AOD.29256853._000015.pool.
↪ root.1
mc20_13TeV.312939.PowhegPythia8EvtGen_ZH_H125_a35a35_4b_ctau100.reco
↪ n.AOD.e7962_e5984_s3126_r13051_r13474/AOD.29256853._000016.pool.
↪ root.1
mc20_13TeV.312939.PowhegPythia8EvtGen_ZH_H125_a35a35_4b_ctau100.reco
↪ n.AOD.e7962_e5984_s3126_r13051_r13474/AOD.29256853._000017.pool.
↪ root.1
mc20_13TeV.312939.PowhegPythia8EvtGen_ZH_H125_a35a35_4b_ctau100.reco
↪ n.AOD.e7962_e5984_s3126_r13051_r13474/AOD.29256853._000018.pool.
↪ root.1
mc20_13TeV.312939.PowhegPythia8EvtGen_ZH_H125_a35a35_4b_ctau100.reco
↪ n.AOD.e7962_e5984_s3126_r13051_r13474/AOD.29256853._000019.pool.
↪ root.1
mc20_13TeV.312939.PowhegPythia8EvtGen_ZH_H125_a35a35_4b_ctau100.reco
↪ n.AOD.e7962_e5984_s3126_r13051_r13474/AOD.29256853._000020.pool.
↪ root.1
```

```
mc20_13TeV.312939.PowhegPythia8EvtGen_ZH_H125_a35a35_4b_ctau100.reco
↪ n.AOD.e7962_e5984_s3126_r13051_r13474/AOD.29256853._000021.pool.
↪ root.1
mc20_13TeV.312939.PowhegPythia8EvtGen_ZH_H125_a35a35_4b_ctau100.reco
↪ n.AOD.e7962_e5984_s3126_r13051_r13474/AOD.29256853._000022.pool.
↪ root.1
mc20_13TeV.312939.PowhegPythia8EvtGen_ZH_H125_a35a35_4b_ctau100.reco
↪ n.AOD.e7962_e5984_s3126_r13051_r13474/AOD.29256853._000023.pool.
↪ root.1
mc20_13TeV.312939.PowhegPythia8EvtGen_ZH_H125_a35a35_4b_ctau100.reco
↪ n.AOD.e7962_e5984_s3126_r13051_r13474/AOD.29256853._000024.pool.
↪ root.1
mc20_13TeV.312939.PowhegPythia8EvtGen_ZH_H125_a35a35_4b_ctau100.reco
↪ n.AOD.e7962_e5984_s3126_r13051_r13474/AOD.29256853._000025.pool.
↪ root.1
mc20_13TeV.312939.PowhegPythia8EvtGen_ZH_H125_a35a35_4b_ctau100.reco
↪ n.AOD.e7962_e5984_s3126_r13051_r13474/AOD.29256853._000026.pool.
↪ root.1
mc20_13TeV.312939.PowhegPythia8EvtGen_ZH_H125_a35a35_4b_ctau100.reco
↪ n.AOD.e7962_e5984_s3126_r13051_r13474/AOD.29256853._000027.pool.
↪ root.1
mc20_13TeV.312939.PowhegPythia8EvtGen_ZH_H125_a35a35_4b_ctau100.reco
↪ n.AOD.e7962_e5984_s3126_r13051_r13474/AOD.29256853._000028.pool.
↪ root.1
mc20_13TeV.312939.PowhegPythia8EvtGen_ZH_H125_a35a35_4b_ctau100.reco
↪ n.AOD.e7962_e5984_s3126_r13051_r13474/AOD.29256853._000029.pool.
↪ root.1
```

```
mc20_13TeV.312939.PowhegPythia8EvtGen_ZH_H125_a35a35_4b_ctau100.reco
↪ n.AOD.e7962_e5984_s3126_r13051_r13474/AOD.29256853._000030.pool.
↪ root.1
```

D.1.2 HAA 5% Overall

```
mc20_13TeV.312939.PowhegPythia8EvtGen_ZH_H125_a35a35_4b_ctau100.reco
↪ n.AOD.e7962_e5984_s3155_s3833_r13625_r13629_r13625/AOD.29203965.
↪ _000007.pool.root.1
mc20_13TeV.312939.PowhegPythia8EvtGen_ZH_H125_a35a35_4b_ctau100.reco
↪ n.AOD.e7962_e5984_s3155_s3833_r13625_r13629_r13625/AOD.29203965.
↪ _000008.pool.root.1
mc20_13TeV.312939.PowhegPythia8EvtGen_ZH_H125_a35a35_4b_ctau100.reco
↪ n.AOD.e7962_e5984_s3155_s3833_r13625_r13629_r13625/AOD.29203965.
↪ _000009.pool.root.1
mc20_13TeV.312939.PowhegPythia8EvtGen_ZH_H125_a35a35_4b_ctau100.reco
↪ n.AOD.e7962_e5984_s3155_s3833_r13625_r13629_r13625/AOD.29203965.
↪ _000010.pool.root.1
mc20_13TeV.312939.PowhegPythia8EvtGen_ZH_H125_a35a35_4b_ctau100.reco
↪ n.AOD.e7962_e5984_s3155_s3833_r13625_r13629_r13625/AOD.29203965.
↪ _000015.pool.root.1
mc20_13TeV.312939.PowhegPythia8EvtGen_ZH_H125_a35a35_4b_ctau100.reco
↪ n.AOD.e7962_e5984_s3155_s3833_r13625_r13629_r13625/AOD.29203965.
↪ _000017.pool.root.1
mc20_13TeV.312939.PowhegPythia8EvtGen_ZH_H125_a35a35_4b_ctau100.reco
↪ n.AOD.e7962_e5984_s3155_s3833_r13625_r13629_r13625/AOD.29203965.
↪ _000018.pool.root.1
mc20_13TeV.312939.PowhegPythia8EvtGen_ZH_H125_a35a35_4b_ctau100.reco
↪ n.AOD.e7962_e5984_s3155_s3833_r13625_r13629_r13625/AOD.29203965.
↪ _000021.pool.root.1
```

```
mc20_13TeV.312939.PowhegPythia8EvtGen_ZH_H125_a35a35_4b_ctau100.reco
↪ n.AOD.e7962_e5984_s3155_s3833_r13625_r13629_r13625/AOD.29203965.
↪ _000022.pool.root.1
mc20_13TeV.312939.PowhegPythia8EvtGen_ZH_H125_a35a35_4b_ctau100.reco
↪ n.AOD.e7962_e5984_s3155_s3833_r13625_r13629_r13625/AOD.29203965.
↪ _000023.pool.root.1
mc20_13TeV.312939.PowhegPythia8EvtGen_ZH_H125_a35a35_4b_ctau100.reco
↪ n.AOD.e7962_e5984_s3155_s3833_r13625_r13629_r13625/AOD.29203965.
↪ _000024.pool.root.1
mc20_13TeV.312939.PowhegPythia8EvtGen_ZH_H125_a35a35_4b_ctau100.reco
↪ n.AOD.e7962_e5984_s3155_s3833_r13625_r13629_r13625/AOD.29203965.
↪ _000025.pool.root.1
mc20_13TeV.312939.PowhegPythia8EvtGen_ZH_H125_a35a35_4b_ctau100.reco
↪ n.AOD.e7962_e5984_s3155_s3833_r13625_r13629_r13625/AOD.29203965.
↪ _000026.pool.root.1
mc20_13TeV.312939.PowhegPythia8EvtGen_ZH_H125_a35a35_4b_ctau100.reco
↪ n.AOD.e7962_e5984_s3155_s3833_r13625_r13629_r13625/AOD.29203965.
↪ _000027.pool.root.1
mc20_13TeV.312939.PowhegPythia8EvtGen_ZH_H125_a35a35_4b_ctau100.reco
↪ n.AOD.e7962_e5984_s3155_s3833_r13625_r13629_r13625/AOD.29203965.
↪ _000028.pool.root.1
mc20_13TeV.312939.PowhegPythia8EvtGen_ZH_H125_a35a35_4b_ctau100.reco
↪ n.AOD.e7962_e5984_s3155_s3833_r13625_r13629_r13625/AOD.29203965.
↪ _000029.pool.root.1
mc20_13TeV.312939.PowhegPythia8EvtGen_ZH_H125_a35a35_4b_ctau100.reco
↪ n.AOD.e7962_e5984_s3155_s3833_r13625_r13629_r13625/AOD.29203965.
↪ _000030.pool.root.1
```

```
mc20_13TeV.312939.PowhegPythia8EvtGen_ZH_H125_a35a35_4b_ctau100.reco
↪ n.AOD.e7962_e5984_s3155_s3833_r13625_r13629_r13625/AOD.29203965.
↪ _000031.pool.root.1
mc20_13TeV.312939.PowhegPythia8EvtGen_ZH_H125_a35a35_4b_ctau100.reco
↪ n.AOD.e7962_e5984_s3155_s3833_r13625_r13629_r13625/AOD.29203965.
↪ _000032.pool.root.1
mc20_13TeV.312939.PowhegPythia8EvtGen_ZH_H125_a35a35_4b_ctau100.reco
↪ n.AOD.e7962_e5984_s3155_s3833_r13625_r13629_r13625/AOD.29203965.
↪ _000033.pool.root.1
```

D.1.3 HAA +10% IBL

```
mc20_13TeV.312939.PowhegPythia8EvtGen_ZH_H125_a35a35_4b_ctau100.reco
↪ n.AOD.e7962_e5984_s3156_s3833_r13626_r13630_r13626/AOD.29203969.
↪ _000003.pool.root.1
mc20_13TeV.312939.PowhegPythia8EvtGen_ZH_H125_a35a35_4b_ctau100.reco
↪ n.AOD.e7962_e5984_s3156_s3833_r13626_r13630_r13626/AOD.29203969.
↪ _000004.pool.root.1
mc20_13TeV.312939.PowhegPythia8EvtGen_ZH_H125_a35a35_4b_ctau100.reco
↪ n.AOD.e7962_e5984_s3156_s3833_r13626_r13630_r13626/AOD.29203969.
↪ _000005.pool.root.1
mc20_13TeV.312939.PowhegPythia8EvtGen_ZH_H125_a35a35_4b_ctau100.reco
↪ n.AOD.e7962_e5984_s3156_s3833_r13626_r13630_r13626/AOD.29203969.
↪ _000006.pool.root.1
mc20_13TeV.312939.PowhegPythia8EvtGen_ZH_H125_a35a35_4b_ctau100.reco
↪ n.AOD.e7962_e5984_s3156_s3833_r13626_r13630_r13626/AOD.29203969.
↪ _000007.pool.root.1
```

```
mc20_13TeV.312939.PowhegPythia8EvtGen_ZH_H125_a35a35_4b_ctau100.reco
↪ n.AOD.e7962_e5984_s3156_s3833_r13626_r13630_r13626/AOD.29203969.
↪ _000008.pool.root.1
mc20_13TeV.312939.PowhegPythia8EvtGen_ZH_H125_a35a35_4b_ctau100.reco
↪ n.AOD.e7962_e5984_s3156_s3833_r13626_r13630_r13626/AOD.29203969.
↪ _000009.pool.root.1
mc20_13TeV.312939.PowhegPythia8EvtGen_ZH_H125_a35a35_4b_ctau100.reco
↪ n.AOD.e7962_e5984_s3156_s3833_r13626_r13630_r13626/AOD.29203969.
↪ _000010.pool.root.1
mc20_13TeV.312939.PowhegPythia8EvtGen_ZH_H125_a35a35_4b_ctau100.reco
↪ n.AOD.e7962_e5984_s3156_s3833_r13626_r13630_r13626/AOD.29203969.
↪ _000011.pool.root.1
mc20_13TeV.312939.PowhegPythia8EvtGen_ZH_H125_a35a35_4b_ctau100.reco
↪ n.AOD.e7962_e5984_s3156_s3833_r13626_r13630_r13626/AOD.29203969.
↪ _000012.pool.root.1
mc20_13TeV.312939.PowhegPythia8EvtGen_ZH_H125_a35a35_4b_ctau100.reco
↪ n.AOD.e7962_e5984_s3156_s3833_r13626_r13630_r13626/AOD.29203969.
↪ _000013.pool.root.1
mc20_13TeV.312939.PowhegPythia8EvtGen_ZH_H125_a35a35_4b_ctau100.reco
↪ n.AOD.e7962_e5984_s3156_s3833_r13626_r13630_r13626/AOD.29203969.
↪ _000014.pool.root.1
mc20_13TeV.312939.PowhegPythia8EvtGen_ZH_H125_a35a35_4b_ctau100.reco
↪ n.AOD.e7962_e5984_s3156_s3833_r13626_r13630_r13626/AOD.29203969.
↪ _000015.pool.root.1
mc20_13TeV.312939.PowhegPythia8EvtGen_ZH_H125_a35a35_4b_ctau100.reco
↪ n.AOD.e7962_e5984_s3156_s3833_r13626_r13630_r13626/AOD.29203969.
↪ _000016.pool.root.1
```

```
mc20_13TeV.312939.PowhegPythia8EvtGen_ZH_H125_a35a35_4b_ctau100.reco
↪ n.AOD.e7962_e5984_s3156_s3833_r13626_r13630_r13626/AOD.29203969.
↪ _000017.pool.root.1
mc20_13TeV.312939.PowhegPythia8EvtGen_ZH_H125_a35a35_4b_ctau100.reco
↪ n.AOD.e7962_e5984_s3156_s3833_r13626_r13630_r13626/AOD.29203969.
↪ _000018.pool.root.1
mc20_13TeV.312939.PowhegPythia8EvtGen_ZH_H125_a35a35_4b_ctau100.reco
↪ n.AOD.e7962_e5984_s3156_s3833_r13626_r13630_r13626/AOD.29203969.
↪ _000019.pool.root.1
mc20_13TeV.312939.PowhegPythia8EvtGen_ZH_H125_a35a35_4b_ctau100.reco
↪ n.AOD.e7962_e5984_s3156_s3833_r13626_r13630_r13626/AOD.29203969.
↪ _000020.pool.root.1
mc20_13TeV.312939.PowhegPythia8EvtGen_ZH_H125_a35a35_4b_ctau100.reco
↪ n.AOD.e7962_e5984_s3156_s3833_r13626_r13630_r13626/AOD.29203969.
↪ _000021.pool.root.1
mc20_13TeV.312939.PowhegPythia8EvtGen_ZH_H125_a35a35_4b_ctau100.reco
↪ n.AOD.e7962_e5984_s3156_s3833_r13626_r13630_r13626/AOD.29203969.
↪ _000022.pool.root.1
```

D.1.4 HAA +25 % PP0

```
mc20_13TeV.312939.PowhegPythia8EvtGen_ZH_H125_a35a35_4b_ctau100.reco
↪ n.AOD.e7962_e5984_s3818_s3833_r13627_r13631_r13627AOD.29203973._
↪ 000001.pool.root.1
mc20_13TeV.312939.PowhegPythia8EvtGen_ZH_H125_a35a35_4b_ctau100.reco
↪ n.AOD.e7962_e5984_s3818_s3833_r13627_r13631_r13627AOD.29203973._
↪ 000002.pool.root.1
```

```
mc20_13TeV.312939.PowhegPythia8EvtGen_ZH_H125_a35a35_4b_ctau100.reco⌋
↪ n.AOD.e7962_e5984_s3818_s3833_r13627_r13631_r13627AOD.29203973._⌋
↪ 000005.pool.root.1
mc20_13TeV.312939.PowhegPythia8EvtGen_ZH_H125_a35a35_4b_ctau100.reco⌋
↪ n.AOD.e7962_e5984_s3818_s3833_r13627_r13631_r13627AOD.29203973._⌋
↪ 000006.pool.root.1
mc20_13TeV.312939.PowhegPythia8EvtGen_ZH_H125_a35a35_4b_ctau100.reco⌋
↪ n.AOD.e7962_e5984_s3818_s3833_r13627_r13631_r13627AOD.29203973._⌋
↪ 000007.pool.root.1
mc20_13TeV.312939.PowhegPythia8EvtGen_ZH_H125_a35a35_4b_ctau100.reco⌋
↪ n.AOD.e7962_e5984_s3818_s3833_r13627_r13631_r13627AOD.29203973._⌋
↪ 000011.pool.root.1
mc20_13TeV.312939.PowhegPythia8EvtGen_ZH_H125_a35a35_4b_ctau100.reco⌋
↪ n.AOD.e7962_e5984_s3818_s3833_r13627_r13631_r13627AOD.29203973._⌋
↪ 000012.pool.root.1
mc20_13TeV.312939.PowhegPythia8EvtGen_ZH_H125_a35a35_4b_ctau100.reco⌋
↪ n.AOD.e7962_e5984_s3818_s3833_r13627_r13631_r13627AOD.29203973._⌋
↪ 000013.pool.root.1
mc20_13TeV.312939.PowhegPythia8EvtGen_ZH_H125_a35a35_4b_ctau100.reco⌋
↪ n.AOD.e7962_e5984_s3818_s3833_r13627_r13631_r13627AOD.29203973._⌋
↪ 000014.pool.root.1
mc20_13TeV.312939.PowhegPythia8EvtGen_ZH_H125_a35a35_4b_ctau100.reco⌋
↪ n.AOD.e7962_e5984_s3818_s3833_r13627_r13631_r13627AOD.29203973._⌋
↪ 000018.pool.root.1
mc20_13TeV.312939.PowhegPythia8EvtGen_ZH_H125_a35a35_4b_ctau100.reco⌋
↪ n.AOD.e7962_e5984_s3818_s3833_r13627_r13631_r13627AOD.29203973._⌋
↪ 000019.pool.root.1
```

```
mc20_13TeV.312939.PowhegPythia8EvtGen_ZH_H125_a35a35_4b_ctau100.reco⌋
↪ n.AOD.e7962_e5984_s3818_s3833_r13627_r13631_r13627AOD.29203973._⌋
↪ 000020.pool.root.1
mc20_13TeV.312939.PowhegPythia8EvtGen_ZH_H125_a35a35_4b_ctau100.reco⌋
↪ n.AOD.e7962_e5984_s3818_s3833_r13627_r13631_r13627AOD.29203973._⌋
↪ 000021.pool.root.1
mc20_13TeV.312939.PowhegPythia8EvtGen_ZH_H125_a35a35_4b_ctau100.reco⌋
↪ n.AOD.e7962_e5984_s3818_s3833_r13627_r13631_r13627AOD.29203973._⌋
↪ 000022.pool.root.1
mc20_13TeV.312939.PowhegPythia8EvtGen_ZH_H125_a35a35_4b_ctau100.reco⌋
↪ n.AOD.e7962_e5984_s3818_s3833_r13627_r13631_r13627AOD.29203973._⌋
↪ 000023.pool.root.1
mc20_13TeV.312939.PowhegPythia8EvtGen_ZH_H125_a35a35_4b_ctau100.reco⌋
↪ n.AOD.e7962_e5984_s3818_s3833_r13627_r13631_r13627AOD.29203973._⌋
↪ 000024.pool.root.1
mc20_13TeV.312939.PowhegPythia8EvtGen_ZH_H125_a35a35_4b_ctau100.reco⌋
↪ n.AOD.e7962_e5984_s3818_s3833_r13627_r13631_r13627AOD.29203973._⌋
↪ 000025.pool.root.1
mc20_13TeV.312939.PowhegPythia8EvtGen_ZH_H125_a35a35_4b_ctau100.reco⌋
↪ n.AOD.e7962_e5984_s3818_s3833_r13627_r13631_r13627AOD.29203973._⌋
↪ 000026.pool.root.1
mc20_13TeV.312939.PowhegPythia8EvtGen_ZH_H125_a35a35_4b_ctau100.reco⌋
↪ n.AOD.e7962_e5984_s3818_s3833_r13627_r13631_r13627AOD.29203973._⌋
↪ 000027.pool.root.1
mc20_13TeV.312939.PowhegPythia8EvtGen_ZH_H125_a35a35_4b_ctau100.reco⌋
↪ n.AOD.e7962_e5984_s3818_s3833_r13627_r13631_r13627AOD.29203973._⌋
↪ 000029.pool.root.1
```

D.1.5 HAA QGSP_BIC

```
mc20_13TeV.312939.PowhegPythia8EvtGen_ZH_H125_a35a35_4b_ctau100.reco
↪ n.AOD.e7962_e5984_s3819_s3833_r13628_r12253_r13628/AOD.29203977.
↪ _000009.pool.root.1
mc20_13TeV.312939.PowhegPythia8EvtGen_ZH_H125_a35a35_4b_ctau100.reco
↪ n.AOD.e7962_e5984_s3819_s3833_r13628_r12253_r13628/AOD.29203977.
↪ _000010.pool.root.1
mc20_13TeV.312939.PowhegPythia8EvtGen_ZH_H125_a35a35_4b_ctau100.reco
↪ n.AOD.e7962_e5984_s3819_s3833_r13628_r12253_r13628/AOD.29203977.
↪ _000012.pool.root.1
mc20_13TeV.312939.PowhegPythia8EvtGen_ZH_H125_a35a35_4b_ctau100.reco
↪ n.AOD.e7962_e5984_s3819_s3833_r13628_r12253_r13628/AOD.29203977.
↪ _000020.pool.root.1
mc20_13TeV.312939.PowhegPythia8EvtGen_ZH_H125_a35a35_4b_ctau100.reco
↪ n.AOD.e7962_e5984_s3819_s3833_r13628_r12253_r13628/AOD.29203977.
↪ _000021.pool.root.1
mc20_13TeV.312939.PowhegPythia8EvtGen_ZH_H125_a35a35_4b_ctau100.reco
↪ n.AOD.e7962_e5984_s3819_s3833_r13628_r12253_r13628/AOD.29203977.
↪ _000022.pool.root.1
mc20_13TeV.312939.PowhegPythia8EvtGen_ZH_H125_a35a35_4b_ctau100.reco
↪ n.AOD.e7962_e5984_s3819_s3833_r13628_r12253_r13628/AOD.29203977.
↪ _000023.pool.root.1
mc20_13TeV.312939.PowhegPythia8EvtGen_ZH_H125_a35a35_4b_ctau100.reco
↪ n.AOD.e7962_e5984_s3819_s3833_r13628_r12253_r13628/AOD.29203977.
↪ _000027.pool.root.1
mc20_13TeV.312939.PowhegPythia8EvtGen_ZH_H125_a35a35_4b_ctau100.reco
↪ n.AOD.e7962_e5984_s3819_s3833_r13628_r12253_r13628/AOD.29203977.
↪ _000028.pool.root.1
```

```
mc20_13TeV.312939.PowhegPythia8EvtGen_ZH_H125_a35a35_4b_ctau100.reco⌋
↪ n.AOD.e7962_e5984_s3819_s3833_r13628_r12253_r13628/AOD.29203977.⌋
↪ _000029.pool.root.1
mc20_13TeV.312939.PowhegPythia8EvtGen_ZH_H125_a35a35_4b_ctau100.reco⌋
↪ n.AOD.e7962_e5984_s3819_s3833_r13628_r12253_r13628/AOD.29203977.⌋
↪ _000030.pool.root.1
mc20_13TeV.312939.PowhegPythia8EvtGen_ZH_H125_a35a35_4b_ctau100.reco⌋
↪ n.AOD.e7962_e5984_s3819_s3833_r13628_r12253_r13628/AOD.29203977.⌋
↪ _000031.pool.root.1
mc20_13TeV.312939.PowhegPythia8EvtGen_ZH_H125_a35a35_4b_ctau100.reco⌋
↪ n.AOD.e7962_e5984_s3819_s3833_r13628_r12253_r13628/AOD.29203977.⌋
↪ _000032.pool.root.1
mc20_13TeV.312939.PowhegPythia8EvtGen_ZH_H125_a35a35_4b_ctau100.reco⌋
↪ n.AOD.e7962_e5984_s3819_s3833_r13628_r12253_r13628/AOD.29203977.⌋
↪ _000033.pool.root.1
mc20_13TeV.312939.PowhegPythia8EvtGen_ZH_H125_a35a35_4b_ctau100.reco⌋
↪ n.AOD.e7962_e5984_s3819_s3833_r13628_r12253_r13628/AOD.29203977.⌋
↪ _000034.pool.root.1
mc20_13TeV.312939.PowhegPythia8EvtGen_ZH_H125_a35a35_4b_ctau100.reco⌋
↪ n.AOD.e7962_e5984_s3819_s3833_r13628_r12253_r13628/AOD.29203977.⌋
↪ _000035.pool.root.1
mc20_13TeV.312939.PowhegPythia8EvtGen_ZH_H125_a35a35_4b_ctau100.reco⌋
↪ n.AOD.e7962_e5984_s3819_s3833_r13628_r12253_r13628/AOD.29203977.⌋
↪ _000036.pool.root.1
mc20_13TeV.312939.PowhegPythia8EvtGen_ZH_H125_a35a35_4b_ctau100.reco⌋
↪ n.AOD.e7962_e5984_s3819_s3833_r13628_r12253_r13628/AOD.29203977.⌋
↪ _000037.pool.root.1
```

```
mc20_13TeV.312939.PowhegPythia8EvtGen_ZH_H125_a35a35_4b_ctau100.reco
↪ n.AOD.e7962_e5984_s3819_s3833_r13628_r12253_r13628/AOD.29203977.
↪ _000038.pool.root.1
mc20_13TeV.312939.PowhegPythia8EvtGen_ZH_H125_a35a35_4b_ctau100.reco
↪ n.AOD.e7962_e5984_s3819_s3833_r13628_r12253_r13628/AOD.29203977.
↪ _000043.pool.root.1
```

D.2 HNL samples used

D.2.1 HNL Nominal

```
mc20_13TeV.311633.Pythia8EvtGen_A14NNPDF23LO_WmuHNL50_10G_lt10dd.rec
↪ on.AOD.e7422_e5984_a875_r13051_r13474/AOD.29256973._000001.pool.
↪ root.1
mc20_13TeV.311633.Pythia8EvtGen_A14NNPDF23LO_WmuHNL50_10G_lt10dd.rec
↪ on.AOD.e7422_e5984_a875_r13051_r13474/AOD.29256973._000002.pool.
↪ root.1
mc20_13TeV.311633.Pythia8EvtGen_A14NNPDF23LO_WmuHNL50_10G_lt10dd.rec
↪ on.AOD.e7422_e5984_a875_r13051_r13474/AOD.29256973._000003.pool.
↪ root.1
mc20_13TeV.311633.Pythia8EvtGen_A14NNPDF23LO_WmuHNL50_10G_lt10dd.rec
↪ on.AOD.e7422_e5984_a875_r13051_r13474/AOD.29256973._000004.pool.
↪ root.1
mc20_13TeV.311633.Pythia8EvtGen_A14NNPDF23LO_WmuHNL50_10G_lt10dd.rec
↪ on.AOD.e7422_e5984_a875_r13051_r13474/AOD.29256973._000005.pool.
↪ root.1
mc20_13TeV.311633.Pythia8EvtGen_A14NNPDF23LO_WmuHNL50_10G_lt10dd.rec
↪ on.AOD.e7422_e5984_a875_r13051_r13474/AOD.29256973._000006.pool.
↪ root.1
```

```
mc20_13TeV.311633.Pythia8EvtGen_A14NNPDF23LO_WmuHNL50_10G_lt10dd.rec
↪ on.AOD.e7422_e5984_a875_r13051_r13474/AOD.29256973._000007.pool.
↪ root.1
mc20_13TeV.311633.Pythia8EvtGen_A14NNPDF23LO_WmuHNL50_10G_lt10dd.rec
↪ on.AOD.e7422_e5984_a875_r13051_r13474/AOD.29256973._000008.pool.
↪ root.1
mc20_13TeV.311633.Pythia8EvtGen_A14NNPDF23LO_WmuHNL50_10G_lt10dd.rec
↪ on.AOD.e7422_e5984_a875_r13051_r13474/AOD.29256973._000009.pool.
↪ root.1
mc20_13TeV.311633.Pythia8EvtGen_A14NNPDF23LO_WmuHNL50_10G_lt10dd.rec
↪ on.AOD.e7422_e5984_a875_r13051_r13474/AOD.29256973._000010.pool.
↪ root.1
mc20_13TeV.311633.Pythia8EvtGen_A14NNPDF23LO_WmuHNL50_10G_lt10dd.rec
↪ on.AOD.e7422_e5984_a875_r13051_r13474/AOD.29256976._000001.pool.
↪ root.1
mc20_13TeV.311633.Pythia8EvtGen_A14NNPDF23LO_WmuHNL50_10G_lt10dd.rec
↪ on.AOD.e7422_e5984_a875_r13051_r13474/AOD.29256976._000002.pool.
↪ root.1
mc20_13TeV.311633.Pythia8EvtGen_A14NNPDF23LO_WmuHNL50_10G_lt10dd.rec
↪ on.AOD.e7422_e5984_a875_r13051_r13474/AOD.29256976._000003.pool.
↪ root.1
mc20_13TeV.311633.Pythia8EvtGen_A14NNPDF23LO_WmuHNL50_10G_lt10dd.rec
↪ on.AOD.e7422_e5984_a875_r13051_r13474/AOD.29256976._000004.pool.
↪ root.1
mc20_13TeV.311633.Pythia8EvtGen_A14NNPDF23LO_WmuHNL50_10G_lt10dd.rec
↪ on.AOD.e7422_e5984_a875_r13051_r13474/AOD.29256976._000005.pool.
↪ root.1
```

```
mc20_13TeV.311633.Pythia8EvtGen_A14NNPDF23LO_WmuHNL50_10G_lt10dd.rec
↪ on.AOD.e7422_e5984_a875_r13051_r13474/AOD.29256976._000006.pool.
↪ root.1
mc20_13TeV.311633.Pythia8EvtGen_A14NNPDF23LO_WmuHNL50_10G_lt10dd.rec
↪ on.AOD.e7422_e5984_a875_r13051_r13474/AOD.29256976._000007.pool.
↪ root.1
mc20_13TeV.311633.Pythia8EvtGen_A14NNPDF23LO_WmuHNL50_10G_lt10dd.rec
↪ on.AOD.e7422_e5984_a875_r13051_r13474/AOD.29256976._000008.pool.
↪ root.1
mc20_13TeV.311633.Pythia8EvtGen_A14NNPDF23LO_WmuHNL50_10G_lt10dd.rec
↪ on.AOD.e7422_e5984_a875_r13051_r13474/AOD.29256976._000009.pool.
↪ root.1
mc20_13TeV.311633.Pythia8EvtGen_A14NNPDF23LO_WmuHNL50_10G_lt10dd.rec
↪ on.AOD.e7422_e5984_a875_r13051_r13474/AOD.29256976._000010.pool.
↪ root.1
```

D.2.2 HNL 5% Overall

```
mc20_13TeV.311633.Pythia8EvtGen_A14NNPDF23LO_WmuHNL50_10G_lt10dd.rec
↪ on.AOD.e7422_e5984_s3155_s3833_r13625_r13629_r13625/AOD.29203993
↪ ._000001.pool.root.1
mc20_13TeV.311633.Pythia8EvtGen_A14NNPDF23LO_WmuHNL50_10G_lt10dd.rec
↪ on.AOD.e7422_e5984_s3155_s3833_r13625_r13629_r13625/AOD.29203993
↪ ._000002.pool.root.1
mc20_13TeV.311633.Pythia8EvtGen_A14NNPDF23LO_WmuHNL50_10G_lt10dd.rec
↪ on.AOD.e7422_e5984_s3155_s3833_r13625_r13629_r13625/AOD.29203993
↪ ._000003.pool.root.1
```

```
mc20_13TeV.311633.Pythia8EvtGen_A14NNPDF23LO_WmuHNL50_10G_lt10dd.rec⌋
↪ on.AOD.e7422_e5984_s3155_s3833_r13625_r13629_r13625/AOD.29203993⌋
↪ ._000004.pool.root.1
mc20_13TeV.311633.Pythia8EvtGen_A14NNPDF23LO_WmuHNL50_10G_lt10dd.rec⌋
↪ on.AOD.e7422_e5984_s3155_s3833_r13625_r13629_r13625/AOD.29203993⌋
↪ ._000005.pool.root.1
mc20_13TeV.311633.Pythia8EvtGen_A14NNPDF23LO_WmuHNL50_10G_lt10dd.rec⌋
↪ on.AOD.e7422_e5984_s3155_s3833_r13625_r13629_r13625/AOD.29203993⌋
↪ ._000006.pool.root.1
mc20_13TeV.311633.Pythia8EvtGen_A14NNPDF23LO_WmuHNL50_10G_lt10dd.rec⌋
↪ on.AOD.e7422_e5984_s3155_s3833_r13625_r13629_r13625/AOD.29203993⌋
↪ ._000007.pool.root.1
mc20_13TeV.311633.Pythia8EvtGen_A14NNPDF23LO_WmuHNL50_10G_lt10dd.rec⌋
↪ on.AOD.e7422_e5984_s3155_s3833_r13625_r13629_r13625/AOD.29203993⌋
↪ ._000009.pool.root.1
mc20_13TeV.311633.Pythia8EvtGen_A14NNPDF23LO_WmuHNL50_10G_lt10dd.rec⌋
↪ on.AOD.e7422_e5984_s3155_s3833_r13625_r13629_r13625/AOD.29203993⌋
↪ ._000010.pool.root.1
mc20_13TeV.311633.Pythia8EvtGen_A14NNPDF23LO_WmuHNL50_10G_lt10dd.rec⌋
↪ on.AOD.e7422_e5984_s3155_s3833_r13625_r13629_r13625/AOD.29203993⌋
↪ ._000011.pool.root.1
```

D.2.3 HNL +10% IBL

```
mc20_13TeV.311633.Pythia8EvtGen_A14NNPDF23LO_WmuHNL50_10G_lt10dd.rec
↪ on.AOD.e7422_e5984_s3156_s3833_r13626_r13630_r13626/AOD.29203997
↪ ._000011.pool.root.1
mc20_13TeV.311633.Pythia8EvtGen_A14NNPDF23LO_WmuHNL50_10G_lt10dd.rec
↪ on.AOD.e7422_e5984_s3156_s3833_r13626_r13630_r13626/AOD.29203997
↪ ._000012.pool.root.1
mc20_13TeV.311633.Pythia8EvtGen_A14NNPDF23LO_WmuHNL50_10G_lt10dd.rec
↪ on.AOD.e7422_e5984_s3156_s3833_r13626_r13630_r13626/AOD.29203997
↪ ._000013.pool.root.1
mc20_13TeV.311633.Pythia8EvtGen_A14NNPDF23LO_WmuHNL50_10G_lt10dd.rec
↪ on.AOD.e7422_e5984_s3156_s3833_r13626_r13630_r13626/AOD.29203997
↪ ._000014.pool.root.1
mc20_13TeV.311633.Pythia8EvtGen_A14NNPDF23LO_WmuHNL50_10G_lt10dd.rec
↪ on.AOD.e7422_e5984_s3156_s3833_r13626_r13630_r13626/AOD.29203997
↪ ._000015.pool.root.1
mc20_13TeV.311633.Pythia8EvtGen_A14NNPDF23LO_WmuHNL50_10G_lt10dd.rec
↪ on.AOD.e7422_e5984_s3156_s3833_r13626_r13630_r13626/AOD.29203997
↪ ._000016.pool.root.1
mc20_13TeV.311633.Pythia8EvtGen_A14NNPDF23LO_WmuHNL50_10G_lt10dd.rec
↪ on.AOD.e7422_e5984_s3156_s3833_r13626_r13630_r13626/AOD.29203997
↪ ._000017.pool.root.1
mc20_13TeV.311633.Pythia8EvtGen_A14NNPDF23LO_WmuHNL50_10G_lt10dd.rec
↪ on.AOD.e7422_e5984_s3156_s3833_r13626_r13630_r13626/AOD.29203997
↪ ._000018.pool.root.1
mc20_13TeV.311633.Pythia8EvtGen_A14NNPDF23LO_WmuHNL50_10G_lt10dd.rec
↪ on.AOD.e7422_e5984_s3156_s3833_r13626_r13630_r13626/AOD.29203997
↪ ._000021.pool.root.1
```

```
mc20_13TeV.311633.Pythia8EvtGen_A14NNPDF23LO_WmuHNL50_10G_lt10dd.rec
↪ on.AOD.e7422_e5984_s3156_s3833_r13626_r13630_r13626/AOD.29203997
↪ ._000022.pool.root.1
```

D.2.4 HNL +25% PP0

```
mc20_13TeV.311633.Pythia8EvtGen_A14NNPDF23LO_WmuHNL50_10G_lt10dd.rec
↪ on.AOD.e7422_e5984_s3818_s3833_r13627_r13631_r13627/AOD.29204002
↪ ._000017.pool.root.1
mc20_13TeV.311633.Pythia8EvtGen_A14NNPDF23LO_WmuHNL50_10G_lt10dd.rec
↪ on.AOD.e7422_e5984_s3818_s3833_r13627_r13631_r13627/AOD.29204002
↪ ._000018.pool.root.1
mc20_13TeV.311633.Pythia8EvtGen_A14NNPDF23LO_WmuHNL50_10G_lt10dd.rec
↪ on.AOD.e7422_e5984_s3818_s3833_r13627_r13631_r13627/AOD.29204002
↪ ._000019.pool.root.1
mc20_13TeV.311633.Pythia8EvtGen_A14NNPDF23LO_WmuHNL50_10G_lt10dd.rec
↪ on.AOD.e7422_e5984_s3818_s3833_r13627_r13631_r13627/AOD.29204002
↪ ._000021.pool.root.1
mc20_13TeV.311633.Pythia8EvtGen_A14NNPDF23LO_WmuHNL50_10G_lt10dd.rec
↪ on.AOD.e7422_e5984_s3818_s3833_r13627_r13631_r13627/AOD.29204002
↪ ._000022.pool.root.1
mc20_13TeV.311633.Pythia8EvtGen_A14NNPDF23LO_WmuHNL50_10G_lt10dd.rec
↪ on.AOD.e7422_e5984_s3818_s3833_r13627_r13631_r13627/AOD.29204002
↪ ._000024.pool.root.1
mc20_13TeV.311633.Pythia8EvtGen_A14NNPDF23LO_WmuHNL50_10G_lt10dd.rec
↪ on.AOD.e7422_e5984_s3818_s3833_r13627_r13631_r13627/AOD.29204002
↪ ._000025.pool.root.1
```

```
mc20_13TeV.311633.Pythia8EvtGen_A14NNPDF23LO_WmuHNL50_10G_lt10dd.rec
↪ on.AOD.e7422_e5984_s3818_s3833_r13627_r13631_r13627/AOD.29204002
↪ ._000028.pool.root.1
mc20_13TeV.311633.Pythia8EvtGen_A14NNPDF23LO_WmuHNL50_10G_lt10dd.rec
↪ on.AOD.e7422_e5984_s3818_s3833_r13627_r13631_r13627/AOD.29204002
↪ ._000030.pool.root.1
mc20_13TeV.311633.Pythia8EvtGen_A14NNPDF23LO_WmuHNL50_10G_lt10dd.rec
↪ on.AOD.e7422_e5984_s3818_s3833_r13627_r13631_r13627/AOD.29204002
↪ ._000031.pool.root.1
```

D.2.5 HNL QGSP_BIC

```
mc20_13TeV.311633.Pythia8EvtGen_A14NNPDF23LO_WmuHNL50_10G_lt10dd.rec
↪ on.AOD.e7422_e5984_s3819_s3833_r13628_r12253_r13628/AOD.29204007
↪ ._000011.pool.root.1
mc20_13TeV.311633.Pythia8EvtGen_A14NNPDF23LO_WmuHNL50_10G_lt10dd.rec
↪ on.AOD.e7422_e5984_s3819_s3833_r13628_r12253_r13628/AOD.29204007
↪ ._000012.pool.root.1
mc20_13TeV.311633.Pythia8EvtGen_A14NNPDF23LO_WmuHNL50_10G_lt10dd.rec
↪ on.AOD.e7422_e5984_s3819_s3833_r13628_r12253_r13628/AOD.29204007
↪ ._000013.pool.root.1
mc20_13TeV.311633.Pythia8EvtGen_A14NNPDF23LO_WmuHNL50_10G_lt10dd.rec
↪ on.AOD.e7422_e5984_s3819_s3833_r13628_r12253_r13628/AOD.29204007
↪ ._000014.pool.root.1
mc20_13TeV.311633.Pythia8EvtGen_A14NNPDF23LO_WmuHNL50_10G_lt10dd.rec
↪ on.AOD.e7422_e5984_s3819_s3833_r13628_r12253_r13628/AOD.29204007
↪ ._000015.pool.root.1
```

```
mc20_13TeV.311633.Pythia8EvtGen_A14NNPDF23LO_WmuHNL50_10G_lt10dd.rec
↪ on.AOD.e7422_e5984_s3819_s3833_r13628_r12253_r13628/AOD.29204007
↪ ._000016.pool.root.1
mc20_13TeV.311633.Pythia8EvtGen_A14NNPDF23LO_WmuHNL50_10G_lt10dd.rec
↪ on.AOD.e7422_e5984_s3819_s3833_r13628_r12253_r13628/AOD.29204007
↪ ._000017.pool.root.1
mc20_13TeV.311633.Pythia8EvtGen_A14NNPDF23LO_WmuHNL50_10G_lt10dd.rec
↪ on.AOD.e7422_e5984_s3819_s3833_r13628_r12253_r13628/AOD.29204007
↪ ._000018.pool.root.1
mc20_13TeV.311633.Pythia8EvtGen_A14NNPDF23LO_WmuHNL50_10G_lt10dd.rec
↪ on.AOD.e7422_e5984_s3819_s3833_r13628_r12253_r13628/AOD.29204007
↪ ._000019.pool.root.1
mc20_13TeV.311633.Pythia8EvtGen_A14NNPDF23LO_WmuHNL50_10G_lt10dd.rec
↪ on.AOD.e7422_e5984_s3819_s3833_r13628_r12253_r13628/AOD.29204007
↪ ._000020.pool.root.1
```

References

1. CERN. Our History. https://home.cern/about/who-we-are/our-history. Accessed: 2025-09-02. 2025 (cit. on p. 1)
2. CERN. Facts and figures about the LHC. 2025. Available from: https://home.cern/resources/faqs/facts-and-figures-about-lhc [Accessed on: 2025 Sep 2] (cit. on p. 1)
3. Aamodt K et al. The ALICE experiment at the CERN LHC. JINST 2008; 3:S08002. DOI: 10.1088/1748-0221/3/08/S08002 (cit. on pp. 1, 4)
4. Aad G et al. The ATLAS Experiment at the CERN Large Hadron Collider. JINST 2008; 3. Also published by CERN Geneva in 2010:S08003. DOI: 10.1088/1748-0221/3/08/S08003 (cit. on pp. 1, 5, 14, 22)
5. Chatrchyan S et al. The CMS experiment at the CERN LHC. JINST 2008; 3:S08004. DOI: 10.1088/1748-0221/3/08/S08004 (cit. on pp. 1, 5)
6. Alves AA et al. The LHCb Detector at the LHC. JINST 2008; 3:S08005. DOI: 10.1088/1748-0221/3/08/S08005 (cit. on pp. 1, 5)
7. Commissioning L. Longer term LHC schedule. https://lhc-commissioning.web.cern.ch/schedule/images/2024/Complex-Long-Term-June24.png. [Accessed 30-09-2024]. 2024 (cit. on p. 2)
8. Landua F. The CERN accelerator complex layout in 2022. 2022. General Photo (cit. on p. 3)
9. Evans LR. The Large Hadron Collider. 1996 (cit. on p. 4)

10. Acharya S et al. The ALICE experiment: a journey through QCD. Eur. Phys. J. C 2024; 84:813. DOI: 10.1140/epjc/s10052-024-12935-y (cit. on p. 4)

11. CMS Collaboration. CMS Experiment Physics Goals. CERN TWiki. Accessed: Thursday 15th January, 2026. 2024 (cit. on p. 5)

12. Chatrchyan S et al. Observation of a new boson at a mass of 125 GeV with the CMS experiment at the LHC. Physics Letters B 2012 Sep; 716:30–61. ISSN: 0370-2693. DOI: 10.1016/j.physletb.2012.08.021 (cit. on pp. 5, 23)

13. CERN. LHCb experiment. https://home.cern/science/experiments/lhcb. Accessed: 2025-05-22. 2025 (cit. on p. 5)

14. Davies E. PHY206 Lecture 7: Neutrino Mixing and the PMNS Matrix. https://www.hep.shef.ac.uk/edaw/PHY206/Site/2012_course_files/phy206rlec7.pdf. Accessed: 2025-05-22. 2012 (cit. on p. 8)

15. ATLAS Collaboration. Glossary — ATLAS Open Data — opendata.atlas.cern. https://opendata.atlas.cern/docs/8TeVDoc/glossary#pseudorapidity. [Accessed 30-09-2024]. 2024 (cit. on p. 8)

16. Hoecker A. ATLAS Status and Plans. Slide 27 of 48. University College London, 2025 Jan (cit. on p. 9)

17. ATLAS Collaboration. Data Quality Results. https://twiki.cern.ch/twiki/bin/view/AtlasPublic/DataQualityResults#Data_Quality. [Accessed 27-02-2025]. 2025 (cit. on p. 10)

18. Aaboud M et al. LuminosityPublicResultsRun3 < AtlasPublic < TWiki — twiki.cern.ch. https://twiki.cern.ch/twiki/bin/view/AtlasPublic/LuminosityPublicResultsRun3. [Accessed 26-09-2024]. 2024 (cit. on pp. 10, 12)

19. Martini M. An introduction to transverse beam dynamics in accelerators. Tech. rep. Geneva: CERN, 1996 (cit. on p. 12)

20. Group PD. Review of Particle Physics. Progress of Theoretical and Experimental Physics 2022 Aug; 2022:083C01. ISSN: 2050-3911. DOI: 10.1093/ptep/ptac097 (cit. on p. 12)

21. Steerenberg R. LHC Report: The LHC is full! CERN News. News article on LHC reaching full bunch capacity. 2018 May (cit. on p. 13)

22. Aaboud M et al. Reconstruction of primary vertices at the ATLAS experiment in Run 1 proton–proton collisions at the LHC. The European Physical Journal C 2017 May; 77. ISSN: 1434-6052. DOI: 10.1140/epjc/s10052-017-4887-5 (cit. on p. 13)

23. Trad G, Alexopoulos A, Bravin E, Butti D, Kieffer R, Roncarolo F, Vlachos S, and Wurkner B. LHC Emittance Measurements in Run 2. 2019 :117–23 (cit. on p. 13)

24. Holzer B. Introduction to Transverse Beam Dynamics. 2014 :27–45. DOI: 10.5170/CERN-2013-007.27. arXiv: 1404.0923 (cit. on p. 13)

25. Zimmermann F. Parameter Space Beyond 1034. Tech. rep. Please see Figure 5. 2010 (cit. on p. 14)

26. Pernegger H. The Pixel Detector of the ATLAS Experiment for LHC Run-2. Tech. rep. 06. Geneva: CERN, 2015. DOI: 10.1088/1748-0221/10/06/C06012 (cit. on p. 15)

27. ATLAS Collaboration. Inner Detector. https://atlas.cern/Discover/Detector/Inner-Detector. 26th February 2025. 2025 (cit. on pp. 15–16)

28. ATLAS Collaboration. Alignment of the ATLAS Inner Detector in Run-2. Eur. Phys. J. C 2020; 80:1194. DOI: 10.1140/epjc/s10052-020-08700-6. arXiv: 2007.07624 (cit. on p. 16)

29. ATLAS Collaboration. The Expected Performance of the ATLAS Inner Detector. Tech. rep. Geneva: CERN, 2008 (cit. on pp. 17–19)

30. Aleksa M and Diemoz M. Discussion on the electromagnetic calorimeters of ATLAS and CMS. Tech. rep. Geneva: CERN, 2013 (cit. on p. 20)

31. ATLAS Collaboration. ATLAS tile calorimeter: Technical Design Report. Technical design report. ATLAS. Geneva: CERN, 1996. DOI: 10.17181/CERN.JRBJ.7028 (cit. on p. 20)

32. Artamonov A et al. The ATLAS Forward Calorimeter. JINST 2008; 3:P02010. DOI: 10.1088/1748-0221/3/02/P02010 (cit. on p. 21)

33. Fabjan CW and Gianotti F. Calorimetry for Particle Physics. Rev. Mod. Phys. 2003; 75:1243–86. DOI: 10.1103/RevModPhys.75.1243 (cit. on pp. 21–22)

34. ATLAS muon spectrometer. Technical design report. ATLAS. Geneva: CERN, 1997 (cit. on p. 22)

35. ATLAS Collaboration. Observation of a new particle in the search for the Standard Model Higgs boson with the ATLAS detector at the LHC. Physics Letters B 2012 Sep; 716:P1–29. ISSN: 0370-2693. DOI: 10.1016/j.physletb.2012.08.020 (cit. on pp. 23, 53)

36. Experiment A. Trigger and Data Acquisition System — atlas.cern. https://atlas.cern/Discover/Detector/Trigger-DAQ. [Accessed 17-10-2024]. 2024 (cit. on p. 25)

37. ATLAS. Performance of the ATLAS trigger system in 2015. The European Physical Journal C 2017 May; 77. ISSN: 1434-6052. DOI: 10.1140/epjc/s10052-017-4852-3 (cit. on p. 25)

38. ATLAS. Performance of the ATLAS muon triggers in Run 2. Journal of Instrumentation 2020 Sep; 15:P09015–P09015. ISSN: 1748-0221. DOI: 10.1088/1748-0221/15/09/p09015 (cit. on pp. 25, 27)

39. Novotny L. B physics studies at the ATLAS experiment. Studium B fyziky na experimentu ATLAS. Section 5.1.2, page 93. Czech Technical University in Prague, 2023 (cit. on p. 26)

40. Aad G et al. The ATLAS Fast TracKer system. Journal of Instrumentation 2021 Jul; 16:P07006. ISSN: 1748-0221. DOI: 10.1088/1748-0221/16/07/p07006 (cit. on p. 27)

41. Aad G et al. Operation of the ATLAS trigger system in Run 2. JINST 2020; 15:P10004. DOI: 10.1088/1748-0221/15/10/P10004. arXiv: 2007.12539 (cit. on p. 29)

42. Collaboration A. ATLAS data quality operations and performance for 2015–2018 data-taking. Journal of Instrumentation 2020 Apr; 15:P04003–P04003. ISSN: 1748-0221. DOI: 10.1088/1748-0221/15/04/p04003 (cit. on p. 29)

43. ATLAS Collaboration. Luminosity determination in pp collisions at $\sqrt{s} = 13$ TeV using the ATLAS detector at the LHC. Tech. rep. Geneva: CERN, 2019 (cit. on p. 29)

44. Avoni G et al. The new LUCID-2 detector for luminosity measurement and monitoring in ATLAS. Journal of Instrumentation 2018 Jul; 13:P07017. DOI: 10.1088/1748-0221/13/07/P07017 (cit. on p. 29)

45. Smizanska M. B-physics with ATLAS. Nuclear Physics B - Proceedings Supplements 1997; 55:269–76. ISSN: 0920-5632. DOI: https://doi.org/10.1016/S0920-5632(97)00186-2 (cit. on pp. 29–30)

46. ATLAS Collaboration. The ATLAS Magnet System. Accessed: 2025-01-22. 2025 (cit. on p. 30)

47. The ATLAS Collaboration Software and Firmware. Tech. rep. Geneva: CERN, 2021 (cit. on pp. 31, 180)

48. Brun R and Rademakers F. ROOT – An Object Oriented Data Analysis Framework. Nuclear Instruments and Methods in Physics Research Section A: Accelerators, Spectrometers, Detectors and Associated Equipment 1997; 389. Proceedings of the AIHENP'96 Workshop, Lausanne, Sep. 1996; See also

"ROOT" [software], Release vX.YY/ZZ, dd/mm/yyyy:81–6 (cit. on pp. 31, 146, 150)

49. Agostinelli S et al. Geant4—a simulation toolkit. Nuclear Instruments and Methods in Physics Research Section A: Accelerators, Spectrometers, Detectors and Associated Equipment 2003; 506:250–303. ISSN: 0168-9002. DOI: https://doi.org/10.1016/S0168-9002(03)01368-8 (cit. on pp. 31, 87, 172)

50. The Pythia Collaboration. Pythia Monte Carlo Event Generator. Website. Accessed on April 28, 2025 (cit. on pp. 31, 33)

51. The Herwig Collaboration. Herwig Event Generator. Website. Accessed on April 28, 2025 (cit. on pp. 31, 33)

52. Canmore J. The ATLAS data processing chain. Presentation at the University of Oslo. Presented on 8th February 2016. 2016 Feb (cit. on p. 32)

53. Siegert F. A practical guide to event generation for prompt photon production with Sherpa. J. Phys. G 2017; 44:044007. DOI: 10.1088/1361-6471/aa5f29. arXiv: 1611.07226 [hep-ph] (cit. on p. 33)

54. Bellm J, Bewick G, Ravasio SF, Gieseke S, Grellscheid D, and al. et. Herwig 7.2 release note. European Physical Journal C 2020; 80:452. DOI: 10.1140/epjc/s10052-020-8011-x (cit. on p. 33)

55. The Sherpa Team. Sherpa Monte Carlo Event Generator. Website. Accessed on April 28, 2025 (cit. on p. 33)

56. Siegert F. A practical guide to event generation for prompt photon production with Sherpa. J. Phys. G 2017; 44:044007. DOI: 10.1088/1361-6471/aa5f29. arXiv: 1611.07226 [hep-ph] (cit. on p. 33)

57. Shiers J. The Worldwide LHC Computing Grid (worldwide LCG). Comput. Phys. Commun. 2007; 177:219–23. DOI: 10.1016/j.cpc.2007.02.021 (cit. on p. 34)

58. CERN. The Worldwide LHC Computing Grid (WLCG). https://wlcg.web.cern.ch/. Accessed: 16 September 2025 (cit. on p. 35)

59. Calace N. Track and Vertex reconstruction in ATLAS for LHC Run-3 and High-Luminosity phases. 2021 (cit. on p. 36)

60. ATLAS Collaboration. ATLAS Track Reconstruction – General Overview. https://atlassoftwaredocs.web.cern.ch/internal-links/tracking-tutorial/idoverview/. Published: 24 August 2024. Accessed: 30 April 2025. 2024 Aug (cit. on pp. 37–38)

61. Aad G et al. Performance of the reconstruction of large impact parameter tracks in the ATLAS inner detector. Tech. rep. Geneva: CERN, 2017 (cit. on p. 38)

62. Frühwirth R. Application of Kalman filtering to track and vertex fitting. Nuclear Instruments and Methods in Physics Research Section A: Accelerators, Spectrometers, Detectors and Associated Equipment 1987; 262:444–50. ISSN: 0168-9002. DOI: https://doi.org/10.1016/0168-9002(87)90887-4 (cit. on p. 38)

63. NASA. Building Blocks. https://science.nasa.gov/universe/overview/building-blocks/. Last updated Oct 22, 2024; accessed 2025-10-02. 2024 (cit. on p. 45)

64. Commons W. Standard Model of Elementary Particles. 2019. Available from: https://commons.wikimedia.org/wiki/Standard_Model#/media/File:Standard_Model_of_Elementary_Particles.svg (cit. on p. 46)

65. Fukuda Y et al. Evidence for Oscillation of Atmospheric Neutrinos. Physical Review Letters 1998 Aug; 81:1562–7. ISSN: 1079-7114. DOI: 10.1103/physrevlett.81.1562 (cit. on p. 46)

66. Thomson JJ. XL. Cathode Rays. The London, Edinburgh, and Dublin Philosophical Magazine and Journal of Science 1897; 44:293–316. DOI: 10.1080/14786449708621070 (cit. on p. 47)

67. Rutherford E. LXXIX. The scattering of and particles by matter and the structure of the atom. The London, Edinburgh, and Dublin Philosophical Magazine and Journal of Science 1911; 21:669–88. DOI: 10.1080/14786440508637080 (cit. on p. 48)

68. Chadwick J. The existence of a neutron. Proceedings of The Royal Society A 1932 Jun; 136. DOI: https://doi.org/10.1098/rspa.1932.0112 (cit. on p. 48)

69. Maxwell JC. A Dynamical Theory of the Electromagnetic Field. Philosophical Transactions of the Royal Society of London 1865; 155:459–512. DOI: https://doi.org/10.1098/rstl.1865.0008 (cit. on p. 48)

70. Hertz H. Electric waves : being researches on the propagation of electric action with finite velocity through space. London : Macmillan, 1889 (cit. on p. 48)

71. Einstein A. Über einen die Erzeugung und Verwandlung des Lichtes betreffenden heuristischen Gesichtspunkt. Annalen der Physik 1905; 322:132–48. DOI: https://doi.org/10.1002/andp.19053220607 (cit. on p. 49)

72. Dunne P. A reappraisal of the mechanism of pion exchange and its implications for the teaching of particle physics. Physics Education 2002 May; 37:211. DOI: 10.1088/0031-9120/37/3/305 (cit. on p. 50)

73. Neddermeyer SH and Anderson CD. Note on the Nature of Cosmic-Ray Particles. Phys. Rev. 1937 May; 51(10):884–6. DOI: 10.1103/PhysRev.51.884 (cit. on p. 50)

74. Lattes Cea. Processes Involving Charged Mesons. Nature 1947; 159:649–97. DOI: https://doi.org/10.1038/159694a0 (cit. on p. 50)

75. CERN. Clifford Butler and George Rochester discover the kaon, first strange particle — timeline.web.cern.ch — timeline.web.cern.ch. https://timeline.web.cern.ch/clifford-butler-and-george-rochester-discover-kaon-first-strange-particle. [Accessed 30-09-2024]. 1947 (cit. on p. 50)

76. Brown LM, Dresden M, and Hoddeson L. Pions to quarks: particle physics in the 1950s. *Pions to Quarks: Particle Physics in the 1950s*. Ed. by Brown LM, Dresden M, and Hoddeson L. Cambridge University Press, 1989 :3–39 (cit. on p. 51)

77. Mersits U. High-energy physics from 1945 to 1952/53. Tech. rep. Geneva: CERN, 1985 (cit. on p. 51)

78. Gell-Mann M. The Eightfold Way: A Theory Of Strong Interaction Symmetry. 1961 Mar. DOI: 10.2172/4008239 (cit. on p. 51)

79. Novotny L. B physics studies at the ATLAS experiment. Studium B fyziky na experimentu ATLAS. specific figure reference Figure 1.1 of the thesis. Czech Technical University in Prague, 2023 (cit. on pp. 51, 93)

80. Bloom ED et al. High-Energy Inelastic $e-p$ Scattering at 6° and 10°. Phys. Rev. Lett. 1969 Oct; 23(16):930–4. DOI: 10.1103/PhysRevLett.23.930 (cit. on p. 52)

81. Greenberg OW. Visits with Einstein and Discovering Color in Quarks — ias.edu. https://www.ias.edu/ideas/2015/greenberg-color. [Accessed 04-11-2024]. 2015 (cit. on p. 52)

82. Fritzsch H, Gell-Mann M, and Leutwyler H. Advantages of the color octet gluon picture. Physics Letters B 1973; 47:365–8. ISSN: 0370-2693. DOI: https://doi.org/10.1016/0370-2693(73)90625-4 (cit. on p. 52)

83. Aubert JJ et al. Experimental Observation of a Heavy Particle J. Phys. Rev. Lett. 1974 Dec; 33(23):1404–6. DOI: 10.1103/PhysRevLett.33.1404 (cit. on p. 52)

84. Augustin J et al. Discovery of a Narrow Resonance in e^+e^- Annihilation. Phys. Rev. Lett. 1974 Dec; 33(23):1406–8. DOI: 10.1103/PhysRevLett.33.1406 (cit. on p. 52)

85. SLAC National Accelerator Laboratory. The November Revolution in Physics. SLAC History Bits. Accessed: February 27, 2025 (cit. on p. 52)

86. Herb SW et al. Observation of a Dimuon Resonance at 9.5-GeV in 400-GeV Proton-Nucleus Collisions. Phys. Rev. Lett. 1977; 39:252–5. DOI: 10.1103/PhysRevLett.39.252 (cit. on p. 52)

87. CDF Collaboration FA et al. Observation of Top Quark Production in $\overline{p}p$ Collisions with the Collider Detector at Fermilab. Phys. Rev. Lett. 1995 Apr; 74(14):2626–31. DOI: 10.1103/PhysRevLett.74.2626 (cit. on p. 52)

88. Wilson FL. Fermi's Theory of Beta Decay. American Journal of Physics 1968 Dec; 36:1150–60. ISSN: 0002-9505. DOI: 10.1119/1.1974382 (cit. on p. 52)

89. Glashow SL, Iliopoulos J, and Maiani L. Weak Interactions with Lepton-Hadron Symmetry. Phys. Rev. D 1970 Oct; 2(7):1285–92. DOI: 10.1103/PhysRevD.2.1285 (cit. on p. 53)

90. UA1 C. Experimental observation of isolated large transverse energy electrons with associated missing energy at s=540 GeV. Physics Letters B 1983; 122:103–16. ISSN: 0370-2693. DOI: https://doi.org/10.1016/0370-2693(83)91177-2 (cit. on p. 53)

91. UA2 C. Observation of single isolated electrons of high transverse momentum in events with missing transverse energy at the CERN pp collider. Physics Letters B 1983; 122:476–85. ISSN: 0370-2693. DOI: https://doi.org/10.1016/0370-2693(83)91605-2 (cit. on p. 53)

92. CERN C. La découverte du Z° confirmée. 1983. Issued on 22 July 1983 (cit. on p. 53)

93. Higgs PW. Broken Symmetries and the Masses of Gauge Bosons. Phys. Rev. Lett. 1964 Oct; 13(16):508–9. DOI: 10.1103/PhysRevLett.13.508 (cit. on p. 53)

94. Englert F and Brout R. Broken Symmetry and the Mass of Gauge Vector Mesons. Phys. Rev. Lett. 1964 Aug; 13(9):321–3. DOI: 10.1103/PhysRevLett.13.321 (cit. on p. 53)

95. Dirac PAM. The quantum theory of the emission and absorption of radiation. Proc. R. Soc. Lond. A 1927 Mar; 114(767):0. DOI: https://doi.org/10.1098/rspa.1927.0039 (cit. on p. 54)

96. Anderson CD. The Positive Electron. Phys. Rev. 1933 Mar; 43(6):491–4. DOI: 10.1103/PhysRev.43.491 (cit. on p. 54)

97. Chamberlain O, Segrè E, Wiegand C, and Ypsilantis T. Observation of Antiprotons. Phys. Rev. 1955 Nov; 100(3):947–50. DOI: 10.1103/PhysRev.100.947 (cit. on p. 54)

98. Cowan CL, Reines F, Harrison FB, Kruse HW, and McGuire AD. Detection of the free neutrino: A Confirmation. Science 1956; 124:103–4. DOI: 10.1126/science.124.3212.103 (cit. on p. 54)

99. Danby G, Gaillard JM, Goulianos K, Lederman LM, Mistry NB, Schwartz M, and Steinberger J. Observation of High-Energy Neutrino Reactions and the Existence of Two Kinds of Neutrinos. Phys. Rev. Lett. 1962 Jul; 9(1):36–44. DOI: 10.1103/PhysRevLett.9.36 (cit. on p. 55)

100. Kodama K et al. Observation of tau neutrino interactions. Physics Letters B 2001 Apr; 504:218–24. ISSN: 0370-2693. DOI: 10.1016/s0370-2693(01)00307-0 (cit. on p. 55)

101. Wess J and Zumino B. Supergauge Transformations in Four-Dimensions. Nucl. Phys. B 1974; 70. Ed. by Salam A and Sezgin E:39–50. DOI: 10.1016/0550-3213(74)90355-1 (cit. on p. 56)

102. Haber HE and Kane GL. The Search for Supersymmetry: Probing Physics Beyond the Standard Model. Phys. Rept. 1985; 117:75–263. DOI: 10.1016/0370-1573(85)90051-1 (cit. on p. 56)

103. Fukugita M and Yanagida T. Baryogenesis Without Grand Unification. Phys. Lett. B 1986; 174:45–7. DOI: 10.1016/0370-2693(86)91126-3 (cit. on p. 56)

104. Fong CS, Nardi E, and Riotto A. Leptogenesis in the Universe. Advances in High Energy Physics 2012; 2012:1–59. ISSN: 1687-7365. DOI: 10.1155/2012/158303 (cit. on p. 56)

105. Sakharov AD. Violation of CP Invariance, C asymmetry, and baryon asymmetry of the universe. Pisma Zh. Eksp. Teor. Fiz. 1967; 5:32–5. DOI: 10.1070/PU1991v034n05ABEH002497 (cit. on p. 56)

106. Bödeker D and Buchmüller W. Baryogenesis from the weak scale to the grand unification scale. Rev. Mod. Phys. 2021 Aug; 93(3):035004. DOI: 10.1103/RevModPhys.93.035004 (cit. on p. 56)

107. Encyclopaedia Britannica. Electroweak theory. https://www.britannica.com/science/electroweak-theory. Accessed: 2025-10-06. 2023 (cit. on p. 60)

108. B.P. Abbot et al. The LIGO Scientific Collaboration tVC. Observation of Gravitational Waves from a Binary Black Hole Merger. Physical Review Letters 2016 Feb; 116. ISSN: 1079-7114. DOI: 10.1103/physrevlett.116.061102 (cit. on p. 61)

109. Noether E. Invariant Variation Problems. Trans. by Tavel MA. Transport Theory and Statistical Physics 1971; 1. English translation of the 1918 German original: "Invariante Variationsprobleme":183–207. DOI: 10.1080/00411457108231446 (cit. on p. 61)

110. Particle Data Group. Review of Particle Physics. Phys. Rev. D 2024; 110. See section on the CKM Quark-Mixing Matrix, standard parameterization:030001. DOI: 10.1103/PhysRevD.110.030001 (cit. on pp. 65, 94)

111. Particle Data Group. Review of Particle Physics. Progress of Theoretical and Experimental Physics 2022 Aug; 2022:083C01. ISSN: 2050-3911. DOI: 10.1093/ptep/ptac097 (cit. on p. 66)

112. Particle Data Group. Review of Particle Physics: CKM Matrix. Tech. rep. 2022 (cit. on p. 68)

113. Hollik WG. Neutrino Mixing from SUSY breaking. PoS 2015; CORFU2014. See page 2:077. DOI: 10.22323/1.231.0077 (cit. on p. 69)

114. Denton PB. A Return To Neutrino Normalcy. See Section IV: *Current Status and Future Prospects*. 2021. arXiv: 2003.04319 [hep-ph] (cit. on p. 69)

115. Lee TD and Yang CN. Question of Parity Conservation in Weak Interactions. Phys. Rev. 1956 Oct; 104(1):254–8. DOI: 10.1103/PhysRev.104.254 (cit. on p. 69)

116. Wu CS et al. Experimental Test of Parity Conservation in Beta Decay. Phys. Rev. 1957 Feb; 105(4):1413–5. DOI: 10.1103/PhysRev.105.1413 (cit. on p. 69)

117. Christenson JH, Cronin JW, Fitch VL, and Turlay R. Evidence for the 2π Decay of the K_2^0 Meson. Phys. Rev. Lett. 1964 Jul; 13(4):138–40. DOI: 10.1103/PhysRevLett.13.138 (cit. on p. 70)

118. Catmore JR. $B_s^0 \to J/\psi\,\phi$ with LHC-ATLAS: simulations and sensitivity studies. Figures 2.1 through to 2.4. Lancaster U., 2007 (cit. on p. 72)

119. Young HD, Freedman RA, Ford AL(L, Sears FW, and Zemansky MW. University physics with modern physics. eng. Harlow: Pearson, 2020. ISBN: 9781292314730 (cit. on p. 73)

120. Aaij R et al. Measurement of the Semileptonic CP Asymmetry in B^0–$\bar{B}^0$ Mixing. Physical Review Letters 2015; 114. DOI: 10.1103/PhysRevLett.114.041601 (cit. on p. 73)

121. Aad G et al. Measurement of the CP-violating phase ϕ_s in $B_s^0 \to J/\psi\phi$ decays in ATLAS at 13 TeV. Eur. Phys. J. C 2021; 81:342. DOI: 10.1140/epjc/s10052-021-09011-0. arXiv: 2001.07115 (cit. on pp. 73, 86, 137, 152, 157–161)

122. Angelopoulos A et al. Search for CP violation in the decay of tagged $\overline{K}^0$ and K^0 to $\pi^0\pi^0\pi^0$. Phys. Lett. B 1998; 425:391. DOI: 10.1016/S0370-2693(98)00256-1 (cit. on p. 73)

123. Bigi II and Sanda AI. CP violation. eng. Cambridge monographs on particle physics, nuclear physics, and cosmology ; 9. Cambridge, U.K. ; Cambridge University Press, 2000. ISBN: 0521443490 (cit. on pp. 76, 80)

124. Navas S et al. Review of particle physics. Phys. Rev. D 2024; 110. Specifically, the mesons summary document, rpp2024-sum-mesons, pages 29 and 30 for Kaons, and page 131 for the B meson.:030001. DOI: 10.1103/PhysRevD.110.030001 (cit. on pp. 78, 81)

125. Shapiro G. Physics 226 Lecture 16. PowerPoint presentation (cit. on pp. 79–80)

126. Charles J et al. Current status of the standard model CKM fit and constraints on $\Delta F = 2$ new physics. Physical Review D 2015 Apr; 91. ISSN: 1550-2368. DOI: 10.1103/physrevd.91.073007 (cit. on pp. 85, 137, 140)

127. Bona M et al. The unitarity triangle fit in the standard model and hadronic parameters from lattice QCD: a reappraisal after the measurements of Δm_s and $BR(B \to \tau\nu_\tau)$. Journal of High Energy Physics 2006 Oct; 2006:81–81. ISSN: 1029-8479. DOI: 10.1088/1126-6708/2006/10/081 (cit. on p. 85)

128. Artuso M, Borissov G, and Lenz A. CP Violation in the B_s^0 system. 2019. arXiv: 1511.09466 [hep-ph] (cit. on pp. 86, 137, 140)

129. Abazov VM et al. Measurement of the CP-violating phase $\phi_s^{J/\psi\phi}$ using the flavor-tagged decay $B_s^0 \to J/\psi\phi$ in 8 fb^{-1} of $p\overline{p}$ collisions. Physical Review D 2012 Feb; 85. ISSN: 1550-2368. DOI: 10.1103/physrevd.85.032006 (cit. on p. 86)

130. Collaboration C. Measurement of the Bottom-Strange Meson Mixing Phase in the Full CDF Data Set. Physical Review Letters 2012 Oct; 109. ISSN: 1079-7114. DOI: 10.1103/physrevlett.109.171802 (cit. on p. 86)

131. Aaij R et al. Precision Measurement of CP Violation in $B_S^0 \to J/\Psi K^+K^-$ Decays. Physical Review Letters 2015 Jan; 114. ISSN: 1079-7114. DOI: 10.1103/physrevlett.114.041801 (cit. on pp. 86, 139)

132. Aad G et al. Measurement of the CP-violating phase s and the B s 0 meson decay width difference with B s 0 →J/ decays in ATLAS. Journal of High Energy Physics 2016 Aug; 2016. ISSN: 1029-8479. DOI: 10.1007/jhep08(2016)147 (cit. on pp. 86, 118, 139)

133. Measurement of the CP violating phase ϕ_s in the $B_s \to J/\psi\,\phi(1020) \to \mu^+\mu^-\,K^+K^-$ channel in proton-proton collisions at $\sqrt{s} = 13$ TeV. Tech. rep. Geneva: CERN, 2020 (cit. on pp. 86, 137–140)

134. Aaij R et al. Updated measurement of time-dependent CP-violating observables in $B_s^0 \to J/\psi K^+K^-$ decays. The European Physical Journal C 2019 Aug; 79. DOI: 10.1140/epjc/s10052-019-7159-8 (cit. on pp. 86, 137, 139–140)

135. Aaij R et al. Resonances and CP violation in B_s^0 and $\overline{B}_s^0 \to J/\psi K^+K^-$ decays in the mass region above the $\phi(1020)$. Journal of High Energy Physics 2017 Aug; 2017. ISSN: 1029-8479. DOI: 10.1007/jhep08(2017)037 (cit. on p. 86)

136. Aad G et al. Measurement of the CP-violating phase ϕ_s in $B_s^0 \to J/\psi\phi$ decays in ATLAS at 13 TeV. The European Physical Journal C 2021 Apr; 81. ISSN: 1434-6052. DOI: 10.1140/epjc/s10052-021-09011-0 (cit. on pp. 86, 140)

137. Aaij R et al. First study of the CP-violating phase and decay-width difference in $B_s^0 \to \psi(2S)\,\phi$ decays. Physics Letters B 2016 Nov; 762:253–62. ISSN: 0370-2693. DOI: 10.1016/j.physletb.2016.09.028 (cit. on p. 86)

138. Aaij R et al. Measurement of the CP-violating phase ϕ_s in $\overline{B}_s^0 \to D_s^+D_s^-$ decays. Physical Review Letters 2014 Nov; 113. ISSN: 1079-7114. DOI: 10.1103/physrevlett.113.211801 (cit. on p. 86)

139. Aaij R et al. Measurement of the CP-violating phase ϕ_s in $\overline{B}_s^0 \to J/\psi\,\pi^+\pi^-$ decays. Physics Letters B 2014 Sep; 736:186–95. ISSN: 0370-2693. DOI: 10.1016/j.physletb.2014.06.079 (cit. on p. 86)

140. Aaij R et al. Measurement of the CP-violating phase ϕ_s from $B_s^0 \to J/\psi\,\pi^+\pi^-$ decays in 13 TeV pp collisions. Physics Letters B 2019 Oct; 797:134789. ISSN: 0370-2693. DOI: 10.1016/j.physletb.2019.07.036 (cit. on p. 86)

141. Tanabashi M et al. Review of Particle Physics. Phys. Rev. D 2018 Aug; 98(3):030001. DOI: 10.1103/PhysRevD.98.030001 (cit. on pp. 86, 120, 126, 138–139, 160)

142. Aaij R et al. Observation of B_s^0 – $\overline{B}_s^0$ mixing and measurement of mixing frequencies using semileptonic B decays. The European Physical Journal C 2013 Dec; 73. ISSN: 1434-6052. DOI: 10.1140/epjc/s10052-013-2655-8 (cit. on pp. 86, 138)

143. Aaij R et al. Precision measurement of the B0s–$\overline{\mathrm{B}}_{\mathrm{s}}^0$ oscillation frequency with the decay B0s→ Ds+. New Journal of Physics 2013 May; 15:053021. ISSN: 1367-2630. DOI: 10.1088/1367-2630/15/5/053021 (cit. on pp. 86, 138)

144. Abulencia A et al. Observation of B_s^0–$\overline{B}_s^0$ oscillations. Physical Review Letters 2006 Dec; 97. ISSN: 1079-7114. DOI: 10.1103/PhysRevLett.97.242003 (cit. on pp. 86, 138)

145. ATLAS Pythia 8 tunes to 7 TeV data. Tech. rep. Geneva: CERN, 2014 (cit. on p. 87)

146. Aad G et al. Public ATLAS Online Luminosity Plots for Run-2 of the LHC. https://atlas.web.cern.ch/Atlas/GROUPS/DATAPREPARATION/PublicPlots/2017/DataSummary/figs/mu_2015_2017.png. Accessed: 2025-10-13; from ATLAS Public results on luminosity, Run 2. 2017 (cit. on p. 88)

147. Aad G et al. Configuration and performance of the ATLAS b-jet triggers in Run 2. Eur. Phys. J. C 2021; 81:1087. DOI: 10.1140/epjc/s10052-021-09775-5. arXiv: 2106.03584 (cit. on p. 90)

148. Aad G et al. Improved electron reconstruction in ATLAS using the Gaussian Sum Filter-based model for bremsstrahlung. Tech. rep. All figures including auxiliary figures are available at https://atlas.web.cern.ch/Atlas/GR

OUPS/PHYSICS/CONFNOTES/ATLAS-CONF-2012-047. Geneva: CERN, 2012 (cit. on p. 97)

149. Aad G et al. Electron and photon performance measurements with the ATLAS detector using the 2015–2017 LHC proton-proton collision data. Journal of Instrumentation 2019 Dec; 14:P12006–P12006. ISSN: 1748-0221. DOI: 10.1088/1748-0221/14/12/p12006 (cit. on p. 101)

150. Aad G et al. Topological cell clustering in the ATLAS calorimeters and its performance in LHC Run 1. Eur. Phys. J. C 2017; 77:490. DOI: 10.1140/epjc/s10052-017-5004-5. arXiv: 1603.02934 [hep-ex] (cit. on p. 102)

151. Cacciari M, Salam GP, and Soyez G. The anti-ktjet clustering algorithm. Journal of High Energy Physics 2008 Apr; 2008:63–63. ISSN: 1029-8479. DOI: 10.1088/1126-6708/2008/04/063 (cit. on pp. 102, 108)

152. Cacciari M, Salam GP, and Soyez G. FastJet user manual: (for version 3.0.2). The European Physical Journal C 2012 Mar; 72. ISSN: 1434-6052. DOI: 10.1140/epjc/s10052-012-1896-2 (cit. on pp. 102, 109)

153. Aad G et al. ATLAS b-jet identification performance and efficiency measurement with $t\bar{t}$ events in pp collisions at $\sqrt{s} = 13$ TeV. The European Physical Journal C 2019 Nov; 79. ISSN: 1434-6052. DOI: 10.1140/epjc/s10052-019-7450-8 (cit. on pp. 102, 108)

154. ATLAS Collaboration. Jets. https://opendata.atlas.cern/docs/documentation/physic_objects/jets. ATLAS Open Data Documentation. CERN, 2024 (cit. on p. 107)

155. Aad G et al. Transforming jet flavour tagging at ATLAS. 2025. arXiv: 2505.19689 [hep-ex] (cit. on p. 107)

156. Aad G et al. Jet reconstruction and performance using particle flow with the ATLAS Detector. The European Physical Journal C 2017 Jul; 77. ISSN: 1434-6052. DOI: 10.1140/epjc/s10052-017-5031-2 (cit. on p. 108)

157. Aad G et al. ATLAS flavour-tagging algorithms for the LHC Run 2 *pp* collision dataset. Eur. Phys. J. C 2023; 83:681. DOI: 10.1140/epjc/s10052-023-11699-1. arXiv: 2211.16345 (cit. on pp. 109, 111)

158. Aad G et al. Precision measurement of the B^0 meson lifetime using $B^0 \to J/\psi K^{*0}$ decays with the ATLAS detector. The European Physical Journal C 2025; 85. The figure shown corresponds to a pre-version of Figure 4 in this publication. DOI: 10.1140/epjc/s10052-025-14232-8 (cit. on pp. 109–110)

159. Aad G et al. Time-dependent angular analysis of the decay $B_s^0 \to J/\psi\phi$ and extraction of s and the CP-violating weak phase s by ATLAS. Journal of High Energy Physics 2012 Dec; 2012. ISSN: 1029-8479. DOI: 10.1007/jhep12(2012)072 (cit. on pp. 114, 119)

160. Dighe A, Dunietz I, and Fleischer R. Extracting CKM phases and $B_s - \overline{B}_s$ mixing parameters from angular distributions of non-leptonic B decays. The European Physical Journal C 1999 Jan; 6:647–62. ISSN: 1434-6052. DOI: 10.1007/s100529800954 (cit. on p. 114)

161. Stone S and Zhang L. S-waves and the measurement of CP violating phases in B_s decays. Physical Review D 2009 Apr; 79. ISSN: 1550-2368. DOI: 10.1103/physrevd.79.074024 (cit. on p. 116)

162. Flatté S. Coupled-channel analysis of the and KK systems near KK threshold. Physics Letters B 1976; 63:224–7. ISSN: 0370-2693. DOI: https://doi.org/10.1016/0370-2693(76)90654-7 (cit. on pp. 116, 125)

163. Oakes LB. Measurement of the CP violating phase β_s in $B_s^0 \to J/\psi\,\phi$ decays. Figure 1.10, page 27. PhD thesis. Oxford, United Kingdom: University of Oxford, 2010 Jan. DOI: 10.2172/1007268 (cit. on p. 117)

164. Azfar F et al. Formulae for the analysis of the flavor-tagged decay $B_s^0 \to J/\psi\phi$. Journal of High Energy Physics 2010 Nov; 2010. ISSN: 1029-8479. DOI: 10.1007/jhep11(2010)158 (cit. on p. 116)

165. Aaij R et al. Determination of the Sign of the Decay Width Difference in the B_s^0 System. Physical Review Letters 2012 Jun; 108. ISSN: 1079-7114. DOI: 10.1103/physrevlett.108.241801 (cit. on p. 116)

166. Collaboration L. Updated average f_s/f_d b-hadron production fraction ratio for 7 TeV pp collisions. 2013 (cit. on p. 120)

167. Aubert B et al. Search for the $Z(4430)^-$ at BABAR. Physical Review D 2009 Jun; 79. ISSN: 1550-2368. DOI: 10.1103/physrevd.79.112001 (cit. on p. 120)

168. Aaij R et al. Study of the kinematic dependences of Λ_b^0 production in pp collisions and a measurement of the $\Lambda_b^0 \to \Lambda_c^+\pi^-$ branching fraction. Journal of High Energy Physics 2014 Aug; 2014. ISSN: 1029-8479. DOI: 10.1007/jhep08(2014)143 (cit. on p. 120)

169. Aaij R et al. Study of the production of Λ_b^0 and Ξ_b^0 hadrons in pp collisions and first measurement of the $\Xi_b^0 \to \Xi_c^+\pi^-$ branching fraction. Chinese Physics C 2016 Jan; 40:011001. ISSN: 1674-1137. DOI: 10.1088/1674-1137/40/1/011001 (cit. on p. 120)

170. Aaij R et al. Observation of $J/\psi p$ Resonances Consistent with Pentaquark States in $\Lambda_b^0 \to J/\psi K^- p$ Decays. Physical Review Letters 2015 Aug; 115. ISSN: 1079-7114. DOI: 10.1103/physrevlett.115.072001 (cit. on p. 120)

171. Aaij R et al. Measurement of the polarization amplitudes in $B^0 \to J/\psi K^*(892)^0$ decays. Physical Review D 2013 Sep; 88. ISSN: 1550-2368. DOI: 10.1103/physrevd.88.052002 (cit. on p. 120)

172. Aad G et al. Studies of radial distortions of the ATLAS Inner Detector. Tech. rep. Geneva: CERN, 2018 (cit. on p. 123)

173. Aaij R et al. Measurement of the polarization amplitudes in $B^0 \to J/\psi K^*(892)^0$ decays. Physical Review D 2013 Sep; 88. ISSN: 1550-2368. DOI: 10.1103/physrevd.88.052002 (cit. on p. 124)

174. Barton AE et al. Measurement of the CP-violating phase ϕ_s and other system parameters in $B_s^0 \to J/\psi\,\phi$ decay in ATLAS at 13 TeV. Tech. rep. Accessed: 2025-10-30. Geneva: CERN, 2019 (cit. on p. 125)

175. Khachatryan V et al. Measurement of the CP-violating weak phase ϕ_s and the decay-width difference $\Delta\Gamma_s$ using the $B_s^0 \to J/\psi\,\phi(1020)$ decay channel in pp collisions at $\sqrt{s} = 8\,\text{TeV}$. Physics Letters B 2016 Jun; 757:97–120. ISSN: 0370-2693. DOI: 10.1016/j.physletb.2016.03.046 (cit. on p. 139)

176. Punzi G. Comments on Likelihood fits with variable resolution. 2004. arXiv: physics/0401045 [physics.data-an] (cit. on pp. 141–142)

177. Lyons L. Statistical Issues in Particle Physics. *Particle Physics Reference Library: Volume 2: Detectors for Particles and Radiation*. Ed. by Fabjan CW and Schopper H. Cham: Springer International Publishing, 2020 :645–92. ISBN: 978-3-030-35318-6. DOI: 10.1007/978-3-030-35318-6_15 (cit. on p. 143)

178. Aad G et al. Precision measurement of the B^0 meson lifetime using $B^0 \to J/\psi K^{*0}$ decays with the ATLAS detector. 2024. arXiv: 2411.09962 [hep-ex] (cit. on pp. 145, 158–159)

179. Pivk M and Le Diberder F. : A statistical tool to unfold data distributions. Nuclear Instruments and Methods in Physics Research Section A: Accelerators, Spectrometers, Detectors and Associated Equipment 2005 Dec; 555:356–69. ISSN: 0168-9002. DOI: 10.1016/j.nima.2005.08.106 (cit. on pp. 148, 150, 152)

180. Chelluri R. Background Estimation using Multivariate Techniques – A Case Study with the ATLAS Experiment. Chapter 6 discusses sPlot technique for background estimation. mastersthesis. Siegen: Universität Siegen, 2020 (cit. on pp. 150, 152)

181. Sampson EJ. Large Radius Tracking systematics based off Inner Detector material map variations. Tech. rep. ATL-COM-SOFT-2023-122. Geneva: CERN, 2023 (cit. on p. 168)

182. Experiment A. The Inner Detector — atlas.cern. `https://atlas.cern/Discover/Detector/Inner-Detector`. [Accessed 26-09-2024]. 2024 (cit. on p. 169)

183. Facini G. Jira, https://its.cern.ch/jira/browse/ATLIDTRKCP-389. April 13th, 2023. 2022 (cit. on p. 169)

184. Burzynski JC. Improved Track Reconstruction Performance for Long-lived Particles in ATLAS. ATL-PHYS-PROC-2022-050. Geneva, 2022 (cit. on p. 170)

185. Aad G et al. Performance of the reconstruction of large impact-parameter tracks in the ATLAS inner detector. ATL-PHYS-PUB-2017-014. Geneva, 2017 (cit. on p. 170)

186. Navas S et al. Review of Particle Physics. Phys. Rev. D 2024; 110. Section 45: "Monte Carlo Particle Numbering Scheme". See page 1 of the PDF.:030001. DOI: `10.1103/PhysRevD.110.030001` (cit. on p. 173)

187. Uncertainties. Uncertainties package. `https://pythonhosted.org/uncertainties/`. Accessed: 2023-05-28 (cit. on pp. 173, 175)